Self-assembly of ferromagnetic micro/nano-particles with perpendicular magnetic anisotropy

Michael Richard Stanton

Supervisor: **Prof. Russell Cowburn**

Department of Physics

University of Cambridge

This thesis is submitted for the degree of *Doctor of Philosophy*

St. Edmund's College

October 2020

For Mom, Dad, and Alexander,
who we love and miss

Declaration

This thesis is the result of my own work and includes nothing which is the outcome of work done in collaboration except as declared in the Preface and specified in the text. It is not substantially the same as any that I have submitted, or, is being concurrently submitted for a degree or diploma or other qualification at the University of Cambridge or any other University or similar institution except as declared in the Preface and specified in the text. I further state that no substantial part of my thesis has already been submitted, or, is being concurrently submitted for any such degree, diploma or other qualification at the University of Cambridge or any other University or similar institution except as declared in the Preface and specified in the text. It does not exceed the prescribed word limit of 60,000 words, excluding table of contents, photographs, diagrams, figure captions, list of figures/diagrams, list of abbreviations/acronyms, bibliography, and acknowledgements, for the Physics and Chemistry Degree Committee.

Michael Richard Stanton

October 2020

Abstract

Self-assembly of ferromagnetic micro/nano-particles with perpendicular magnetic anisotropy

Michael Richard Stanton

Magnetic particles offer an interesting platform for self-assembly, as their dipolar interactions and response to magnetic fields can be used to drive and manipulate assembly. Many magnetic particles used so far in these applications are quite simple in their properties, such as iron oxide particles or magnetic colloids. To grow the potential of magnetic self-assembly, more complex particles are being developed to increase the complexity and functionality of the assemblies. In this vein, this work has created magnetic particles based on thin films of CoFeB/Pt with perpendicular magnetic anisotropy (PMA) to use for self-assembly. PMA films have been long developed for magnetic recording and computing applications, so they are well understood and optimized. Their high moment and strong anisotropy make them good candidates for a highly directional equilibrium self-assembly system. The particle construction was first optimized in films, looking at both the magnetic and structural properties needed for particles. The particles are then patterned from the film using top-down lithographic methods. Using top down methods, as opposed to the chemical synthesis methods used for most magnetic particles, is what allows the tuneable magnetic film properties to be transferred to particles. Once in liquid, the individual field response and interactions of the particles were analysed, to understand how they would best assemble. Then, the particles were assembled into 1D and 2D structures, which were then manipulated with magnetic fields to understand how these assemblies could be controlled and actuated. Assemblies of 3D structures on chip were also created and observed. These results demonstrate the fundamental assembly capabilities of the system and begin to show how it might be applied in microrobotics or micromachinery.

Acknowledgements

My first thanks must go to the NanoDTC, which is the reason I was able to come to Cambridge and have the wonderful experience I did here. To Profs. Jeremy Baumberg, Stephan Hofmann, and Erwin Reisner, for their work in setting up and managing the program, and especially to Dr. Karishma Jain, along with Emma Clark and Kimberly Cole, whose day-to-day efforts and enthusiasm have created a wonderful community and amazing program for the development of researchers. Alongside the NanoDTC I must also acknowledge and thank the Cambridge Trust for their financial support, without which none of this would have been possible.

Through the NanoDTC I was able to undertake this PhD, moving through the program to the supervision of Prof. Russell Cowburn and Prof. Erika Eiser. It is through Russell and the group he has created here that such a project was able to happen, as he has built a space where we can really explore interesting and unique corners of science, leading to novel creations and unexpected ideas. I'm grateful for the resources, both in the lab and the people who make it up, that he has brought together and the way he supports it all. Erika as well has always been a welcoming and interested presence, keeping engaged and supportive of the work even though the project didn't end up strongly matching her work, and I'm grateful for that unconditional support. Alongside Russell and Erika, I must especially thank Dr. Dorothée Petit, without whom this thesis and this project would never have reached the level that it did. With your deep knowledge of magnetism and keen attention to detail, you help make sure everything our group produces meets a high standard and keep all of us pushing deeper to understand and explore everything we do.

Of course, nothing in science is accomplished in a vacuum, and I would like to acknowledge and thank all the members of the Cowburn group who I have worked alongside these years. First, to Tarun and Dédalo – two of the best scientists I have ever met. Thank you for always providing good ideas and better friendship, and for always being happy to answer a question or lend a hand, whether for this thesis, a first year report, or on a random day around the lab. Next, to Emma, for being a wonderful companion in the lab and many trips around the world, it was great to have someone to share the work and experience (and some rowing chat) with. To Jung-Wei and Jake, two of the hardest working and most selfless people I have ever met, I'm grateful the way you're both always so willing to help anytime and anywhere, and for all the assistance you gave to me. To Alex, Amalio, Spencer, Lucy, Jerry, Holly, Selma, Luka, Fanfan, Claire and many more from the group over these past years, thank you for making our lab a fun and interesting environment to help cut through the (occasional) daily drudgery of physics research.

Of course, my time in Cambridge encompassed much more than what happened in the lab, and it is the community I had here that helped me stay sane and motivated through this work. First, all

the other members of the NanoDTC 2015 cohort, from those early practicals to evenings at Nanohaus to now, it's remarkable how far we've all come and I was glad to do it together with you all. Next, I must mention all the friends from St. Edmund's and the Cambridge community that helped make this a wonderful journey. Patrick, Glen, Jia, Ming, Sam, Timarie, Maanik, Flo, Floss, Reuben, Sonja, Max, Sam, Ali, Clare, Alex, Ethan, TJ, Robin, Basil, Rohan, Alex, Marta, Lianne, Ben, and many many more, thank you all for being great friends and making Cambridge such an amazing place to work and live.

Finally, I must thank my mom and dad for their consistent and incredible support for me in whatever I choose to do. I appreciate that you are both always so unwavering, even if I decide to move an ocean away, and the way you could understand and sympathize with the challenges of a PhD. With this I hope we can now add one more doctor to the family.

Table of contents

List of figures

List of tables

Glossary of acronyms

PMA	perpendicular magnetic anisotropy
HDD	hard disk drive
TMR	tunnel magneto-resistance
GMR	giant magneto-resistance
MTJ	magnetic tunnel junction
STT	spin-torque transfer
MRAM	magnetic random access memory
DNA	deoxyribonucleic acid
CGS	centimetre-gram-second
SI	Système international
MCA	magneto-crystalline anisotropy
GPU	graphics processing unit
MOKE	magneto-optical Kerr effect
VSM	vibrating sample magnetometry
AFM	atomic force microscope
DC	direct current
LOR	lift-off resist
DMSO	dimethyl sulfoxide
CMOS	complementary metal-oxide-semiconductor
SEM	scanning electron microscope
FEG	field emission gun
SRT	spin-reorientation transition
RKKY	Ruderman–Kittel–Kasuya–Yosida
SAF	synthetic anti-ferromagnet
JKR	Johnson-Kendall-Roberts

1 Introduction

Perhaps every person has, at some point in their life, experimented with magnetic self-assembly. Whether it was through building boxes and pyramids from collections of neodymium spheres, through watching the interplay of two bar magnets as they snap together, or even through tracing patterns in piles of magnetized iron filings with a horseshoe magnet, the interactions of magnetic particles can be used to build and manipulate structures in a number of ways, both on the macro- and micro-scale. It is these properties embodied by magnets—interaction at a distance and response to an external magnetic field, along with the great variety of shapes, compositions, and anisotropies offered by the range of magnetic materials—that interest in magnetic self-assembly on smaller scales has evolved. This work will look specifically at one class of magnetic materials: magnetic thin films with perpendicular magnetic anisotropy (PMA). By translating these films into particles, their anisotropic properties can be leveraged in a self-assembly system. To help understand the background which has led to this work, we will explore the development of these films, as they evolved from fundamental scientific discovery to magnetic recording and current advances in spintronics. In addition to this, the history and advancement of self-assembly will be explored. Advances in fabrication and synthesis of micro- and nano-particles in the last century have opened up many new systems through which self-assembly of unique and functional structures can be performed. In the context of this greater field of self-assembly, the value of magnetic, especially anisotropic magnetic, particles will be highlighted.

1.1 The development of thin films with PMA

The initial discovery of perpendicular magnetic anisotropy in thin films comes from work by Néel in 1954, who theoretically predicted the existence of such anisotropy due to the free surface of a thin film.[1] The specific physical interactions responsible for such an effect will be further addressed in Chapter 2, but the discovery sparked great fundamental scientific interest and spawned a new field focused on magnetic films with PMA. This discovery was verified experimentally over a decade later in Cu/NiFe films and repeated in a number of different oligatomic (single crystal of few atomic layer) films, such as Co and Fe.[2–5] PMA was further discovered as an interfacial effect in multilayer films consisting of magnetic and non-magnetic layers.[5,6] The interesting physics governing this anisotropy also led to an extensive range of theoretical modelling and analysis of the surface and interface anisotropy, to elucidate the quantum mechanical origins of the effect.[7–10] However, as these early experimental studies relied on single crystal epitaxial films, it remained an area of theoretical and scientific interest, having not yet reached a level of accessibility sufficient to be incorporated into applications.

A major breakthrough in PMA film formation was the discovery of sputtered Co/Pd multilayers by Carcia in 1985, and the subsequent creation of Co/Pt layers in 1988.[11,12] By retaining PMA in multilayers using more accessible sputter- and vapour-deposition techniques, PMA materials became an interesting candidate for applications such as magnetic recording.[13] Following this work, other multilayer combinations, such as Co/Au, Co/Ru, Fe/W, Fe/Au and many more, were discovered and characterized.[14–17] With the new ability to create such a variety of film structure came great interest in the potential applications of such material systems. The improvement of magnetic recording technology was one of the primary drivers of such research, and indeed is cited in Carcia's 1985 paper as the primary potential applications of the Co/Pd films. To help understand how the magnetic recording industry drove research into PMA films, we will track the progress and needs of magnetic recording that necessitated new technologies like PMA materials.

1.1.1 Magnetic recording

Magnetic recording has a long history, with devices being made to store and read back data stored in magnetic materials more than 120 years ago.[18] Magnetic materials offer obvious advantages for data storage, as bits can be easily encoded into the magnetization direction of anisotropic magnetic materials, and these bits can be read and written using applied field and non-invasive magnetic field sensors. While initial inventions of recording media used steel wires or tape coated in iron particles, it was not until the advent of the information revolution and advances in electronic and computing technology that high-density magnetic recording media was truly realized and implemented. Magnetic tape still plays a crucial role in long-term data storage, but in the early days of computer storage development it was quickly eclipsed by magnetic disks and hard disk drives (HDD), which allowed for greater write and read speeds to match the processing capacity of computers.[19,20] Initial hard disk drives relied on longitudinal magnetic media, where the in-plane shape anisotropy of materials was used to store data. Constant efforts were made to improve the areal storage density of the disks, which eventually encountered limits on the densities that longitudinal recording could achieve. As bit size was reduced to increase storage density, issues of thermal instability began to arise. The thermal barrier to switching of a magnetic particle is proportional to the anisotropy and volume of the particle.[21] Thus, as bit sizes decrease, anisotropy needs to be increased to maintain stability against random thermal fluctuations. After decades of development and use, longitudinal recording media began to reach fundamental density limits of around 100 Gbits/in^2, which necessitated alternative technology such as perpendicular magnetic recording.[22]

Perpendicular recording was found to be able to reach higher bit densities than longitudinal recording.[22] This is due primarily to the high anisotropy achievable in perpendicular media, but also because of the way perpendicular bits can be addressed in writing. It was possible to address the perpendicular media with larger write fields than in longitudinal media, thus allowing high anisotropy,

high coercivity materials with better thermal stability to be used in perpendicular recording. This type of perpendicular media was first explored by Iwasaki in 1977, who used CoCr alloy films with perpendicular anisotropy to demonstrate the advantages of the technology.[23] While IBM had experimented with perpendicular recording media in the 1950s as it was developing the first disk drive technology, a number of failures in the development led to longitudinal media becoming the preferred technology.[24] Iwasaki's work renewed interest in perpendicular media and coincided well with the advances in PMA films discussed previously. Throughout the 1980s and 1990s it was increasingly cited as the motivation for improvements in PMA films. It was still many years before the application of perpendicular recording was realized, but, due the limitations of longitudinal media and calls for ever-increasing storage density, it was inevitable that perpendicular recording would become the standard for magnetic disk drives, and it did, with the first commercial releases in the early 2000s.[25] Figure 1.1 shows the introduction of perpendicular recording media on the timeline of hard disk drive (HDD) development. Its introduction has helped spur continued growth in storage density, allowing drives to far surpass the longitudinal limit of 100 Gbit/in^2, reach over 1 Tbit/in^2 and greater in recent years. It is clear that the increased interest in perpendicular magnetic recording played a key role in helping develop PMA films.

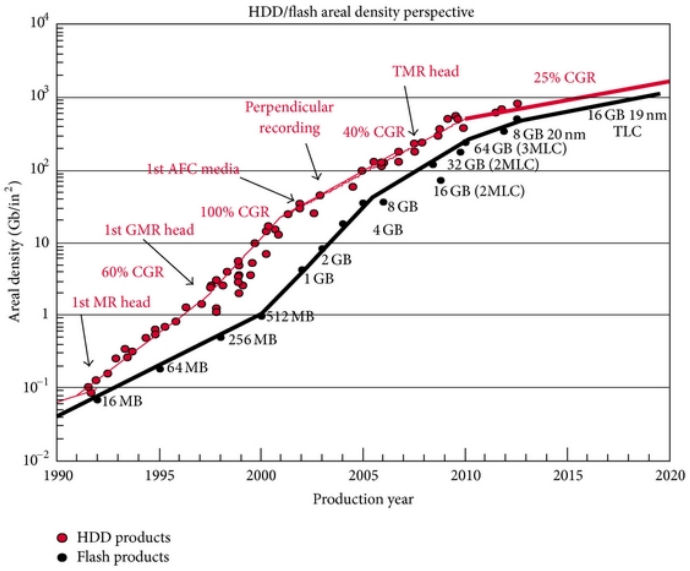

Figure 1.1 Comparison of HDD and flash storage technology since 1990
Comparison of magnetic HDD and flash storage density since 1990 is made, with significant stages of magnetic HDD development. Reproduced under Creative Commons Attribution License (CC BY 3.0) from Ref 26.[26]

Another significant impact on the magnetic recording and computing industry is the implementation of spin-based devices, both as read and write components in traditional HDDs and to open a new frontier for magnetic computing technologies. The discovery of tunnel magnetoresistance

(TMR) by Julliere and of giant magneto-resistance (GMR) by Fert and Grünberg, along with the demonstration of current-driven switching of magnetic layers by Slonczewski, created a new paradigm in which current, spin, and magnetization can be combined for more efficient detection and manipulation of magnetic states, with great benefit for the magnetic recording industry and beyond.[27–30] All of these discoveries relied on magnetic thin film technology and created new opportunities for applications of thin films, including PMA thin films. As can be seen in Figure 1.1, GMR and TMR technologies were crucial in increasing storage density through improvements in read head technology, allowing smaller heads to read higher density media.

These new discoveries also enabled progression to more advanced magnetic computing and storage technology, such as magnetic random access memory (MRAM) and spin-torque transfer MRAM.[31] The use of TMR in magnetic tunnel junctions (MTJs) allows for different junction resistance states depending on the relative magnetization states in the junction, which can then be used in memory devices. Additionally, these discoveries helped enable the use of spin-polarized currents. When a spin-polarized current is passed through a magnetic layer, the spin-polarized electrons will exert a torque on the magnetization that can be used to switch the magnetization direction.[32] Combining these functions has led to the development of STT-MRAM, which combines the non-volatility of magnetic storage with the addressability and speed of a current-driven read and write process. Similar to recording media, these technologies were initially formed using in-plane magnetic thin films. However, as the technology has improved, with a demand for higher densities and greater performance, in-plane materials began to reach stability limits which were difficult to overcome.[31] Again, PMA films offered increased performance and stability, allowing greater densities of devices to be achieved.[33] The use of PMA films in MTJs and STT-MRAM was especially accelerated with the discovery of CoFeB/MgO, a perpendicular magnetic film with excellent TMR properties.[34] The combination of high TMR ratio, small size, and low switching current allows spintronic devices based on PMA materials to reach new levels of performance. This has driven a further increase in research into PMA films, as these materials will underpin the next generation of magnetic storage and computing devices.

Overall, it is clear how the development of PMA films closely tracks the growth of magnetic recording in the latter half of the 20th century and the current advancement of spin-based devices. For the purposes of this work, the continued research on PMA films over the last five decades has generated a wealth of materials and techniques that can be leveraged for the creation of magnetic particles and a self-assembly system based on those particles.

1.2 Self –Assembly

Self-assembly is ubiquitous in our world and has been for hundreds of millions of years. Nature has used self-assembly in the creation of all biological systems – we, and all other living organisms, are the finest examples of hierarchical self-assembly that have ever been created. Advances in micro- and nano-fabrication and nano synthesis have opened up the possibility of designed self-assembly systems on micro- and nano-length scales, as these advances have helped create the building blocks needed to form interesting and functional assemblies. Starting from this perspective, we will explore the principles and recent advances in self-assembly.

1.2.1 Building from the bottom

As with many works discussing nanotechnology and related disciplines, such as self-assembly, we will start from the ubiquitously (and perhaps overly) referenced talk by Richard Feynman in 1959: 'There's Plenty of Room at the Bottom.'[35] In this lecture he espouses the benefits and possibilities of working on the micro- and nano-scales, with potential for encoding information and controlling materials all the way down to the single atom. It is in this vein that micro- and nanotechnology arose, with the computing industry leading the charge towards miniaturization for improvement in performance and capability.

When creating objects on the nanoscale, there are two approaches: top-down and bottom-up. Top-down approaches have long dominated the semiconductor industry, where photolithography has been the standard tool for patterning silicon to create nanoscale devices. While great advances are constantly being made to improve these top-down approaches, they are still fundamentally limited in some ways, such as by the two-dimensional nature of patterns and difficulty and costs associated with increased miniaturization.[36] These difficulties can be overcome by using a bottom-up approach, where small building blocks self-assemble into desired structures. The building blocks are tuned to direct their own assembly into the desired structure. In theory, such a system would be an easy-to-manufacture platform from which a number of nanoscale devices could be created. This would call for systems of particles with tuneable and controllable interactions and a range of sizes, shapes, materials, and functions, so a wide variety of assemblages can be formed.

1.2.2 Evolution of self-assembling systems

The field of self-assembly initially grew out of organic chemistry and the assembly of supramolecular structures.[37] While the chemical bonding between atoms can be used to create molecules up to certain sizes and forms, larger assemblages of molecules, such as molecular crystals,

self-assembled monolayers, or lipid bilayers, will rely on non-bonding interactions to drive molecules into a larger equilibrium state. In this way, self-assembly offers a method for creating ordered structures at sizes between the molecular and macroscopic length scales. Due to the highly interdisciplinary nature of self-assembly and the number of different systems that can be included in such a concept, efforts have been made to define the field and put some sort of characterization of what constitutes self-assembly. Whitesides distinguishes 'self-assembly' from 'formation' by limiting self-assembly to "processes that involve pre-existing components (separate or distinct parts of a disordered structure), are reversible, and can be controlled by proper design of the components."[38] In another work by Grzybowski, it is defined as "spontaneous formation of organized structures from many discrete components that interact with one another directly… and/or indirectly, through their environment," with key distinction being the creation of ordered structures and the use of discrete, designed building blocks to do so.[39] As we can see, there is agreement that self-assembly must be a process involving the ordering of designed components into a larger structure, where the interactions between the components are designed and used to drive toward the desired assembly. Within this defined space of self-assembly, there are two distinct types: static and dynamic assembly.[38] Static self-assembly occurs when the structure forms at a local or global equilibrium and does not require continued energy input to maintain the assembly, while in the case of dynamic self-assembly the structures exist in a non-equilibrium state, which is maintained by a constant energy input, such as a magnetic or electric field.[39] Additional sub-categorizations exist, such as directed self-assembly, where external fields or gradients are used to influence alignment of components, or templated self-assembly, where some structure or feature of the surroundings influences the static or dynamic assembly of components.[38,40] To reduce external forces, such as friction, that could impede assembly, self-assembly almost always takes place in liquids, as it will in this work.

Self-assembly depends on the reversibility, specificity, directionality, and complexity of the interactions.[39] For this reason, often more than one mode of interaction between components is used, to provide tuneable complexity to the system. Some examples of different interactions used to mediate self-assembly processes include van der Waals, hydrophobic/hydrophilic, magnetic/electric dipolar, capillary, entropic, and steric.[38,39] Not all interactions are necessarily attractive by design, as the balance between attractive and repulsive forces can be used to build unique and modifiable forms. In pursuit of more interesting interactions and assemblies, many efforts are made to increase the anisotropy in particles, as particle anisotropies, whether in shape, interaction (through patchiness), or aspect ratio, will lead to differences in interaction and assembly.[41]

Self-assembly systems have been created with a range of different materials. While early work focused on different interesting molecules, such as dumbbell-shaped rotaxane or discs of cyanuric acid and melamine, efforts quickly evolved to a wide range of nano-, micro-, and even macro-particles to study the various interactions and assemblies that could be accomplished.[36] On the nanoscale, assembly of metallic nanoparticle lattices are common, formed either in two dimensions at

air-liquid or liquid-liquid interfaces or through evaporation, or in three dimensions by magnetic or electric dipole interactions.[42,43] Microscale assemblies can be constructed from electrically polarized metallic micro-rods or microscale colloids that use DNA to mediate interaction.[44,45] At larger dimensions many experiments have used air-liquid or liquid-liquid interfaces to trap millimetre-size particles and study the simple assembly rules that different shapes and interaction potentials can cause.[46,47] It is difficult to explicitly cover all the various materials, shapes, length scales, interactions, and anisotropies that have been experimented with to investigate self-assembly, but hopefully these examples provide a flavour of the different areas undertaken. However, outside of this overview, special acknowledgement must be given to DNA self-assembly, which has become a robust area of research due to the amazing specificity of interaction provided by DNA. Since the discovery of DNA origami and its potential for 2D and even 3D designed patterning, many self-assembly systems have incorporated DNA as a key component.[48] Examples include using DNA for templating or as an interactive element on nanoparticles or colloidal structures, as well as the creation of pure DNA superstructures in three dimensions, with high complexity, and programmable shapes.[49–54] While DNA does lack the potential robustness of inorganic building blocks and cannot be easily addressed with external stimuli, compared to magnetic or electrically polarized particles, it still has set a standard for what self-assembly can accomplish with the right building blocks. With this wide variety of assembly systems, a number of applications in photonics, medicine, energy harvesting and storage, micro- and nano-fabrication, and micromachines have been found for self-assembly, and more continue to be investigated as new building blocks are discovered.[55–59]

1.2.3 Magnetic self-assembly

In this work, we will focus specifically on magnetic self-assembly. Magnetic self-assembly covers a range of static and dynamic self-assembly systems, including a variety of magnetic or polarizable particles.[58] Due to the ease with which magnetic fields can be used to influence and guide assemblies, dynamic or directed strategies are often employed, where the specific applied field sequence can be altered to change the resulting structure. Equally, static assemblies can be formed, driven by the magnetic moments of the individual particles. Magnetic interactions between particles and larger magnetic field sources can also be an interesting avenue for templated assembly, such as the assembly of magnetic nanoparticle arrays on a hard disk drive platter.[60,61] Magnetic assembly systems are interesting because of the inherent interaction given by the particle magnetism and the way this magnetism can be tuned by the particle composition, along with the ability to manipulate the assemblies and particles with external magnetic fields. Additionally, magnetic assemblies, whether dynamic or static, can potentially be dis-assembled or reversed through application of an applied field, which is useful for creating reconfigurable assemblies, where one set of particles can form multiple different structures.

Interests and research into magnetic self-assembly grew out of work with ferrofluids, which are colloidal solutions of magnetic nanoparticles. The chaining of particles within ferrofluids was studied to characterize these formations and understand how they affected the properties of the fluid.[62,63] From these early studies on chaining and aggregation, interest developed around how ordered structures could be created from different building blocks, such as cubic particles.[64] Following on this early work, a vast library of particle and assembly combinations have been developed. These include simple spherical ferromagnetic or superparamagnetic nanoparticles, which can be used for the creation of one-, two-, and three-dimensional structures, as well as more anisotropic particles, such as two-sided Janus particle or patchy colloids.[65–67] Spherical particles can be used to create structures like chains, sheets, and 3D crystals.[65,68] By changing particle interactions and anisotropy through, for instance, using differently shaped particle, interesting assemblies like ribbons and 3D helical structures can be formed.[69,70] Notably for this work, nanoplatelets of Co and barium hexaferrite with in- and out-of-plane anisotropy have been chemically synthesised and shown assembly into chain and interesting flower-like structures.[71,72] Many of these different assembly methods use field-guided or dynamic assembly. This is especially necessary when organizing paramagnetic particle which do not have their own intrinsic moment to drive interactions. Magnetic particles can also work as a guide for self-assembly of non-magnetic particle, where the application of a magnetic field to a ferrofluid helps organize particles into ordered arrays or other type of superstructures.[73,74] Magnetic self-assembly is also commonly used as a method for building micro-machines, such as micro-swimmers that use assembled flagella for propulsion, or swarms of magnetic micro-robots made from chains of magnetic particles.[75,76] Such micro-machines have mainly found applications in biological and medical fields, where these machines can perform functions like sorting and separation, cell manipulation, sensing, or even targeted therapies.[75] One large benefit of such magnetic machines is the ability of driving magnetic fields to manipulate the machines at a distance, even in liquids or biological tissue.[77] Other varied applications exist for the different assembled structures listed above, such as the formation of tuneable photonic structures from ordered arrays, creation of nanoparticle-based high-density magnetic recording devices, or nano- and micro-manufacturing of desired structures.[78,79]

One common thread in these varied magnetic self-assembly systems is the use of anisotropy in the particle form to drive new and interesting interactions. By changing shape, coatings, magnetic properties, response to applied fields, and other factors, particles can be designed to form more complex and intricate assemblies, opening up new applications and avenues for magnetic self-assembly.[80,81]

1.3 Thesis aims – self-assembly of micro-/nano-particles with perpendicular magnetic anisotropy

PMA thin films offer an interesting class of magnetic materials that is well-developed and tuneable in its properties. Decades of research in the fields of magnetic recording and spin-based devices have led to a large range of materials and methods that can be exploited to create PMA films with a range of properties. The films offer magnetic properties, such as strong perpendicular magnetic anisotropy, that are rarely found in current magnetic self-assembly systems. Furthermore, the particles created from the magnetic thin films will have a unique planar geometry with a high aspect ratio. This type of particle geometry, combined with the perpendicular magnetic anisotropy of the film, offers a novel approach to be exploited for self-assembly. As outlined above, self-assembly systems have worked to develop anisotropy in particles to increase the complexity of particle interaction, and thus, the complexity and properties of assemblies. With planar particles with PMA, the high moment and small inter-particle distance will promote sustained static assemblies that do not require magnetic field input, leaving magnetic fields free for particle actuation and control. Actuation could be improved in these particles versus existing systems given the high moment and large magnetic anisotropy of the particles.

The aim of this thesis is to create a self-assembly system using ferromagnetic planar micro-/nano-particles with PMA as the building blocks. We will first develop the properties that are desired in a magnetic particle for self-assembly, among them a high moment, large perpendicular anisotropy, and controllable coercivity. Using this framework, we will optimize the magnetic thin film, looking at the magnetic and non-magnetic components of the multilayer film, including the addition of non-magnetic layers for the purpose of structural support, which is necessary for the high aspect ratio particles being created from this film. After optimizing the properties of the magnetic thin film, the film will then be patterned and combined with a release layer, creating micron-sized particles that can be released into liquid. This particle patterning and release system will use top-down lithographic techniques, building on capabilities previously developed for synthetic anti-ferromagnetic thin film particles.[82] The patterning and release process will be adjusted and improved to meet the needs of particle self-assembly. Once the particles are created, their behaviour in liquid will be analysed, looking at the stability, interactions, and field response of single particles. Then, particles will be assembled in liquid. The form of the assemblies and their response to externally applied magnetic field will be analysed. Additionally, templated assembly of the particles will be undertaken, to see the range of assemblies such particles can form. The development of this self-assembly system will explore how these unique anisotropic magnetic particles can be leveraged to create assemblies with interesting properties and responses, with a view toward potential applications.

1.4 References

1. Neel, L. L'approche à la saturation de la magnétostriction. *J. Phys. le Radium* **15**, 376–378 (1954).
2. Gradmann, U. & Müller, J. Flat Ferromagnetic, Epitaxial 48Ni/52Fe(111) Films of few Atomic Layers. *Phys. status solidi* **27**, 313–324 (1968).
3. Gradmann, U. Magnetism in oligatomic films. *J. Appl. Phys.* **40**, 1182–1186 (1969).
4. Gradmann, U. & Müller, J. Ferromagnetism of monoatomic cobalt films. *Czechoslov. J. Phys.* **21**, 553–556 (1971).
5. Koepke, R. & Bergmann, G. Magnetic interface-anisotropy of amorphous iron in contact with nonmagnetic metals. *Zeitschrift für Phys. B Condens. Matter Quanta* **21**, 185–191 (1975).
6. Gradmann, U. Magnetism of surfaces and interfaces. *J. Magn. Magn. Mater.* **6**, 173–182 (1977).
7. Gradmann, U. Ferromagnetism near surfaces and in thin films. *Appl. Phys.* **3**, 161–178 (1974).
8. Bennett, A. J. & Cooper, B. R. Origin of the magnetic 'surface anisotropy' of thin ferromagnetic films. *Phys. Rev. B* **3**, 1642–1649 (1971).
9. Gay, J. G. & Richter, R. Spin anisotropy of ferromagnetic films. *Phys. Rev. Lett.* **56**, 2728–2731 (1986).
10. Bruno, P. Tight-binding approach to the orbital magnetic moment and magnetocrystalline anisotropy of transition-metal monolayers. *Phys. Rev. B* **39**, 865–868 (1989).
11. Carcia, P. F., Meinhaldt, A. D. & Suna, A. Perpendicular magnetic anisotropy in Pd/Co thin film layered structures. *Appl. Phys. Lett.* **47**, 178–180 (1985).
12. Carcia, P. F. Perpendicular magnetic anisotropy in Pd/Co and Pt/Co thin-film layered structures. *J. Appl. Phys.* **63**, 5066–5073 (1988).
13. Zeper, W. B., Greidanus, F. J. A. M. A. M., Carcia, P. F. & Fincher, C. R. Perpendicular magnetic anisotropy and magneto-optical Kerr effect of vapor-deposited Co/Pt-layered structures. *J. Appl. Phys.* **65**, (1989).
14. Den Broeder, F. J. A., Kuiper, D., Van De Mosselaer, A. P. & Hoving, W. Perpendicular magnetic anisotropy of Co-Au multilayers induced by interface sharpening. *Phys. Rev. Lett.* **60**, 2769–2772 (1988).
15. Sakurai, M., Takahata, T. & Moritani, I. Magnetic and magneto-optical properties of Co/Ru multilayers. *J. Magn. Soc. Japan* **15**, 411–414 (1991).
16. Elmers, H. J. & Gradmann, U. Magnetic anisotropies in Fe(110) films on W(110). *Appl. Phys. A Solids Surfaces* **51**, 255–263 (1990).
17. Johnson, M. T. *et al.* Magnetic anisotropy in metallic multilayers. *Reports Prog. Phys.* **59**, 1409–1458 (1996).

18. Engel, F., Hammar, P. & Hess, R. L. *A Selected History of Magnetic Recording The Premiere of the Magnetophon Audio Tape Recorder in Berlin, 1935 The Development and First Implementa-tion of Magnetic Recording*.
19. Lantz, M. Why the Future of Data Storage is (Still) Magnetic Tape - IEEE Spectrum. (2018). Available at: https://spectrum.ieee.org/computing/hardware/why-the-future-of-data-storage-is-still-magnetic-tape. (Accessed: 24th September 2020)
20. Goda, K. & Kitsuregawa, M. The history of storage systems. in *Proceedings of the IEEE* **100**, 1433–1440 (Institute of Electrical and Electronics Engineers Inc., 2012).
21. Weller, D. *et al.* High ku materials approach to 100 gbits/in2. *IEEE Trans. Magn.* **36**, 10–15 (2000).
22. Bertram, H. N. & Williams, M. SNR and density limit estimates: A comparison of longitudinal and perpendicular recording. *IEEE Trans. Magn.* **36**, 4–9 (2000).
23. Iwasaki, S. ichi & Nakamura, Y. An analysis for the magnetization mode for high density magnetic recording. *IEEE Trans. Magn.* **13**, 1272–1277 (1977).
24. Hoagland, A. S. History of magnetic disk storage based on perpendicular magnetic recording. in *IEEE Transactions on Magnetics* **39**, 1871–1875 (2003).
25. Iwasaki, S. I. Perpendicular magnetic recording - Its development and realization. in *Journal of Magnetism and Magnetic Materials* **324**, 244–247 (North-Holland, 2012).
26. Marchon, B., Pitchford, T., Hsia, Y. T. & Gangopadhyay, S. The head-disk interface roadmap to an areal density of 4 Tbit/in 2. *Advances in Tribology* (2013). doi:10.1155/2013/521086
27. Julliere, M. *TUNNELING BETWEEN FERROMAGNETIC FILMS. PHYSICS LETTERS* **54**, (1975).
28. Baibich, M. N. *et al.* Giant magnetoresistance of (001)Fe/(001)Cr magnetic superlattices. *Phys. Rev. Lett.* **61**, 2472–2475 (1988).
29. Binasch, G., Grünberg, P., Saurenbach, F. & Zinn, W. Enhanced magnetoresistance in layered magnetic structures with antiferromagnetic interlayer exchange. *Phys. Rev. B* **39**, 4828–4830 (1989).
30. Slonczewski, J. C. *Current-driven excitation of magnetic multilayers*. *Journal of Magnetism and Magnetic Materials* **159**, 1–7 (1996).
31. Bhatti, S. *et al.* Spintronics based random access memory: a review. *Materials Today* **20**, 530–548 (2017).
32. Webster, J. G. *et al.* Magnetic Tunnel Junctions for Spintronics: Principles and Applications. in *Wiley Encyclopedia of Electrical and Electronics Engineering* 1–16 (John Wiley & Sons, Inc., 2014). doi:10.1002/047134608x.w8231
33. Nishimura, N. *et al.* Magnetic tunnel junction device with perpendicular magnetization films for high-density magnetic random access memory. *J. Appl. Phys.* **91**, 5246–5249 (2002).
34. Ikeda, S. *et al.* A perpendicular-anisotropy CoFeB-MgO magnetic tunnel junction. *Nat. Mater.*

9, 721–724 (2010).

35. Feynman, R. P. There's Plenty of Room at the Bottom. *Eng. Sci.* **23**, 22–36 (1960).
36. Philp, D. & Fraser Stoddart, J. Self-Assembly in natural and unnatural systems. *Angew. Chemie (International Ed. English)* **35**, 1154–1196 (1996).
37. Whitesides, G. M. & Boncheva, M. Beyond molecules: Self-assembly of mesoscopic and macroscopic components. *Proc. Natl. Acad. Sci. U. S. A.* **99**, 4769–4774 (2002).
38. Whitesides, G. M. Self-Assembly at All Scales. *Science (80-.).* **295**, 2418–2421 (2002).
39. Grzybowski, B. A., Wilmer, C. E., Kim, J., Browne, K. P. & Bishop, K. J. M. Self-assembly: From crystals to cells. *Soft Matter* **5**, 1110–1128 (2009).
40. Furst, E. M. Directed self-assembly. doi:10.1039/c3sm90126b
41. Glotzer, S. C. & Solomon, M. J. Anisotropy of building blocks and their assembly into complex structures. *Nat. Mater.* **6**, 557–562 (2007).
42. Nie, Z., Petukhova, A. & Kumacheva, E. Properties and emerging applications of self-assembled structures made from inorganic nanoparticles. *Nature Nanotechnology* **5**, 15–25 (2010).
43. Ding, T., Song, K., Clays, K. & Tung, C. H. Fabrication of 3D photonic crystals of ellipsoids: Convective self-assembly in magnetic field. *Adv. Mater.* **21**, 1936–1940 (2009).
44. Davies Wykes, M. S. *et al.* Dynamic self-assembly of microscale rotors and swimmers. *Soft Matter* **12**, 4584–4589 (2016).
45. Milam, V. T., Hiddessen, A. L., Crocker, J. C., Graves, D. J. & Hammer, D. A. DNA-Driven Assembly of Bidisperse, Micron-Sized Colloids. *Langmuir* **19**, 10317–10323 (2003).
46. Grzybowski, B. A., Stone, H. A. & Whitesides, G. M. Dynamic self-assembly of magnetized, millimetre-sized objects rotating at a liquid-air interface. *Nature* **405**, 1033–1036 (2000).
47. Iyer, A. S. & Paul, K. Self-assembly: A review of scope and applications. *IET Nanobiotechnology* **9**, 122–135 (2015).
48. Rothemund, P. W. K. Folding DNA to create nanoscale shapes and patterns. doi:10.1038/nature04586
49. Ong, L. L. *et al.* Programmable self-assembly of three-dimensional nanostructures from 10,000 unique components. *Nature* **552**, 72–77 (2017).
50. Yan, H., Park, S. H., Finkelstein, G., Reif, J. H. & LaBean, T. H. DNA-templated self-assembly of protein arrays and highly conductive nanowires. *Science (80-.).* **301**, 1882–1884 (2003).
51. Li, H., Carter, J. D. & LaBean, T. H. Nanofabrication by DNA self-assembly. *Materials Today* **12**, 24–32 (2009).
52. Douglas, S. M. *et al.* Self-assembly of DNA into nanoscale three-dimensional shapes. *Nature* **459**, 414–418 (2009).
53. Chhabra, R., Sharma, J., Liu, Y., Rinker, S. & Yan, H. DNA Self-assembly for Nanomedicine.

Advanced Drug Delivery Reviews **62**, 617–625 (2010).

54. He, Y. *et al.* Hierarchical self-assembly of DNA into symmetric supramolecular polyhedra. *Nature* **452**, 198–201 (2008).
55. Arpin, K. A. *et al.* Three-dimensional self-assembled photonic crystals with high temperature stability for thermal emission modification. *Nat. Commun.* **4**, 1–8 (2013).
56. Thorkelsson, K., Bai, P. & Xu, T. Self-assembly and applications of anisotropic nanomaterials: A review. *Nano Today* **10**, 48–66 (2015).
57. Walther, A. & Mueller, A. H. E. Janus Particles: Synthesis, Self-Assembly, Physical Properties, and Applications. *Chem. Rev.* **113**, 5194–5261 (2013).
58. Singamaneni, S., Bliznyuk, V. N., Binek, C. & Tsymbal, E. Y. Magnetic nanoparticles: recent advances in synthesis, self-assembly and applications. *J. Mater. Chem.* **21**, 16819 (2011).
59. Alapan, Y., Yigit, B., Beker, O., Demirörs, A. F. & Sitti, M. Shape-encoded dynamic assembly of mobile micromachines. *Nat. Mater.* **18**, 1244–1251 (2019).
60. Henderson, J. R. & Crawford, T. M. Repeatability of magnetic-field driven self-assembly of magnetic nanoparticles. *J. Appl. Phys.* **109**, 07D329 (2011).
61. Mohtasebzadeh, A., Ye, L. & Crawford, T. Magnetic Nanoparticle Arrays Self-Assembled on Perpendicular Magnetic Recording Media. *Int. J. Mol. Sci.* **16**, 19769–19779 (2015).
62. Thomas, J. R. Preparation and magnetic properties of colloidal cobalt particles. *J. Appl. Phys.* **37**, 2914–2915 (1966).
63. Teixeira, P. I. C., Tavares, J. M. & Telo Da Gama, M. M. Effect of dipolar forces on the structure and thermodynamics of classical fluids. *J. Phys. Condens. Matter* **12**, R411 (2000).
64. Ozaki, M., Suzuki, H., Takahashi, K. & Matijević, E. Reversible ordered agglomeration of hematite particles due to weak magnetic interactions. *J. Colloid Interface Sci.* **113**, 76–80 (1986).
65. Singamaneni, S., Bliznyuk, V. N., Binek, C. & Tsymbal, E. Y. Magnetic nanoparticles: Recent advances in synthesis, self-assembly and applications. *J. Mater. Chem.* **21**, 16819–16845 (2011).
66. Yan, J., Bae, S. C. & Granick, S. Rotating crystals of magnetic Janus colloids. *Soft Matter* **11**, 147–153 (2015).
67. Sacanna, S., Rossi, L. & Pine, D. J. Magnetic click colloidal assembly. *J. Am. Chem. Soc.* **134**, 6112–6115 (2012).
68. Lisiecki, I., Albouy, P. A. & Pileni, M. P. Face-centered cubic 'supracrystals' of cobalt nanocrystals. *Adv. Mater.* **15**, 712–716 (2003).
69. Yan, J., Chaudhary, K., Chul Bae, S., Lewis, J. A. & Granick, S. Colloidal ribbons and rings from Janus magnetic rods. *Nat. Commun.* **4**, 1–9 (2013).
70. Singh, G. *et al.* Self-assembly of magnetite nanocubes into helical superstructures. *Science* **345**, 1149–53 (2014).

71. Cheng, J. P. *et al.* Evolution of cobalt hydroxide from 2D microplatelets to a 3D hierarchical structure mediated by precursor concentration. *RSC Adv.* **3**, 13304–13310 (2013).
72. Lisjak, D. & Mertelj, A. Anisotropic magnetic nanoparticles: A review of their properties, syntheses and potential applications. *Progress in Materials Science* **95**, 286–328 (2018).
73. Yellen, B. B., Hovorka, O. & Friedman, G. Arranging matter by magnetic nanoparticle assemblers. *Proc. Natl. Acad. Sci. U. S. A.* **102**, 8860–8864 (2005).
74. Erb, R. M., Son, H. S., Samanta, B., Rotello, V. M. & Yellen, B. B. Magnetic assembly of colloidal superstructures with multipole symmetry. *Nature* **457**, 999–1002 (2009).
75. Peyer, K. E., Zhang, L. & Nelson, B. J. Bio-inspired magnetic swimming microrobots for biomedical applications. *Nanoscale* **5**, 1259–1272 (2013).
76. Yigit, B., Alapan, Y. & Sitti, M. Programmable Collective Behavior in Dynamically Self-Assembled Mobile Microrobotic Swarms. *Adv. Sci.* **6**, 1801837 (2019).
77. Chen, X. Z. *et al.* Recent developments in magnetically driven micro- and nanorobots. *Applied Materials Today* **9**, 37–48 (2017).
78. Sun, S., Fullerton, E. E., Weller, D. & Murray, C. B. Compositionally controlled FePt nanoparticle materials. in *IEEE Transactions on Magnetics* **37**, 1239–1243 (2001).
79. He, L., Wang, M., Ge, J. & Yin, Y. Magnetic assembly route to colloidal responsive photonic nanostructures. *Acc. Chem. Res.* **45**, 1431–1440 (2012).
80. Wyatt Shields Iv, C. *et al.* Field-directed assembly of patchy anisotropic microparticles with defined shape. *Soft Matter* **9**, 9219–9229 (2013).
81. Deng, K., Luo, Z., Tan, L. & Quan, Z. Self-assembly of anisotropic nanoparticles into functional superstructures. *Chem. Soc. Rev.* **49**, 6002–6038 (2020).
82. Vemulkar, T., Mansell, R., Petit, D. C. M. C., Cowburn, R. P. & Lesniak, M. S. Highly tunable perpendicularly magnetized synthetic antiferromagnets for biotechnology applications. *Appl. Phys. Lett.* **107**, 012403 (2015).

2 Theory

Note: In this work, we will use CGS units as opposed to the standard of SI units. This is due to historical trends in magnetism research that have favoured CGS units. Due to this tradition of CGS units, almost all of the relevant literature and instrumentation in the magnetism field use the CGS system, and for consistency we have done the same. The relationships for flux density B in the two systems are $B_{SI} = \mu_0(H + M)$ *and* $B_{CGS} = H + 4\pi M$*. The relevant units for magnetic flux B, magnetic field H, and magnetization (moment/volume) M are tesla (T), A/m, and A/m respectively in SI, while the same quantities take units of gauss (G), oersteds (Oe), and emu/cm*^{3} *in CGS. For conversion between SI and CGS, 1 T =* 10^4 *G, 1 kA/m = 12.57 Oe, and 1 kA/m = 1 emu/cm*^{3}*. The constant* μ_0 *in SI is equal to* 4π *x* 10^{-7} *Tm/A, while in CGS it is equal to 1 G/Oe (and is generally excluded from equations). From this relation, it is clear that the units of B and H in CGS are equivalent. For this work, field values will be quoted in oersted or kilo-oersted, while magnetization will be quoted in emu/cm*^{3}*.*

2.1 Perpendicular magnetic anisotropy (PMA)

This work will focus on magnetic thin films with perpendicular magnetic anisotropy. In order to understand this form of magnetic anisotropy, it is important to first have a general understanding of magnetic anisotropy in magnetic materials and the different origins of the contributions to magnetic anisotropy.

Fundamentally magnetic anisotropy means that there is a low energy, preferred direction for the orientation of the magnetization in a material. While there is no specific directionality in the spin quantization axis, making the direction of magnetization isotropic from an atomic basis, this isotropy is broken by dipolar interactions and spin-orbit coupling within the material. It is these two interactions which create the anisotropy seen in magnetic materials.[1,2] These effects lead to shape anisotropy through dipolar interactions and magneto-crystalline anisotropy (MCA) due to spin-orbit coupling with the crystal structure of the material.[1]

[1] Dipolar effects do also play a role in MCA, but they can be neglected due to their small size relative to spin-orbit coupling, MCA will be explained just through the lens of spin-orbit coupling.[1]

Shape anisotropy

The dipolar interaction is the interaction of the magnetization of a material with the collective field generated by this magnetization, termed the demagnetizing field. The energy of this interaction is called the demagnetizing, or magnetostatic, self-energy E_{demag} seen in *Eq. 2-1*.[3]

$$E_{demag} = -\frac{1}{2}\int_V H_d \cdot M d^3 r \qquad \textit{Eq. 2-1}$$

While the magnetization of a material will not change with the shape, the demagnetizing field will. The demagnetizing field is determined by the demagnetizing factors. *Eq.2-2* outlines this relationship.

$$H_{di} = -N_{ij} M_j \qquad \textit{Eq.2-2}$$

In this equation, Einstein notation is used, with {i, j} = (x, y, z) and *N* is the demagnetizing tensor. By combining *Eq. 2-1* and *Eq.2-2*, we can come to the energy expression in *Eq. 2-3* for cases where the sample has uniform magnetization and a shape where the demagnetizing factor is well-defined, such as an ellipsoid or infinite sheet. It is clear that the energy can be minimized by orienting the magnetization along the direction with the smallest demagnetizing factor.

$$E_{demag} = \frac{1}{2} V N M^2 \qquad \textit{Eq. 2-3}$$

Another way to consider this problem is through the idea of magnetic charges created by the magnetization of the material. Magnetization normal to a surface can be seen as creating a distribution of magnetic surface charges. These charges can then be used to calculate the demagnetizing field through a potential function. In order to minimize the demagnetizing field, and thus, the demagnetizing energy, the material will favour an orientation of the magnetization that creates the smallest amount of surface charge (for a full explanation of the surface charge approach, see 2.3).

Either by this surface charge approach or by considering the demagnetizing factors of different sample shapes, it can be seen that the preferred direction of magnetization will be along the long axis of the sample, as it minimizes the energy of the dipolar interaction. This preferred orientation is the shape anisotropy of the material.

Magneto-crystalline anisotropy

While dipolar interactions explain shape anisotropy, they are not sufficient to account for magneto-crystalline anisotropy, which originates from spin-orbit coupling within the material.[1,2] Spin-orbit coupling is the interaction between the electron spin and the magnetic field resulting from the

orbital motion of this moving charge. Since the orbital motion is itself coupled to the positive nuclei of the atoms that make up the crystal lattice, spin-orbit coupling provides a connection between the crystalline structure of the material and the magnetization.[1] This coupling can be expressed in terms of the spin-orbit Hamiltonian shown in *Eq. 2-4*.[1]

$$\mathcal{H}_{s.o.} = \xi l \cdot s \qquad \textit{Eq. 2-4}$$

l and s are the orbital magnetic and spin quantum numbers, respectively. ξ is the spin-orbit constant, which is equal to $\xi(r)$, the radial average taken, in this case, over the electron 3d orbitals. Since the magnetism of interest in this work originates in the 3d band electrons of the metal used (Co), the interaction is solved for d-electrons. However, in the 3d series in bulk materials, the orbital moments of the electrons are quenched, due to the electric fields from the nuclei in the crystal lattice (often termed the 'crystal field'). The crystal field leads to new hybridized orbitals for the d-band, which are hybridized from orbitals of +m and –m moments, leading to a net zero moment in the new quenched orbitals.[1,4] The spin-orbit coupling between the magnetic spins and quenched orbits has a small effect on the orbital moment, slightly removing the quenching. The specific wavefunction, and thus, form and energy, of the orbitals will depend on the neighbouring atoms that generate the crystal field. The spin-orbit interaction with these different orbitals will lead to differences in orbital moment and thus differences in energy for these spin-orbit interactions. These differences in energy are then responsible for the creation of low energy, preferred interactions. Since the crystal field that causes the quenching of the orbitals arises from the crystal lattice, it will contain the symmetry of the lattice, leading to a symmetry influence on the energies of the spin-orbit coupling, resulting in a MCA that relates to the underlying crystal structure of the material. This MCA will be further explored below, as it is this type of interaction that leads to the PMA seen in magnetic thin films.

Uniaxial anisotropy

Uniaxial anisotropy is the simplest form of magnetic anisotropy and applies well to the PMA films in this work. The energy of the uniaxial anisotropy E_{ua} is presented in *Eq. 2-5*.[4]

$$E_{ua} = K_1 \sin^2\theta + K_2 \sin^4\theta + \cdots \qquad \textit{Eq. 2-5}$$

K_n are the anisotropy constants and θ is the angle between the magnetization and the easy anisotropy direction. In this work we will simplify the anisotropy to a first-order anisotropy, which is a useful simplification for the perpendicular anisotropy of PMA materials. The experimental determination and use of the anisotropy constant will be further outlined in 2.1.3.

2.1.1 Origin of PMA

The anisotropy in magnetic thin films with perpendicular anisotropy can be viewed as a competition between a strong out-of-plane MCA and the shape anisotropy that favours an in-plane magnetization. If the thin film is taken as an infinite plane in the x- and y-directions with a small thickness in the perpendicular (z) direction, the demagnetizing tensor of the shape is shown in *Eq. 2-6*.[3]

$$N_{thin\ film} = \begin{pmatrix} 0 & 0 & 0 \\ 0 & 0 & 0 \\ 0 & 0 & 4\pi \end{pmatrix} \qquad \textit{Eq. 2-6}$$

From the principles established in *Eq. 2-3*, it is clear that a perpendicular orientation of the magnetization will lead to energy of $2\pi M^2$ per unit volume of the film, while the energy of an in-plane orientation is 0. In this geometry, shape anisotropy strongly favours an in-plane magnetization direction, with a driving force $-2\pi M^2$. In order to overcome this shape anisotropy, the PMA thin films must have a strong MCA that favours the perpendicular direction.

The existence of large perpendicular anisotropy generated by a surface was first theorized by Néel.[5,6] The surface of a material does not have the same symmetric arrangement of atoms as the bulk, which alters the crystal field and its effect on orbital moment. Because of this, the orbital moments in the perpendicular direction (relative to the surface) are not quenched to the same degree. *Eq. 2-7* - *Eq. 2-9* outline how a difference in the perpendicular and parallel orbital moment at a surface can lead to an energy difference in the spin-orbit coupling. These equations were developed in a theoretical study of metallic monolayers and experimental results were able to confirm the existence of the surface anisotropy in thin films.[1,6–8]

$$m_{orb} = m_{orb}^{\perp} + (m_{orb}^{\parallel} - m_{orb}^{\perp}) \sin^2\theta \qquad \textit{Eq. 2-7}$$

$$E_{SO} = -\frac{1}{2}\frac{\xi}{2\mu_B}[m_{orb}^{\perp} + (m_{orb}^{\parallel} - m_{orb}^{\perp}) \sin^2\theta] \qquad \textit{Eq. 2-8}$$

The energy difference between the spin-orbit coupling energy for the in-plane (hard axis) and out-of-plane (easy axis) direction in a monolayer can be seen in *Eq. 2-9*. When the out-of-plane orbital moment is greater than the in-plane moment, then the spin-orbit coupling energy will favour an out-of-plane magnetization.

$$\Delta E_{SO} = -\frac{1}{2}\frac{\xi}{2\mu_B}[m_{orb}^{\perp} - m_{orb}^{\parallel}] \qquad \textit{Eq. 2-9}$$

Through the use of perturbation theory calculations the anisotropy can be estimated as an order-of-magnitude from the spin-orbit coupling. The coupling constant is much smaller than the bandwidth of the material, allowing this small change to be evaluated using perturbation theory. *Eq. 2-10* shows the relationship.[1]

$$K \sim \frac{\xi^2}{W} \qquad \textit{Eq. 2-10}$$

W is the bandwidth of the d band in the material. From the spin-orbit coupling energy and the anisotropy expression, we can understand how the spin-orbit coupling leads to PMA and how the value of that anisotropy can be estimated.

The generation of PMA by symmetry-breaking at the surface of the material led to intensive research that included research into interface anisotropy, where multilayers of magnetic and non-magnetic materials would generate a similar symmetry-breaking effect at the layer interfaces, which could equally be used to create PMA.[9] The existence of PMA, either from a surface or interface, necessitates a thin film of material. Since the difference in orbital moment occurs only at the surface or interface, the surface or interface atoms must make up a significant portion of the material in order for this effect to be noticeable.

2.1.2 PMA in Co/Pt and CoFeB/Pt

In this work, our magnetic films will be composed of CoFeB/Pt multilayers, which are a derivative of the widely researched Co/Pt system. The $Co_{60}Fe_{20}B_{20}$ alloy provides various morphological benefits compared to Co that will be discussed in the later chapters. The multilayer structure of Co/Pt will create PMA due to the interfacial effects discussed previously. Co/Pt is an especially robust system for perpendicular anisotropy because the interplay between the Co and Pt electronic structures can enhance the anisotropy. Both the spin-orbit constant ξ and the bandwidth W can be affected by hybridization between the 3d Co and the 5d Pt orbitals.[7] This can lead to an enhancement in spin-orbit coupling due to the 5d Pt that leads to an increase in the observed anisotropy. Pt also shows large spin-polarization which can further contribute to out-of-plane orbital moment at the interface.[7] Other non-magnetic materials, such as Ag or Cu, do not see this spin-polarization due to their filled 3d bands.[10] While such materials can still be used to create PMA, Pt offers increased anisotropy due to its stronger interactions with the magnetic Co.

2.1.3 Empirical understanding of PMA

It is necessary to understand the quantum mechanical origins of PMA; however, it most situations it is preferable to treat PMA on an empirical basis that addresses the uniaxial anisotropy in a more accessible fashion. The anisotropy constant K can be related to the anisotropy field H_k, which is the field needed to saturate a uniaxially anisotropic material along its hard axis (90° to the easy axis). This can be accomplished by treating the angle-dependent energies of a magnet in an applied field, which include the anisotropy and Zeeman energy for a material with a perpendicular easy axis (*Eq. 2-11*). This analysis of anisotropy used the hard-axis limit of the Stoner-Wohlfarth model (discussed in 2.2).

$$E = (K_i - 2\pi M^2)V \sin^2\theta - MVHcos(\alpha - \theta) \qquad \textit{Eq. 2-11}$$

K_i is the intrinsic anisotropy, which encompasses the MCA including interface anisotropy, while the shape anisotropy is equal to $2\pi M^2$. α is the angle between the applied field H and the easy axis, and θ is the angle between the magnetization and the easy axis. M is the magnetization of the material (= M_s under the assumption of uniform magnetization) and V is the material volume. The intrinsic and shape anisotropy can be combined into one anisotropy term $K_{eff} = K_i - 2\pi M^2$. The anisotropy of the film can then be determined by experimental measurements of the hard axis saturation field H_k. By applying a field in the hard axis direction ($\alpha = {}^{\pi}/_{2}$) and minimizing the function, it can be found that $K_{eff} = \frac{H_k M}{2}$.[3,11] Through this relation the anisotropy of the perpendicular films can be measured by saturation along the film's hard axis. Figure 2.1 outlines how the anisotropy can be extracted from the hard axis measurement for different magnetization orientations. If the value of $K_{eff} < 0$, then the demagnetizing energy is larger than the intrinsic anisotropy and the easy axis of the film will lie in the plane. In this case, as shown in Figure 2.1 (a), the hard axis saturation field can be used to find the anisotropy of the film.

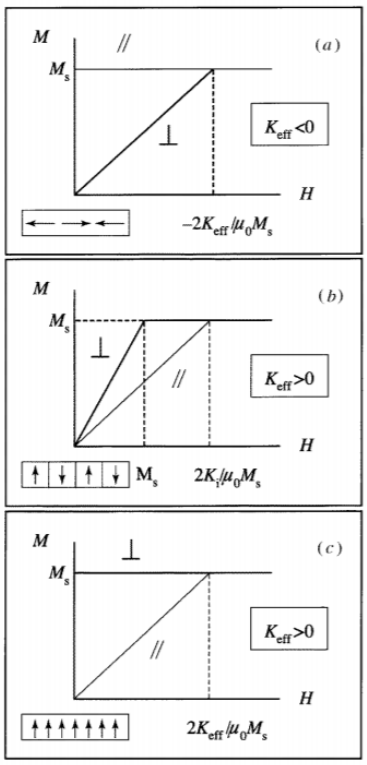

Figure 2.1 Comparison of anisotropy constants for in-plane and perpendicular magnetic films
The M-H curves parallel and perpendicular to the easy axis are shown for a sample with an (a) in-plane easy axis and (b,c) perpendicular easy axis. (b) shows a sample with many small anti-parallel domains while (c) has a remanent structure of large parallel domains. Reproduced from Ref. 11 on license from IOP Publishing.[11]

Similarly, in Figure 2.1 (c), a fully remanent perpendicular film ($K_{eff} > 0$) can be saturated along the hard axis to find the anisotropy through the relationship established before. However, in the case shown in Figure 2.1 (b), where the perpendicular film has many small domains, the magnetostatic energy is determined by the interactions between domains. We can no longer use the expression (*Eq. 2-3*) that was established for the case of a uniformly magnetized material, so the hard axis saturation field for this case cannot be related to K_{eff}. In this work all the thin films will be fully remanent, as in Figure 2.1 (c), so the relationship $K_{eff} = \frac{H_k M}{2}$ will be valid and used to determine anisotropy.

PMA can also be treated as a competition between the interface and volume anisotropies of the thin film. As was previously established, it is the interfacial spin-orbit coupling that is responsible for PMA, while the bulk film will favour in-plane anisotropy. The earliest studies of perpendicular films found an inverse relationship between the perpendicular anisotropy and the thickness of the film.[12] From this relationship, another expression for K_{eff} can be created that balances the volume and interface anisotropy terms. This relationship is especially useful for thin films as it can be used to find the thickness as which the film will change from a perpendicular to in-plane anisotropy, which is

known as the spin-reorientation transition (SRT). The relationship (*Eq. 2-12*) separates the anisotropy into a volume component K_v, which contains the all the bulk anisotropies, such as shape and magnet-crystalline terms. The interface components K_s accounts for the interfacial anisotropy, and it is assumed the anisotropies of the two interfaces are equal, giving the leading factor of 2.

$$K_{eff} = K_v + {}^{2K_s}/_{t} \qquad \textit{Eq. 2-12}$$

A positive K_{eff} denotes perpendicular anisotropy, while K_{eff} is negative for in-plane anisotropy. This formulation is extremely useful experimentally, as it allows connection between the structure of the magnetic film and the anisotropy. By plotting this equation as $K_{eff}t$ vs t, an example of which is given in Figure 2.2, various values such as the thickness of the SRT, K_v, and K_s can be easily extracted.

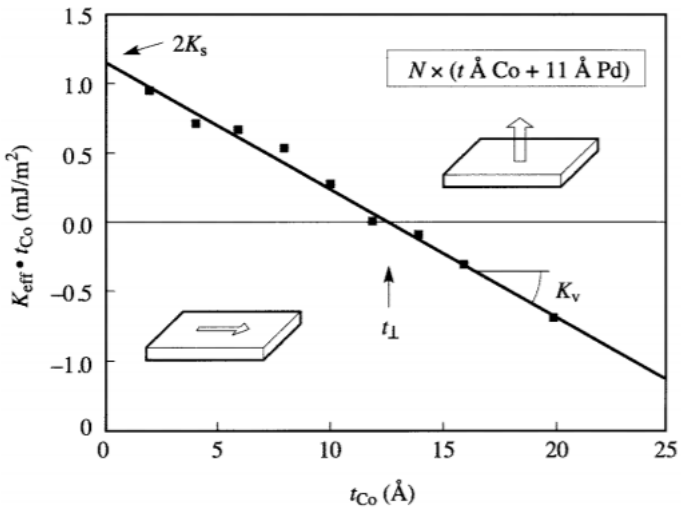

Figure 2.2 Plot of volume vs surface anisotropy for a Co/Pd multilayer
Eq. 2-12 is used to plot the K_v vs K_s for data taken from a Co/Pd multilayer. The various points of interest, such as the SRT ($t_\perp$), are shown. The line at $K_{eff}t = 0$ denotes the transitions from perpendicular to in-plane anisotropy. Reproduced from Ref. 11 on license from IOP Publishing.[11]

By connecting the values of the anisotropy constant with measurable properties of the magnetic film, such as the anisotropy field H_k and the film thickness t, it is possible to experimentally determine and catalogue the anisotropy in PMA films, so it can be modified and optimized as experimental requirements dictate.

2.2 Stoner-Wohlfarth model

The Stoner-Wohlfarth model is the simplest model of magnetic behaviour that includes hysteresis.[13] This makes it a useful tool for characterizing the behaviour of magnetic materials in an accessible and applicable manner. The model considers zero-temperature coherent reversal of a uniformly magnetized prolate ellipsoid (axes lengths of b = c < a) in an externally applied magnetic field. This assumption of uniform magnetization is an example of a 'macrospin' approximation, which does not consider the real exchange and domain behaviour in a real magnet, but just treats the magnet as one uniformly aligned spin. We will employ the macrospin approximation in modelling the behaviour of our magnetic films and particles throughout this work, so it is important to have an applicable model and an understanding of how this model works.

In the Stoner-Wohlfarth model, the magnetic behaviour is dependent on the competition between the Zeeman energy of the magnetization in the externally applied field and the uniaxial anisotropy of the ellipsoid. In this case, the uniaxial anisotropy is due to the shape anisotropy of the prolate ellipsoid. By balancing these two energy terms to determine the equilibrium magnetization direction, the hysteretic reversal behaviour at different applied field magnitudes and angles can be determined. *Eq 2-13* outlines the total energy, while *Eq. 2-14* and *Eq. 2-15* give the forms of the demagnetizing energy (shape anisotropy) and Zeeman energy, respectively. M is the sample magnetization, V is the sample volume, H is the applied field, N_x are the demagnetizing factors along the ellipsoid axes (where $N_a + N_b + N_c = 4\pi$), and ψ_x are the direction cosines of M along the axes. The angle α is the angle between the applied field and the easy anisotropy axis, while θ is the angle between the magnetization and the same easy axis. Figure 2.3 shows the a-b cross-section of the ellipsoid, outlining the geometry and relations between the different components.

$$E = E_D + E_Z \qquad \textit{Eq 2-13}$$

$$E_D = \frac{1}{2} V M^2 (N_a {\psi_a}^2 + N_b {\psi_b}^2 + N_c {\psi_c}^2) \qquad \textit{Eq. 2-14}$$

$$E_Z = -MHV\cos(\alpha - \theta) \qquad \textit{Eq. 2-15}$$

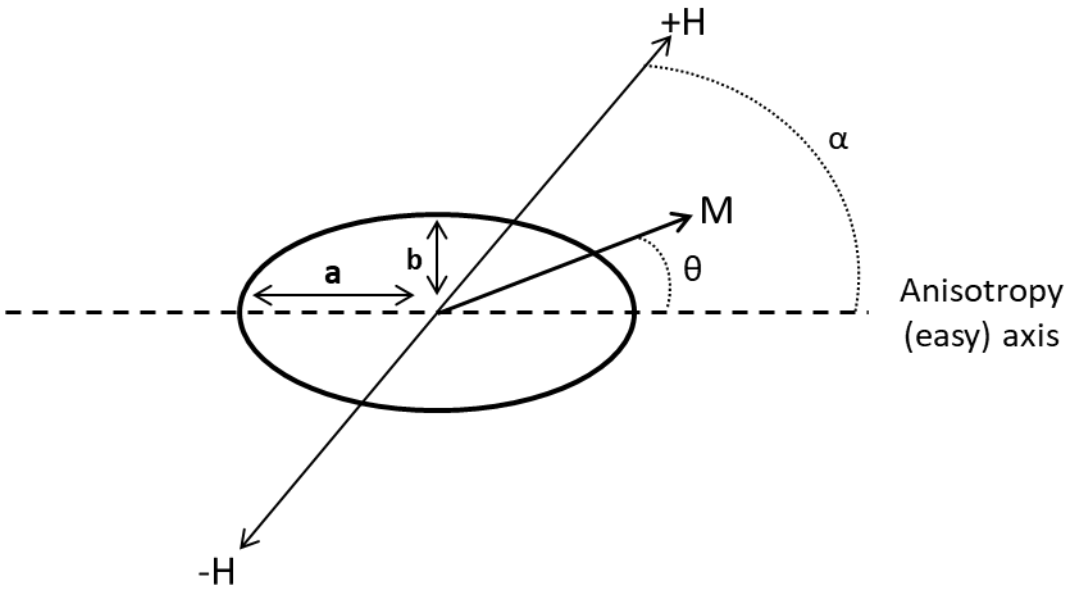

Figure 2.3 Schematic diagram showing the cross-section of a Stoner-Wohlfarth ellipsoid
A cross-section of a Stoner-Wohlfarth ellipsoid shows the geometry of the ellipsoid, including definition of the angles between the easy anisotropy axis, magnetization, and applied field.

Since H will only be applied and rotated in the a-b plane, as shown in Figure 2.3, the demagnetizing factor along the c-axis can be discounted. Thus, the expression in *Eq. 2-14* can be simplified and re-written as shown in *Eq. 2-16*.

$$E_D = \frac{1}{2}VM^2(N_a \cos^2\theta + N_b \sin\theta^2) = \frac{1}{2}VM^2(N_b - N_a)\sin^2\theta + \frac{1}{2}VM^2N_a \qquad \textit{Eq. 2-16}$$

By combining the angle-dependent portion of *Eq. 2-16* with *Eq. 2-15* to form the angle-dependent total energy (*Eq 2-13*), the resulting equation can be found that governs the energy of the ellipsoid.

$$E = \frac{1}{2}VM^2(N_b - N_a)\sin^2\theta - MHVcos(\alpha - \theta) \qquad \textit{Eq. 2-17}$$

Eq. 2-17 takes the form of a combination of uniaxial anisotropy energy and Zeeman energy, with the anisotropy constant $K_{eff} = \frac{1}{2}VM^2(N_b - N_a)$. This equation can then be used to find the energy minima under a set applied field angle α and magnitude, by minimizing it with respect to θ. The

conditions for finding the magnetization angle that corresponds to an energy minimum are set out in *Eq. 2-18*.

$$\frac{dE}{d\theta} = 0$$
$$\frac{d^2E}{d\theta^2} > 0 \qquad \textit{Eq. 2-18}$$

Using a reduced field $h = H/H_k$, where $H_k = 2K_{eff}/M$, *Eq. 2-17* can be differentiated according to *Eq. 2-18*, yielding *Eq. 2-19*.[14]

$$\sin\theta\cos\theta + h\sin(\alpha - \theta) = 0$$
$$\cos 2\theta + h\cos(\alpha - \theta) > 0 \qquad \textit{Eq. 2-19}$$

These equations can only be solved analytically for applied field angles of $\alpha = 0, {}^{\pi}/_{4}, {}^{\pi}/_{2}$. For other angles, the solutions can be computed numerically. By plotting the reduced field h versus the component of magnetization parallel to the applied field $m_{\parallel}$, a series of hysteresis loops can be constructed for various applied field angles. Figure 2.4 shows a series of these hysteresis loops, either solved analytically or numerically. It can be seen how, at different applied field angles, the Stoner-Wohlfarth particle will undergo a combination of coherent rotation and irreversible switching of the magnetization.

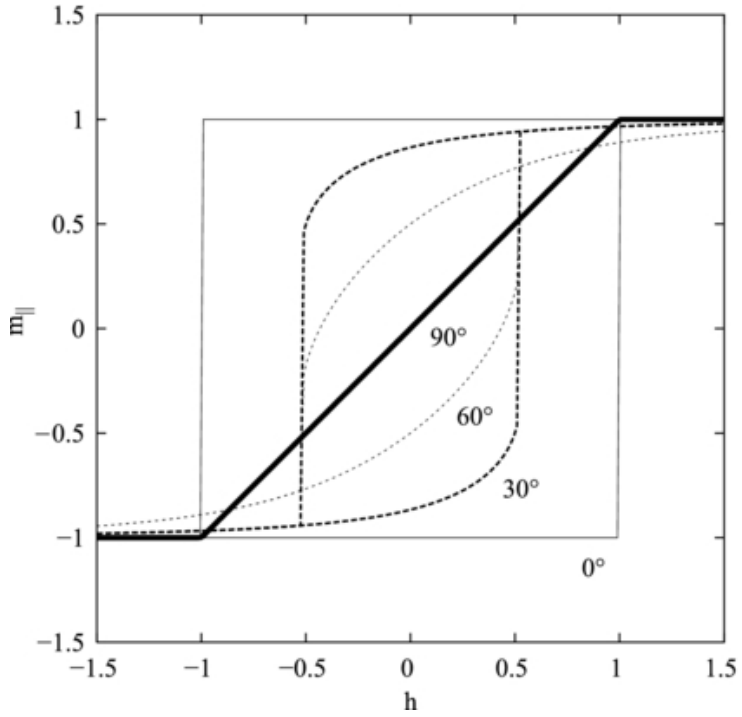

Figure 2.4 Stoner-Wohlfarth hysteresis loop for different applied field angles α
The plot shows hysteresis loops constructed by either analytical (0°, 90°) or numerical (30°, 60°) minimization of the energy of a Stoner-Wohlfarth particle. Solid lines represent cases solved analytically, while dashed lines show cases which were solved numerically. Reproduced from Ref. 14, © European Physical Society. Reproduced by permission of IOP Publishing. All rights reserved .[14]

We can address the analytical case of $\alpha = 0$ to examine the model and connect the results with the hysteresis loops in Figure 2.4. At a value of $-1 < h < 1$, 0 and π are both solutions for θ to the equations in *Eq. 2-19*. It is not until $h > 1$ or $h < -1$ that there is only one solution. At $h > 1$, $\theta = 0$ is the solution, while for $h < -1$, $\theta = \pi$. From this we can see the origin of hysteresis. If the magnitude of h is below 1, the magnetization will remain at an angle of $\theta = 0$ or π, depending on its starting orientation. Then, only once an anti-parallel field of sufficient magnitude is applied will there be one minimum, leading to switching of the particle.

Stoner-Wohlfarth astroid

While it is easy to simply understand a case with an applied field angle of $\alpha = 0$, more tools are needed to understand the conditions for switching under an applied field of arbitrary magnitude and angle. In order to do so, we can construct a Stoner-Wohlfarth astroid.[15] As we can see from the example above, at low applied fields, there will always be two stable minima. Switching will occur when the system transitions to conditions where only one stable minimum exists, which happens when one of the minima ceases to exist. In the case of $\alpha = 0$, this was when h = -1, 1. In order to solve this, we can find a field condition where $\frac{dE}{d\theta} = 0$ and $\frac{d^2E}{d\theta^2} = 0$, as this will represent the point at

which an energy minimum becomes unstable, leaving only one global minimum and causing switching to occur. To accomplish this, a general expression can be found. The applied field is split into two components that are parallel and perpendicular to the easy axis, with forms $h_{\parallel} = \frac{H}{H_k}\cos\alpha$ and $h_{\perp} = \frac{H}{H_k}\sin\alpha$. Using these components, the standard total energy equation in *Eq. 2-20* can be transformed into the field component form in *Eq. 2-21*.[3]

$$E = K_{eff}\sin^2\theta - MHVcos(\alpha - \theta) \qquad \textit{Eq. 2-20}$$

$$E = K_{eff}[\sin^2\theta - 2h_{\parallel}\cos\theta - 2h_{\perp}\sin\theta] \qquad \textit{Eq. 2-21}$$

Eq. 2-21 can then be differentiated according to $\frac{dE}{d\theta} = 0$ to find the equilibrium angles for θ, which leads to *Eq.2-22*.

$$\frac{h_{\perp}}{\sin\theta} - \frac{h_{\parallel}}{\cos\theta} = 1 \qquad \textit{Eq.2-22}$$

Then *Eq. 2-21* is further differentiated according to $\frac{d^2E}{d\theta^2} = 0$, which finds the point of instability for the minimum, leading to *Eq. 2-23*.

$$\cos^2\theta - \sin^2\theta + h_{\parallel}\cos\theta + h_{\perp}\sin\theta = 0 \qquad \textit{Eq. 2-23}$$

Eq.2-22 and *Eq. 2-23* can then be solved together to yield the parametric equations in *Eq. 2-24*.

$$h_{\perp_{sw}} = \sin^3\theta \qquad \textit{Eq. 2-24}$$
$$h_{\parallel_{sw}} = -\cos^3\theta$$

From these parametric equations and *Eq.2-22*, θ can be eliminated to give the final relationship in *Eq. 2-25*.

$$h_{\parallel_{sw}}{}^{2/3} + h_{\perp_{sw}}{}^{2/3} = 1 \qquad \textit{Eq. 2-25}$$

Eq. 2-25 defines the locus of points at which switching will occur. The relation can be plotted versus the parallel and perpendicular field components to create the Stoner-Wohlfarth astroid. This can then be used to find the switching behaviour of a particle at an arbitrary applied field strength and

angle. Figure 2.5 shows how such an astroid looks, where the points inside the astroid represent the region with two minima, and all locations outside the astroid have one minimum. Switching occurs by moving from the inside of the astroid through the boundary.

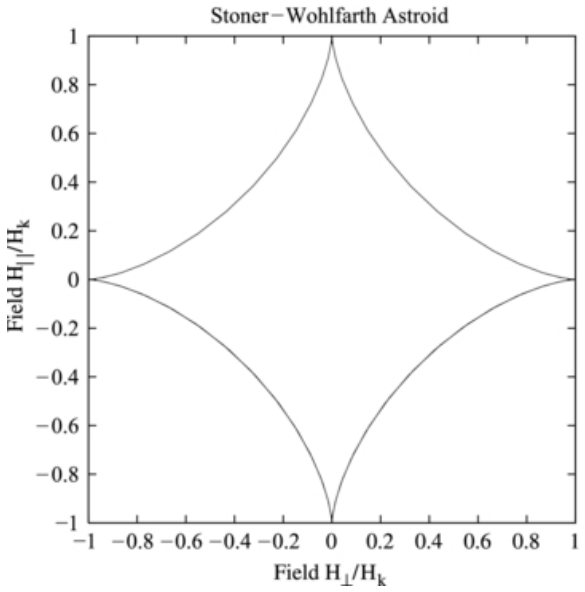

Figure 2.5 An example of an ideal Stoner-Wohlfarth astroid
Reproduced from Ref. 14, © European Physical Society. Reproduced by permission of IOP Publishing. All rights reserved.[14]

The Stoner-Wohlfarth model and Stoner-Wohlfarth astroid provide powerful tools for understanding the behaviour of simple magnetic particles. It will prove especially useful for understanding the behaviour of magnetic particles in liquid, where the orientation of the particle magnetization in an applied field is needed to understand the particle's mechanical response to the field. However, while the Stoner-Wohlfarth mode is a useful model for thin films with strong uniaxial anisotropy and full remanence, the real reversal behaviour of films and particles in this work is much different than that predicted by the Stoner-Wohlfarth model, due to the coercivity of the films and particles that is much lower than the material's anisotropy.[14]

2.3 Calculation of magnetic particle interactions

In this work we will be harnessing the magnetic interactions between particles to drive self-assembly. For this reason, it is important that we can calculate and understand the interaction energies and forces between the particles. Since force is the negative gradient of the magnetic potential energy, by calculating the interaction energy, we can understand both the force and energy which drive interaction between particles.[3] The magnetic interaction energy between two uniform permanent magnets can be, in its simplest form, written as *Eq. 2-26*.[3]

$$E = -m \cdot B \qquad \textit{Eq. 2-26}$$

E is the interaction energy, m is the magnetic moment, and B is the magnetic flux acting on the moment. In the case of two permanent magnets m_1 and m_2, the total interaction energy is equal to $\frac{1}{2}[(-m_1 \cdot B_2) + (-m_2 \cdot B_1)]$, where B_1 (B_2) is the field created by particle m_1 (m_2) and the factor of $\frac{1}{2}$ is due to the reciprocity theorem.[3] While the moments of the uniformly magnetized magnets are simple to find from the magnetization M of the material, the magnetic flux created by the magnetic is much more complex. The flux from a permanent magnet is due to the magnetostatic field, or demagnetizing field H_d, of the particle through the relation $B = (H_{ext} + H_d) + 4\pi M$. Outside the magnetic particle and with no externally applied field (H_{ext}), this expression reduces to $B = H_d$. The demagnetizing field depends on the demagnetizing factor N of the magnet, which defines the strength and form of the field, with $H_d = -NM$. The demagnetizing factors of 3D shapes can be very complex. A few examples, such as a prolate ellipsoid or infinite sheet, referenced earlier, can be simply calculated.[16] For more complex geometries, these factors are often calculated numerically. However, analytical expressions have been found for a number of different geometries with simplifying assumptions, such as rectangular prisms with uniform magnetization.[17,18] The PMA block-like particles created in this work can be defined as a uniformly magnetized rectangular prism, and thus, we can take advantage of analytical solutions that exist for this geometry to find the demagnetizing field and interaction energies between particles.

However, the calculation of demagnetizing energies of uniform rectangular prisms can also be approached differently, without directly calculating the demagnetizing field. This was the approach used by Rhodes and Rowlands in 1954.[19] In order to find the demagnetizing energy of these prisms, they used the Coulombian approach, where the magnetization is substituted for a distribution of magnetic charges.[3] From this charge distribution, a scalar potential can be determined from the static, uniform magnetization. The combination of the charge distribution and potential can then be used to find the energies of the particles. While Rhodes and Rowlands did not directly solve the demagnetizing factor for the rectangular prism geometry, they were able to find a result that was equivalent to the average first-order demagnetizing field for the prism.[17] The first-order demagnetizing field is the field calculated under an assumption of uniform magnetization. Based on this early work by Rhodes and Rowlands, analytical expressions were found by Akoun and Yonnet for the interaction of uniformly magnetized rectangular prisms, which are implemented in this work to find the interaction energies and forces.[19,20]

Beginning from that approach, we will build up the solution found for the interaction energy of two uniformly magnetized rectangular prisms.

2.3.1 The Coulombian approach

The Coulombian approach uses the concept of surface and volume magnetic charges, and then evaluates the interactions between these charges using principles developed in calculations of electrostatics. The magnetization is divided into a collection of volume magnetic charges in the bulk of the material and surface charges on the surfaces, with the following expressions (*Eq. 2-27*):[3]

$$\rho_m = -\nabla \cdot M \qquad \sigma_m = M \cdot e_n \qquad \textit{Eq. 2-27}$$

where ρ_m is the volume charge distribution, M is the magnetization, σ_m is the surface charge distribution, and e_n is a normal vector pointing outward from the surface.

Using this charge distribution, Poisson's equation can be solved to find a potential function. This was undertaken by Stoner and implemented by Rhodes and Rowlands, giving the general potential from a magnetized body as *Eq. 2-28*

$$V = \int \frac{M \cdot e_n}{r} dS - \int \frac{\nabla \cdot M}{r} dv \qquad \textit{Eq. 2-28}$$

where V is the potential, the first term is the surface integral of the surface charge distribution, and the second term is the volume integral of the volume charge distribution. In a uniformly magnetized body, the volume magnetization will not diverge, meaning the second integral term becomes zero. From this potential, the field H can be found as the gradient of the potential $H = -\nabla V$.

Additionally, Rhodes and Rowlands use this potential to find the mutual energy, or interaction energy, between two magnetic surfaces. For the interaction of two parallel rectangular magnetic surfaces, which we will denote surface 1 and surface 2, the equations are as follows:

$$E_m = \sigma_2 \int\int V(x_2, y_2, c)\, dx_2 dy_2 \qquad \textit{Eq. 2-29}$$

$$V(x_2, y_2, c) = \sigma_1 \int\int \{(x_2 - x_1)^2 + (y_2 - y_1)^2 + c^2\}^{-1/2}\, dx_1 dy_1 \qquad \textit{Eq.2-30}$$

Surface charge densities are σ_1 and σ_2 and the surfaces are separated by a distance c, giving an energy of mutual interaction E_m (*Eq. 2-29*). *Eq.2-30* calculates the potential from surface 1 on a point of the surface 2 and is integrated over the area of surface 1. By integrating this potential over the area of surface 2 in *Eq. 2-29*, the energy of interaction can be found. Analytical solutions for these integrations were found for an analogous electrostatics problem and extended by Rhodes and

Rowlands to give an analytical solution for interaction energy of rectangular prism magnets with uniform magnetization.[19,21]

Building on these fundamental forms, Akoun and Yonnet used this method to create analytical expressions of the magnetic field and interaction energies for 3D cuboidal magnets, which are shown below.

2.3.2 Demagnetizing field

An expression for the demagnetizing field from a surface with a uniform charge density is presented here. This expression, derived by Akoun and Yonnet, is a direct extension of the Coulombian method outlined above.[20] Figure 2.6 shows the schematic diagram of the surface, defining the geometry and variables used in the calculation.

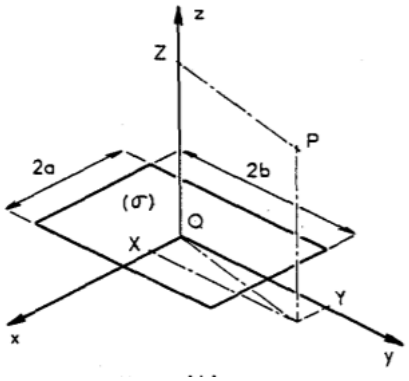

Figure 2.6 Schematic diagram for demagnetizing field calculation
The schematic diagram for the calculation of the demagnetizing field from a sheet 2a x 2b, with uniform magnetic charge density σ, for a point P. Reproduced with permission from Ref. 20, © 1984 IEEE.[20]

From this schematic diagram, the equations that define the field can be understood. *Eq. 2-31* gives the analytical summation that is used to calculate the demagnetizing field from the surface, while *Eq. 2-32* and *Eq. 2-33* are a series of helper functions needed to complete the calculation.

$$H_l = \frac{\sigma}{4\pi\mu_0} \sum_{i=\{0,1\}} \sum_{j=\{0,1\}} (-1)^{i+j} \varepsilon_l(S_i, T_j, R) \ , l = x,\ y, z \qquad \textit{Eq. 2-31}$$

with

$$\varepsilon_x = \ln (R - T)$$
$$\varepsilon_y = \ln (R - S) \qquad \textit{Eq. 2-32}$$

$$\varepsilon_z = \tan^{-1}\frac{ST}{RZ}$$

$$S_i = X - (-1)^i a$$
$$T_j = Y - (-1)^j b \qquad \textit{Eq. 2-33}$$
$$R = (S_i^2 + T_j^2 + Z^2)^{1/2}$$

Using these equations, the demagnetizing field of a uniformly charged surface parallel to the xy plane can be found. Thus, building on these equations, the field from a magnetized rectangular prism with uniform magnetization along z (composed of two parallel surfaces) can be calculated. Index permutations are performed to find the field from arbitrarily magnetized prisms.

2.3.3 Interaction energy and force

The calculation of the interaction energy follows a similar form to the demagnetizing field, and the similarity between the equations below and *Eq. 2-29* and *Eq.2-30* are clear. Two blocks of uniform magnetization, both pointing along the z axis, are shown in Figure 2.7, with the dimensions of the blocks and their relative locations defined.

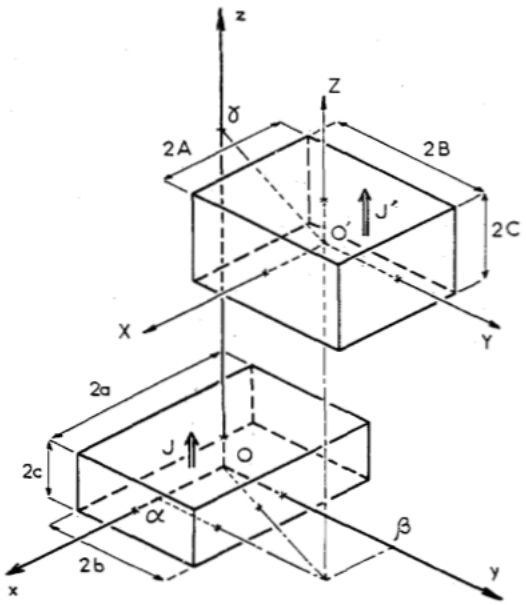

Figure 2.7 Schematic diagram for calculation of interaction energy between two blocks
The schematic diagram for the calculation of the interaction energy between blocks 2a x 2b x 2c and 2A x 2B x 2C, with uniform magnetization J and J' respectively.
Reproduced with permission from Ref. 20, © 1984 IEEE [20]

From these two blocks charged surfaces are created, and it is the integration of the uniform surface charge interactions over those surfaces that yields the total interaction energy. The surface charge density σ is equal to the magnetization J, as the magnetization is restricted to being normal to a surface. The general form of the integration for the energy between two charged surfaces is presented in *Eq. 2-34*, with a helper function *Eq. 2-35* that defines the inter-charge distance r.

$$E = \int_{-a}^{a} dx \int_{-b}^{b} dy \int_{-A}^{A} dX \int_{-B}^{B} dY \frac{\sigma\sigma'}{4\pi\mu_0 r} \qquad \textit{Eq. 2-34}$$

$$r = [(\alpha + X - x)^2 + (\beta + Y - y)^2]^{1/2} \qquad \textit{Eq. 2-35}$$

The specifics of the analytical form of the equation and the derivation of this form can be found in Ref. 20.[20] Furthermore, the interaction energy equation can be used to find the interaction forces between the blocks, following the relation in *Eq. 2-36*.

$$\vec{F} = -\vec{\nabla}E \qquad \textit{Eq. 2-36}$$

Using this relationship, Akoun and Yonnet also derive analytical solutions for the force between uniformly magnetized prisms, which we will implement alongside the energy calculations.

2.4 Simulation of particle properties

In the case of large or complex geometries, the demagnetizing factors, and thus the demagnetizing fields and interaction energy, must be calculated numerically. This can be done by subdividing the complex shape into smaller parallelepipeds in which the magnetization can be considered uniform and using numerical methods to find total demagnetizing field, summing over the smaller shapes. Micromagnetics packages have such numerical capabilities, which we can use as another tool to find particle demagnetizing fields and interaction energies.

Micromagnetics is a powerful tool that can incorporate quantum mechanical effects like exchange energy while using a continuous spatial distribution of magnetization, which effectively incorporates classical and quantum behaviour in what is sometimes dubbed a 'semi-classical' system.[22] This allows investigation of domain behaviour and magnetization dynamics of system without requiring the computational intensity of atomistic simulations. Recent advances in computing power and simulation software has made the technique more accessible and useful. Micromagnetic simulation uses a discretized mesh, usually in a finite difference or finite element method, in order to solve numerically the complex partial differential equations needed to define time- and space-varying magnetic behaviour.

However, for this work, we will not use the full power offered by micromagnetics simulation. Rather, micromagnetics simulation offers a different route by which the demagnetizing field and energies of particles can be solved, while still using a 'macrospin' approach to the magnetic properties of the particle. Micromagnetics simulation will allow verification of calculations performed by the methods listed above, while also allowing access to greater range of potential geometries compared to the cuboidal magnets prescribed by the work of Akoun and Yonnet.[20]

The micromagnetics simulation in this work will be undertaken using Mumax3, and it will be used to solve for the demagnetizing field and interaction energy of particles.

2.4.1 MuMax3

MuMax3 is a recently developed micromagnetics simulator that takes advantage of GPU (graphical processing unit)-acceleration to increase its computation speed.[23] It uses finite difference discretization, with orthorhombic cells geometries that fit well with the mostly rectangular particle shapes developed in this work. It also allows for a number of different shapes (spheres, discs,

ellipsoids) and translation and rotation of shapes, all of which are not achievable with the analytical methods outlined previously.

MuMax3 calculates how the unit magnetization vector $\vec{m}(\vec{r}, t)$ varies over time and space. This can then be related to the overall magnetization of the system $\vec{M} = M_s\vec{m}(\vec{r}, t)$. In this work, given a static and uniform magnetization of the macrospin approximation, these variations will not exist and $\vec{M} = M_s$ at all points. This magnetization can then be applied for the calculations of demagnetizing field and energy.

2.4.2 Demagnetizing field

In MuMax3, the demagnetizing field is calculated by a convolution of the magnetization and a demagnetizing kernel that represents the demagnetization tensor of the simulation space. The convolution of these values leads to the demagnetizing field in *Eq. 2-37*.

$$\vec{B}_{demag,i} = \widehat{K_{ij}} * \widehat{M_j} \qquad \textit{Eq. 2-37}^{23}$$

K is the demagnetizing kernel and B is the demagnetizing field (which is equivalent to H_{demag}, but is listed as such due to match the notation used in MuMax3). Einstein notation is used to relate the values. The demagnetizing kernel, or tensor, can be calculated by finding the potential in each uniformly magnetized cell of the discretized simulation space. This potential function is equivalent to that found in 2.3. The gradient of this function can then be used to find H_{demag}. Mathematically, this can be expressed as the convolution of the demagnetizing tensor and the magnetization. Ref. 22[22] provides a full mathematical explanation for this procedure. The convolution can then be efficiently solved using a fast Fourier transform.[23] This allows the demagnetizing field to be easily calculated for different geometries and magnetizations.

2.4.3 Interaction energy

With the magnetization and demagnetizing field defined, it is simple to determine the demagnetizing energy of a particle and the interaction energy between multiple magnetic particles. The energy density is simply defined as *Eq. 2-38*, which is proportional, through the volume of the particles, to the expressions already outlined (*Eq. 2-26*).

$$\varepsilon_{demag} = -\frac{1}{2}\vec{M} \cdot \vec{B}_{demag} \qquad \textit{Eq. 2-38}$$

It is important to note that this calculation is for the entire demagnetizing energy of the system, which includes the self-demagnetizing energy of the magnets. In order to find only the interaction energy between particles, the individual self-demagnetizing energies must be subtracted from the total demagnetizing energy of the system.

MuMax3 provides a useful option for verifying and extending the results of the analytical expressions for demagnetizing field and energy. While the micromagnetics simulation does require greater computational resources and time compared to the analytical solutions, it also provides additional geometries and orientations not offered in the limited analytical cases, and a convenient alternative for magnetics calculations.

2.5 References

1. Bruno, P. Physical Origins and Theoretical Models of Magnetic Anisotropy. in *Ferienkurse des Forschungszentrums Julich* 24.1-24.25 (KFA Jülich, 1993).
2. Van Vleck, J. H. On the anisotropy of cubic ferromagnetic crystals. *Phys. Rev.* **52**, 1178–1198 (1937).
3. Coey, J. *Magnetism and Magnetic Materials*. (Cambridge University Press, 2010).
4. Chikazumi, S. & Graham, C. D. *Physics of ferromagnetism*. (Oxford: Clarendon Press, 1997).
5. Neel, L. L'approche à la saturation de la magnétostriction. *J. Phys. le Radium* **15**, 376–378 (1954).
6. Bruno, P. Tight-binding approach to the orbital magnetic moment and magnetocrystalline anisotropy of transition-metal monolayers. *Phys. Rev. B* **39**, 865–868 (1989).
7. Weller, D. *et al.* Orbital magnetic moments of Co in multilayers with perpendicular magnetic anisotropy. *Phys. Rev. B* **49**, 12888–12896 (1994).
8. Gradmann, U. Ferromagnetism near surfaces and in thin films. *Appl. Phys.* **3**, 161–178 (1974).
9. den Broeder, F. J. A., Hoving, W. & Bloemen, P. J. H. Magnetic anisotropy of multilayers. *J. Magn. Magn. Mater.* **93**, 562–570 (1991).
10. Daalderop, G. H. O., Kelly, P. J. & Schuurmans, M. F. H. First-principles calculation of the magnetic anisotropy energy of (Co)n/(X)m multilayers. *Phys. Rev. B* **42**, 7270–7273 (1990).
11. Johnson, M. T. *et al.* Magnetic anisotropy in metallic multilayers. *Reports Prog. Phys.* **59**, 1409–1458 (1996).
12. Gradmann, U. & Müller, J. Flat Ferromagnetic, Epitaxial 48Ni/52Fe(111) Films of few Atomic Layers. *Phys. status solidi* **27**, 313–324 (1968).
13. Stoner, E. C. & Wohlfarth, E. P. A mechanism of magnetic hysteresis in heterogeneous alloys. *Philos. Trans. R. Soc. London. Ser. A, Math. Phys. Sci.* **240**, 599–642 (1948).
14. Tannous, C. & Gieraltowski, J. The Stoner-Wohlfarth model of ferromagnetism. *Eur. J. Phys.* **29**, 475–487 (2008).
15. Slonczewski, J. C. Theory of Magnetic Hysteresis in Films and Its Application to Computers. *IEEE Trans. Magn.* **45**, 8–14 (2009).
16. Stoner, E. C. XCVII. The demagnetizing factors for ellipsoids. *London, Edinburgh, Dublin Philos. Mag. J. Sci.* **36**, 803–821 (1945).
17. Joseph, R. I. & Schlömann, E. Demagnetizing field in nonellipsoidal bodies. *J. Appl. Phys.* **36**, 1579–1593 (1965).
18. Aharoni, A. Demagnetizing factors for rectangular ferromagnetic prisms. *J. Appl. Phys.* **83**, 3432–3434 (1998).
19. Rhodes, P. & Rowlands, G. Demagnetising Energies of Uniformly Magnetised Rectangular

Blocks. *Proc. Leeds Philos. Lit. Soc.* **6**, 191 (1954).

20. Akoun, G. & Yonnet, J.-P. 3D analytical calculation of the forces exerted between two cuboidal magnets. *IEEE Trans. Magn.* **20**, 1962–1964 (1984).
21. Wright, C. E. X. Note on the potential and attraction of rectangular bodies . *London, Edinburgh, Dublin Philos. Mag. J. Sci.* **10**, 110–127 (1930).
22. Abert, C. Micromagnetics and spintronics: models and numerical methods. *Eur. Phys. J. B* **92**, 120 (2019).
23. Vansteenkiste, A. *et al.* The design and verification of MuMax3. *AIP Adv.* **4**, 107133 (2014).

3 Experimental Methods

In order to create magnetic thin films and then transform these films into particles, a number of different methods are used to deposit, pattern, and characterize the materials used. The fabrication involves a combination of standard physical vapour deposition methods – magnetron sputtering and thermal evaporation – where different methods were chosen depending on compatibility with the materials required. The films were then patterned into particles using standard lithographic techniques and released into liquid using two different lift-off processes: the photoresist and germanium processes. These have benefits and drawbacks that are explored fully in Chapter 4.4. The magnetic materials used were characterized, both in bulk and particle form, using the polar magneto-optical Kerr effect (MOKE) and vibrating sample magnetometry (VSM). Physical characterization using atomic force microscopy (AFM), electron microscopy, and optical microscopy were also needed to understand the physical shape and morphology of the particles and understand their assembly behaviour, in real-time and after the completion of assembly.

3.1 Particle Fabrication

3.1.1 Physical vapour deposition

Sputtering

Sputter deposition was used to fabricate the majority of the films presented in this work, including all magnetic multilayers. Sputtering itself has a surprisingly long history, with usage dating back to the mid-1800s, but it is the more recent development of magnetron sputtering that allows the effective film growth shown in this work.[1]

Sputtering works by applying a strong electric potential to a feed gas in the vicinity of a target of material to be sputtered. This potential creates a glow discharge in the gas, forming plasma. The potential gradient is such that the ions in the discharge are then accelerated toward the target, where they impact and eject target atoms. These ejected atoms then travel through the sputtering chamber by diffusive transport, eventually depositing on an available surface. Thus, in order to maximize the efficiency of the sputtering process, the plasma must be highly confined to the target and the chamber pressure must be minimized. The confined plasma ensures the glow discharge can be sustained by high-energy collisions of gas atoms and electrons, and the low pressure helps to increase the mean free path of the sputtered atoms, ensuring they reach the substrate.[2] To meet these requirements, modern sputtering systems use a magnetron to confine the plasma. The magnetron, which is a series of magnets with alternating polarity distributed under the target, provides a closed magnetic field near

the target surface, which helps to confine the plasma and increase the efficiency of the sputtering process.[2,3] Combined with high-vacuum technologies, magnetron sputtering has become a laboratory and industry standard due to its high deposition rates, high purity, and excellent uniformity.[4]

In this work, deposition was accomplished using direct current (DC) magnetron sputtering, with argon as the feed gas to drive the sputtering process. A six target sputter system was used to deposit films of Al, Au, CoFeB, Ru, Pt, and Ta, in order to form the magnetic and structural components of the films and particles. Sputtering was carried out at an argon pressure of 6 – 9 x 10^{-3} mbar and a base chamber pressure of 1 – 8 x 10^{-8} mbar. Deposition rates for each material were calibrated by sputtering thick calibration samples (~20 nm) for a given sputtering power and known length of time and measuring the sample thickness with an atomic force microscope (AFM). In this system, a 1 s delay in the opening and closing of the sputter target shutters provides a lower limit on thickness achievable, as no material can be sputtered for a shorter time than this delay. This leads to a functional resolution limit of about 0.2 nm for most materials sputtered and no thicknesses in this work are grown below this limit. In order to modify the growth rate, the power of the sputtering can also be changed. This power is directly related to the voltage and current applied to the plasma, thus changing the density of the plasma and the amount of material sputtered per unit time. In order to ensure uniform sputtering, the substrate being coated is rotated at 20 rpm.

Evaporation

Thermal evaporation was used to fabricate limited portions of some films. Certain materials were not available for magnetron sputtering, or needed in quantities that required prohibitively long sputter times, so thermal evaporation was chosen to take advantage of its higher possible deposition rates.

In thermal evaporation, the source material is place in a crucible or on a wire made from a high melting point material, usually tungsten. The crucible/wire is then resistively heated until the source material passes its evaporation point, where the material vaporises and then condenses on the substrate. The evaporation takes place in a vacuum, to ensure the source material vapour can reach the substrate without colliding with other gas molecules, and also to prevent any oxidation of the source material as it is heated.[5]

A BOC Edwards Auto 306 thermal evaporator was used to deposit films of Al, Ti, and Ge. The source material was place in tungsten boats or around tungsten wires, depending on the form of the source material. The system was used with a base vacuum pressure of 5 x 10^{-7} mbar and a deposition pressure of 5 – 9 x 10^{-6} mbar. Depending on the melting point of the source material, deposition currents of 1.5 – 4 A were used. The growth rate and overall thickness deposited were monitored *in situ* using a quartz crystal monitor (QCM). Since the evaporated films were only used as

structural components in magnetic films/particles which did not require precise thickness control, the QCM with standard calibrations provided sufficient.

3.1.2 Patterning

As the methods of particle fabrication evolved, different methods were used and improved. The two methods used in this work are a pre-existing photoresist-based release method and a developed germanium-based release method. In both cases, the magnetic film that forms the particle is patterned on a release layer, which can then be dissolved to release the particles into liquid. The experimentations with and results from these different release methods are outlined in 4.4, where Figure 4.17 shows a schematic diagram of the different fabrication and pattern methods used.

To complete the lithographic patterning in both cases, a Durham Magneto-Optics Microwriter ML2 direct laser write system was used. This system uses a software mask and a 405 nm laser with a 0.6 μm spot size to write lithographic patterns into photoresist. While a direct write system is slower than conventional mask lithography, it offers complete flexibility in patterning without needing to create different physical masks, allowing for easy changes in particle shape, size, and patterning density. The system was used with a range of different laser power and focus settings, depending on the optimum conditions for each type of photoresist.

Photoresist release process

In the photoresist release process, the magnetic film is deposited on top of pillars of photoresist. Positive photoresist in three different conditions were used to find the best photoresist-based release. In all cases Shipley S1813 positive photoresist was the main component, and was spin coated on the Si substrates to a thickness of 1 μm. The first condition was just a simple pillar pattern of S1813. The second was a combination of S1813 with Lift-off resist (LOR) B, which was spin coated underneath the S1813 layer with a thickness of 600 nm. The LOR provides an artificial undercut to the top S1813 layer. The third condition combined S1813 with a chlorobenzene soak. The chlorobenzene hardens the top portion of the resist, causing it etches more slowly during development than the rest of the resist and therefore allowing the positive resist to have a negative sidewall profile. These undercut geometries in the second and third conditions prevent conformal coating of the metallic film across the whole substrate. By creating this non-conformal coating, the patterned film (particles) can then be released by dissolution of the resist. Schematic diagrams and real examples of particles made from these three photoresist methods can be seen in Figure 4.19. All photoresist patterns were developed using AZ 326 developer, and dissolution of the resist to release the particle was achieved using either acetone or dimethyl sulfoxide (DMSO) in combination with ultrasonication.

Germanium release process

The germanium release process uses a series of lithography and ion milling steps to define the particle atop a germanium underlayer. Germanium is thermally evaporated onto the Si substrate at a thickness of 50 nm, and the Ge-coated chip is then sputtered with the desired magnetic film. A layer of photoresist is spin coated on top of the film to define a mask for ion milling. In this case, ma-N1410, a negative photoresist, is used, as it has a natural negative sidewall profile that works more effectively as a milling mask. Following the patterning and development of the photoresist in ma-D533s developer, the substrate is subjected to argon ion milling, to remove any un-masked magnetic film, leaving only the parts of the film defined by the photoresist pattern.

In the ion milling process, argon ions are generated by passing the gas through a coil emitting thermionic electrons. These ions are then passed through an accelerating grid, where a 600V positive potential accelerates the ions toward the substrate. A final neutralizing filament adds thermionic electrons to the accelerated ion beam to balance the charge of the positive ion stream, thus reducing the divergence of the beam and increasing the milling efficiency. Milling was calibrated on a series of reference samples to determine the speed at which various materials can be etched. The process takes place in a vacuum chamber with a base pressure of $1 – 9 \times 10^{-8}$ mbar and a milling pressure of 1×10^{-4} mbar.

Following ion milling sufficient to remove the un-masked magnetic film, the sample is then soaked in DMSO and ultrasonicated to remove the photoresist mask. Finally, the particles are released by dissolving the germanium underlayer in H_2O_2. A full schematic diagram of this process, along with examples of real particles made using it, can be found in Figures 4.23 and 4.24.

3.2 Magnetic characterization

3.2.1 Polar magneto-optical Kerr effect

Magneto-optics has its foundations in Michael Faraday's seminal work on light and magnetism, where he found that the polarization of light changes when transmitting through a magnetized material.[6] Building on the Faraday effect, John Kerr discovered the Kerr effect, showing that polarized light reflected off a magnetic substrate similarly showed changes in polarization related to the magnetization.[7,8] The proportionality between polarization and magnetization makes magneto-optical effects an extremely powerful tool to quickly and easily probe the behaviour of magnetic materials, especially thin films and nanostructures. The effect can be probed in three configurations related to the orientation of the sample magnetization and incident beam: longitudinal, transverse, and polar. As the longitudinal and transverse Kerr effects both evolve from in-plane sample magnetization, they are not used in this work. Thus, we will focus only on the mechanism and

measurement of polar MOKE, where the incident light is normal to the sample surface and parallel to the sample magnetization.

The magneto-optical Kerr effect can be described phenomenologically as arising from differences in the way right- and left-handed circularly polarized light interact with a magnetic material. A linearly polarized incident beam is a combination of two opposite circularly polarized beams of equal magnitude, so when this incident beam is reflected off of a magnetic sample, the asymmetric changes in the circularly polarized components of the light will lead to a net change in the polarization of the beam.

These asymmetric changes come from asymmetry in the material's index of refraction, which is composed of the electrical permittivity and magnetic permeability of the material. As the frequency of light is many orders larger than any magnetic precession or resonance processes in the material, the permeability can be taken as a constant, leaving the light interaction wholly dependent on the electrical permittivity, and thus, the dielectric tensor that defines this quantity.[9] When magnetized, materials have an asymmetric dielectric tensor (*Eq. 3-1*) due to spin-orbit coupling in the atoms of the materials.[10,11] This coupling leads to a spin-dependent anomalous Zeeman effect, which will change how the material will interact with circularly polarized light, as the angular momentum of the light must be conserved on interaction.

$$\epsilon = \epsilon_{xx}\begin{pmatrix} 1 & -iQm_z & iQm_y \\ iQm_z & 1 & -iQm_x \\ -iQm_y & iQm_x & 1 \end{pmatrix} \qquad \textit{Eq. 3-1}^{12}$$

In this case, it is assumed that $\epsilon_{xx} = \epsilon_{zz}$. Furthermore, $Q = \frac{i\epsilon_{xy}}{\epsilon_{xx}}$, and (m_x, m_y, m_z) are the direction cosine components of the magnetization.[12] Considering only the polar Kerr components of the tensor (those involving m_z) and using an eigenvalue equation $\epsilon E = n^2 E$, the index of refraction for polar Kerr reflections can be found from solving for the eigenvalues of a matrix containing only the m_z components.[9] This leads to eigenvalues of $n = \epsilon_{zz}^{\frac{1}{2}}(1 \pm Q)^{1/2}$ and eigenmodes of $E_x \pm iE_y$.[9] The two eigenmodes are related to the left and right circularly-polarized light, and the different eigenvalues associated with these modes show how the index of refraction will differ for the different components of the light, causing circular birefringence, which in turn leads to a phase shift of the light and a rotation of the initial plane of polarization. Additionally, the aforementioned Zeeman effect of spin-orbit coupling leads to different electronic transition energies and populations for absorption of the two circular components.[13] This circular dichroism changes the amplitude of the reflected components, changing the ellipticity of the reflected wave. More complete mathematical constructions of these magneto-optical effects can be found in references 12[12], 14[14], and15[15].

To implement measurements of polar MOKE, a Durham Magneto Optics NanoMOKE3 was used. This commercial system is a fully contained MOKE magnetometer, using a laser combined with polarizing optics and filters. The setup allows the polarization of the reflected beam to be compared with a reference polarization state to find the changes in Kerr rotation and ellipticity with high sensitivity. For polar measurements the beam is normal to the sample surface, and the system has a dipole magnet with field direction oriented parallel to the sample normal, allowing oscillating fields of up to 6500 Oe and at frequencies of up to 20 Hz (not simultaneously) to be applied to samples during measurement. Since MOKE is an optical measurement, it is limited by the spot size of the laser, so the measurements will be local measurements of the sample. The spot size used for measurements is roughly 10 μm, but it can be focused as small as 2 μm to improve lateral resolution.[16] Additionally, the measurement is surface-sensitive, so the MOKE signal is attenuated by sample depth. The NanoMOKE3 system can measure polarization changes of 0.5 mdeg and reflectivity changes of 0.02 %.[16] With such limits the sensitivity of the system is 6 x 10^{-12} emu.[17] While the MOKE measurements obviously lack any quantitative information about the sample magnetization, it is incredibly useful for quickly probing the switching behaviour of a sample. It is used to measure both magnetic films and, crucially, particles down to sizes of 5 μm. The NanoMOKE3 system also includes a Hamamatsu C11440 CMOS camera that can be used for sample imaging. The camera has a 6.5 x 6.5 μm pixel size that provides the limit of resolution for the system.

3.2.2 Vibrating sample magnetometry

Vibrating sample magnetometry (VSM) offers essential capabilities not captured by MOKE magnetometry. Primarily, VSM is a global magnetometry tool which be used to quantitatively characterize sample moment and, thus, magnetization. Coincidentally, the larger applied field of the VSM system allows it to probe the hard axis anisotropy of films and particles, which is necessary to understand the PMA present in the samples and how it changes under changing sample geometries and compositions.

The VSM oscillates the magnetic sample at a set frequency between a set of detection coils and in a uniform magnetic field, with the oscillation axis perpendicular to the field direction.[18] The change of magnetic flux into the coils created by the stray field of the vibrating magnetic sample induces an electromotive force (emf) in the coils, which can be measured as a voltage or current. The origin of the emf in the coils can be taken from the integral form of the Maxwell Faraday equation (*Eq. 3-2*).

$$\oint_{\partial\Sigma} E \cdot dl = -\frac{d}{dt}\int_{\Sigma} B \cdot dA \qquad \textit{Eq. 3-2}$$

Where the left side of the equation is a contour integral over the contour $\partial\Sigma$ for the electric field E induced by the time-varying magnetic field B, integrated through the area of the surface Σ. When looking at the equation in the context of varying magnetic flux through a wire, as in the VSM, the left side of this equation is directly a calculation of the emf (ε) in wire, by integrating the total induced electric field, while the right side is a calculation of the magnetic flux through the surface bounded by the wire. Thus, the equation can be re-written as

$$\varepsilon = -\frac{d\Phi_B}{dt} \qquad \textit{Eq. 3-3}$$

Applying this to a general case for the VSM, where a sample, taken to be a spherical point dipole with moment m, is oscillating with a simple harmonic potential $\vec{k}\delta\sin(\omega t)$.[19] k is a unit vector parallel to the direction of oscillation.[19] Combining this case with *Eq. 3-3*, where the expression for the B-field from a point dipole m, using the harmonic potential to determine the distance from the magnetic dipole to the coil, is integrated to find the flux density in the wire area, leading to

$$\varepsilon = \mu_0\omega\delta\vec{m}\cdot\vec{g}\cos(\omega t) \qquad \textit{Eq. 3-4}^{19}$$

In this equation g is a geometric factor, to account for the specific coil geometry of the system. The expression in *Eq. 3-4* connects the time-varying oscillation of the sample and its magnetic moment with the emf generated in the detection coils. This emf can then be detected electronically to very high sensitivities by using a lock-in amplifier to look only at the signals with a frequency equal to the frequency of oscillation.[20] Since the signal is directly proportional to m, the VSM offers an excellent quantitative measurement of sample moment.

The VSM measurements in this work were all conducted using a Microsense EZ7 VSM. This system oscillates at a frequency of 75 Hz and has a maximum applied field of 1.75 T. The noise level of the system is $1\text{x}10^{-6}$ emu, which provides the resolution limit of the system. The system is regularly calibrated using a Ni reference sample and all measurements use a subtracted background correction to account for the influence of the sample holder or other systematic errors in the measurement.

3.3 Physical characterization

3.3.1 Atomic force microscopy

Atomic force microscopy is a standard tool for understanding and characterizing surface properties, especially roughness. As the roughness of various surfaces in the thin film structure affects the interfaces, and thus the magnetic properties, of the film, it is important to be able to measure and understand this physical property.

A Park XE 100 AFM in non-contact mode was used with NSC15/ Al BS (r = 10 nm) and SSS-NCHR (r = 2 nm) tips. In non-contact mode, the AFM cantilever, which contains the tip on its end, is oscillated by a piezoelectric actuator just above the resonant frequency of the cantilever. As the tip of the cantilever interacts with the sample surface through van der Waals interactions, the amplitude of oscillation changes.[21] By reflecting a laser off the back of the cantilever onto a four-quadrant photodetector, the change in oscillation can be detected, and the height of the tip can be compensated to its original state, thereby recording information about the height changes of the surface.

Scans of 1 x 1 μm with 512 lines per scan were taken, and each scan was post-processed using Gwyddion to flatten, zero, align, and remove artefacts from the image.[22] These processed images were then analysed to find the roughness of the surface. At this scan size and conditions, the system has a lateral resolution of 1.95 nm and a vertical resolution of 0.9 Å.

3.3.2 Scanning electron microscopy

Scanning electron microscopy (SEM) is a crucial tool for observing and understanding the morphology and behaviour of the micro- and nano-scale magnetic particles. Particles and particle assemblies can be imaged at different stages of the particle creation and assembly process to understand and characterize these processes. While SEM cannot be used to perform *in situ* observations of particles, as all these occur in liquid, the higher resolution of the SEM compared to optical microscopy offers a way to check, in detail, particles and assemblies before and after liquid interactions.

To accomplish the imaging in this work, an FEI XL30 FEG (field emission gun) was used. A standard SEM, the XL30 uses a tungsten field emission gun, which provides a more collimated and brighter electron beam than other source types. The image was constructed from secondary electron emissions of the sample, collected by an Everhart-Thornley detector. All imaging was accomplished at an accelerating voltage of 5 kV, using a variety of tilt angles (0 - 45° from the beam axis) when required. At this voltage, the SEM has a resolution of 2.5 nm.

3.3.3 *In situ* optical microscopy

One of the most important ways to understand magnetic particles and assembly behaviour is direct observation the particles in liquid and under applied magnetic fields, so the response and interactions of the particles can be tracked in real-time. The need for liquid discounts vacuum-based technologies like SEM, and the wide area of observation desired, to capture many particles and their interactions, precludes AFM or scanning probe techniques. Optical microscopy is the ideal tool to for this application.

In order to capture particles in liquid without ruining the microscope objectives and be able to simultaneously apply magnetic fields, a custom microscope setup was created for this work. The system uses an Olympus BXFM modular microscope mount, which allows the whole microscope assembly to be positioned above the sample area, leaving the area free for a magnet. The microscope employs a number of super long working distance objectives (25x, 50x, 100x) to give a range of magnifications and fields of view. The resolution of the different objectives is 1.1, 0.79, and 0.46 μm, respectively. This resolution is calculated assuming an intermediate visible light wavelength of 550 nm. In reality the microscope uses white light for illumination. The long working distance allows the microscope and objectives to be positioned relatively far from the sample, which keeps the objectives away from the liquid sample and leaves enough room for the magnet. A 5 megapixel colour video camera is used to record both images and videos of the samples, and a dipole magnet is used to apply magnetic fields of up to 4000 Oe and 10 Hz perpendicular to the imaging axis. Figure 3.1 show a schematic diagram and pictures of the *in situ* optical microscope setup.

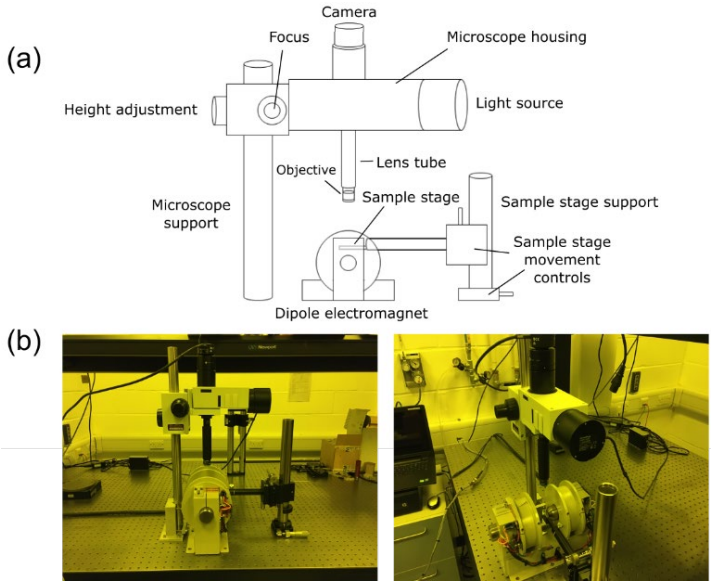

Figure 3.1 Schematic diagram and picture of *in situ* optical microscopy setup
(a) Schematic diagram of the *in situ* optical microscope setup, along with (b) images of the setup, with a side (left) and front (right) view.

3.4 References

1. Greene, J. E. Review Article: Tracing the recorded history of thin-film sputter deposition: From the 1800s to 2017. *J. Vac. Sci. Technol. A Vacuum, Surfaces, Film.* **35**, 05C204 (2017).
2. Kelly, P. J. & Arnell, R. D. Magnetron sputtering: A review of recent developments and applications. *Vacuum* **56**, 159–172 (2000).
3. Kelly, P. J. & Arnell, R. D. The influence of magnetron configuration on ion current density and deposition rate in a dual unbalanced magnetron sputtering system. *Surf. Coatings Technol.* **108**–**109**, 317–322 (1998).
4. Tudose, I. V. *et al.* Chemical and physical methods for multifunctional nanostructured interface fabrication. in *Functional Nanostructured Interfaces for Environmental and Biomedical Applications* 15–26 (Elsevier, 2019). doi:10.1016/B978-0-12-814401-5.00002-5
5. Lévy, F. Film Growth and Epitaxy: Methods. *Encycl. Condens. Matter Phys.* 210–222 (2005). doi:10.1016/B0-12-369401-9/00418-6
6. Schatz, P. N. & Mccaffery, A. J. *The Faraday Effect*.
7. Kerr, J. XLIII. On rotation of the plane of polarization by reflection from the pole of a magnet . *London, Edinburgh, Dublin Philos. Mag. J. Sci.* **3**, 321–343 (1877).
8. Kerr, J. XXIV. On reflection of polarized light from the equatorial surface of a magnet . *London, Edinburgh, Dublin Philos. Mag. J. Sci.* **5**, 161–177 (1878).
9. Coey, J. *Magnetism and Magnetic Materials*. (Cambridge University Press, 2010).
10. Hulme, H. The Faraday effect in ferromagnetics. *Proc. R. Soc. London. Ser. A, Contain. Pap. a Math. Phys. Character* **135**, 237–257 (1932).
11. Argyres, P. N. Theory of the Faraday and Kerr effects in ferromagnetics. *Phys. Rev.* **97**, 334–345 (1955).
12. You, C. Y. & Shin, S. C. Derivation of simplified analytic formulae for magneto-optical Kerr effects. *Appl. Phys. Lett.* **69**, 1315–1317 (1996).
13. Spaldin, N. *Magnetic Materials Fundamentals and Applications*. (Cambridge University Press, 2011).
14. Zak, J., Moog, E. R., Liu, C. & Bader, S. D. Universal approach to magneto-optics. *J. Magn. Magn. Mater.* **89**, 107–123 (1990).
15. Qiu, Z. Q. & Bader, S. D. Surface magneto-optic Kerr effect. *Review of Scientific Instruments* **71**, 1243–1255 (2000).
16. *Durham Magneto Optics Ltd NanoMOKE3 ® Specifications Marketed by Quantum Design*.
17. Allwood, D. A. *et al.* Magneto-optical Kerr effect analysis of magnetic nanostructures. *J. Phys. D. Appl. Phys.* **36**, 2175–2182 (2003).
18. Foner, S. Vibrating sample magnetometer. *Review of Scientific Instruments* **27**, 548 (1956).

19. Pacyna, A. W. General theory of the signal induced in a vibrating magnetometer. *J. Phys. E.* **15**, 663 (1982).
20. Gerber, J. A., Burmester, W. L. & Sellmyer, D. J. Simple vibrating sample magnetometer. *Rev. Sci. Instrum.* **53**, 691–693 (1982).
21. Binnig, G., Quate, C. F. & Gerber, C. Atomic force microscope. *Phys. Rev. Lett.* **56**, 930–933 (1986).
22. Nečas, D. & Klapetek, P. Gwyddion: An open-source software for SPM data analysis. *Central European Journal of Physics* **10**, 181–188 (2012).

4 Particle Design

Collaboration: The development of inorganic release layers for particle creation (Section 4.4.2) was done in collaboration with Emma Welbourne and Dr. Tarun Vemulkar.

4.1 Introduction

Out of the many PMA film systems that have been discovered, Co/Pt multilayers have been extensively researched for a number of different applications, on account of their excellent magnetic properties and tunability.[1,2] Specifically, Co/Pt (and the related Co/Pd and CoFeB-based system) was developed for use in magnetic recording and magnetic memory in a number of different forms. Chapter 1 covered the push toward perpendicular recording that inspired these developments. Here we will look specifically at the Co/Pt system: its development, its current status, and its relevance to this work.

Initial research of Co/Pt multilayer systems was inspired by the search for suitable materials to use in perpendicular magnetic recording.[3] The first iteration of this work was Co/Pd, as an advancement on PMA Co-Cr alloys discovered previously.[4,5] Soon followed the discovery of Co/Pt layered structures that showed the same PMA from interfacial effects identified in Co/Pd.[6] In addition to investigations into the suitability for perpendicular recording media, these materials were also quickly adapted for magneto-optical recording, where the magnetic state of the bit would be read out optically using the Kerr effect.[7] The Co/Pt system was found to have high Kerr rotation, especially at shorter wavelengths, which would enable smaller laser spots and denser magneto-optical storage.[8] Research in these directions continued apace into the 2000s, generating an immense amount of interest and knowledge about Co/Pt and related systems.[9–11]

At the same time as early Co/Pt system were being investigated, the seminal discovery of giant magnetoresistance (GMR) was taking place, initiating research into spin electronics.[12–14] This, along with the earlier discovery of tunnel magnetoresistance (TMR), opened an entirely new avenue for magnetic materials, especially layered structures such as Co/Pt.[15] These initial discoveries were made using in-plane magnetic materials, but it was soon found that the effects could be enhanced in perpendicular films, resulting in ever-increasing interest in systems like Co/Pt.[16–18] Incorporation of these concepts into devices quickly led to new read head development for improved magnetic storage density and the creation of magnetic random-access memory (MRAM).[19] Additionally, further research into the spin polarized currents resulting from these effects found that angular momentum transfer from the spin current could be used to switch magnetization.[20,21] This concept, known as spin-torque transfer (STT), now allowed electrical switching of magnetic states, opening further avenues

for creating logic and memory devices with higher densities and greater performance, such as STT-MRAM.[14] The low current density, high thermal stability, high magnetoresistance values, and high spin-torque efficiencies offered by PMA materials have made them especially valuable for these applications.[22,23] Further, the discovery of excellent TMR ratios in materials like perpendicular CoFeB/MgO offered another interesting avenue of development for this class of materials, which is useful for the CoFeB/Pt system used in this work.

Along with the great strides being made in spintronic devices, Co/Pt was also heavily researched for magnetic and domain wall logic, and other domain wall-based systems such as racetrack memory.[24–26] PMA materials like Co/Pt are especially well suited for domain wall-based applications, because the strong anisotropy of the systems leads to very small domain wall widths (domain wall width $\delta \sim (A/K_{eff})^{1/2}$, where A is the exchange constant and K_{eff} is the anisotropy, with typical values of $\delta \approx 5 - 10$ nm for Co/Pt), which allows the walls to move at greater velocities for lower current densities.[27–30]

A number of further fields have spawned from the development of Co/Pt and PMA films. Some recent examples include taking advantage of the vertical dimension of thin films with a soliton ratchet as a precursor for more advanced 3D data storage in Co/Pt films, the development of skyrmions as a new stable information carrier, or the use of voltage as a new method for switching magnetic devices.[31–36]

Through these decades of advancement, a wealth of knowledge has been generated about the Co/Pt and CoFeB/Pt systems. Films of Co/Pt and CoFeB/Pt have been well-optimized for high anisotropy and magnetization, and there is a strong understanding of how the film material, thickness, and configuration can be used to control its magnetic properties.[1] We will be able to draw on this knowledge, with an added twist: we will turn these films into particles. Magnetic particles have been created by combining physical vapour deposition and lithographic techniques to incorporate useful magnetic properties, such as high moment, perpendicular anisotropy, or anti-ferromagnetism, into particle and liquid systems.[37–41] Such particles offer a number of interesting biomedical applications, and the same ideas can be used design particle for self-assembly. We can combine the CoFeB/Pt thin films with previous work developed in the Cowburn group for creating PMA particles from film, in order to build a self-assembly system based on PMA magnetic particles, [40]

In this chapter, we will begin by outlining the properties desired in the magnetic particles and the films from which they are created. Using these constraints, we will show the optimization process that was followed to build up the ideal thin film, first focusing on the magnetic properties of the CoFeB/Pt multilayer, then by understanding how the addition of structural buffers will impact these magnetic properties. Finally, we will show the process by which these films are turned into particles. The particles are initially attached to the substrate upon which they are grown and subsequently released into solution. Various methods for particle formation and release will be experimented with in this process. There will be reference to a number of different thin film layer structures. These layer

structures will take the form {Au(40)/ Ta(2)/ Pt(2)/[CoFeB(0.55)/ Pt(0.7)]$_4$/ CoFeB(0.55)/ Pt(2)}, which lists the whole film structure in order of growth. For each layer the composition and thickness (in nm) are given, so Au(40) is a 40 nm thick layer of gold. For repeated multilayer, a subscript is used to denote the number of repeats, where [CoFeB(0.55)/Pt(0.7)]$_4$ represents four repeats of the 0.55 nm CoFeB and 0.7 nm Pt layers. While some literature uses the word 'multilayer' to denote films that have more than one total layer (i.e. almost all thin films structures), in this work, we will use the terms single layer and multilayer to refer to the number of magnetic layers in the structure.

4.2 Design constraints

In order to optimize the magnetic film and particles, the desired properties for the particles must be understood. In this case, we hope to create a system of magnetic particles that can undergo equilibrium self-assembly, in the absence of any externally applied field or force. To enable this form of self-assembly the particles must have both high magnetic moment and high remanence (M_r), so the magnetic moment can drive the inter-particle interactions. Additionally, it is important that particle interactions are directional. To ensure directionality of interaction, the direction of magnetization must be strongly defined by a strong magnetic anisotropy. Finally, in order to be able to control the specificity of interactions, it is important to be able to control the initial magnetic state of the particles and create particles with differing initial magnetization states. To have this control, the particles must have sharp reversal behaviour and well-defined, controllable coercivity (H_c).

Figure 4.1 shows a schematic diagram of the ideal hysteresis behaviour of the particles, fitting all the requirements listed above. The square loop shape with high magnetization (and thus, high moment) along with high anisotropy is the perfect base for creating this self-assembly system. This loop also schematically shows the values of various useful quantities: remanent magnetization (M_r), saturation magnetization (M_s), and coercivity (H_c).

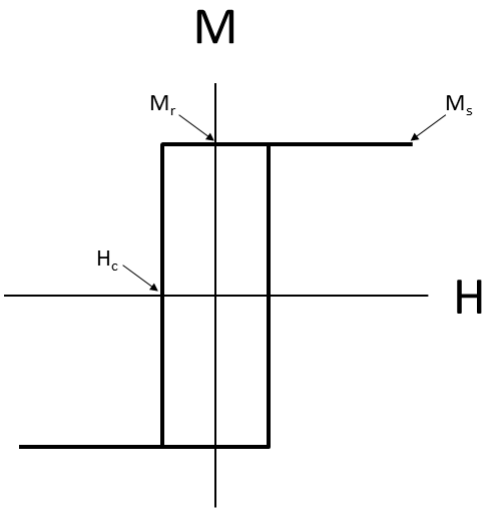

Figure 4.1 Ideal magnetic behaviour for film and particles
The figure shows an idealized M-H loop of the magnetic behaviour of the film, and particles, being designed in this work. The ideal look is perfectly square with high moment (high magnetization x thickness). The values of remanent magnetization (M_r), saturation magnetization (M_s), and coercivity (H_c) are defined.

PMA materials, as outlined previously, are a perfect match for this purpose, because the many of the properties optimized in the search for improved magnetic recording media, such as high remanence, high anisotropy, and sharp reversal, are exactly the same as what is desired for this case.[8,11,42,43]

A full outline of each property and how it will be defined in this work is listed below.

High remanence

High remanence is the most important property of any magnetic particle created for this self-assembling application. In order for the particles to assemble in the absence of an external magnetic field, the inter-particle interactions must be able to drive assembly, and that can only be accomplished when the particle has a high remanence. Full remanence is achieved when the magnetization reversal only occurs in an applied field with a sign opposite to the magnetization.[8] Thus, the material will remain saturated in the absence of any external field. Full remanence is a key property of Co/Pt and CoFeB/Pt multilayers.[8] In PMA materials, the strong anisotropy prevents the easy nucleation of reverse domains, because of the high energy barrier to nucleation resulting from the high anisotropy, an idea further investigated below. Remanence will be quantified by taking the ratio of remanent to saturation magnetization (M_r/M_s). These values will be derived from MOKE hysteresis loops. While MOKE is not quantitative with respect to magnetization, it can be used to compute a ratio from data taken under identical conditions, such as in the same hysteresis loop, since the Kerr signal is proportional to M. Any value of $M_r/M_s > 0.99$ will be considered as full remanence.

High magnetic moment

Along with high remanence, the particles need high magnetic moment to drive the desired interactions, as magnetic moment, along with separation distance, is the key determinant of the force and energy of particle interactions. Additionally, a high magnetic moment will ensure that high torques can be applied to the magnetic particles or their assemblies, since the torque is equal to the cross-product of moment and applied field.[44] This torque will enable actuation of the particles or assemblies, allowing greater functional use of the particles and assemblies. Magnetization will be measured using VSM, and the moment will be quoted as a moment per area, M_st, where t is the total thickness of the CoFeB in the film. M_st is a better quantification of moment for thin films and the particles created from them, as it can be used to compare the moments of particles of different lateral size. It is also important to note that although the calculation is made using just the thickness of CoFeB, the Pt layers also contribute to the overall magnetization of the sample through induced polarization of the Pt atoms.[45] Additional variations in magnetization values of the CoFeB could be seen due to the moment enhancement of the Co from interfacial spin-orbit interactions.[46,47] For consistency this work will use t_{CoFeB} throughout for these calculations, understanding that the M_st could potentially vary with both Pt and CoFeB thickness. Optimizing magnetic moment will be a combination of maintaining M_s while also maximizing the thickness of magnetic material in the film.

Sharp reversal and controllable coercivity

Sharp reversal and a controllable coercivity are important aspects to have for promoting specificity and laying a foundation for being able to create more complex particles, by using combinations of magnetization directions in separate regions of the particle or sections of the multilayer to control interaction strength and likelihood.

To understand how reversal characteristics can be controlled, we must first understand the dominant reversal processes in PMA materials. The reversal behaviour of many materials was initially a point of contention during the early development of micromagnetics theory, leading to Brown's Paradox.[48] Brown's theorem held that coercivity should be equal to or greater than the anisotropy field minus the demagnetizing field, as switching occurred by coherent rotation of the magnetization through the hard axis.[49] However, coercivities in almost all magnetic materials, including PMA materials, are significantly lower than the anisotropy field, leading to the aforementioned paradox. In PMA materials, coercive fields can be on the order of tens to hundreds of Oe versus anisotropy fields of 5 – 10+ kOe. The discrepancy between these values comes from inhomogeneities in materials where the local properties around defects are different from the bulk, allowing reversal to occur at lower field values. Thus, PMA materials switch by a domain nucleation and propagation process, where reverse domains are nucleated and then expand through the sample. To understand the material properties and external factors which govern this process, we will consider the nucleation and

propagation separately. Nucleation can be understood by considering a thermally activated process in inhomogeneous regions.[49,50] This is the idea proposed in the Néel-Brown model (*Eq. 4-1*),

$$\Delta E = K_{eff} V (1 - \frac{H}{H_K})^{\alpha} \qquad \textit{Eq. 4-1}$$

where ΔE is the energy barrier for nucleation, with K_{eff} as the effective anisotropy, V as the switching volume, H as the applied field, H_K as the anisotropy field, and α as a power law exponent related to the angle between the applied field and the easy axis (equal to 2 for a field aligned with the easy axis and opposite the sample's magnetization).[51–53] This model, which was adapted by Sharrock for explaining the time dependence of coercivity and switching fields in a study of magnetic recording materials, still has some deficiencies, such as the lack of consideration of exchange energy in a domain (and domain wall) driven process.[53,54] Thus, it was superseded by the droplet model for nucleation, which uses a standard surface-volume energy comparison to determine critical nuclei size.[53] The energy penalty of forming a domain wall on the nuclei surface is countered by the Zeeman energy gained in aligning the nuclei volume with the applied field. In this model, the energy barrier is expressed as shown in *Eq. 4-2* ,

$$\Delta E = \frac{\pi t \gamma^2}{2\mu_0 M_s} (\frac{1}{H} - \frac{1}{H_0}) \qquad \textit{Eq. 4-2}$$

where γ is the domain wall energy, which is related to $\sqrt{K_{eff} A}$, where A is the exchange constant, t is the magnetic layer thickness, M_s is the saturation magnetization, H is the applied field, and H_0 is the critical field needed to create the initial droplet with radius r_0.[53] Since the droplet can only expand if it reaches the critical nucleus size, the energy barrier in *Eq. 4-2* represents the energy difference from the initial nucleus radius r_0 to the critical nucleus, after which the expansion of the nucleus (and domain) is favourable. Both the Néel-Brown and droplet model lead to a thermal dependence of the nucleation process, as an Arrhenius-type fluctuation of thermal energy will be needed to overcome the energy barrier. Brown provides a complete treatment of the timescales involved in the thermal fluctuations.[55] By understanding the thermal nature of nucleation in magnetic materials such as PMA materials, it is now clear how Brown's Paradox is unlocked. Additionally, the thermal, and thus stochastic, nature of nucleation also explains the field sweep rate dependence of coercivity and switching in PMA. Conclusive proof of this can be seen in large range studies of field sweep rate dependency of coercivity, where at the highest sweep rates the coercivity approaches the anisotropy field.[53] At extremely high sweep rates, the applied field changes too quickly to take advantage of the thermally driven nucleation, so the reversal has to occur by coherent rotation.

The second component of switching in PMA materials is propagation of domain walls. The propagation of domain walls is generally governed by the number and strength of inhomogeneities in the sample, as these defects will pin the domain walls and slow their movement.[56] Bruno offers an excellent treatment of this relationship between defects and pinning field, the result of which is shown in *Eq. 4-3*.[57]

$$H_p \approx \frac{2\sigma^2(2\pi A h_c)^{1/2}}{h^{5/2}\zeta} \qquad \textit{Eq. 4-3}$$

H_p is the pinning field, σ is the thickness fluctuation amplitude, A is the exchange constant, h_c is the transition thickness of the perpendicular film (equal to the thickness at the spin-reorientation transition (SRT)), h is film thickness, and ζ is the correlation length of fluctuations of the domain wall energy, which is closely related to the correlation length of the sample roughness. This general analysis of wall pinning shows that pinning fields are higher for samples with greater roughness and smaller thicknesses (where thickness can be connected to anisotropy, as a smaller thickness below the SRT will lead to a higher K_{eff}). Additionally, the lateral aspect of the roughness, which relates to the correlation length, is important. The combined effect of all these fluctuations in real material is that the energy of a domain wall must change, either through changes in its area or energy per area, as it passes over defects where the material properties vary.[57] This energy change is what must be overcome as the wall moves, leading to pinning. Domain walls also interact most strongly with defects that are on a similar length scale to the wall width.[49] For PMA materials wall widths are usually on the order of ~10 nm.[30] It will be important to understand roughness that exists on this scale to be able to understand the development of pinning in our materials and see the effect on domain propagation.

PMA materials can achieve sharp reversal characteristics, because their reversal is nucleation-limited (propagation-dominated), where a small number of reverse domains can expand easily following nucleation due to weak pinning. This leads to ideal sharp reversal, which is the goal for our films and particles. To maintain this sharp reversal, care must be taken to reduce sample roughness to reduce wall pinning, while minimizing the amount of defects that govern nucleation.[58,59] Both these steps can be accomplished by creating a smooth and low defect film. However, as more layers and complexity are added to films, this will increase the accumulated roughness and defect population, and this roughness may be further enhanced by additional metallic layers added for increased structural stability.[60–62] While the particles will require certain thicknesses for ideal magnetic behaviour and structural stability, it must be ensured that the reversal is not overly impacted by this increase in roughness and pinning, to retain full remanence and also so multilayers of different coercivity can be switched separately without overlap in the transitions. Keeping this sharp reversal is

a key component of controllable coercivity. By being able to control the coercivity of the magnetic material, control of different magnetic states can be achieved to promote specific interaction. It will be important to understand how coercivity in the films can be controlled, with sharp reversal behaviour being a key part of that process. The sharpness of the reversal will be defined by the nucleation field divided by the saturation field H_{nuc}/H_{sat}. An ideally sharp transition would have a value of 1. The field values defining sharpness will be taken from MOKE hysteresis loops, always ensuring the calculation is made using values from the same loop, with the nucleation field being taken as the beginning of the reversal transition and the saturation field as the end. Additionally, to account for the field sweep rate dependence of reversal outlined above, all samples will be measured at the same field sweep rate of 2000 Oe/s.

High anisotropy

PMA materials have exceptionally high anisotropy due to the spin-orbit coupling of the Pt and Co atoms at their interfaces.[46,63–65] A full explanation for this phenomenon is found in Chapter 2. This anisotropy will allow for highly directional interactions between particles, as the particle magnetization is purely in the direction of the surface normal, driving strong face-to-face interactions. This will allow very strong interactions due to the low centre-to-centre separation between particles in such a configuration. Additionally, the well-defined magnetization direction can be used to controllably manipulate the particles and their assemblies in liquid, applying torques that can used to actuate the particles, with the high anisotropy ensuring applied fields will rotate and move the particles themselves, not the magnetic moment. While the anisotropy of these materials is already well-optimized from extensive research and sufficient for these applications, care must be taken that the anisotropy remains stable even with the further additions that will be made to the film architecture, especially because of the $1/t_{CoFeB}$ dependence of this interface anisotropy.[66] The anisotropy will be defined as the effective anisotropy K_{eff}, which is calculated from the magnetization M_s and anisotropy field H_k that is taken from saturation along the sample hard axis (in-plane). The calculations can be made using the relationship $K_{eff} = \frac{H_k M_S}{2}$.

4.2.1 From film to particles

Since the magnetic films are being created with the end goal of forming magnetic particles, it is important to recognize how this dimensional change will affect the magnetic properties of the material. Figure 4.2 shows a comparison between the MOKE hysteresis loops of a film and an array of particles, both from the same film with a layer structure {Au(40)/ Ta(2)/ Pt(2)/[CoFeB(0.55)/ $Pt(0.86)]_4$/ CoFeB(0.55)/ Pt(2)}. As will be shown in this chapter, this film is a layer structure

developed for particle applications, combining the properties outlined here with a structural Au backbone to allow the particles to exist stably in liquid.

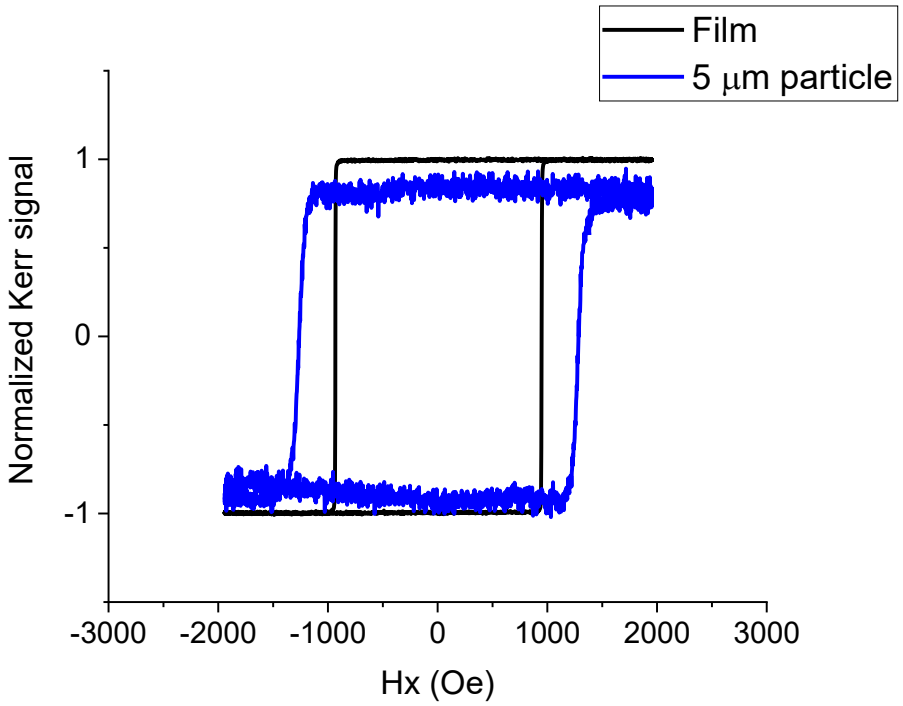

Figure 4.2 Comparison of magnetic properties in film and an array of particle
MOKE hysteresis loops comparing the magnetic properties from the bulk film and a collection of ~10 particles that have been created from the film. The film/particle structure is {Au(40)/ Ta(2)/ Pt(2)/ $[CoFeB(0.55)/ Pt(0.86)]_4$/ CoFeB(0.55)/ Pt(2)}.

The figure shows how the magnetic properties, especially the reversal behaviour, change from the film to the collection of particle. The two main changes visible in reversal behaviour are the increase in coercivity and the decrease in transition sharpness. The increase in coercivity is a consequence of the nucleation-limited reversal seen in highly anisotropic PMA system. Since the reversal occurs through nucleation of a reverse domain, followed by easy wall movement, the process relies on the distribution of these nucleation sites, which often occur on defects where the anisotropy of the material is significantly lowered, thus lowering the energy required to nucleate a reverse domain in that volume. In this nucleation-driven regime, it only takes a small number of nucleation sites to determine the nucleation field, and thus coercivity, of the entire film. However, when the film is patterned into smaller areas, the likelihood of these areas containing one of the low-energy nucleation sites that drives the switching of the film is low.[67] Thus, on average, the particle will nucleate its reversal at a higher field value.[68] While it is possible nucleation (and switching) field can be lowered in structures patterned by ion milling, which is how the particles in Figure 4.2 are created, this effect is only seen at patterning to dimensions of 200 nm or less, much smaller than the particles here.[69] The patterning of the particles by ion milling can also induce edge roughness and damage to

the film that will act as pinning sites, increasing the field needed to propagate domain walls.[69] This will also contribute to the increase in switching field and account for the more slanted reversal behaviour of the particle, as increased pinning interferes with the fast domain expansion that characterizes sharp reversal.

4.3 Particle composition

Designing the particle compositions will focus on two separate parts of the film: the magnetic composition and the structural composition.

The magnetic composition will cover the magnetic properties listed above, with the largest emphasis focused on keeping full remanence with a large moment per area, leading to magnetic behaviour as demonstrated in Figure 4.1. This will be accomplished by building CoFeB/Pt multilayers, testing the layer thickness of both the CoFeB and Pt, along with the number of repeats that can be sustained while retaining all the desired properties. $Co_{60}Fe_{20}B_{20}$ (at. %) is chosen as the magnetic material in this work. CoFeB, due to its amorphous nature and the inclusion of boron, has much lower domain wall pinning fields compared to Co.[70–74] Because the magnetic film will require a structural buffer layer and be patterned, both of which contribute to increases in defects and wall pinning, it is important that wall pinning is minimized from a material standpoint, in order to retain the sharp reversal desired in the transformation from film to particle. While there is a reduction in saturation magnetization and anisotropy compared to Co, these values can still be optimized to sufficient degrees through design of the multilayer. All magnetic films will begin with a 2 nm Ta buffer layer and a 2-4 nm Pt seed layer, which has been established as an effective buffer layer for such CoFeB-based films.[75] At low thicknesses, the Ta layer remains amorphous, acting to promote the growth of (111) Pt, as the smooth amorphous Ta promotes atomic mobility of the deposited Pt, allowing it to reach its energetically favourable, close-packed (111) structure.[76–78] The (111) Pt orientation is crucial for maximizing the perpendicular anisotropy of the film, promoting high out-of-plane anisotropy and magnetization.[76,79]

In addition to the magnetic composition, the structural composition of the film will also be addressed. The structural components refer to additional material that is used to promote the mechanical stability of particles in liquid, as the thin films are prone to mechanical deformation at very low thicknesses. This thickness cannot be accommodated by increasing repeats of the magnetic material, as it will eventually lead to a deviations from the square magnetic behaviour desired and such is unacceptable for the requirements listed above.[1,80] Therefore, it was important to test multiple other materials such as Al, Au, Ru, and Ti, that could provide structural reinforcement while not overly damaging the magnetic properties of the film. A full accounting of the necessity for structural

support in these particles, with examples of the mechanical instabilities various particles showed, is covered in Chapter 5.

4.3.1 Magnetic composition

In order to understand and optimize the magnetic structure of the CoFeB/Pt multilayer, we must investigate the effect of changing CoFeB thickness, Pt thickness, and number of layer repeats in the overall multilayer structure. Beginning with a single CoFeB/Pt layer, this will be built up into multilayer structures with different repeats and Pt interlayers, all with an eye towards finding magnetic properties that match most closely with the guidelines outlined in 4.2.

CoFeB/Pt multilayers: maximizing moment per area

The primary goals of maximizing moment per area and retaining full remanence will be the driving force behind the growth of these CoFeB/Pt multilayers, as these two characteristics are the most essential to self-assembling particles. To maximize moment per area, both the magnetization of the film and the total thickness of CoFeB must be optimized, as the M_st will be maximized through a combination of both values. Magnetization of CoFeB can be enhanced in the layered structure, as Co/Pt multilayers have reported M_s enhancements up to 30% over bulk values, due to a combination of interfacial enhancement of the Co and polarization of Pt.[1,46] Any enhancements in M_s, since they depend on the CoFeB/Pt interface, should be present in all multilayers structures, so we do not expect large variation in M_s in the films. In our films the M_s of CoFeB typically remains around 1200 emu/cm^3, and magnetization measurements will be used to ensure the structure and processing of the film does not cause substantial deviation from this value.[81] Thus, the main determinant for increasing M_st will be the thickness differences available in different multilayers. Multilayers can be grown with total CoFeB thicknesses ranging from 0.3 to 10.0 nm or more. This potential order of magnitude increase in thickness will be the greatest determinant of M_st, and thus, we must understand the thicknesses of CoFeB achievable in multilayers while still retaining the properties of remanence and reversal desired for this application. Starting from a CoFeB/Pt single layer, the possible thicknesses will be probed to determine these limits.

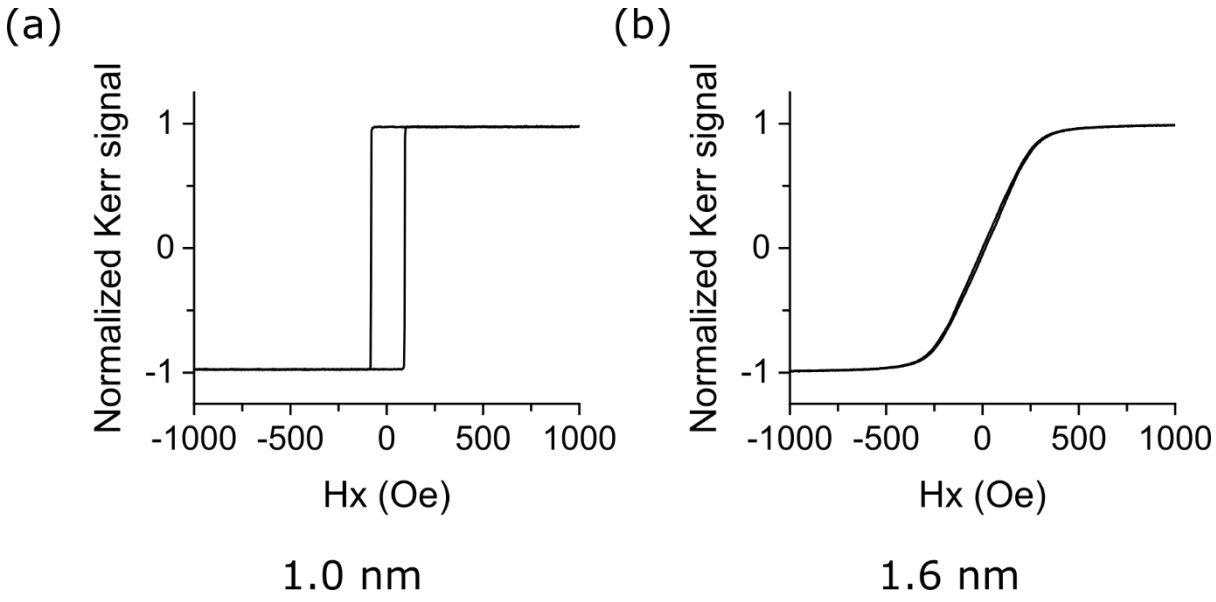

Figure 4.3 CoFeB/Pt single layer limits
A number of samples with the structure {Ta(2)/Pt(2)/CoFeB(**t**)/Pt(2) were grown to find the limits of thickness for CoFeB in a single layer. (a) shows a sample with PMA, while (b) shows a sample beyond the spin-reorientation transition that has lost its PMA.

The limits of the CoFeB/Pt single layer are defined by the percolation limit at the lower end and the spin-reorientation transition at the upper end. At the percolation limit, the film is too thin to make a continuous layer. This kind of formation will complicate the collective reversal desired in these structures. In our system this limit has been shown to be around 0.2 – 0.3 nm, but we hope to avoid any of the low thickness limits as we work to maximize the thickness of the magnetic layers. On the upper limit, the thickness of a single layer is limited by the SRT, which is the thickness at which the interface anisotropy is no longer larger than the shape anisotropy. Due to demagnetizing energy, the volume anisotropy favours an in-plane magnetization, and once the ratio of interface to volume atoms drops too low, the sample will lose its PMA (see Chapter 2 for a full treatment of this phenomenon). This limit was found to be below 1.6 nm for a CoFeB single layer (Figure 4.3, b) on the standard buffer layers of Ta(2)/Pt(2). This can be considered the maximum limit of any individual CoFeB layer. While the thin CoFeB/Pt single layer does exhibit very ideal reversal behaviour (Figure 4.3, a), effort was made to further increase the moment of the film using magnetic multilayers.

CoFeB/Pt multilayers can be constructed that allow the total thickness of CoFeB to exceed the 1.6 nm limit prescribed by the SRT in the single layer. This is because while the total volume of magnetic material increases in a multilayer, each individual thin magnetic layer in the multilayer still has a favourable balance of volume and interface anisotropy, favouring PMA. Figure 4.4 shows the variation of CoFeB thickness in a multilayer with five magnetic layers, with the layer structure {Ta(2)/ Pt(2)/ [CoFeB(**t**)/ Pt(0.7)]$_4$/ CoFeB(**t**)/ Pt(2)}. A multilayer with five magnetic layers was found in literature to represent the limit of an ideally square reversal in a number of different studies, so this was taken as the starting point for building our multilayer film.[80,82]

(a)

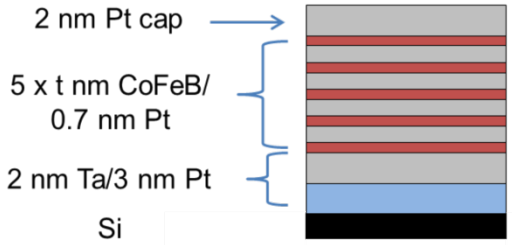

(b)

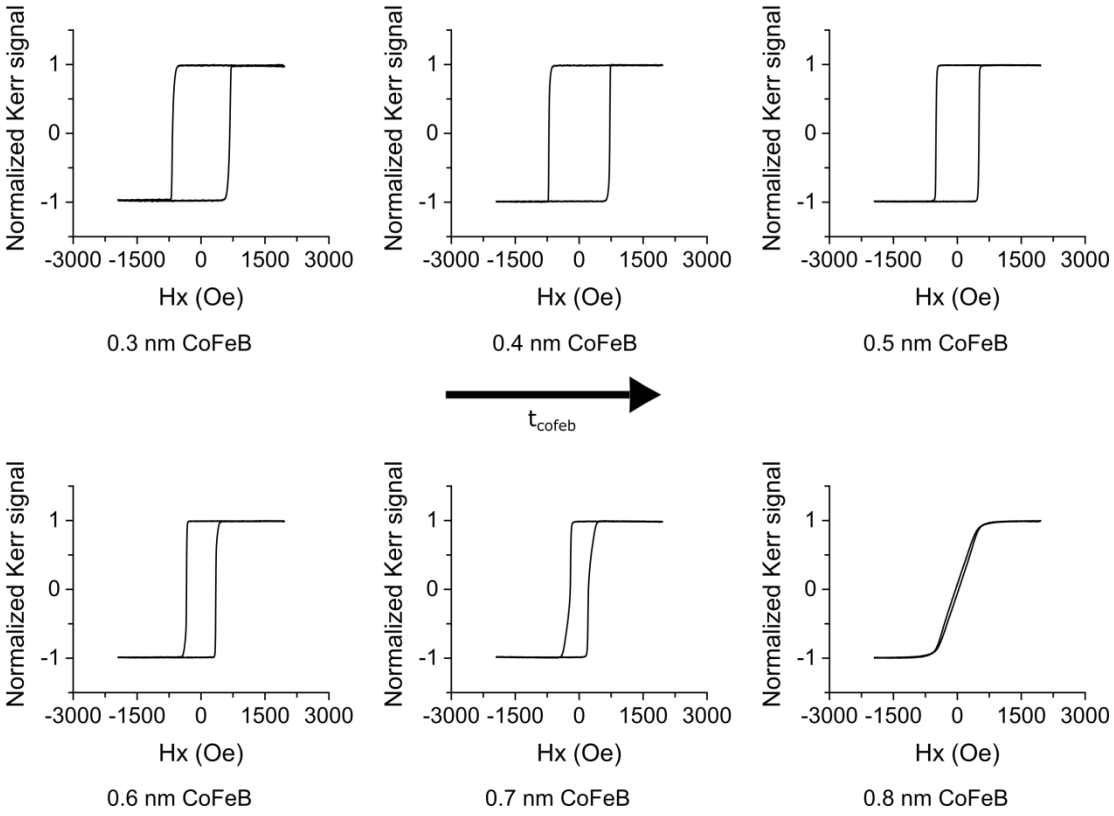

Figure 4.4 Change in magnetic behaviour versus CoFeB thickness in a 5-layer CoFeB/Pt multilayer
The change in magnetic behaviour with increasing CoFeB thickness is showing for a multilayer {Ta(2)/ Pt(2)/ [CoFeB(**t**)/ Pt(0.7)]$_4$/ CoFeB(**t**)/ Pt(2)}, with MOKE hysteresis loops being used to characterize magnetic behaviour. (a) gives a schematic diagram of the multilayer being investigated. (b) shows the change in hysteretic behaviour as the CoFeB thickness is increased for each of the 5 layers of the magnetic multilayer.

In multilayer samples the different magnetic layers are ferromagnetically (FM) coupled, which accounts for the sharp and collective switching seen in the structures. Co/Pt structures have been shown to have an oscillatory interlayer coupling that changes with Pt thickness but is always ferromagnetic and of an RKKY type.[80] This allows the retention of sharp reversal in the multilayers,

at least until the overall thickness of magnetic material is such that stripe domains begin to form, which leads to the change in behaviour seen in the hysteresis loops for the 0.6, 0.7, and 0.8 nm samples.[82] As the overall thickness increases, so does the total demagnetizing energy of the multilayer. This energy can be reduced by forming stripe domains, which is a lamella of oppositely ordered domains, and it is the formation and propagation of these stripe domains that leads to the decreased nucleation field and slanted reversal seen with increasing CoFeB thickness.[82] To further understand the properties of the different multilayers, the samples have been analysed in accordance with the requirements listed previously. Figure 4.5 shows the remanence, coercivity, reversal sharpness, moment per area, and anisotropy of the different multilayers in Figure 4.4.

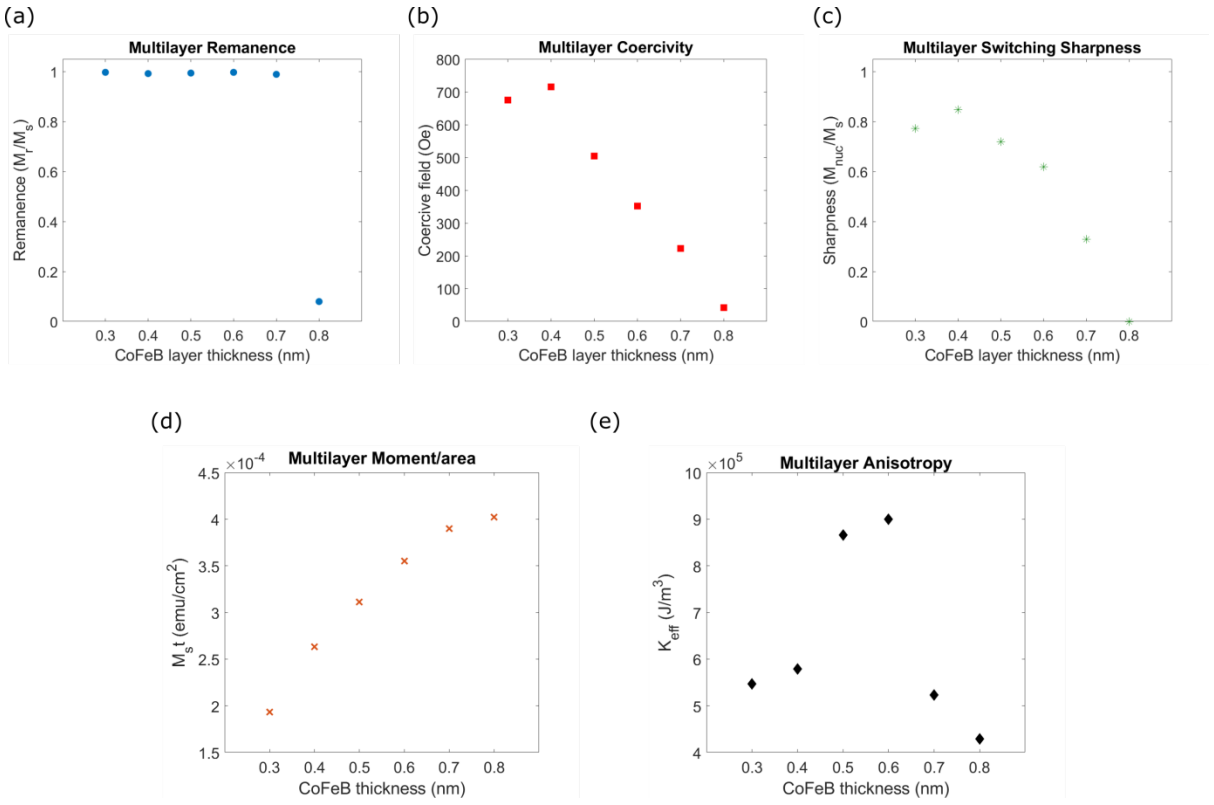

Figure 4.5 Analysis process for multilayer optimization
When optimizing the thickness of CoFeB and number of repeats in the multilayer, five quantities were considered: (a) remanence, (b) coercivity, (c) switching sharpness, (d) moment/area, and (e) anisotropy (K_{eff}). This figure shows the data that was taken for the optimization of the film {Ta(2)/ Pt(2)/ [CoFeB(**t**)/ Pt(0.7)]$_4$/ CoFeB(**t**)/ Pt(2)}, hysteresis loops for which are shown in Figure 4.4.

The multilayer with a CoFeB thickness of 0.8 nm per layer can be immediately discounted due to its low anisotropy and lack of out-of-plane reversal behaviour. Coercivity will not be optimized to any specific value, although control of coercivity is desired, which will be undertaken in 4.3.2. Reversal sharpness shows a large drop past the multilayer with 0.6 nm CoFeB, with all values at thicknesses smaller than 0.6 nm falling roughly between 0.6 and 0.85. Thus, we will take 0.6 nm as

the upper limit to satisfy the reversal requirements. The moment per area of the samples increases with increasing CoFeB thickness and we are able to find the strongest perpendicular anisotropy for the multilayers with t_{CoFeB} = 0.5 - 0.6 nm. Thus, this range is the optimal thickness for retaining all the desired properties in the 5x multilayer. In order to ensure reproducibility of the properties across variations in processing conditions, a slightly thinner layer of 0.55 nm was taken as the ideal 5x multilayer.

This layer of 5x 0.55 nm CoFeB (2.75 nm total thickness) was then compared with multilayers of the same total thickness but made up of different numbers of layers of different thicknesses. The results are shown in Figure 4.6, where 2x, 3x, 4x, 5x, and 6x multilayers were all compared.

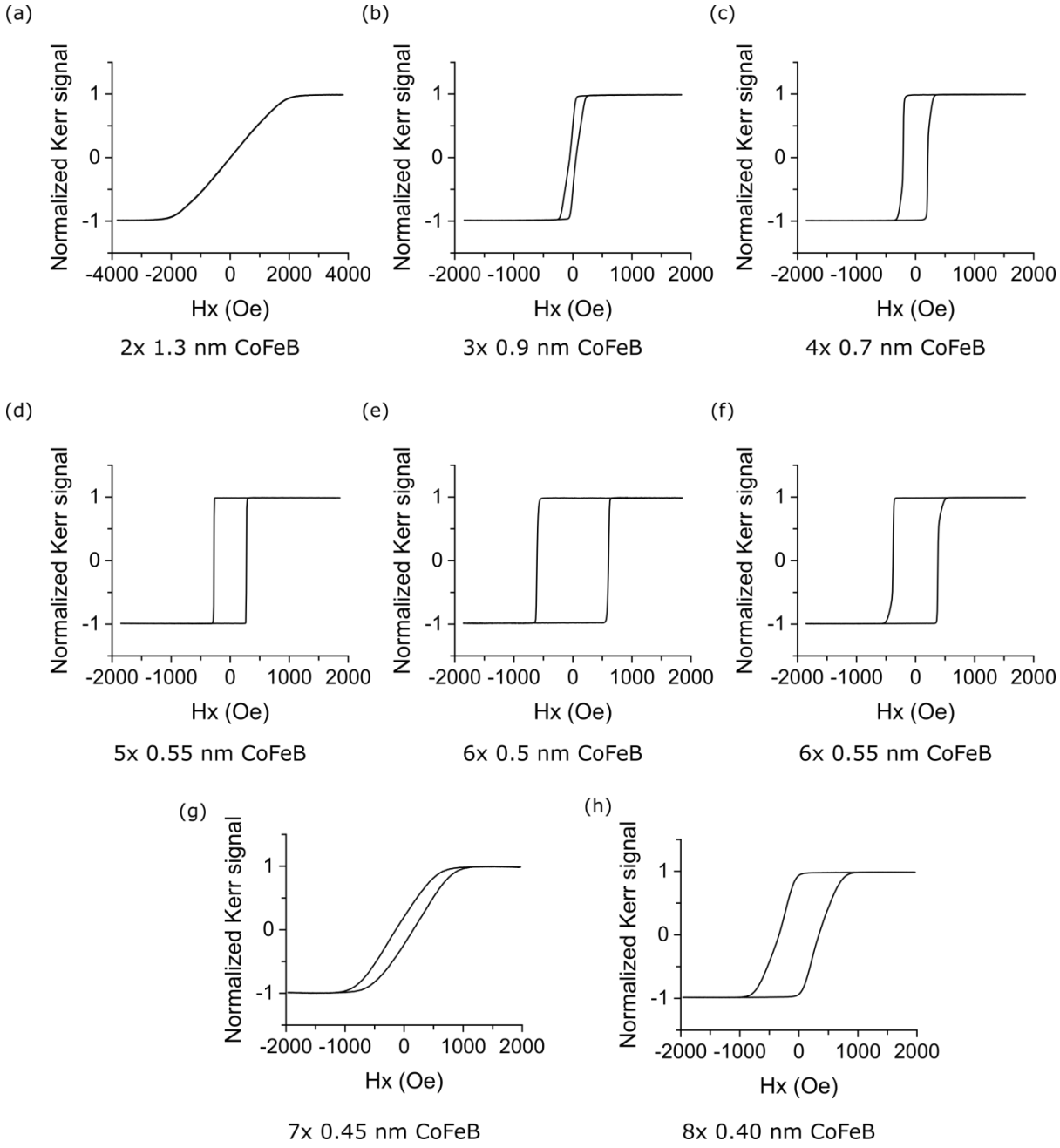

Figure 4.6 Comparison of multilayer with changing number of layers N
Multilayers were formed for N = 2, 3, 4, 5, and 6 while keeping the total thickness near that found in the 5x 0.55 nm CoFeB multilayer (2.75 nm total). The following multilayers were created: (a) 2 x 1.3 nm CoFeB (2.6 nm total), (b) 3x 0.9 nm CoFeB (2.7 nm total), (c) 4x 0.7 nm CoFeB (2.8 nm total), (d) 5x 0.55 nm CoFeB (2.75 nm total), (e) 6x 0.5 nm CoFeB (3.0 nm total), (f) 6x 0.55 nm CoFeB (3.3 nm total), (g) 7x 0.4 nm CoFeB (3.15 nm total), and (h) 8x 0.40 nm CoFeB (3.2 nm total).

For all multilayers with the number of repeats N < 5, stripe domain formation prevents the sharp reversal desired in the film. Additionally, when increasing the total magnetic thickness in an N= 6 multilayer with higher total CoFeB thickness (Figure 4.6, f), the same kind of strip domain reversal behaviour can be seen. It is also seen in 7x (g) and 8x (h) multilayers, which prevents further stacking of thinner layers to increase the total thickness. From this comparison it is clear that to maintain the

ideal magnetic behaviour desired, the film must have a multilayer structure with 7 > N > 4 magnetic layers and a total thickness between 2.5 and 3.0 nm. This range matches well with examples in literature, where large numbers of repeats or thick magnetic layers led to stripe domain formation, while square hysteresis loops could be created at total magnetic material thickness ranges of 2.0 – 4.0 nm.[1,82,83] As seen previously in Figure 4.5, the moment/area of the film will scale with total thickness of the magnetic layers, which is reproduced for the films from Figure 4.6 in Figure 4.7 below.

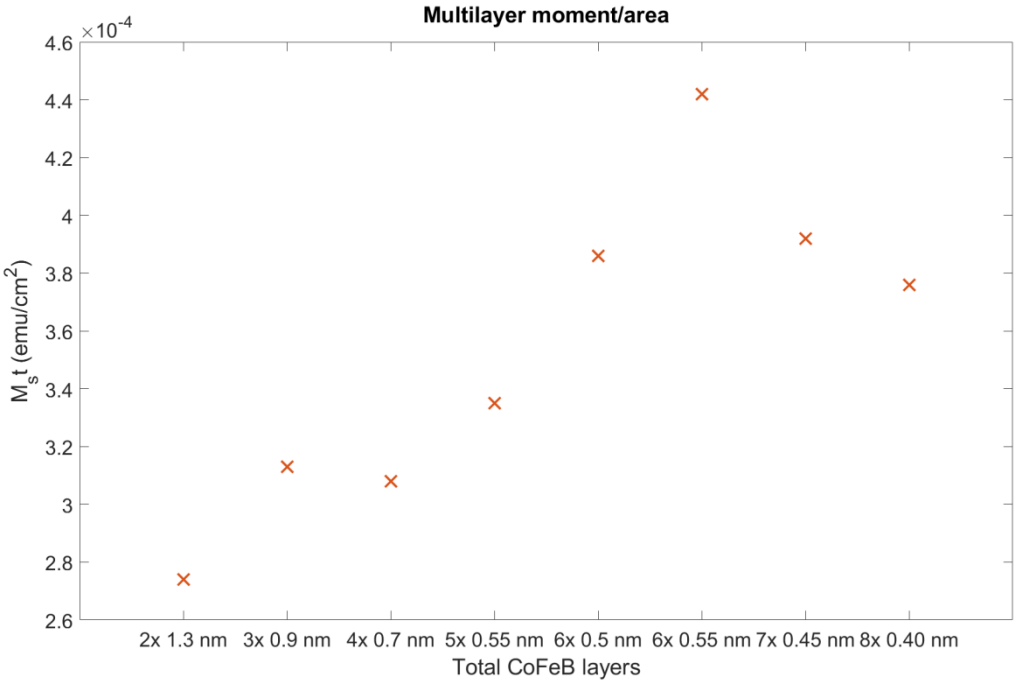

Figure 4.7 Moment per area of multilayers with different numbers of magnetic layer
The moment per area ($M_s t$) is given for the various multilayers presented in Figure 4.6.

This analysis of multilayer repeats finds that 5x 0.55 nm and 6x 0.5 nm are the two best candidates for our application, matching ideal reversal properties with high $M_s t$. While the 6x 0.5 nm system will have a slightly higher $M_s t$, we found that it could not be as consistently formed in the sputtering system. The higher overall magnetic thickness means it is closer to the regime where stripe domains form, which damages the reversal behaviour. As the sputtering system will have slight variations over time in process pressure and sputtering rate that can affect the growth and properties of films, it was found that the layer structure {Ta(2)/ Pt(2)/ [CoFeB(0.55)/ Pt(0.7)]$_4$/ CoFeB(0.55)/ Pt(2)} was the most consistently achievable film that also maximized the properties (moment/area, remanence) desired.

Pt interlayers: stabilizing anisotropy

After testing the CoFeB thickness and number of repeats at a set Pt thickness, we now investigate the optimum Pt thickness in a 5x multilayer at a set CoFeB thickness. Figure 4.8 shows a selection of MOKE hysteresis loops from the Pt thickness series, to analyse the changing in reversal behaviour. Figure 4.9 looks at the change in M_st and K_{eff} with Pt thickness, to find the optimum level for each quantity.

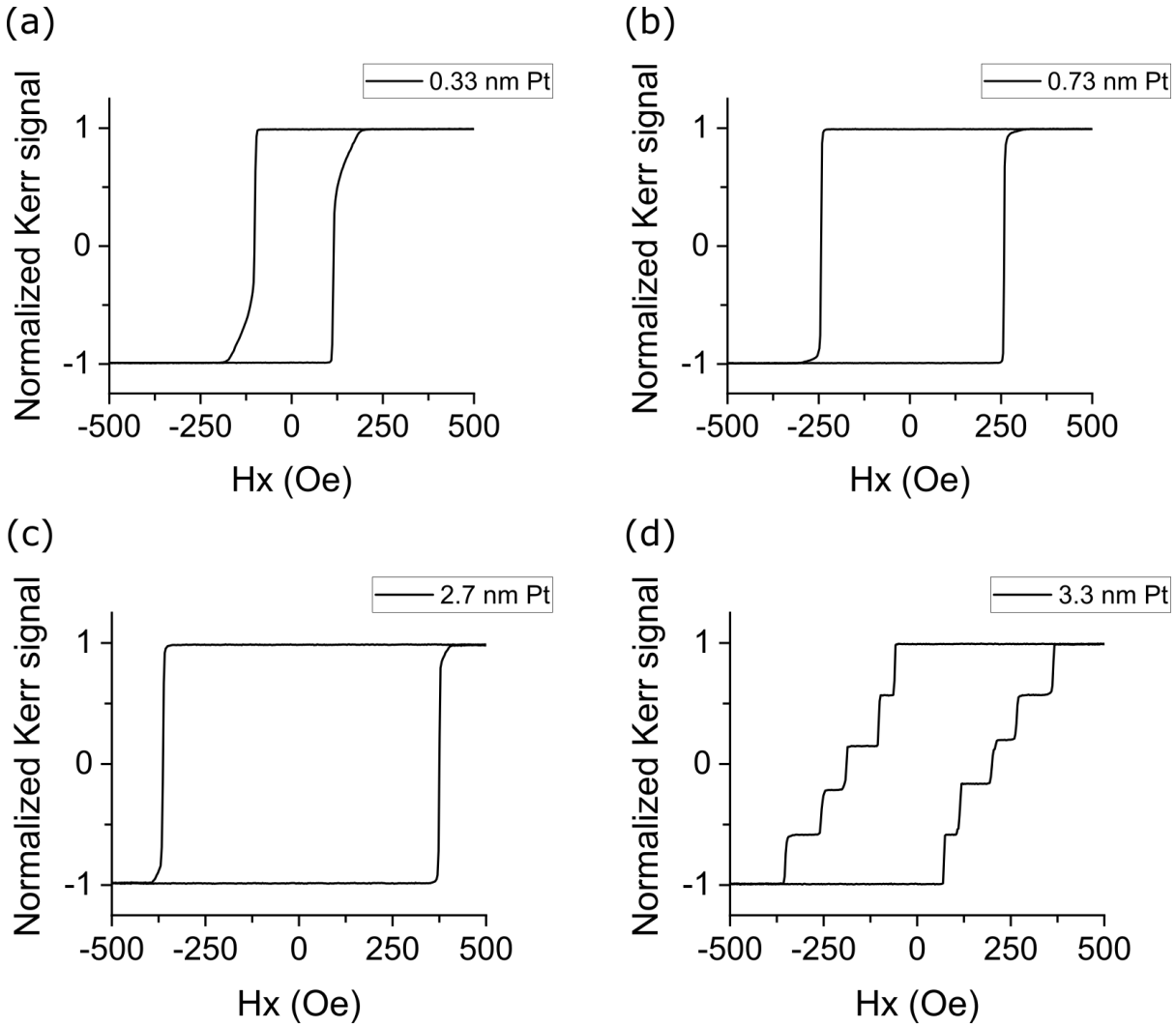

Figure 4.8 Change in magnetic behaviour of a 5x CoFeB/Pt multilayer with increasing Pt thickness
A film series with the structure {Ta(2)/ Pt(2)/ [CoFeB(0.55)/ Pt(t)]$_4$/ CoFeB(0.55)/ Pt(2)} was grown, increasing the thickness of the Pt interlayers to see the effect on magnetic behaviour. The four hysteresis loops show the behaviour as the Pt thickness is increased from 0.33 (a) to 0.73 (b) to 2.7 (c) to 3.3 nm (d).

Figure 4.8 demonstrates how the reversal behaviour changes with increasing Pt thickness. At initial, low values (a), the reversal is not sharp due to a lower coverage by the thin Pt layer, which

means the PMA is not as uniform and the reversal process is not as consistent, leading to slanting in parts of the transition. With increasing Pt thickness, the reversal behaviour stabilizes, with uniformly sharp transitions that are governed by propagation of a small number of nucleated domains.[84] Most of the samples show a slight curve at the end of the transitions, likely due to enhanced roughness leading to wall pinning, meaning the final portion of the reversal is governed by nucleation of many small domains that cannot easily propagate, leading to a smearing of the transition field. This kind of behaviour is evident in many of the multilayer samples, where the accumulated roughness of the thicker film structures can cause such behaviour due to a roughening of the top layers, as defects accumulate and propagated vertically through the structure.[62] At a Pt thickness of 3.3 nm (Figure 4.8, d), the magnetic layers become uncoupled due to the thickness of the Pt and each layer switches independently. A loss of FM coupling at 3.3 nm Pt is roughly in line with some literature values, which found the change to happen at a thickness of 4.0 nm, while others found coupling was retained up to 7.9 nm.[80,85] These discrepancies in literature could be due to differences in the film structure, such as underlayer material. This is likely also true for our film, especially when comparing our CoFeB film with the Co films used in these studies. The lower amount of magnetic material in our layer will induce less polarization and thus lead to a shorter maximum coupling distance.

The changing Pt thickness should have very little impact on the magnetization of the CoFeB as well. Even though the CoFeB/Pt interface will give orbital enhancement to the Co and some induced polarization in the Pt atoms, it will be an interfacial effect and not vary substantially with the thickness of the Pt.[46,86] Indeed, it is even shown that the induced Pt polarization will decrease with Pt thickness, as the thicker Pt layers show less intermixing at the interfaces, consequently reducing the Co-Pt nearest neighbour interactions that drive the Pt polarization.[86] We find that, for the Pt thickness series shown in Figure 4.8 and Figure 4.9, the M_s of the films varies between 1157 and 1330 emu/cm^3, with no dependence on Pt thickness. However, the thickness of Pt does have a more substantial effect on anisotropy (K_{eff}), as shown in Figure 4.9. For thin Pt layers, the anisotropy is lower, but once the Pt reaches a suitable thickness (~0.7 nm), the anisotropy stabilizes. This happens due to better Pt coverage and less intermixing, leading to sharper interfaces that promote stronger anisotropy.[87] We want to ensure our films are grown in this stabilized region so the anisotropy does not vary greatly between samples or within the sample due to small inhomogeneities in Pt thickness from the growth process.

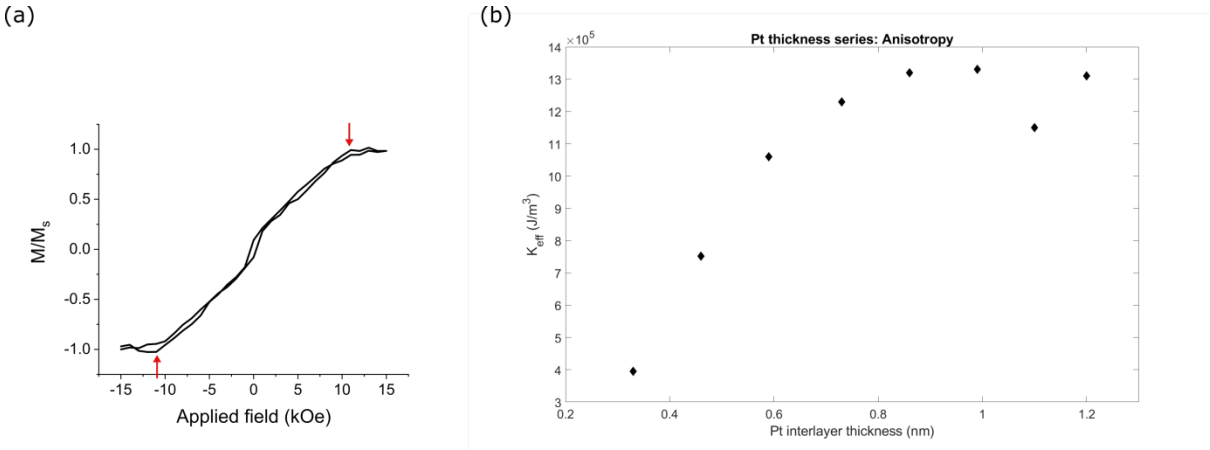

Figure 4.9 Perpendicular anisotropy of a 5x CoFeB/Pt multilayer
Hard axis saturation measurements (a) were used to determine the perpendicular anisotropy of magnetic multilayers with varying Pt thickness. The red arrows indicate the value of the hard axis saturation field which are used to calculate anisotropy. (b) shows the anisotropy values for a multilayer {Ta(2)/ Pt(2)/ [CoFeB(0.55)/ Pt(**t**)]$_4$/ CoFeB(0.55)/ Pt(2)} over a range of Pt interlayer thicknesses. The hard axis hysteresis loop in (a) corresponds to t_{Pt} = 1.1 nm.

This analysis shows that the Pt thickness can be optimized for our purposes in the range of 0.8 – 1.0 nm. This value allows the anisotropy to be maximized to a steady-state regime while leaving the magnetization unaffected.[1,88] This thickness also retains the FM coupling desired in these multilayers to ensure sharp and collective reversal of the magnetic film.

Multilayer reversal

We can also use the transition from coupled to un-coupled multilayer seen in Figure 4.8 to understand the limiting components in multilayer reversal. Figure 4.10 (a) compares a coupled and uncoupled 5x multilayer. The coercivity of the coupled multilayer is closest to that of the hardest layer of the uncoupled sample. Additionally, Figure 4.10 (b) compares a 4x and 5x uncoupled multilayer, showing that the hardest layer is the top layer of the stack, as it is the hardest (most coercive) transition that disappears when going from 5 to 4 magnetic layers in the multilayer.

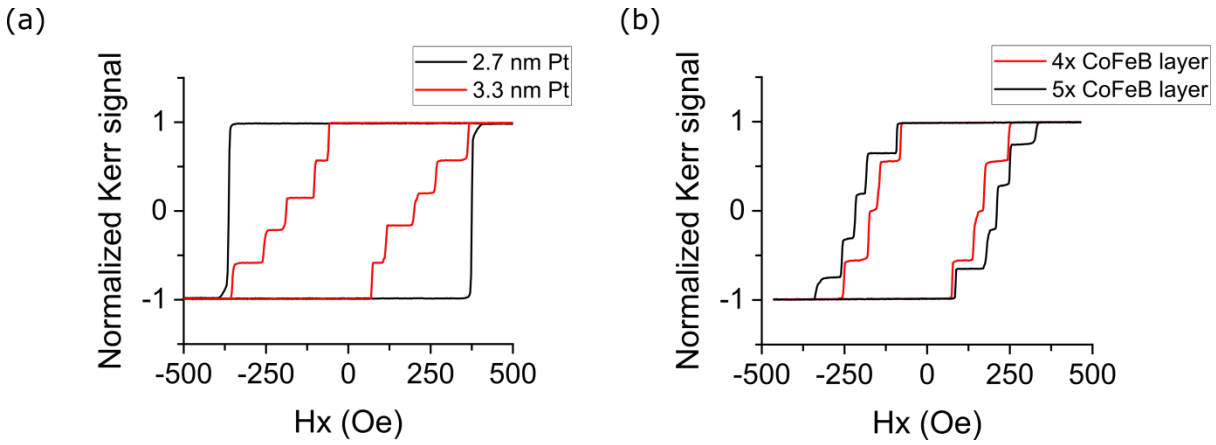

Figure 4.10 Comparison of uncoupled CoFeB/Pt multilayers
A {Ta(2)/ Pt(2)/ [CoFeB(0.55)/ Pt(**t**)]$_4$/ CoFeB(0.55)/ Pt(2)} multilayer is compared with (a) Pt interlayers of 2.7 and 3.3 nm, which leads to a breakdown of FM coupling at the higher thickness. (b) compares the two multilayers {Ta(2)/ Pt(2)/ [CoFeB(0.55)/ Pt(4.0)]$_4$/ CoFeB(0.55)/ Pt(2)} (black) and {Ta(2)/ Pt(2)/ [CoFeB(0.55)/ Pt(4.0)]$_3$/ CoFeB(0.55)/ Pt(2)} (red).

By combining these two ideas, we can show that the reversal of the coupled multilayer is driven by the hardest layer, which will be the top layer of the film. The top layer will also be the most defective layer of the film, containing all the defects that propagate up the multilayer during the layer-by-layer growth. Thus, it is sensible that this layer would have the highest barrier to domain propagation through pinning and the highest coercivity. It will prove especially useful to understand the multilayer reversal when combining the multilayers with different structural underlayer materials in the next section.

Through the series of experiments above, we have found a magnetic film layer structure that matches the requirements laid out earlier in this chapter. The layer structure {Ta(2)/ Pt(2)/ [CoFeB(0.55)/ Pt(0.86)]$_4$/ CoFeB(0.55)/ Pt(2)} gives a high moment per area with full remanence without compromising sharp reversal behaviour. It also retains a strongly defined PMA. This layer structure will now be combined with structural elements to determine their suitability for inclusion in the film structure.

4.3.2 Structural composition

Along with optimizing the magnetic composition of the films, it is important to understand the mechanical requirements of particles that will be created from these films. Simply, at the extremely high aspect ratios of the planar films and particles, where the thickness of the magnetic structure (the CoFeB/Pt multilayer) is 2 – 3 orders of magnitude smaller than the particle's lateral dimensions, the particle is not mechanically stable without further structural reinforcement and will curl up under the strain of the deposited film.

Selection of underlayer material

To test the suitability of different structural layers, a number of materials were tested in combination with the magnetic multilayer, to understand how they affect the magnetic behaviour of the film. Obviously, the structural layer should not seriously damage the magnetic properties of the film; otherwise, it would be unsuitable for such an application. Outside of compatibility with the magnetic film structure, the structural material must be easy to process and inert, given the liquid conditions in which these particles are used. Four materials (Au, Al, Ru, Ti) were tested, the results of which can be seen below. The material in Figure 4.11, e (Ti) was thermally evaporated, while the materials in b – d (Au, Al, Ru) were sputtered. Poor thickness control on the evaporation of Ti, due to poor in-situ thickness monitoring, accounts for the difference in its thickness. While a direct comparison of materials deposited under similar methods would be ideal, the choices were dictated by availability of the various materials in the necessary forms for the deposition techniques.

Figure 4.11 shows the MOKE hysteresis loops of a CoFeB/Pt multilayer {Ta(2)/ Pt(2)/ $[CoFeB(0.55)/ Pt(0.86)]_4$/ CoFeB(0.55)/ Pt(2)} (Figure 4.11, a i) deposited atop the various structural underlayer materials. Figure 4.11 (ii) gives the reversal behaviour of the magnetic multilayer on silicon, which can then be compared to the reversal obtained for the multilayer with the various underlayer materials.

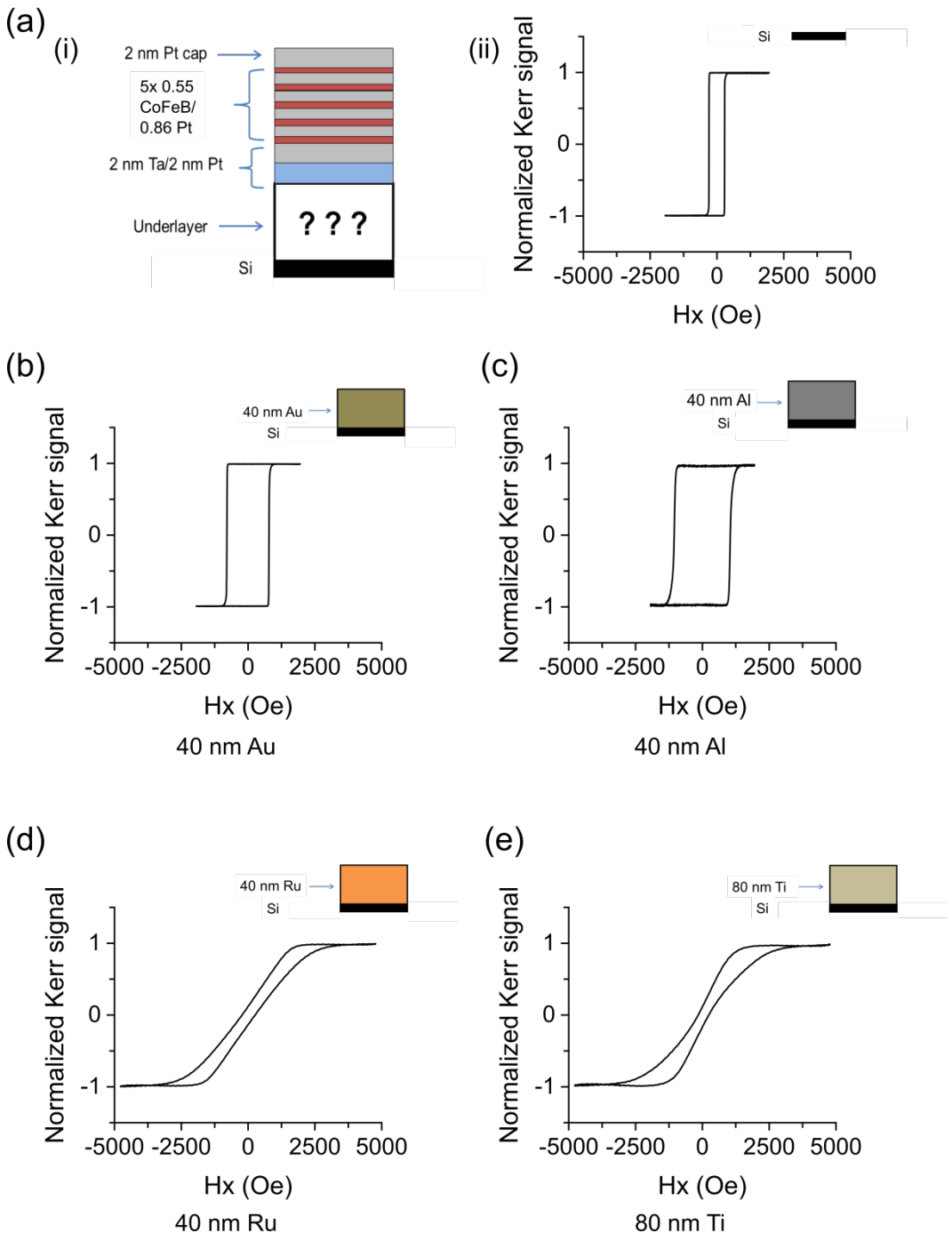

Figure 4.11 Comparison of different underlayer materials
In order to provide structural stability additional material is needed to fabricate free-standing magnetic particles. A number of different materials were tested supporting the same magnetic stack (a, i), containing {Ta(2)/ Pt(2)/ $[CoFeB(0.55)/ Pt(0.86)]_4$/ CoFeB(0.55)/ Pt(2)}. The supporting underlayers tested were (b) 40 nm Au, (c) 40 nm Al, (d) nm Ru, and (e) 80 nm Ti. The MOKE hysteresis loops can be compared with the hysteresis loop of the magnetic film alone (a, ii).

Two of the candidate materials, Ru and Ti (Figure 4.11: e, f), can be immediately discounted. Both clearly disrupt the magnetic multilayer, reducing the remanence and negatively impacting the reversal behaviour. For this reason neither material was optimized further. On the other hand, both Au

and Al (Figure 4.11: b, c) showed the most similar reversal behaviour to the multilayer on silicon, albeit with a higher coercivity. The multilayer on Si has a coercivity of 297 Oe and a reversal sharpness of 0.688, while the multilayer on Al has a coercivity of 1052 Oe and a sharpness of 0.634 and the multilayer on Au has a coercivity of 785 Oe and a sharpness of 0.732. It is clear that either Al or Au buffer are good candidates for underlayers that retain the magnetic multilayer properties. The differences between the multilayer on Si and Al/Au are a consequence of the increased pinning from the roughness of the Al/Au layer, which are inevitable for any structural layer placed under the magnetic multilayer, as most as-grown materials will have an increased roughness compared to the Si wafer on which the original sample is grown. These two top (Au and Al) candidates were further compared to find the most suitable underlayer material.

Au underlayers: benefits and effects

Figure 4.12 outlines a direct comparison between Au and Al. The samples are quite similar to those in Figure 4.11, with the same magnetic multilayer. However, the thickness of the underlayers in Figure 4.12 is smaller, at 20 nm. It was found that the difference in 20 and 40 nm underlayer thickness was negligible, so the thinner underlayer was used. In addition, two variations in Au sputter power, at 50W and 300W, are shown as well. Initially, variation in sputter power was a simple method for increasing the deposition rate of the materials to decrease the processing time for creating the film. However, it was found that the different sputtering powers lead to slightly different surface textures which impact the reversal behaviour of the CoFeB/Pt multilayer. This idea is further explored in Figure 4.14, where the difference in sputtering power can be used to control the coercivity of the magnetic film.

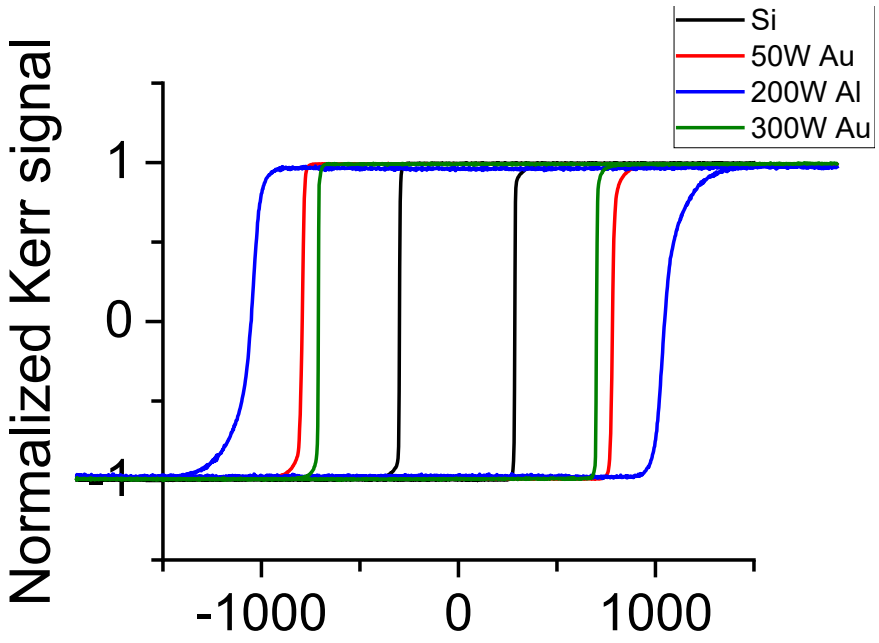

Figure 4.12 Higher power Au underlayer comparison
A higher deposition power (faster deposition rate) Au layer was used and found to retain good magnetic properties combined with the magnetic thin film. All MOKE hysteresis loops shown here are from a {Ta(2)/ Pt(2)/ $[CoFeB(0.55)/ Pt(0.86)]_4$/ CoFeB(0.55)/ Pt(2)} magnetic multilayer with a 20 nm underlayer consisting of the labelled material, which was sputtered at the power given.

The direct comparisons in Figure 4.12 between films with Al and Au underlayers make it immediately clear that Au, either in the 50 or 300W form, more closely matches the reversal behaviour of the multilayer on Si. The Al reversal processes shows a more curved and slanted transition that is characteristic of expansion of multiple domains and high wall pinning. On the other hand, the Au underlayer samples show minimal slanting in the reversal process, maintaining the sharp reversal optimized in the magnetic film. Furthermore, Figure 4.12 illustrates the differences in coercivity that can be achieved by only varying the sputtering power of the Au underlayer.

This opens up an interesting avenue for controlling coercivity, and thus, the magnetization state of the film and particles. Variations of the sputter power, similar to variations in the process pressure during sputtering, change the roughness of the deposited material's surface.[89] The increasing sputter power increases the energy of the deposited atoms, which increases their surface mobility and allows the atoms to reach equilibrium positions that will lead to a smoother film.[90] However, the increase in power also increases the flux of atoms arriving at the substrate surface, leading to faster deposition rates. The change in growth rate is not strictly linear, because at higher rates, a higher number of impacts between sputtered atoms occur in the vacuum, thus slowing the deposition rate to the substrate. Overall, the variations in growth rate and surface mobility caused by changing sputter power will lead to differences in surface roughness which can then be realized as differences in reversal behaviour of the magnetic multilayer. Figure 4.13 (a) shows how the surface roughness of the

Au underlayer varies between sputter powers of 50 to 300 W, along with two examples of AFM images for 50W (Figure 4.13, b) and 250W (Figure 4.13, c). The images were taken in non-contact mode, using an SSS-NCHR tip with a 2 nm radius (see 3.3.1 for more details). Each value was averaged over three measurements at different positions in the film. Both the overall RMS roughness and the RMS roughness with a wavelength of 10 – 20 nm are shown. The different wavelengths of the roughness were calculated by selective integration of the power spectral density function (PSDF) of the roughness data. The 10 – 20 nm region is highlighted specifically because of the theory, explained previously, that this wavelength of roughness is the most relevant for domain walls and their movement in the PMA films.[75]

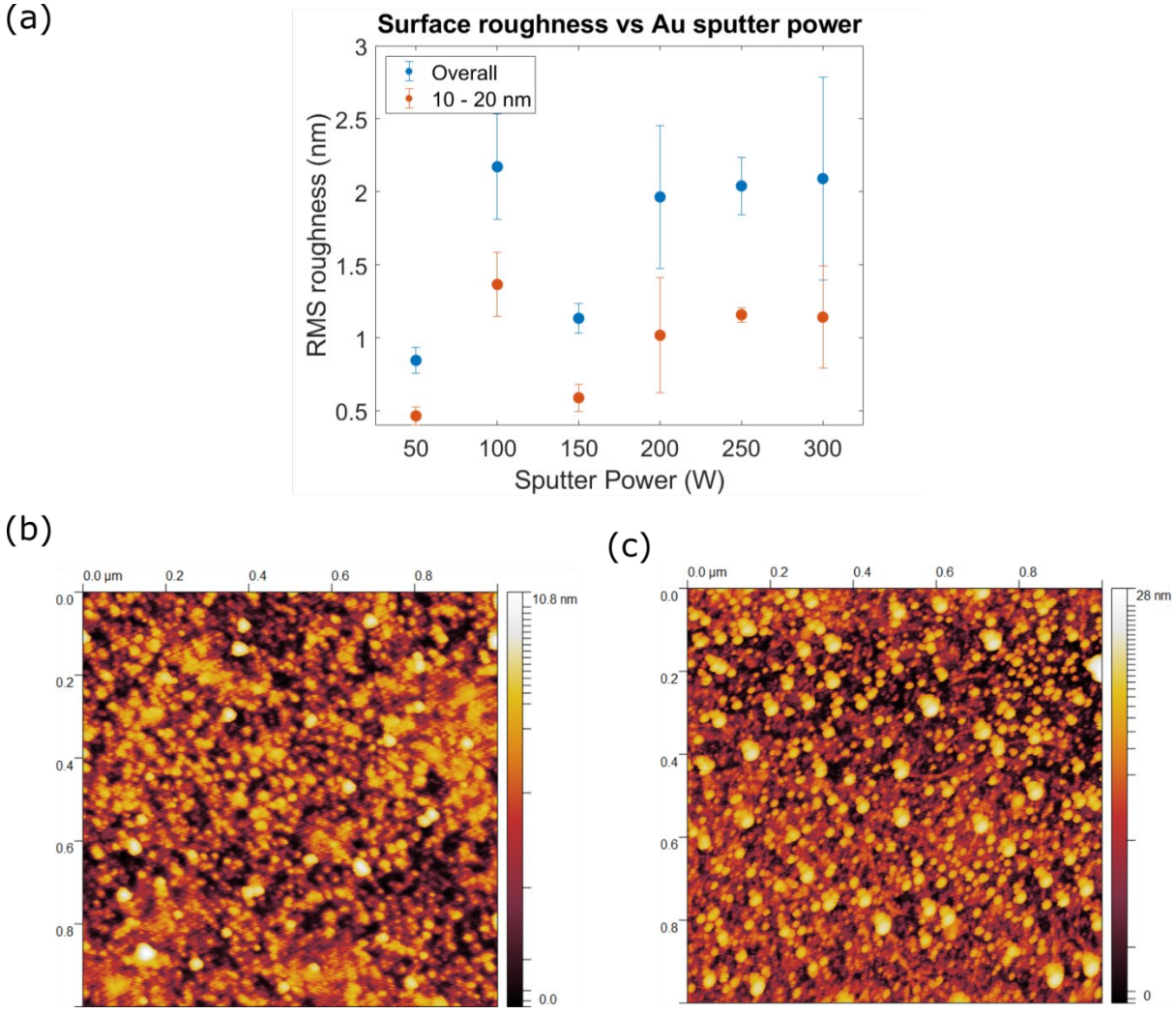

Figure 4.13 Change in Au surface roughness with sputter power
The change in roughness is shown versus the sputter power of Au (a). All Au samples were grown 20 nm thick, and roughness measured with an AFM. The overall RMS roughness and the RMS roughness between 10 – 20 nm are show, with the standard deviation of the measurements given. Examples of AFM images for (b) 50 W Au and (c) 250 W Au are shown. AFM images were taken using an SSS-NCHR tip with a radius of 2 nm.

The roughness does not show a linear relationship with sputter power, as the interplay between changes in surface atom mobility and atom flux can cause non-linear variations in the surface texture. Indeed, it has been shown before on Ti and other materials that, while roughness increases initially with power, it actually peaks and then is reduced at high sputtering powers, such as 300W.[90] Additionally, some of the Au samples show variation in surface roughness in different regions of the sample, as evidence by the large standard deviations in measured surface roughness.

More interesting is not the roughness directly, but the change in reversal behaviour which can be seen in Figure 4.14. Both single and multilayers of CoFeB/Pt were deposited on the various Au surfaces to see how the roughness impacts each. The single layer film on Si shows a coercivity of 71 Oe, while the films deposited on the Au surfaces vary above and below this value, from 87 to 58 Oe. The saturation field of the film on Si is 79 Oe, while the saturation field of the Au-buffered films ranges from 95 to 148 Oe. The increase in coercivity in some samples and the across-the-board increase in saturation field is due to increased wall pinning, which raises the field needed to move domain walls through the samples toward saturation. Defects from the increased surface roughness impede domain wall motion and drive the saturation and coercivity of the films to higher values. The higher wall pinning leads to a more slanted transition and a reversal process governed by wall motion, unlike the nucleation-limited reversal seen in un-buffered films. Importantly, as can be seen in the comparison of hysteresis loops for the samples in Figure 4.14 (a), the changes in H_c, and H_{sat} cause significant overlap between the transitions for these samples, showing that modifying the Au underlayer is not an effective method for controlling the coercivity and reversal in single layer films.

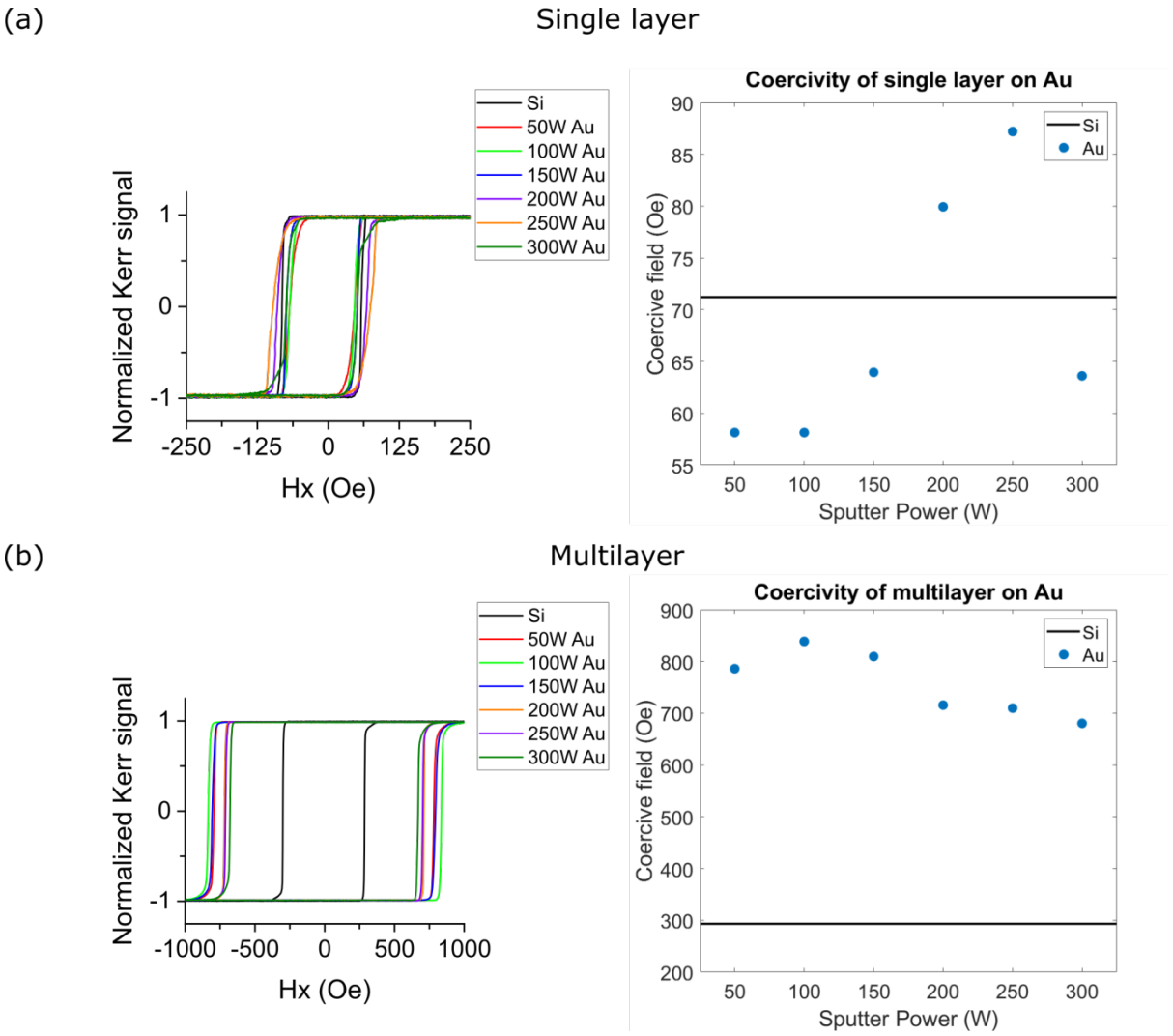

Figure 4.14 Variation of coercivity with different Au underlayers
The MOKE hysteresis loops and compilation of coercivity for a single layer {Au(20)/ Ta(2)/ Pt(2)/ CoFeB(0.7)/ Pt(2)} (a) and multilayer {Au(20)/ Ta(2)/ Pt(2)/ [CoFeB(0.55)/ Pt(0.86)]$_4$/ CoFeB(0.55)/ Pt(2)} (b). The magnetic layer of multilayers were put on Au deposited at various power levels between 50 and 300 W and compared to the switching behaviour of the same film on Si.

However, the multilayered films show a significantly different dependence than the single layer that allows for the use of Au underlayers to change and control coercivity. Unlike the single layer, which showed a range of coercivities around the original value, the multilayer shows a significant increase in coercivity for all samples. The coercivity of the multilayer film on Si is 247 Oe, while all samples deposited on Au have coercivities well in excess of 600 Oe. There is a similar increase in saturation field. While it would be expected that the multilayer experiences similar effects to those described in the single layer, the multilayers also have coupling between the layers. This means, as seen previously in the coupled and uncoupled magnetic multilayers (Figure 4.10), the reversal of the whole multilayer will be determined by the coercivity of the top magnetic layer of the film. Defects will propagate vertically through the multilayer, leading to higher defects, and wall

pinning, in the top magnetic layer of the multilayer. The reversal of the whole film still occurs sharply, because at the reversal field of the hardest, top layer, all the other layers are well above their nucleation and propagation fields and can reverse sharply. Some curving of the transition near saturation can be seen, which is likely due to propagation-limited, highly defective reversal of the top, hardest layer of the film. This can be seen in all the hysteresis loops of the multilayer samples Figure 4.14 (b) and is enhanced by the more difficult wall motion in the rough samples.

Importantly, the roughness-induced changes in the reversal of the multilayer offer an opportunity to create magnetic films with controlled, differentiated coercivity. As can be seen in Figure 4.14 (b), the coercivities of these films can be reliably varied over a range of about 200 Oe. While there is some issue with the overlap over coercivities and saturation fields of different films, by applying field values just at or above the coercivity of selected films, the films can be controllably switched while leaving a harder film in its original state. One example would be comparing an identical multilayer grown on 100W and 200W Au. By applying a field of 770 Oe, the 200W Au multilayer can be effectively saturated in the field direction to 98.6% of saturation while not nucleating the reversal in the 100W Au-buffered multilayer.

Unfortunately, while the effects of the Au underlayers on the reversal characteristics of the single and multilayer can be explained phenomenologically, it was not possible to directly correlate the roughness values with the shifts in coercivity seen. Figure 4.15 shows a plot of RMS roughness of the 10 – 20 nm range, which is predicted to be the most relevant for domain wall motion.[75] While the single layer (Figure 4.15, a) does show a linear correlation for four of the samples, there are two significant outliers that confound this relation. Furthermore, the multilayer samples (b) show no sort of correlation with the roughness. Along with this length scale of roughness, a number of other selections of the wavelength of the roughness were analysed, with similar results. It is likely the relationship between the multilayer reversal behaviour and the roughness has some more complex dependence, such as with how the Au roughness propagates through the multilayer stack. Additionally, it is difficult to match the local AFM roughness measurements with MOKE measurements directly. While the correlation attempt assumes that the series of averaged local AFM measurements can be taken as representative of the sample roughness, it is possible that local outliers, either in the AFM or MOKE measurement, have skewed the relationship.

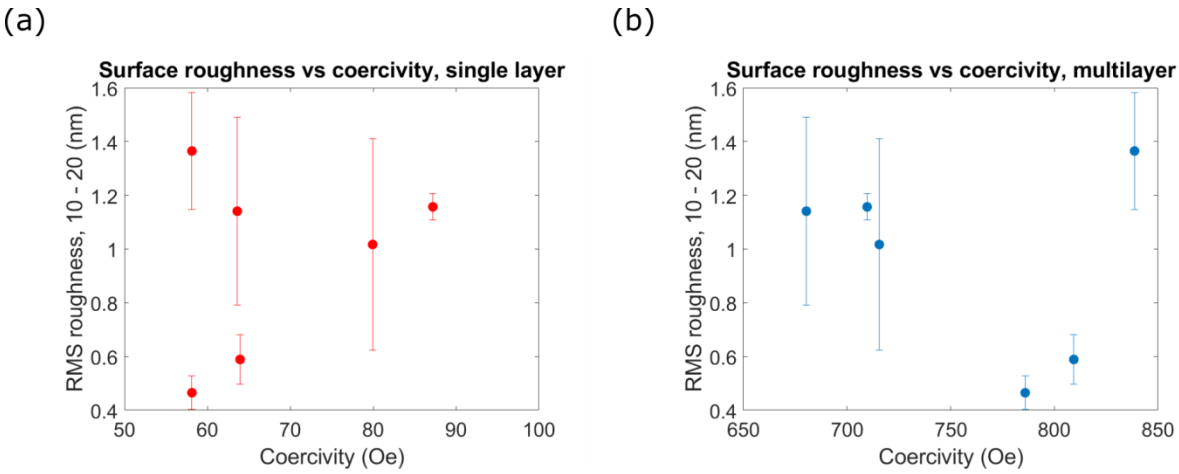

Figure 4.15 Change in coercivity with Au surface roughness
The coercivities of a single layer {Au(20)/ Ta(2)/ Pt(2)/ CoFeB(0.7)/ Pt(2)} and a multilayer {Au(20)/ Ta(2)/ Pt(2)/ $[CoFeB(0.55)/ Pt(0.7)]_4$/ CoFeB(0.55)/ Pt(2)} are plotted against the surface roughness of the Au underlayer in the films. The RMS roughness in the 10 – 20 nm length scale is used, and the roughness was modified through changing Au sputter power. Roughness values were measured by AFM, using an SSS-NCHR tip with a radius of 2 nm.

Au has proven to be a useful underlayer material, both for structural and magnetic purposes. The Au can satisfy the need for additional structural support to maintain the mechanical stability of the particles while also providing interesting effects on the magnetic reversal, especially when combined with magnetic multilayers. It will allow for some control to be achieved over the coercivity of the particles with identical magnetic compositions and overall structures, using only the sputter power of the Au. This will allow for more complex magnetic states to be imparted in particles, allowing greater control over their assembly interactions, primarily through the engineering of the remanent state.

4.3.3 Engineering the remanent state

One way the variations in reversal fields can be used is to engineer the initial remanent state of the particles before they are released into liquid. While it is the goal of this work to create a system of particles that are ferromagnetic and can assemble in the absence of external field, it is also valuable to be able to control when exactly this assembly happens. Fully remanent ferromagnetic particles will begin interacting and assembling as soon as they are released from the substrate into liquid. Although substrate positioning and patterning could be used to influence the relative arrangement of particles and potentially influence their assembly, assembly of the particles directly during the release process is not desirable, as it will be difficult to observe, understand, and control.

To overcome this problem of immediate assembly, the particle can be set to a net zero remanence state which could then be irreversibly switched to a fully remanent ferromagnetic state

when desired. This will allow particles to be released and manipulated before assembling on command, and will help prevent unwanted agglomeration of particles. Figure 4.16 outlines how the multilayered magnetic film can be combined with an Au structural layer that also modifies the switching behaviour of the top magnetic layer. This type of film and particle, referred to in this work as a 'sandwich' particle, will be the basis of much of the particle and assembly behaviour analysed in the subsequent chapters. By putting two separate magnetic multilayers on each side of the film with the layer structure {Ta(2)/ Pt(2)/ $[CoFeB(0.55)/ Pt(0.86)]_4$/ CoFeB(0.55)/ Pt(2)/ Au(20)/ Ta(2)/ Pt(2)/ $[CoFeB(0.55)/ Pt(0.86)]_4$/ CoFeB(0.55)/ Pt(2)}, the particle can have strong magnetic interactions on both faces while avoiding the large number of multilayer repeats that would be needed to create a particle composed entirely of magnetic material. It is not possible to create a particle purely from magnetic layers, as series of magnetic layers thick enough to remain structurally stable will not retain the desired magnetic properties in the film. Thus, the sandwich particle offers a useful alternative with an additional benefit in enabling the engineering of the remanence.

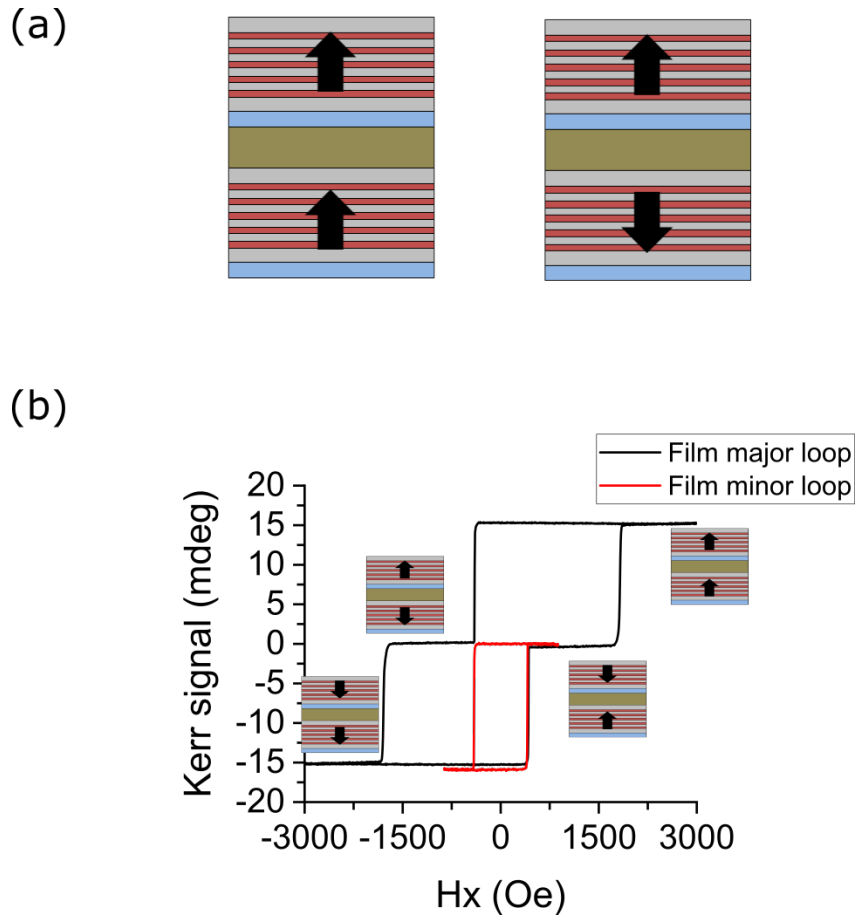

Figure 4.16 Engineering ferromagnetic particles with a zero remanent state
'Sandwich' particles, 5 μm in size, were created from the film in (a). By using an intermediate, non-magnetic layer, both sides of the particle could be switched independently, to create a zero remanent state particle. In (b) the hysteresis loop for the structure {Ta(2)/ Pt(2)/ $[CoFeB(0.55)/ Pt(0.86)]_4$/ CoFeB(0.55)/ Pt(2)/ Au(20)/ Ta(2)/ Pt(2)/ $[CoFeB(0.55)/ Pt(0.86)]_4$/ CoFeB(0.55)/ Pt(2)}is given for the film, showing how just one magnetic layer can be accessed (red) and the various states that can be created.

Figure 4.16 shows the MOKE hysteresis loop of the film made from this layer structure. Due to the differences in coercivity of the two multilayer segments in the sandwich particle, they can be addressed individually using different field pulses. Figure 4.16 (a) shows how, if one layer is independently switched, the particles go from fully remanent to a net zero state, which could then be reversed when needed for assembly. Figure 4.16 (b) shows the reversal in the film, with a distinct coercivity difference for the two magnetic layers. The lower layer of the film is grown directly on the silicon substrate or Ge release layer (see 4.4), which has a low roughness and allows it to approximate the reversal behaviour of the normal multilayer film. The bottom layer will also display a smaller Kerr signal due to the attenuation of the laser beam in the depth of the sample. The upper magnetic layer is grown on an Au structural buffer, the roughness of which drives the coercivity much higher, as explained previously. In the film, the softer layer grown on a Ge release layer has a coercivity of 430 Oe, compared to 1810 Oe for the harder layer grown on the Au structural layer. Figure 4.16 (b) shows

how this difference in coercivity can then be translated into the difference in magnetic states seen in (a). The full hysteresis loop of the film is shown, including a minor loop for just the bottom, lower coercivity layer. The two layers have nominally the same magnetization, barring small variations from the differences in roughness affecting their growth conditions, and should show equal Kerr rotation. By using the coercivity and Kerr signal to identify the two layers, they can be addressed independently to alter the remanent state of the film, and this same behaviour can be translated into particles.

To address the different layers, a field of over 2000 Oe is applied to the whole structure, saturating both layers parallel. Then, a field of 1000 Oe can be applied in the opposite direction, switching only the bottom, lower coercivity layer. Both are applied at a sweep rate of 2000 Oe/s. The exact field sequence applied can be further optimized by using pulsed fields and observing the Kerr rotation, to find when the bottom layer saturates without beginning the reversal process of the harder, top layer.

This sandwich particle system helps overcome the immediate assembly problem by using two, uncoupled magnetic layers with differences in coercivity. By taking advantage of the property changes from the structural Au layer, a strongly magnetic particles can be created with control of the remanent state, allowing it to be turned 'on' from a zero remanent state to a fully remanent one, so the activation of assembly can be controlled.

4.4 Particle patterning and creation

Now that the ideal magnetic film composition and configuration has been determined, the film then needs to be transformed into particles. The processing of the film to particles must ensure that the magnetic properties of the film is retained, in order to preserve the design choices outlined in 4.2 and optimized in 4.3. Additionally, care must be taken to create a pure suspension of particles in liquid. Any non-particle magnetic material that remains in the liquid after particle formation will be nearly impossible to separate from the real particles, either magnetically or by filtration, and will participate in any assembly, potentially disrupting the intended particle interactions. Complicating the process is the fact that the films must be grown on a soluble release layer, so the particles can be released from the substrate into liquid.

Previous work in Cowburn group has fabricated particles by sputtering material atop an array of 2 μm photoresist pillars, which were created through standard mask lithographic techniques.[40,44,91,92] This type of photoresist pillar release method is a known method, having been demonstrated in literature as a way of forming micron-sized planar particles like the ones in desired in this work.[93,94] Alternative release layers such as germanium have been demonstrated with similar types of magnetic particles, such as permalloy vortex discs, where colloidal hole lithography was used to create a mask

for deposition of the disc material.[95] Outside of particles release, other film release concepts can be found in the creation of strain-mediated micro- and nano-tubes, which are formed by selective etching of a release layer.[96,97] A variety of other release layers, such as poly-methyl methylacrylate (PMMA), aluminium, are commonly used in these nano-tube applications, and could be potential candidates for release layers as well.[98,99]

Fundamentally, there are two ways that magnetic films (or any film) can be turned into particles: additive or subtractive. Both were experimented with in this work, and a schematic diagram of the two processes can be seen in Figure 4.17. In the additive method, a release layer is deposited on a substrate and subsequently patterned by lithographic methods. This leaves behind a pillar structure that will both define the particle dimensions and also act as the release layer after deposition. A magnetic film can be deposited atop this pillar, and then the pillar can be dissolved in a solvent of choice to effect release. Alternatively, in the subtractive method, a film of the release layer is deposited, followed by deposition of the magnetic film. Then, a lithographic pattern defining the particle shape is formed on top of the layers. This pattern will act as a mask for ion milling, where the film outside the mask is removed, leaving only the defined particles. As can be seen, in theory, both methods can be used to create the same particles, but each come with their own benefits and difficulties. Namely, the additive method is fast but prone to additional non-particle film being released as a consequence of conformal coating of the sputtered film. On the other hand, the subtractive method avoids conformal coating of non-particle film, creating cleaner particle suspensions, but many more steps are needed, thus adding complexity to the process.

One key aspect of the particle patterning and creation in this work is the use of direct laser-write lithography. As covered in Chapter 3, the direct write system allows great flexibility for prototyping and creating different particle shapes and sizes, which would not be easily available using a flood illumination system. This flexibility potentially presents a unique opportunity to design different particle shapes to drive more specific assembly interactions, at the expense of restrictions on the types of photoresists which can be used for patterning in parts of the release methods.

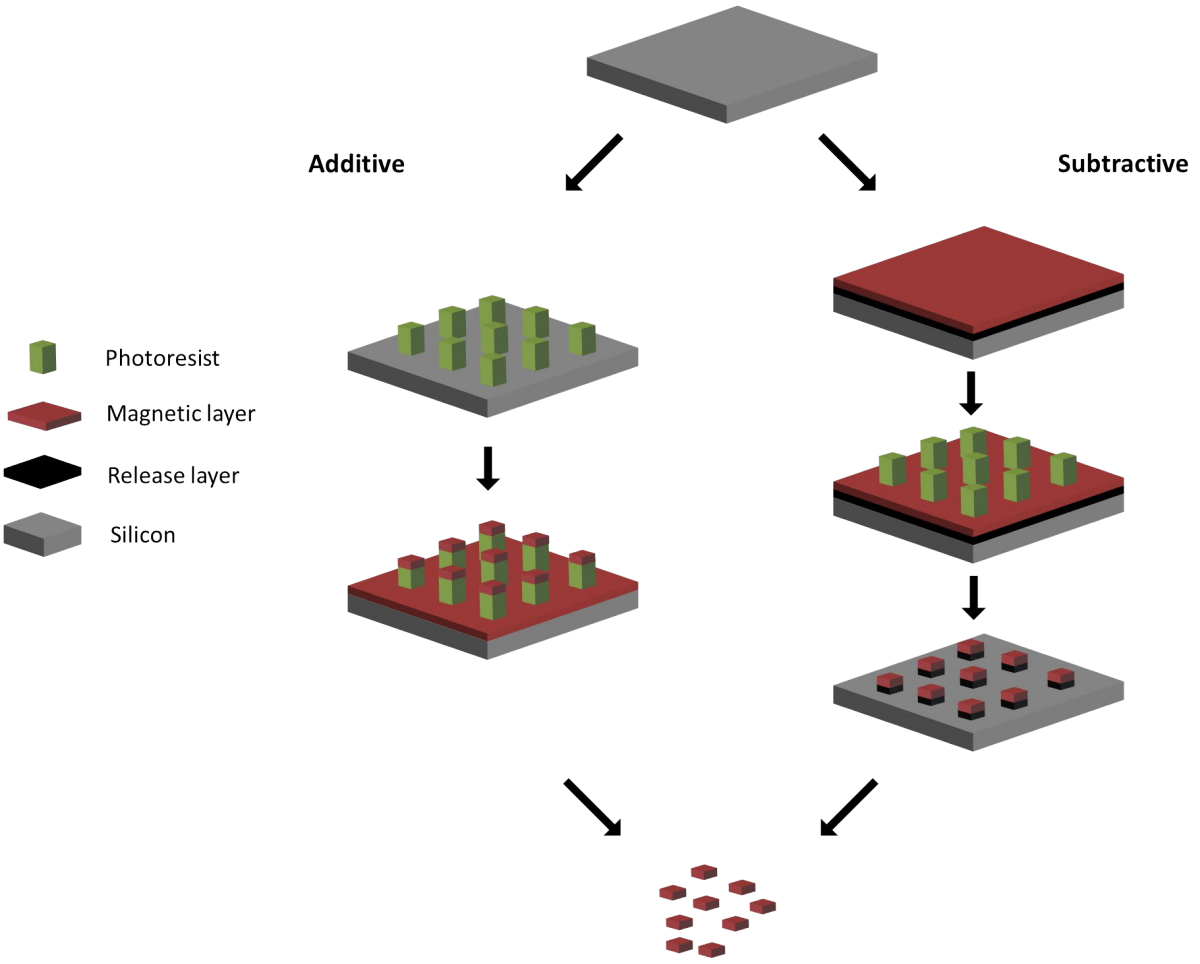

Figure 4.17 Schematic diagram of the two methods for forming particles
Particles can be generally created either through an additive or subtractive process. In an additive process, a pattern is formed and the magnetic film is deposited on top of it. This pattern also acts as the release layer and is dissolved, releasing only film in the desired particle shape. A subtractive process creates a full thin film on top of a release layer (Al, Ge, polymer, etc). A mask is then put on the films to define the particle shape, and all excess film is removed. The particles are then released from the substrate.

Both methods outlined in Figure 4.17 are fully explored here. A photoresist-based additive method and a germanium-based subtractive method are compared, showing the different particles produced from each. In the end, flaws in the additive photoresist method precluded it from use and left the germanium method as the preferred particle creation process.

4.4.1 Photoresist-based release layer

When choosing a photoresist-based release layer, the first step is to consider the various types of photoresist available, and their relative merits. Broadly, photoresists are split into positive and negative resist. Positive resists become more soluble in the resist developer after exposure to light, as the exposure generates free radicals in the photoresist.[100] Alternatively, negative photoresist are cross-linked under exposure, which hardens those areas against dissolution when the material is

developed.[101] For the purposes of particle release, two important aspects related to the resist character must be considered: the surface roughness of the photoresist after exposure and development and the sidewall angle of the photoresist pillar created.

First, in order to retain the magnetic properties and flat planar shape desired in the transition from film to particle, the surface of the photoresist on which the particle is being deposited must be as smooth as possible. Although there is inherent roughness in the polymeric surfaces, the roughness can be compensated with buffer layers up to a certain degree. However, any large amplitude roughness will be detrimental to the particle properties. Roughness of high enough amplitude would also disrupt the consistent planar shape of the particles that is desired. For this reason, positive photoresist was chosen in the photo-resist release layer process. As the positive resist that makes up the release layer/pillars is not actually exposed in the patterning process, it can retain a relatively smooth surface, with a root-mean-square roughness (R_{rms}) of 1.9 nm. In contrast, negative photoresist is directly exposed when forming this pattern. For negative resist exposed in the direct write system, the R_{rms} has been measured at 14.1 nm, with some peak-to-peak heights reaching almost 30 nm, similar to the total film thickness. Comparisons of the roughness of the two surfaces can be seen in Figure 4.18, which are the basis for the R_{rms} calculations. This level of roughness and disruption is unacceptable for magnetic film deposition and creation of well-shaped particles, and thus negative resist was discounted for this application. The reason negative resist is unsuitable and contains such high roughness is due to the direct laser-write method. While the negative resist protocol was used effectively under flood exposure lithography, the light intensity needed for the very short pixel-by-pixel exposures of the direct-write system induce large heating effects into the resist.[102] This excessive heating can impact the surface roughness and morphology, thus making negative resist a poor candidate for this application.

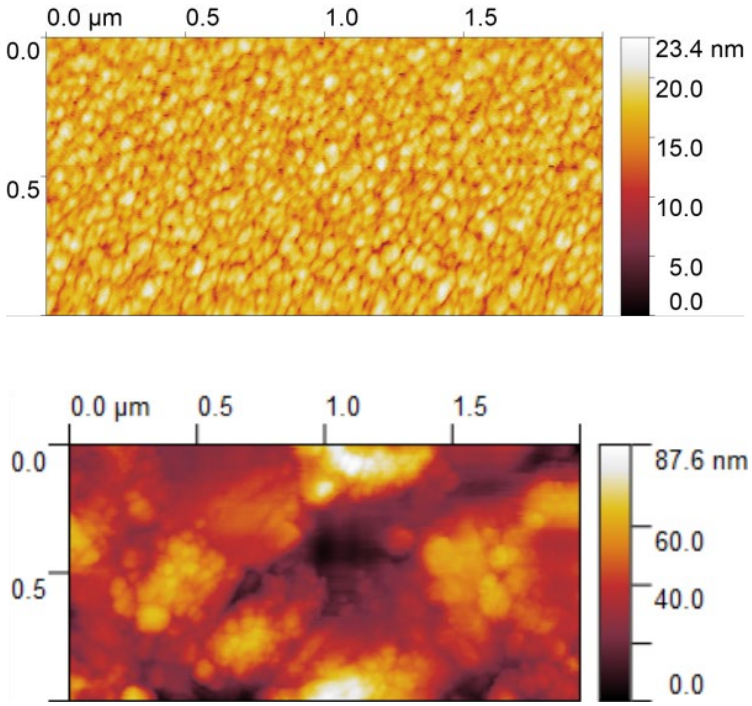

Figure 4.18 Roughness of photoresist surfaces
AFM scans of Shipley S1813 positive photoresist (top) and ma-N1410 negative photoresist (bottom) to find the surface roughness values. Both resists were exposed, developed, and then scanned.

Second, the photoresist needs a negative sidewall angle, or undercut, to prevent the conformal coating of material onto the sides of the pillars, which would prevent particle formation. As sputter coating is conformal, material will be deposited on all surfaces that are in the line-of-site of the sputtering source. Negative photoresist naturally forms with an undercut sidewall, as the lithographic process exposes a greater area on the top of the resist structure than the bottom. By considering the exposure beam as a Gaussian, the tails of the beam will be able to expose the photoresist at the top surface, but as the beam attenuates deeper into the resist, those areas will no longer get exposed. The opposite is true on positive photoresist, as this differential exposure occurs in the part of the pattern being removed. Hence, positive resist will lack an undercut, and take a form as seen in Figure 4.19 (a).

Due to the excessive roughness of negative resist in these process conditions, it cannot be used, even though it possesses necessary sidewall characteristics. Luckily, a number of techniques exist to modify positive resist in order to get the desired undercut for particle formation.

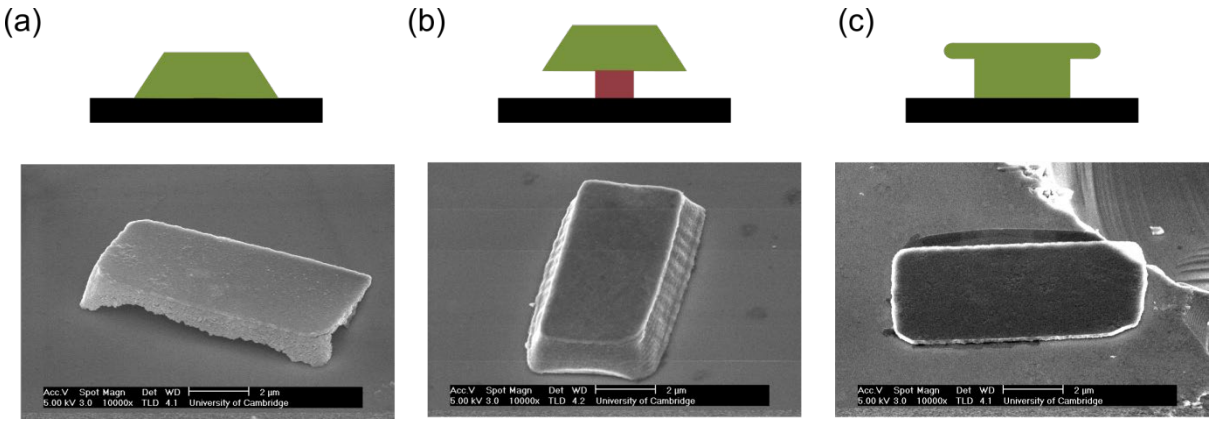

Figure 4.19 Comparison of photoresist-based particle creation methods
Three different photoresist methods were used to see which produced the best planar magnetic particles. (a) shows S1813 positive photoresist, (b) shows S1813 on top of a layer of LOR (lift-off resist) to prevent surface contact between particle and chip, and (c) shows S1813 used with a chlorobenzene soak to give an enhanced undercut.

Three different methods for using positive photoresist (Shipley S1813) to create a platform for particle formation and release are outlined in Figure 4.19. In each case the expected morphology of the resist is shown, along with SEM micrographs of particles created using those methods. In (a), the positive resist is used without modification. As can be seen from the micrograph, this meant that film material was able to coat the side of the photoresist, creating a misshapen particle that does not have the flat aspect desired. Additionally, many particles from this method were unable to be removed from the substrate, as the conformal film coating prevented the dissolution of the photoresist for release. Part (b) shows an alternative method, where a layer of LOR-B is used to create a gap between the positive photoresist and the substrate. This creates an artificial undercut, as the top resist layer will shield deposition onto the side of the LOR layer, preventing a fully conformal film coating. However, as the micrograph shows, the particle will still take on the shape of the positive resist layer, leading to similar problems as in (a). (c) shows the final, and most effective, way the photoresist can be modified. Chlorobenzene is used to soak the photoresist layer following exposure but prior to development. The chlorobenzene hardens the top portion of the photoresist layer, thus making it dissolve slower when developed, creating an ideal undercut in the positive resist structure, and leading to well-shaped planar particles. The chlorobenzene method has been shown previously to make well-shape planar particles, and from this proven efficacy and the results shown above, it was the chosen method used to create the photoresist patterns for this release method.[93]

Flaws and constraints

While the chlorobenzene method allowed positive resist to be used to create and release particles, it still suffered from some flaws which eventually necessitated further improvement. The method did produce mostly planar particles, but, as Figure 4.20 shows, errors in the particle

morphology and creation of additional magnetic pieces prevented this from being a robust and re-usable method.

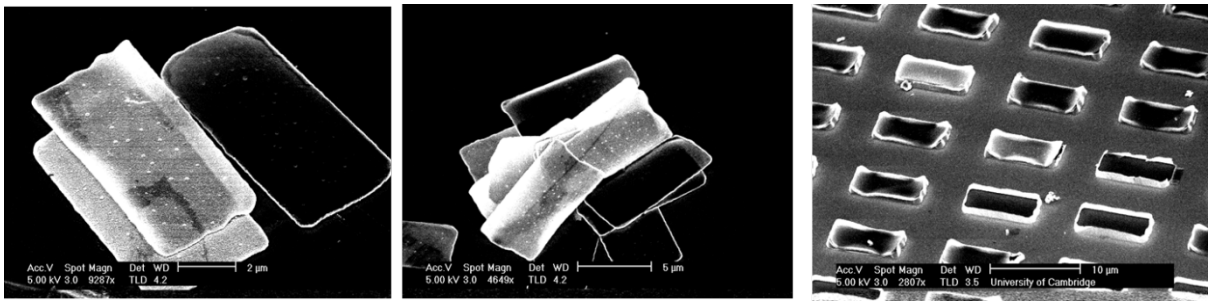

Figure 4.20 S1813 + chlorobenzene liftoff particles and chip
Particles (left, centre) created from the developed S1813 + chlorobenzene liftoff process, showing bending and distortion. Remnants on chip following liftoff (right), demonstrating incomplete particle liftoff and origins of particle distortions

As Figure 4.20 highlights, even with the chlorobenzene undercut, there was still some evidence of conformal film coating that impacted the particle release. Film would still coat the sidewalls and, in some cases, the underside of the photoresist, which meant that particles either did not release at all or were only released by using ultrasonication to disrupts the film. Figure 4.20 (right) shows that the sidewalls of the resist pillar get coated in the release process and in some cases prevent particles from releasing. Because of these connections between the particles and the substrate, the particles that get released successfully have a high number of deformities such as bending or curling. This is due to the release process happening sequentially, instead of all at once, when the photoresist is dissolved. As some parts of the particle remain stuck to the film on the substrate, the forces involved in the dissolving of the resist and sonication impact the particle's mechanical structure. Since planar particles are desired for assembly, this uncontrolled mechanical deformation is detrimental to the particle structures.

Additionally, material is also deposited on the sides of the top platform on which the particles form. These side-particles, which are themselves magnetic, are then released along with the particles and might interfere with assembly experiments. Figure 4.21 shows exactly how these side-particles, or 'skirts', from the resist pillar structure agglomerate along with the magnetic particles, disrupting chain formation and complicating both the ability to form any structures and also analyse and understand what is being formed. Because the 'skirts' are similar to the actual particles in both size and magnetic properties, they cannot be separated once in solution.

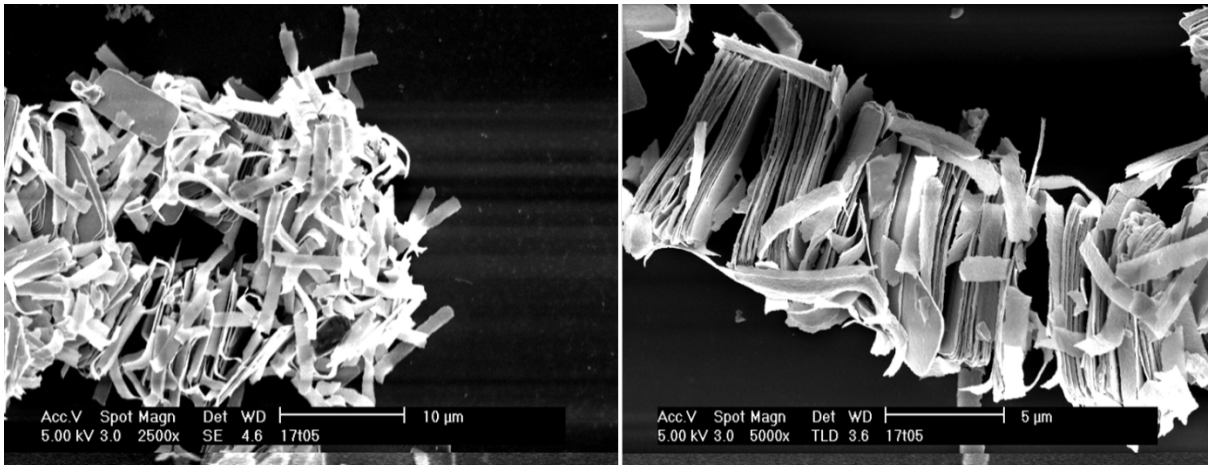

Figure 4.21 Assemblies of rectangular particles with additional magnetic 'skirts'
Magnetic skirts created during the deposition on photoresist patterns liftoff with the particles and impact particle assemblies and experiments.

While the photoresist-based release method offered an easy system, building upon previous work, in which magnetic particles could be made, it proved incompatible with the direct-write patterning and particle requirements in this work.

4.4.2 Inorganic release layer

In order to more effectively make particles, inorganic release layers were explored. As outlined in the schematic diagram in Figure 4.17, the inorganic release layer is deposited underneath the full magnetic film. Photolithography is used to define the particle shape, either as a mask for deposition or for an ion milling process. While this method incorporates more steps, it was found to yield more consistent results by avoiding the geometric issues inherent to depositing on photoresist, where magnetic film would end up in unwanted areas of the release layer.

To find the best process using an inorganic release layer, two materials were tested: aluminium and germanium. Aluminium can be dissolved in hydroxide solutions, while germanium is easily soluble in hydrogen peroxide. While both release layers were found to work, germanium provided a greater ease of use and was eventually adopted as the release layer for the optimized particle creation method.

Aluminium

In testing the aluminium release layer, two methods for defining particle shape were used, both described in Figure 4.22. The first (Figure 4.22 a) uses photoresist as a deposition mask on top of the aluminium release layer already grown on the Si substrate. This provided an alternative to ion milling, as the magnetic film would be deposited through the photoresist mask, which could then be

dissolved, leaving only the desired particle shapes behind. However, as can be seen from the micrograph, this method suffered from some of the same problems as previous resist-based attempts. Namely, the conformation of the film on the photoresist mask could not be completely avoided, which led to damage of the particles as the photoresist mask was removed. The second method (Figure 4.22, b) uses photoresist as a mask for ion milling. This provides very well-defined particles, as seen on the corresponding micrograph.

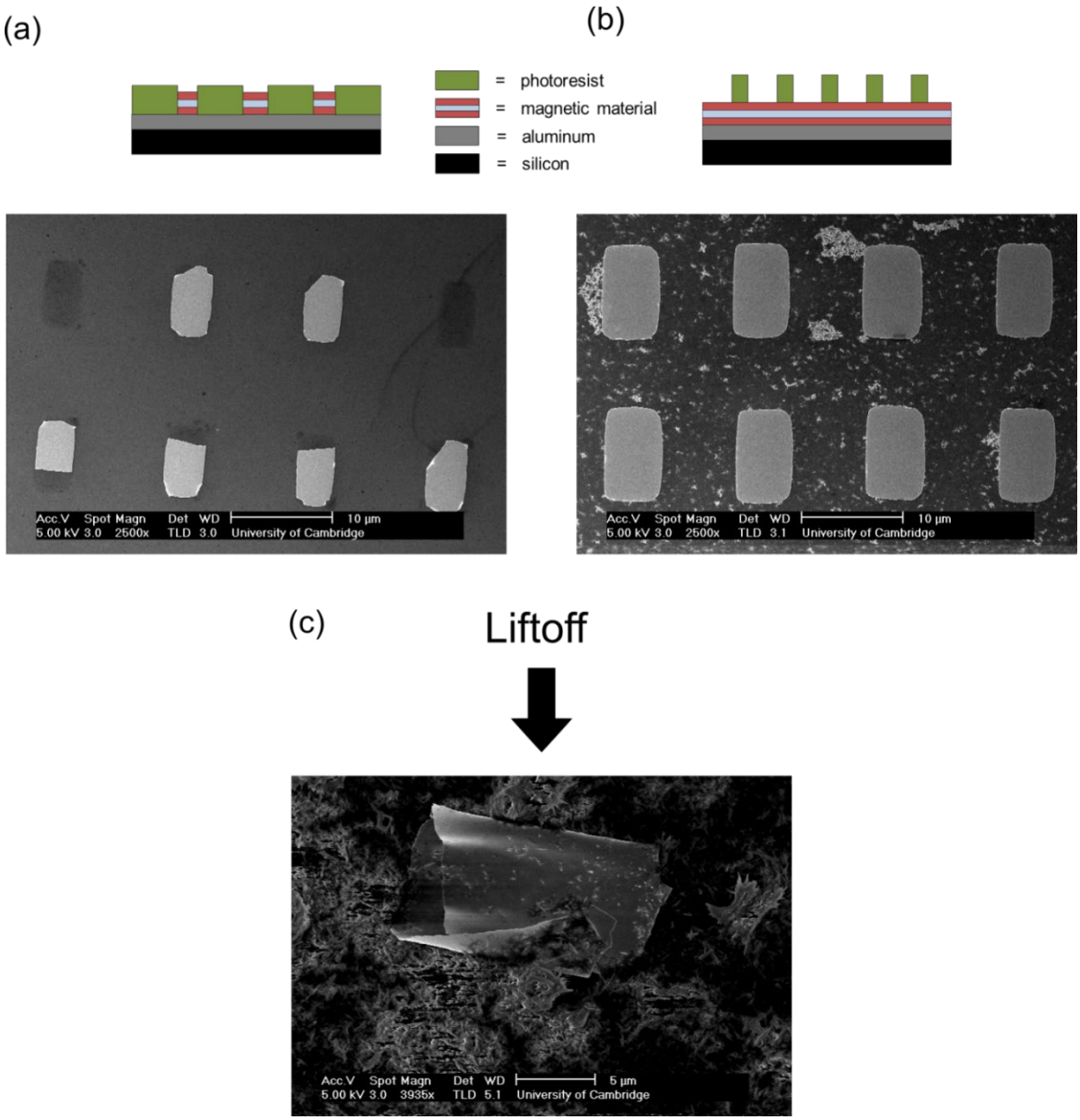

Figure 4.22 Aluminium release layer liftoff
Aluminium was tested as a potential release layer using a deposition process (a) through a photoresist pattern and a milling process (b) with a photoresist mask. The pattern deposition showed poor particle formation following resist removal. While the milling process created good particles, they lacked structural stability (c) once lifted off into liquid.

However, the Al release layer did show a number of flaws. The solvation product of Al and hydroxide is not soluble in water, leaving a cloudy suspension that makes it more difficult to image and observe particles. While this alone is not overly problematic, and can be fixed by washing or replacing the solution, the Al release also led to mechanically unstable particle (Figure 4.22, c). The particles would roll up when created with the Al release layer, even if they were built from compositions that were stable under other release methods. This is likely attributable to strain imparted on the sputtered layers of the particles from the lattice of the crystalline Al. Once the particle is released, the strain relaxed, leading to the particle seen in (c).

Germanium

Because of the flaws found in the Al release process, germanium was also investigated as a release layer candidate. Due to information gained from the aforementioned processes, the Ge process was only conducted using photoresist masking and ion milling, with the process described in Figure 4.23 below.

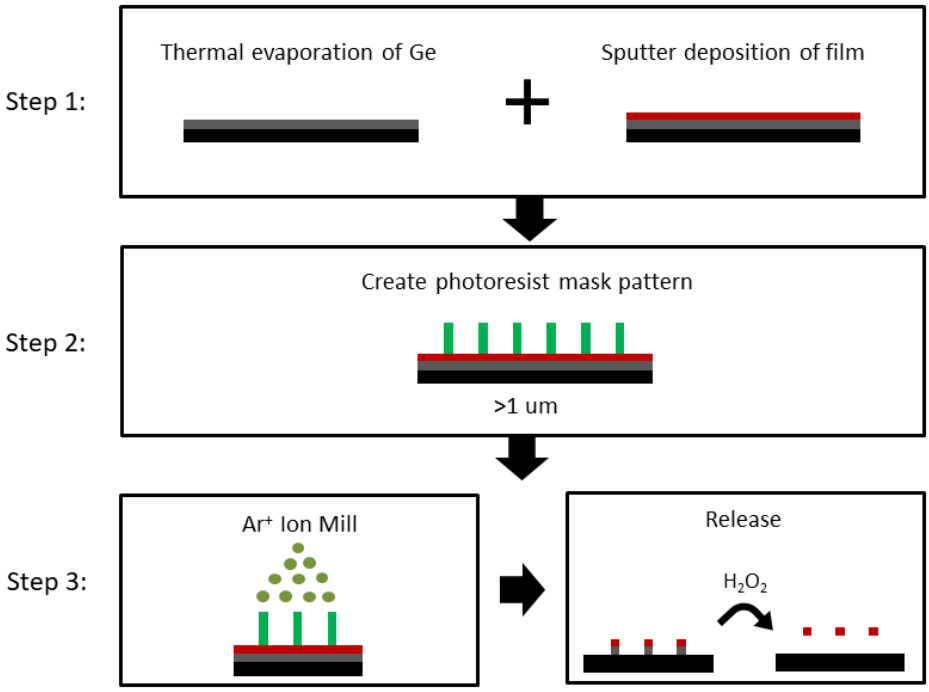

Figure 4.23 Process developed to create magnetic particles using germanium release layer
Germanium (thickness of 50 nm) is deposited under the desired particle film. A pattern mask is then created using photoresist, which can then be Ar^+ ion milled to remove the excess film. The newly patterned particles are then released from the substrate by dissolving the germanium in hydrogen peroxide.

The Ge process led to similarly well-defined particles to those seen in Figure 4.22 (b). The Ge process uses hydrogen peroxide as the solvent for the release layer. The peroxide quickly oxidized the Ge to GeO_2, which is soluble in water. A 50 nm Ge release layer is used, as it was found to work well with the ion milling process and dissolve readily. The silicon chip containing the particles is also sonicated during the Ge dissolution step, to assist the release process and prevent particle redeposition on the chip. In this way, this method offers a much 'cleaner' process, where the reaction product from the release is solvated and does not interfere with further observation. Additionally, as can be seen in Figure 4.24 below, the particles from this method do not show any of the mechanical instability imparted by the Al process.

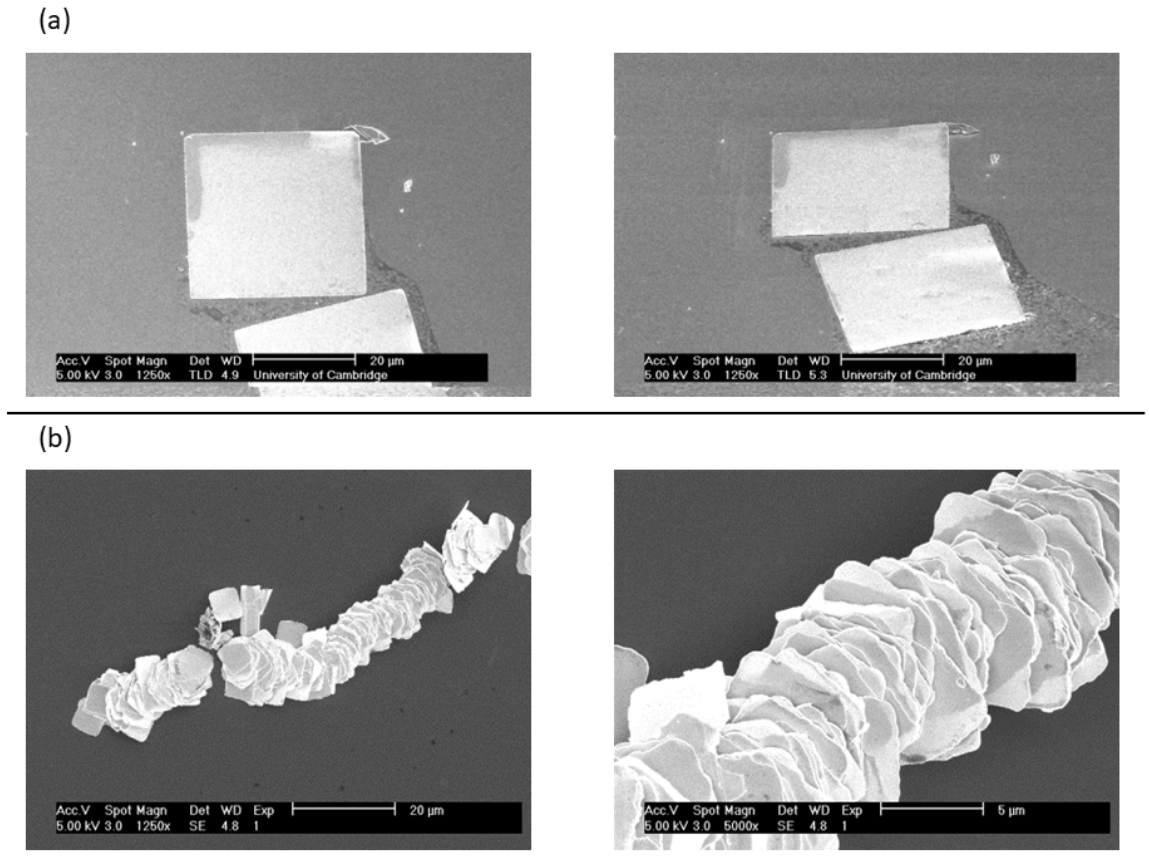

Figure 4.24 Example of particles made using germanium process
(a) 20 µm magnetic particles and (b) 5 µm magnetic particle chains, both created using the germanium process outlined in Figure 4.23.

After a series of iterations in order to optimize the planar shape of particles and consistency of particle formation, a new method for patterning and creating magnetic particles was established. This method, which uses a Ge release layer and ion milling through a photoresist mask, overcomes many of the flaws in previous resist-based or inorganic release processes, ensuring that magnetic particles can be made in an efficient and repeatable manner.

4.4.3 Particle properties

The magnetic behaviour of the particles created from films is shown below (Figure 4.25). The MOKE hysteresis loops of film with a single 5x magnetic multilayer on a structural Au buffer and the 'sandwich' style film are both compared with MOKE loops of single particles. As was expected, the coercivity is higher in the particles, but both types of particle retain the magnetic properties optimized in the film. Additionally, the magnetic layers in the 'sandwich' type particle are also able to be addressed independently (Figure 4.25, e). This show the remanent state can also be controlled in particles as well as the film.

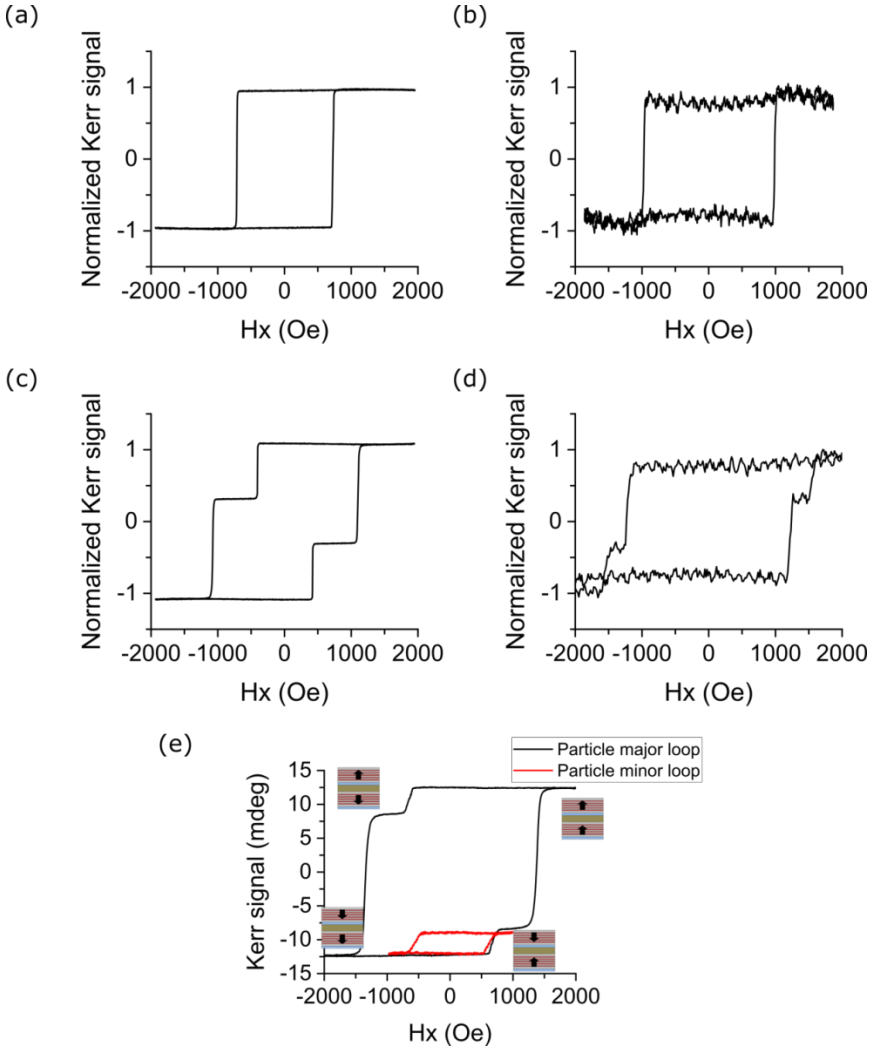

Figure 4.25 Optimized magnetic films and particles
Final (a) film and (b) single particle MOKE hysteresis loops of single magnetic multilayer particles {Au(20)/Ta(2)/ Pt(2)/ [CoFeB(0.55)/ Pt(0.86)]$_4$/ CoFeB(0.55)/ Pt(2)} and 'sandwich' (c) film and (d) single particle {Ta(2)/ Pt(2)/ [CoFeB(0.55)/ Pt(0.86)]$_4$/ CoFeB(0.55)/ Pt(2)/ Au(20)/ Ta(2)/ Pt(2)/ [CoFeB(0.55)/ Pt(0.86)]$_4$/ CoFeB(0.55)/ Pt(2)}. (e) is an array of ~10 'sandwich' type particles, recreating the independent switching of magnetic layers shown in Figure 4.16 in particles.

Table 1 shows the M_s, M_st, and K_{eff} for films with different buffer layers (none, Au, Ge + Au) and set of similarly composed particles. Through the various processing steps and different buffer layers, the films retain roughly the same M_s and K_{eff}. However, these properties are not perfectly maintained on the transition between film and particles. In this case, the anisotropy constant drops by almost a half. This is likely due to the heating of the ion milling process, which leads to diffusion within the magnetic multilayer and damages the ideally sharp layer interfaces that promote PMA. However, even with this change, the particles still maintain a well-defined out-of-plane anisotropy, as required.

Table 1: Properties of magnetic films on various substrates

Substrate	Buffer layer	M_s (emu/cm^3)	M_st (emu/cm^2)	K_{eff} (J/m^3)
Si	n/a	1218.1	3.35×10^{-4}	1.19×10^{6}
Si + 50 nm Ge	n/a	1359.7	3.40×10^{-4}	1.38×10^{6}
Si	20 nm Au	1209.8	3.02×10^{-4}	1.09×10^{6}
Si + 50 nm Ge	20 nm Au	1240.9	3.41×10^{-4}	1.12×10^{6}
Si	'sandwich', 20 nm Au	1274.0	7.01×10^{-4}	1.36×10^{6}
Si + 50 nm Ge (particles)	'sandwich', 20 nm Au	1121.8	6.17×10^{-4}	6.25×10^{5}

4.5 Conclusion

In this chapter, we have identified, optimized, and create the particles that will be subsequently used for self-assembly experiments.

We started by laying out the parameters needed for a strong ferromagnetic particle that can drive its own assembly in liquid. We looked at the various magnetic considerations that need to be accounted for in the particle, such as strong perpendicular anisotropy, high moment per area, full remanence, and sharp reversal. Then, we developed a magnetic film based on CoFeB/Pt multilayers that could satisfy these requirements. The film was optimized for CoFeB thickness, number of repeats, and Pt thickness, eventually leading to a layer structure of the type {Ta(2)/ Pt(2)/ $[CoFeB(0.55)/ Pt(0.86)]_4$/ CoFeB(0.55)/ Pt(2)}.

Next, we addressed the need for a structural support layer, testing a number of different underlayer materials that could be used to provide a mechanical backbone for the magnetic portion of the film, thereby enabling it to exist stably as a particle in liquid. A number of different materials were tested, eventually leading to Au being chosen as the ideal structural material, because the magnetic film could retain its properties best with the Au underlayer. Further investigation was made into the

Au underlayer, finding that the roughness variation of Au deposited at various sputter powers could be used to control the coercivity of the magnetic layer. This roughness effect was investigated for both single and multilayers on Au. This controllable coercivity was then used to engineer the remanent state of the magnetic film, allowing a 'sandwich' type particle with two magnetic multilayers separated by an Au buffer to be formed. This 'sandwich' particle can be set to a zero or fully remanent state, due to the coercivity differences in the layers imparted by the Au, allowing greater control of the magnetization state of the particles to control assembly interactions. The addition of the Au layer and development of the 'sandwich' structure led to a final particle layer structure of {Ta(2)/ Pt(2)/ $[CoFeB(0.55)/ Pt(0.86)]_4$/ CoFeB(0.55)/ Pt(2)/ Au(20)/ Ta(2)/ Pt(2)/ $[CoFeB(0.55)/ Pt(0.86)]_4$/ CoFeB(0.55)/ Pt(2)}.

After fully optimizing the film, both for magnetic and structural purposes, the patterning of the film to particles was developed. Beginning with a photoresist-based particle release method already in use, it was found the photoresist method was not usable for these particles due to high amounts of debris in the solution after release. Thus, inorganic release layers were investigated, focusing on Al and Ge as the release material. It was found that Ge had the best properties for a release layer, and this process was developed and implemented for making particles from films. We confirmed that the properties of the particles match closely those of the original films, showing we can retain the magnetic behaviour optimized in the film construction. Next, the behaviour of the particles in liquid will be addressed in Chapter 5.

4.6 References

1. Lin, C.-J. *et al.* Magnetic and structural properties of Co/Pt multilayers. *J. Magn. Magn. Mater.* **93**, 194–206 (1991).
2. Greaves, S. J., Grundy, P. J. & Pollard, R. J. Magnetic properties of cobalt layers and Co/Pt multilayers. *J. Magn. Magn. Mater.* **121**, 532–535 (1993).
3. Iwasaki, S. I. Perpendicular magnetic recording - evolution and future. *IEEE Trans. Magn.* **20**, 657–662 (1984).
4. Carcia, P. F., Meinhaldt, A. D. & Suna, A. Perpendicular magnetic anisotropy in Pd/Co thin film layered structures. *Appl. Phys. Lett.* **47**, 178–180 (1985).
5. Draaisma, H. J. G., Den Broeder, F. J. A. & De Jonge, W. J. M. Perpendicular anisotropy in Pd/Co multilayers. *J. Appl. Phys.* **63**, 3479–3481 (1988).
6. Carcia, P. F. Perpendicular magnetic anisotropy in Pd/Co and Pt/Co thin-film layered structures. *J. Appl. Phys.* **63**, 5066–5073 (1988).
7. Thomas, G. E. *Future trends in optical recording*. *Philips Tech. Rev* **44**, (1988).
8. Zeper, W. B., Greidanus, F. J. A. M. A. M., Carcia, P. F. & Fincher, C. R. Perpendicular magnetic anisotropy and magneto-optical Kerr effect of vapor-deposited Co/Pt-layered structures. *J. Appl. Phys.* **65**, (1989).
9. Iwasaki, S. I. Lessons from research of perpendicular magnetic recording. in *IEEE Transactions on Magnetics* **39**, 1868–1870 (2003).
10. Ouchi, K. & Honda, N. Overview of latest work on perpendicular recording media. *IEEE Trans. Magn.* **36**, 16–22 (2000).
11. Yoshino, R., Nagaoka, T., Terasaki, R. & Baldwin, C. Co/Pt MULTILAYER MEDIA FOR PERPENDICULAR MAGNETIC RECORDING. *J. Magn. Soc. Japan* **18**, S1_103-106 (1994).
12. Baibich, M. N. *et al.* Giant magnetoresistance of (001)Fe/(001)Cr magnetic superlattices. *Phys. Rev. Lett.* **61**, 2472–2475 (1988).
13. Binasch, G., Grünberg, P., Saurenbach, F. & Zinn, W. Enhanced magnetoresistance in layered magnetic structures with antiferromagnetic interlayer exchange. *Phys. Rev. B* **39**, 4828–4830 (1989).
14. Webster, J. G. *et al.* Magnetic Tunnel Junctions for Spintronics: Principles and Applications. in *Wiley Encyclopedia of Electrical and Electronics Engineering* 1–16 (John Wiley & Sons, Inc., 2014). doi:10.1002/047134608x.w8231
15. Julliere, M. *TUNNELING BETWEEN FERROMAGNETIC FILMS. PHYSICS LETTERS* **54**, 225 - 226 (1975).
16. Zhang, X. G. & Butler, W. H. Large magnetoresistance in bcc Co/MgO/Co and FeCo/MgO/FeCo tunnel junctions. *Phys. Rev. B - Condens. Matter Mater. Phys.* **70**, 1–4 (2004).
17. Nishimura, N. *et al.* Magnetic tunnel junction device with perpendicular magnetization films for high-density magnetic random access memory. *J. Appl. Phys.* **91**, 5246–5249 (2002).

18. Pratt, W. P. *et al.* Perpendicular giant magnetoresistances of Ag/Co multilayers. *Phys. Rev. Lett.* **66**, 3060–3063 (1991).

19. Prinz, G. A. Magnetoelectronics. *Science* **282**, 1660–1663 (1998).

20. Slonczewski, J. C. *Current-driven excitation of magnetic multilayers*. *Journal of Magnetism and Magnetic Materials* **159**, 1–7 (1996).

21. Albert, F. J., Katine, J. A., Buhrman, R. A. & Ralph, D. C. Spin-polarized current switching of a Co thin film nanomagnet. *Appl. Phys. Lett.* **77**, 3809–3811 (2000).

22. Ikeda, S. *et al.* A perpendicular-anisotropy CoFeB–MgO magnetic tunnel junction. *Nat. Mater.* **9**, 721–724 (2010).

23. Mangin, S. *et al.* Current-induced magnetization reversal in nanopillars with perpendicular anisotropy. *Nat. Mater.* **5**, 210–215 (2006).

24. Cowburn, R. P. & Welland, M. E. Room temperature magnetic quantum cellular automata. *Science (80-.).* **287**, 1466–1468 (2000).

25. Allwood, D. A. *et al.* Magnetic domain-wall logic. *Science* **309**, 1688–1692 (2005).

26. Parkin, S. S. P., Hayashi, M. & Thomas, L. Magnetic domain-wall racetrack memory. *Science* **320**, 190–194 (2008).

27. Fukami, S., Suzuki, T., Ohshima, N., Nagahara, K. & Ishiwata, N. Micromagnetic analysis of current driven domain wall motion in nanostrips with perpendicular magnetic anisotropy. *J. Appl. Phys.* **103**, 07E718 (2008).

28. Yamanouchi, M., Chiba, D., Matsukura, F., Dietl, T. & Ohno, H. Velocity of domain-wall motion induced by electrical current in the ferromagnetic semiconductor (Ga,Mn)As. *Phys. Rev. Lett.* **96**, 096601 (2006).

29. Boulle, O. *et al.* Nonadiabatic spin transfer torque in high anisotropy magnetic nanowires with narrow domain walls. *Phys. Rev. Lett.* **101**, 216601 (2008).

30. Metaxas, P. J. *et al.* Creep and flow regimes of magnetic domain-wall motion in ultrathin Pt/Co/Pt films with perpendicular anisotropy. *Phys. Rev. Lett.* **99**, 217208 (2007).

31. Lavrijsen, R. *et al.* Magnetic ratchet for three-dimensional spintronic memory and logic. *Nature* **493**, 647–650 (2013).

32. Fert, A., Cros, V. & Sampaio, J. Skyrmions on the track. *Nature Nanotechnology* **8**, 152–156 (2013).

33. Raju, M. *et al.* The evolution of skyrmions in Ir/Fe/Co/Pt multilayers and their topological Hall signature. *Nat. Commun.* **10**, 1–7 (2019).

34. Bi, C. *et al.* Reversible Control of Co Magnetism by Voltage-Induced Oxidation. *Phys. Rev. Lett.* **113**, 267202 (2014).

35. Hu, J. M., Chen, L. Q. & Nan, C. W. Multiferroic Heterostructures Integrating Ferroelectric and Magnetic Materials. *Advanced Materials* **28**, 15–39 (2016).

36. Bauer, U. *et al.* Magneto-ionic control of interfacial magnetism. *Nat. Mater.* **14**, 174–181 (2015).

37. Hu, W. *et al.* Synthetic antiferromagnetic nanoparticles with tunable susceptibilities. *J. Appl. Phys.* **105**, 07B508 (2009).

38. Leulmi, S. *et al.* Comparison of dispersion and actuation properties of vortex and synthetic antiferromagnetic particles for biotechnological applications. *Appl. Phys. Lett.* **103**, 132412 (2013).

39. Joisten, H. *et al.* Self-polarization phenomenon and control of dispersion of synthetic antiferromagnetic nanoparticles for biological applications. *Appl. Phys. Lett.* **97**, 253112 (2010).

40. Vemulkar, T., Mansell, R., Petit, D. C. M. C., Cowburn, R. P. & Lesniak, M. S. Highly tunable perpendicularly magnetized synthetic antiferromagnets for biotechnology applications. *Appl. Phys. Lett.* **107**, 012403 (2015).

41. Xu, Y. H., Bai, J. & Wang, J. P. High-magnetic-moment multifunctional nanoparticles for nanomedicine applications. *J. Magn. Magn. Mater.* **311**, 131–134 (2007).

42. Ariake, J., Chiba, T., Watanabe, S., Honda, N. & Ouchi, K. Magnetic and structural properties of Co-Pt perpendicular recording media with large magnetic anisotropy. in *Journal of Magnetism and Magnetic Materials* **287**, 229–233 (North-Holland, 2005).

43. Hashimoto, S., Ochiai, Y. & Aso, K. Ultrathin Co/Pt and Co/Pd multilayered films as magneto-optical recording materials. *J. Appl. Phys.* **67**, 2136–2142 (1990).

44. Vemulkar, T., Welbourne, E. N., Mansell, R., Petit, D. C. M. C. & Cowburn, R. P. The mechanical response in a fluid of synthetic antiferromagnetic and ferrimagnetic microdiscs with perpendicular magnetic anisotropy. *Appl. Phys. Lett.* **110**, 042402 (2017).

45. Ebert, H., Ruegg, S., Schütz, G., Wienke, R. & Zeper, W. B. Magnetic properties of Co/Pt-multilayers. *J. Magn. Magn. Mater.* **93**, 601–604 (1991).

46. Weller, D. *et al.* Orbital magnetic moments of Co in multilayers with perpendicular magnetic anisotropy. *Phys. Rev. B* **49**, 12888–12896 (1994).

47. Bruno, P. Tight-binding approach to the orbital magnetic moment and magnetocrystalline anisotropy of transition-metal monolayers. *Phys. Rev. B* **39**, 865–868 (1989).

48. Brown, W. *Micromagnetics*. (Interscience Publishers, 1963).

49. Coey, J. *Magnetism and Magnetic Materials*. (Cambridge University Press, 2010).

50. Vogel, J., Moritz, J. & Fruchart, O. Nucleation of magnetisation reversal, from nanoparticles to bulk materials. *Comptes Rendus Physique* **7**, 977–987 (2006).

51. Wernsdorfer, W. *et al.* Experimental evidence of the Néel-Brown model of magnetization reversal. *Phys. Rev. Lett.* **78**, 1791–1794 (1997).

52. Wernsdorfer, W., Hasselbach, K. & Benoit, A. Measurements of magnetization switching in individual nickel nanowires. *Phys. Rev. B - Condens. Matter Mater. Phys.* **55**, 11552–11559 (1997).

53. Moritz, J. *et al.* Experimental evidence of a 1/H activation law in nanostructures with perpendicular magnetic anisotropy. *Phys. Rev. B - Condens. Matter Mater. Phys.* **71**, 100402 (2005).

54. Sharrock, M. P. Time dependence of switching fields in magnetic recording media (invited). *J. Appl. Phys. J. Appl. Phys. J. Appl. Phys.* **76**, 23903–4129 (1994).

55. Brown, W. F. Thermal fluctuations of a single-domain particle. *Phys. Rev.* **130**, 1677–1686 (1963).

56. Gaunt, P. Ferromagnetic domain wall pinning by a random array of inhomogeneities. *Philos. Mag. B Phys. Condens. Matter; Stat. Mech. Electron. Opt. Magn. Prop.* **48**, 261–276 (1983).

57. Bruno, P. *et al.* Hysteresis properties of ultrathin ferromagnetic films. *J. Appl. Phys.* **68**, 5759–5766 (1990).

58. Kaganovskiy, L., Khizroev, S. & Litvinov, D. Influence of low anisotropy inclusions on magnetization reversal in bit-patterned arrays. *J. Appl. Phys.* **111**, 033924 (2012).

59. Shaw, J. M. *et al.* Intrinsic defects in perpendicularly magnetized multilayer thin films and nanostructures. *Phys. Rev. B - Condens. Matter Mater. Phys.* **82**, 144437 (2010).

60. Li, Z. G., Carcia, P. F. & Cheng, Y. Co thickness dependence of the microstructure of Pt/Co multilayers. *J. Appl. Phys.* **73**, 2433–2437 (1993).

61. Shaw, J. M. *et al.* Effect of microstructure on magnetic properties and anisotropy distributions in Co/Pd thin films and nanostructures. *Phys. Rev. B - Condens. Matter Mater. Phys.* **80**, 184419 (2009).

62. Petit, D. *et al.* Systematic layer-by-layer characterization of multilayers for three-dimensional data storage and logic Related content. *Nanotechnology* **27**, 155203 (2016).

63. Daalderop, G. H. O., Kelly, P. J. & Schuurmans, M. F. H. First-principles calculation of the magnetic anisotropy energy of (Co)n/(X)m multilayers. *Phys. Rev. B* **42**, 7270–7273 (1990).

64. Daalderop, G. H. O., Kelly, P. J. & Schuurmans, M. F. H. Magnetocrystalline anisotropy and orbital moments in transition-metal compounds. *Phys. Rev. B* **44**, 12054–12057 (1991).

65. Kyuno, K., Yamamoto, R. & Asano, S. First-principles calculation of the electronic structure and magnetic anisotropy of Co-based metallic multilayers. *J. Magn. Magn. Mater.* **126**, 268–271 (1993).

66. Johnson, M. T. *et al.* Magnetic anisotropy in metallic multilayers. *Reports Prog. Phys.* **59**, 1409–1458 (1996).

67. Shaw, J. M., Nembach, H. T. & Silva, T. J. Roughness induced magnetic inhomogeneity in Co/Ni multilayers: Ferromagnetic resonance and switching properties in nanostructures. *J. Appl. Phys.* **108**, 093922 (2010).

68. Thomson, T., Hu, G. & Terris, B. D. Intrinsic distribution of magnetic anisotropy in thin films probed by patterned nanostructures. *Phys. Rev. Lett.* **96**, 257204 (2006).

69. Shaw, J. M. *et al.* Reversal mechanisms in perpendicularly magnetized nanostructures. *Phys. Rev. B - Condens. Matter Mater. Phys.* **78**, 024414 (2008).

70. Lavrijsen, R. *et al.* Enhanced field-driven domain-wall motion in Pt/ Co68 B32 /Pt strips. *Appl. Phys. Lett.* **98**, 132502 (2011).

71. Lavrijsen, R. *et al.* Reduced domain wall pinning in ultrathin Pt/ Co100-x B x /Pt with perpendicular magnetic anisotropy. *Appl. Phys. Lett.* **96**, 022501 (2010).

72. Quach, D. T., Chu, T. D., Ngo, D. T. & Kim, D. H. Correlation of hysteresis loop and domain structure of CoFeB/Pd multilayer at various temperatures. *Phys. B Condens. Matter* **577**, 411822 (2020).

73. Ngo, D. *et al.* Perpendicular magnetic anisotropy and the magnetization process in CoFeB/Pd multilayer films. *J. Phys. D. Appl. Phys.* **47**, 445001 (2014).

74. Burrowes, C. *et al.* Low depinning fields in Ta-CoFeB-MgO ultrathin films with perpendicular magnetic anisotropy. *Appl. Phys. Lett.* **103**, 182401 (2013).

75. Vemulkar, T., Mansell, R., Petit, D. C. M. C., Cowburn, R. P. & Lesniak, M. S. The effect of underlayers on the reversal of perpendicularly magnetized multilayer thin films for magnetic micro- and nanoparticles. *J. Appl. Phys.* **121**, 043908 (2017).

76. Law, R., Sbiaa, R., Liew, T. & Chong, T. C. Effects of Ta seed layer and annealing on magnetoresistance in CoFePd -based pseudo-spin-valves with perpendicular anisotropy. *Appl. Phys. Lett.* **91**, 242504 (2007).

77. Gong, H., Litvinov, D., Klemmer, T. J., Lambeth, D. N. & Howard, J. K. Seed layer effects on the magnetoresistive properties of NiFe films. in *IEEE Transactions on Magnetics* **36**, 2963–2965 (2000).

78. Stella, K., Buerstel, D., Franzka, S., Posth, O. & Diesing, D. Preparation and properties of thin amorphous tantalum films formed by small e-beam evaporators. *J. Phys. D. Appl. Phys.* **42**, 135417 (2009).

79. Lee, C. H., Farrow, R. F. C., Lin, C. J., Marinero, E. E. & Chien, C. J. Molecular-beam-epitaxial growth and magnetic properties of Co-Pt superlattices oriented along the [001], [110], and [111] axes of Pt. *Phys. Rev. B* **42**, 11384–11387 (1990).

80. Knepper, J. W. & Yang, F. Y. Oscillatory interlayer coupling in Co Pt multilayers with perpendicular anisotropy. *Phys. Rev. B - Condens. Matter Mater. Phys.* **71**, 224403 (2005).

81. Lavrijsen, R. *et al.* Tuning the interlayer exchange coupling between single perpendicularly magnetized CoFeB layers. *Appl. Phys. Lett.* **100**, 052411 (2012).

82. Hellwig, O., Berger, A., Kortright, J. B. & Fullerton, E. E. Domain structure and magnetization reversal of antiferromagnetically coupled perpendicular anisotropy films. *J. Magn. Magn. Mater.* **319**, 13–55 (2007).

83. Baltz, V., Marty, A., Rodmacq, B. & Dieny, B. Magnetic domain replication in interacting bilayers with out-of-plane anisotropy: Application to Co Pt multilayers. *Phys. Rev. B - Condens. Matter Mater. Phys.* **75**, 014406 (2007).

84. Pommier, J. *et al.* Magnetization reversal in ultrathin ferromagnetic films with perpendicular anistropy: Domain observations. *Phys. Rev. Lett.* **65**, 2054–2057 (1990).

85. Liu, Z. Y., Yu, G. H., Han, G. & Wang, Z. C. Investigation of ferromagnetic coupling between Co layers in a Co/Pt multilayer with perpendicular anisotropy. *J. Magn. Magn. Mater.* **299**, 120–126 (2006).

86. An, Y., Duan, L., Liu, T., Wu, Z. & Liu, J. Structural and magnetic properties of Pt in Co/Pt multilayers. *Appl. Surf. Sci.* **257**, 7427–7431 (2011).

87. Bertero, G. A., Sinclair, R., Park, C. H. & Shen, Z. X. Interface structure and perpendicular magnetic anisotropy in Pt/Co multilayers. *J. Appl. Phys.* **77**, 3953–3959 (1995).

88. Zhang, Z., Wigen, P. E. & Parkin, S. S. P. P. Pt layer thickness dependence of magnetic properties in Co/Pt multilayers. 5649–5651 (1991).

89. Ng, V., Hu, J. F., Adeyeye, A. O., Wang, J. P. & Chong, T. C. Factors affecting surface roughness and coercivity of thin films ARTICLES YOU MAY BE INTERESTED IN. *J. Appl. Phys.* **91**, 7206 (2002).

90. Jin, Y. *et al.* Effect of sputtering power on surface topography of dc magnetron sputtered Ti

thin films observed by AFM. *Appl. Surf. Sci.* **255**, 4673–4679 (2009).

91. Mansell, R. *et al.* Magnetic particles with perpendicular anisotropy for mechanical cancer cell destruction. *Sci. Rep.* **7**, 1–7 (2017).

92. Cheng, Y. *et al.* Rotating magnetic field induced oscillation of magnetic particles for in vivo mechanical destruction of malignant glioma. *J. Control. Release* **223**, 75–84 (2016).

93. Brown, A. B. D., Smith, C. G. & Rennie, A. R. Fabricating colloidal particles with photolithography and their interactions at an air-water interface. *Phys. Rev. E - Stat. Physics, Plasmas, Fluids, Relat. Interdiscip. Top.* **62**, 951–960 (2000).

94. Hernandez, C. J., Zhao, K. & Mason, T. G. Pillar-Deposition Particle Templating: A High-Throughput Synthetic Route for Producing LithoParticles. *Soft Mater.* **5**, 1–11 (2007).

95. Goiriena-Goikoetxea, M., García-Arribas, A., Rouco, M., Svalov, A. V. & Barandiaran, J. M. High-yield fabrication of 60 nm Permalloy nanodiscs in well-defined magnetic vortex state for biomedical applications. *Nanotechnology* **27**, 175302 (2016).

96. Songmuang, R., Deneke, C. & Schmidt, O. G. Rolled-up micro- and nanotubes from single-material thin films. *Appl. Phys. Lett.* **89**, 223109 (2006).

97. Mei, Y. *et al.* Versatile approach for integrative and functionalized tubes by strain engineering of nanomembranes on polymers. *Adv. Mater.* **20**, 4085–4090 (2008).

98. Li, J. *et al.* Dry-Released Nanotubes and Nanoengines by Particle-Assisted Rolling. *Adv. Mater.* **25**, 3715–3721 (2013).

99. Chun, I. S. *et al.* InGaAs/GaAs 3D architecture formation by strain-induced self-rolling with lithographically defined rectangular stripe arrays. *J. Cryst. Growth* **310**, 2353–2358 (2008).

100. Ronse, K. Optical lithography-a historical perspective. *Comptes Rendus Physique* **7**, 844–857 (2006).

101. KING, M. C. Principles of Optical Lithography. in **1**, 41–81 (Elsevier, 1981).

102. www.MicroChemicals.com. *Chapter 01 MicroChemicals ®-Fundamentals of Microstructuring https://www.microchemicals.com/technical_information/exposure_photoresist.pdf*.

5 Particle behaviour in liquid

Collaboration: Dr. Dédalo Sanz Hernández provided expertise and computing resources for the Mumax3 micromagnetics simulations used to determine particle stray fields (Section 5.3.2).

5.1 Introduction

The collective and individual responses of magnetic particles in liquid have long been investigated, in order to take advantage of the control offered by these magnetic systems for a range of different environments and applications. Initial work focused on magnetic fluids such as magnetorheological liquids and ferrofluids, where the collective excitation of magnetic particles is used to change the property of the liquid. First developed the mid-1900s, magnetorheological liquids combined a fluid medium with micron-sized magnetic particles, often made of iron.[1,2] By application of a strong magnetic field, the viscosity of the fluid can be changed over many orders of magnitude, lending it to application in mechanical systems. Similar in nature are ferrofluids, which are colloidal suspensions of Co- and Fe- containing nanoparticles, such as magnetite particles.[3] Ferrofluids have similar applications in mechanical systems as seals or dampers, acting as a magnetorheological fluid, but as nanoparticle synthesis methods and capabilities have improved, the breadth of applications for ferrofluids has grown immensely, ranging from cancer therapeutics to magneto-optical devices.[4–8] Specifically, magnetic hyperthermia, where a high frequency alternating magnetic field is used to create heat from magnetic nanoparticles and destroy cancerous cells, has spawned a large amount of research, even leading to clinical applications.[9,10] Further biomedical applications such as the use of ferrofluids for imaging contrast, biological separation, and sensing have shown great promise as well.[11–13] All these systems use quite simple magnetic nanoparticles, such as superparamagnetic single-domain iron oxide particle. Ferrofluids and magnetic liquids have been further advanced by using more complex magnetic particles, often with anisotropic magnetic properties that can translate into unique fluid response. For instance, barium hexaferrite can be used to create nanoplatelets with perpendicular anisotropy, which then translates to interesting magneto-optical responses when coupled with a liquid crystal.[14,15] Magnetic Janus particles of various types can be used to create unique fluidic structures through their asymmetric interactions, which can translate applications such as photonics or more advanced mechanical control of the liquid.[16–18]

Most of the ferrofluids and magnetic liquids listed above use magnetic particles to create interesting collective responses of the fluid to magnetic fields. Recent work on more advanced magnetic particle types focuses on creating unique individual particle responses that can then be used for a more complex application. The particles incorporate properties such as vortex configurations,

perpendicular anisotropy, and anti-ferromagnetism that lead to new and interesting responses to magnetic fields.[19,20] Examples of such particles include vortex microdiscs and synthetic anti-ferromagnetic microparticles, which have found a number of biomedical applications, including in cancer therapy.[21–25] Further uses of individual response of magnetic particles can include multi-plexed sensing and microrobotics.[26–28] Microrobotics is an especially interesting application for an individual or collection of particles that can display complex field responses, and it will be explored more thoroughly in Chapter 6. The particles created in this work, and the assemblies we will make from them, fall squarely within this final category of advanced magnetic particles, where the individual field response of particles or assemblies can be tailored to and harnessed for complex applications.

In order to take advantage of such properties, we must first understand the fundamentals of how the individual particles interact and respond to each other and to applied magnetic fields. Building on the principles established in Chapter 4 to create magnetic particles with PMA, this chapter will investigate the behaviour of the particles in three different areas: stability, interaction, and magnetic field response. All three areas will be analysed with an eye towards self-assembly of the particles. We will focus on particles created from the two film layer structures optimized in Chapter 4: the single multilayer particle {Au(20)/ Ta(2)/ Pt(2)/[CoFeB(0.55)/ Pt(0.86)]$_4$/ CoFeB(0.55)/ Pt(2)} and the 'sandwich' particle {Ta(2)/ Pt(2)/ [CoFeB(0.55)/ Pt(0.86)]$_4$/ CoFeB(0.55)/ Pt(2)/ Au(20)/ Ta(2)/ Pt(2)/[CoFeB(0.55)/ Pt(0.86)]$_4$/ CoFeB(0.55)/ Pt(2)}. The first area of interest is particle stability, as the particles must retain their desired shape to interact effectively. Second, the interaction of particles in the absence of an applied field will be analysed, to understand their ability to assemble. Both stability and shape will be investigated over a range of particle sizes with the aforementioned film layer structures, to establish if there are any restrictions on particle size or composition that would impede future assembly. Third, the individual particle response to an applied field will be examined, with the primary goal of understanding how the different remanent states of the particles, established in Chapter 4, can be manipulated and used to drive on-demand assembly. By fully probing these three areas, we can find the ideal size and composition for particles and know the way the particles can be addressed and activated by an external magnetic field, in order to then use these particles in a self-assembly system.

5.2 Particle stability in liquid

An essential requirement for the functional self-assembly of particles is that the particles must retain their shape and mechanical structure in liquid. If the particles distort or deform when in liquid, the magnetization will no longer be well-defined with respect to the particle shape and assembly cannot occur in a predictable or repeatable manner. Because of the high aspect ratio of these particles (around 1000, with thicknesses of 20 – 50 nm and lateral sizes of 5 – 20 μm) they are especially susceptible to

deformation under the inherent stresses present in layered metallic thin film structures and care must be taken in the formation of these particles to prevent this instability.[29] As was outlined in Chapter 4, Au has been established as a component that can be added into the thin film layer structure to add thickness, and thus, structural stability. To find the best film structure for stable particles, we have investigated the stability of a number of different film layer structures at different particle sizes. In this section, we will outline some of the factors leading to instability in thin film particles, and then show the different size, thickness, and composition combinations that were used to create mechanically stable particles.

5.2.1 Origins of instability

During sputter deposition of thin films, stresses develop in the materials due to accumulation of crystallographic flaws and defects. These defects impart an intrinsic stress on the films that can potentially affect material properties and the stability of the thin film.[29] This is especially important for this work, as the release of particles from the deposition substrate allows greater opportunity for relaxation of the stress, which would damage particle morphology. Many factors play a role in the stress of sputtered films, such as sputtering pressure, substrate temperature, and materials parameters, like melting temperature.[29,30] The complex interplay of these factors makes it very difficult to fully understand the development of stress in films.[30] While many methods such as annealing or alloying can be used to impact the film's stress state, we are more concerned with tailoring the magnetic properties of our films, as seen in Chapter 4. For this reason, we will not attempt to change our materials or growth system to reduce the stress, but only look for ways to better control it when forming particles.

There are a number of factors on which we can focus to mitigate stress in our films and particles. The first is with the Au structural layer. Au develops high stress states when sputtered, and it is known that the stress increases with thickness of the Au layer.[31,32] Second, balancing the stress from different multilayer interfaces can be a method for reducing overall film stress and deformation.[30] Third, amorphous materials can exhibit lower stress states due to the lack of crystalline order and grain structure, helping to lower the overall stress of the system.[30,33] In our film, CoFeB and Ta are both amorphous layers, which is especially useful in the case of CoFeB, as it reduces the large crystal mismatch and associated stress seen in crystalline Co/Pt multilayers.[34] The lateral size of the films can also influence its stability. In studies of micrometre-sized Au tensile specimens, larger specimens had lower yield stresses, making the structure more susceptible to deformation.[35,36] By accounting for these various factors, we can experiment with different particle parameters to help minimize the stress and maximize particle stability.

5.2.2 Size, thickness, and composition

In order to investigate the effects of different parameters on particle stability, particles were created with varying size, thickness, and composition. The particles were all grown as squares, and variations were made in both the lateral size of the particles and their thickness. To cover a range of sizes that can be achieved with high precision on the direct laser write lithography system (edge lengths >1 μm), particles were made with lateral areas of 5 x 5, 10 x 10, 15 x 15, and 20 x 20 μm^2. The thickness and composition of particles was also varied, as a different thickness or composition of film should help balance and resist the stresses that cause particle deformation. Two compositions of films were chosen with the following layer structures: the first is a magnetic multilayer on an Au backbone {Au(**t**)/ Ta(2)/ Pt(2)/[CoFeB(0.55)/ Pt(0.86)]$_4$/ CoFeB(0.55)/ Pt(2)} where **t** = 10, 20, 30, and 40 nm of Au; the second is a 'sandwich' film made of two magnetic multilayers sandwiched around an Au structural layer (as introduced in Chapter 4.3.3) {Ta(2)/ Pt(2)/ [CoFeB(0.55)/ Pt(0.86)]$_4$/ CoFeB(0.55)/ Pt(2)/ Au(20)/ Ta(2)/ Pt(2)/[CoFeB(0.55)/ Pt(0.86)]$_4$/ CoFeB(0.55)/ Pt(2)}. Since the magnetic multilayer structure {Ta(2)/ Pt(2)/[CoFeB(0.55)/ Pt(0.86)]$_4$/ CoFeB(0.55)/ Pt(2)} has a total thickness of about 12 nm, the overall thickness of the particle from the 'sandwich' film is comparable to the thickness of the single multilayer particle with $\mathbf{t_{Au}}$ = 30 nm. By creating particles over this size, thickness, and composition range, we can get a full understanding of how these different properties will affect the stability of the particles. An example of the deformation that can be seen in the particles is given in Figure 5.1, which compares a 5 x 5 μm^2 'sandwich' particle with a 5 x 5 μm^2 particle that is composed of only the magnetic multilayer, equivalent to the first particle type mentioned with t_{Au} = 0 ({Ta(2)/ Pt(2)/[CoFeB(0.55)/ Pt(0.86)]$_4$/ CoFeB(0.55)/ Pt(2)}).

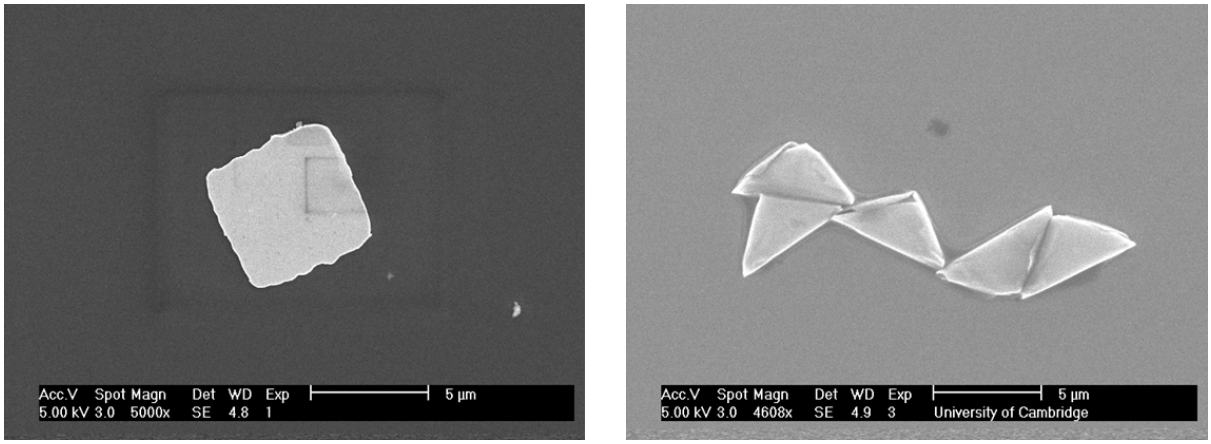

Figure 5.1 Stability of thin film particles at different thicknesses
Comparison of a 5 x 5 μm^2 square particle made from a 40 nm thick magnetic film (left) of the structure {Ta(2)/ Pt(2)/ [CoFeB(0.55)/ Pt(0.86)]$_4$/ CoFeB(0.55)/ Pt(2)/ Au(20)/ Ta(2)/ Pt(2)/ [CoFeB(0.55)/ Pt(0.86)]$_4$/ CoFeB(0.55)/ Pt(2)} with a particle of 12 nm thick with the structure {Ta(2)/ Pt(2)/ [CoFeB(0.55)/ Pt(0.86)]$_4$/ CoFeB(0.55)/ Pt(2)}

Figure 5.1 highlights the difference in stabilities that can be seen in particles of different composition and thickness, as the 'sandwich' particle retains its shape while the thinner particle, composed of only the magnetic multilayer, deforms.

Defining particle stability

To effectively analyse the stability of particles, we must first have a metric to describe it. To do this, we will use the lateral aspect ratio of square particles, determined by imaging the particles and computing the length of the axes l_1 and l_2 of the particle using ImageJ, with l_1 being the short axis of the particle and l_2 as the long axis of the particle, keeping the two axes perpendicular during measurement. Figure 5.2 (a) shows how this can be measured on a stable particle and a deformed particle. By using this construction, an ideal square particle will have an aspect ratio of 1, and any value below that will be indicative of some sort of deformation. There is some processing-related variation in the dimensions of the lithographically formed particles, so any particle exceeding a measured lateral aspect ratio of 0.95 will be considered un-deformed. Because of the relatively large size of the particles, optical microscope images, such as those in Figure 5.2 (b), were used to conduct the lateral aspect ratio measurements. To create the particle samples used here, particles in water were deposited on silicon chips, and the water was allowed to dry. The particles were then imaged on the surface of the silicon chip after drying.

Figure 5.2 (c) shows the result of the stability tests on the various particle sizes, thicknesses, and compositions. In each case, the aspect ratios were taken from 20 – 30 particles, which are then averaged to create a value for that particle type. It is immediately clear that particles with a single magnetic multilayer on a structural buffer will deform as the lateral size of the particle increases. The deformation becomes worse as the particle is made thicker, which matches results from literature that show the stress of Au layers increases with thickness.[31] As the thickness of the structural Au layer goes from 10 nm (Figure 5.2 (b), blue points) to 20 and 30 nm (yellow and orange points), the stability of the particles actually gets worse, demonstrated by the smaller average aspect ratio. Once the Au layer reaches a thickness of 40 nm (purple points), there is some improvements, as the aspect ratio of the 10 and 20 µm particles is improved versus the same size at Au thicknesses of 20 and 30 nm. However, in general, the single multilayer particle proves insufficiently stable at all thicknesses for sizes above 5 µm. The best stability results are seen for the 'sandwich' type particle for all size cases.

(a)

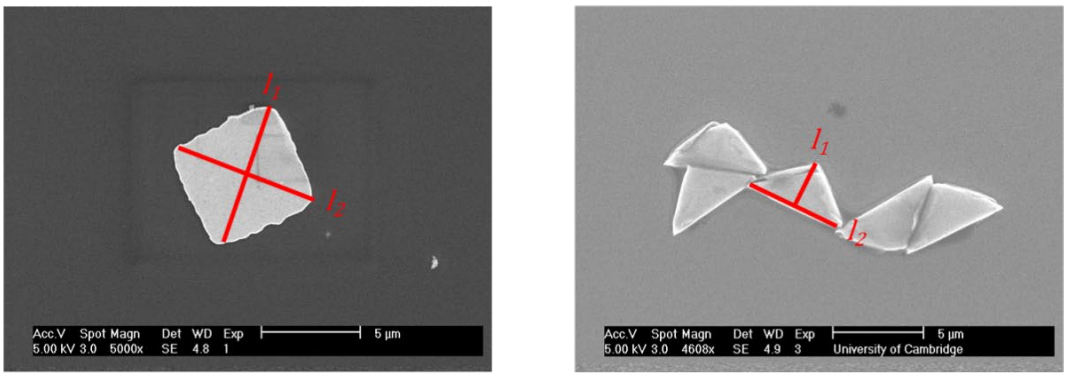

(b)

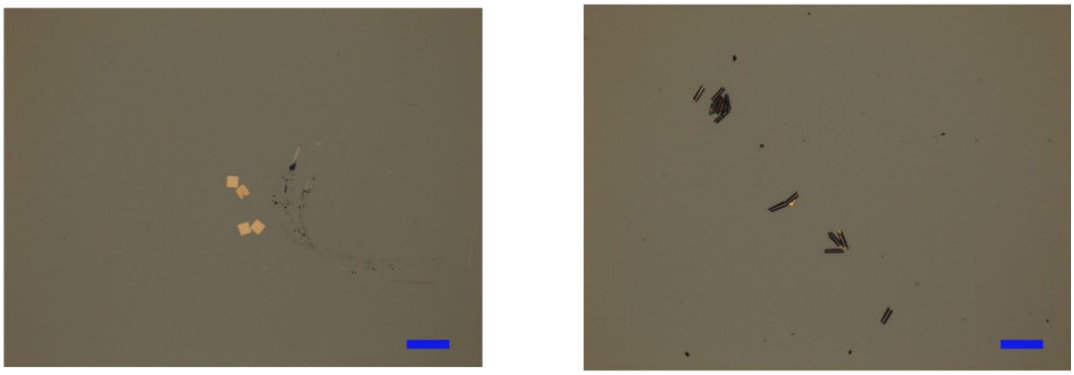

(c)

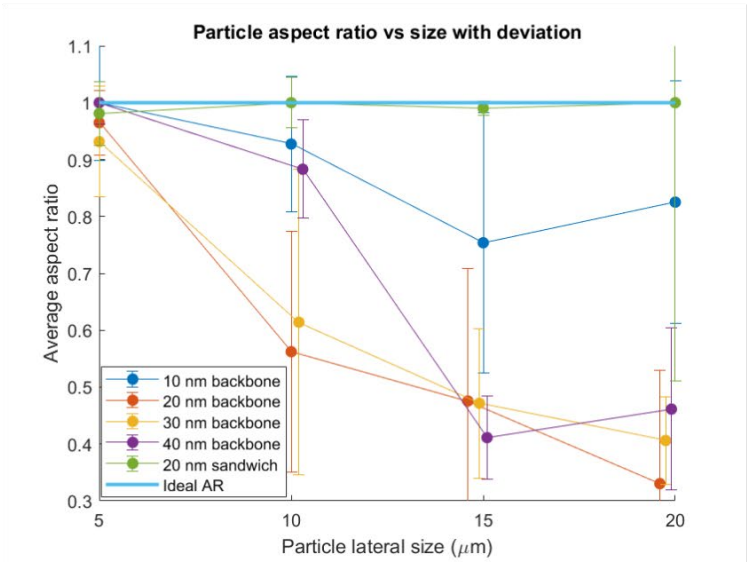

Figure 5.2 Measuring particle stability versus composition using aspect ratio
The aspect ratio of a series of particle of different composition and size were measured, using the method shown in (a). Ensembles of particles of different size and composition were categorized in this way using optical microscope images (b), where the blue scale bar corresponds to 20 µm. A comparison between the different types of particles is given in (c). The error bars represent one standard deviation around the average aspect ratio. Some lateral size values were slightly shifted to improve readability – all particles were made in sizes of 5, 10, 15, and 20 µm. A particle with a backbone is a single 5x magnetic multilayer on an Au layer of the given thickness, while a sandwich particle is two 5x magnetic multilayers surrounding a central Au structural layer of the given thickness.

When compared with the ideal aspect ratio of 1, represented by the thick cyan line, the 'sandwich' type particles are able to maintain ideal or near-ideal stability at all sizes. With the Au layer in the middle surrounded by two identical magnetic multilayers, it is likely the stresses in the particle are more balanced compared to the single multilayer particles. It is also possible that, by beginning the growth of the particle on the Ge release layer using amorphous Ta, instead of crystalline Au, there is less stress induced in the structure due to mismatch of the crystalline layers. Additionally, Au films grow with poor adhesion on oxides, and Ge forms a passivating oxide layer.[37,38] This poor adhesion can lead to a less continuous film and could account for the poorer stability of particles in which there is a Ge/Au interface.

Overall, particles can be created to be mechanically stable and consistent using the 'sandwich' configuration at all particle sizes from 5 – 20 μm. Additionally, single multilayer particles can also be made with Au structural layers of either 10 or 40 nm, as long as the size is kept below 10 μm. Except where explicitly noted, the subsequent experiments in this work (including assembly experiments presented in Chapter 6) will use 'sandwich' particles in all cases to take advantage of the superior stability of the structure.

5.3 Particle interactions in liquid

After looking into the stability of different particles sizes, it is important to investigate how the interactions between particles change with their size. To create an equilibrium self-assembly system using the magnetic particles, inter-particle interactions must be able to drive the assembly of particles in the absence of an external magnetic field or other energy input. The energy of the interaction, and thus, the force between particles, is determined by the interaction of the stray field from one particle with the moment of another, taking the form $E = -m \cdot B$. We have previously addressed in Chapter 4 the necessity for high moment particles and have optimized the particle construction in that direction. All particles will use the same magnetic film layer structure {Ta(2)/ Pt(2)/[CoFeB(0.55)/ Pt(0.86)]$_4$/ CoFeB(0.55)/ Pt(2)}, which means all the particles will have the same magnetization per unit area. Thus, the moment of the particles will scale with the lateral area of the particle. The increase in moment with particle size would initially, according to the equation above, seem beneficial for driving stronger interactions. However, the other component of the interaction, the magnetic flux B from the stray field of the particle, is not favoured in larger particles in the near field. This is because the larger a particle of PMA thin film material becomes, the more it approximates an infinite sheet with perpendicular magnetization. In the extreme case of an infinite sheet, the demagnetizing factor N of the sheet is 4π in the Z (perpendicular) direction and the sheet does not produce any external stray field, as a consequence of Gauss's law. Gauss's law defines $\nabla \cdot B = 0$. In the infinite sheet, $B =$

$(H + 4\pi M)$ and $H = H_{ext} + H_{demag}$. With no external field and $H_{demag} = -NM,\ B = 0$ inside the sheet and must also equal zero outside to satisfy $\nabla \cdot \mathrm{B} = 0$. Two infinite sheets would then have interaction energy of zero, as there would be no magnetic flux between the particles to drive the interaction. As particles get larger, then, the interaction energy will not just increase proportionally to the increasing moment, but be moderated by the change in field profile of the larger particles. Additionally, as the particles grow in size, the mass of the particle scales with the particle volume as well. Increased mass can be a factor in the strength of frictional and drag forces that act on particles in liquid, which could also potentially impede their self-assembly.

We have experimentally investigated the interactions between single particles of different sizes, analysing the propensity of the different particles to assemble in the absence of an external magnetic field. We have compared these experimental results with calculations of the interaction energy and forces of the particles and the stray field profile of the particles, to help understand the ideal size for particle interactions and assembly.

5.3.1 Interaction vs size

Experiments of particle interactions with particles of varying size were conducted. The particles, all of the same 'sandwich' type with the layer structure {Ta(2)/ Pt(2)/ [CoFeB(0.55)/ Pt(0.86)]$_4$/ CoFeB(0.55)/ Pt(2)/ Au(20)/ Ta(2)/ Pt(2)/ [CoFeB(0.55)/ Pt(0.86)]$_4$/ CoFeB(0.55)/ Pt(2)}, were created with lateral sizes of 5 x 5, 10 x 10, 15 x 15, and 20 x 20 μm^2. The particles were then deposited in water onto a silicon chip. The particles were continuously observed and imaged while in a droplet of water which was on the silicon chip, and the focal plane of the microscope was at the surface of the silicon chip, to allow stable imaging of the particles, as focusing on actively settling particles was not feasible. While being imaged, the particles were saturated under a magnetic field of 4000 Oe. The field was then turned off, and particles were left to interact in the absence of field, under the influence of their own magnetic moments to drive interactions. A small remanent field from the magnet still exists and aids in aligning the particles for assembly. However, as we will explain below, while the remanent field helps with particle alignment, it is not large enough to drive the interactions seen. A number of different pair-wise particle interactions were observed, examples of which are given below for the four sizes studied. Figure 5.3 shows the interactions for 5 x 5 (Figure 5.3, a) and 10 x 10 (Figure 5.3, b) μm^2 particles, which were both able to effectively interact and assemble under these conditions. Both particle types showed similar behaviour. First, the particles slowly moved until their surface normal were aligned and coaxial, while also slowly moving closer together. This can be seen in the left-most images in Figure 5.3 in both cases. Then, the particles were quickly drawn to assemble. Figure 5.3 provides timescales for the intervals between these steps. The first alignment process is the longest, while the rest of the interaction proceeds much more swiftly in both cases. This can be understood because the highly anisotropic particles have their magnetic

moment aligned with the surface normal, so the energy and forces driving interaction are strongest when the particles are aligned along this direction. The particles interact and align in this fashion because of the small remanent field of the electromagnet, which keeps the particle moments parallel and prevents rotation of the particles. Due to the geometry of the imaging setup, it is difficult to avoid this remanent field, which has a magnitude of about 5 Oe. The remanent field is mostly uniform leading to a field gradient of ~0.05 Oe/mm. The force from this gradient can be estimated at ~10^{-17} N, which is much smaller than the magnetic interaction force between particles, which range from 10^{-8} to 10^{-14} N. Thus, while the remanent field aids in alignment, it is not responsible for the forces seen causing particle interactions.

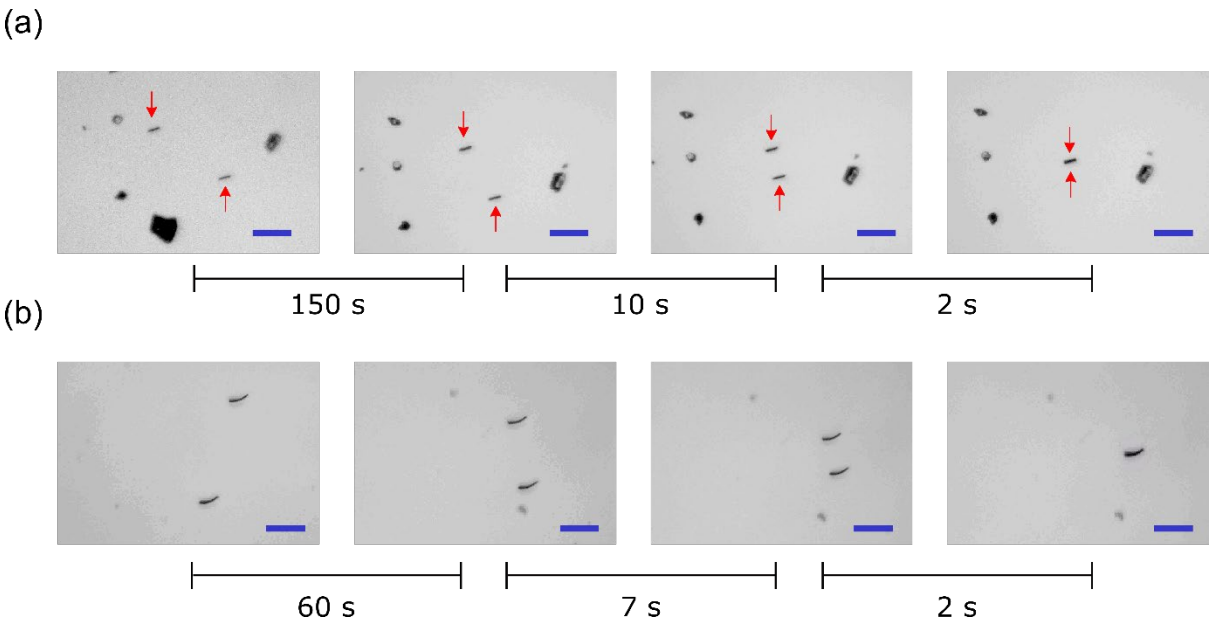

Figure 5.3 Interactions of 5 x 5 and 10 x 10 µm^2 square particles
The interactions between (a) 5 x 5 µm^2 and (b) 10 x 10 µm^2 particles are shown. The four pictures represent the sequence of the interaction of two saturated particles in the absence of an applied magnetic field. The time intervals separating the pictures are given. Red arrows denote the interacting 5 x 5 um^2 particles, to distinguish them from debris in the image. The blue scale bars correspond to 20 µm.

Both the 5 x 5 and 10 x 10 µm^2 particles were able to assemble with only the remanent field influence from long distances (>40 µm of initial separation). This is a strong preliminary proof that these particles can be used to self-assemble larger structures, even in sparse liquid suspensions of particles.

The same experiment was repeated with 15 x 15 and 20 x 20 µm^2 particles, the results of which are displayed in Figure 5.4. However, in the case of the larger particles, assembly did not proceed smoothly. As the figure shows, both of the larger particles required external energy input into the system, either in the form of mechanical agitation or application of a large field gradient (~10 Oe/mm, 10^{-14} N force). The field gradient allowed particles to be drawn closer together, while

mechanical agitation allows to particles to be ‘un-stuck’ from the silicon surface onto which they had settled. None of the particles used here are colloidal, so all are expected to settle out of the liquid over time (usually on timescales of minutes to hours). However, the larger 15 x 15 and 20 x 20 μm^2 particles are seen to be prevented from assembling after settling onto the silicon surface, likely because of their larger size and mass.

Figure 5.4 does show that the larger particles are interacting and attempting to assemble, but they cannot easily overcome these inertial and frictional barriers to complete the process. In both cases, the particles would sit at separations of 20 μm or less but would not show any visible interaction or proceed towards assembly on an observation times of more than 300 seconds. This separation is far smaller than the separations overcome by the 5 x 5 and 10 x 10 μm^2 particles, demonstrated in Figure 5.3. It was only with the addition of agitation or other external energy inputs that the interaction could proceed. When it did, the assembly could occur quite quickly, as seen in Figure 5.4 (b).

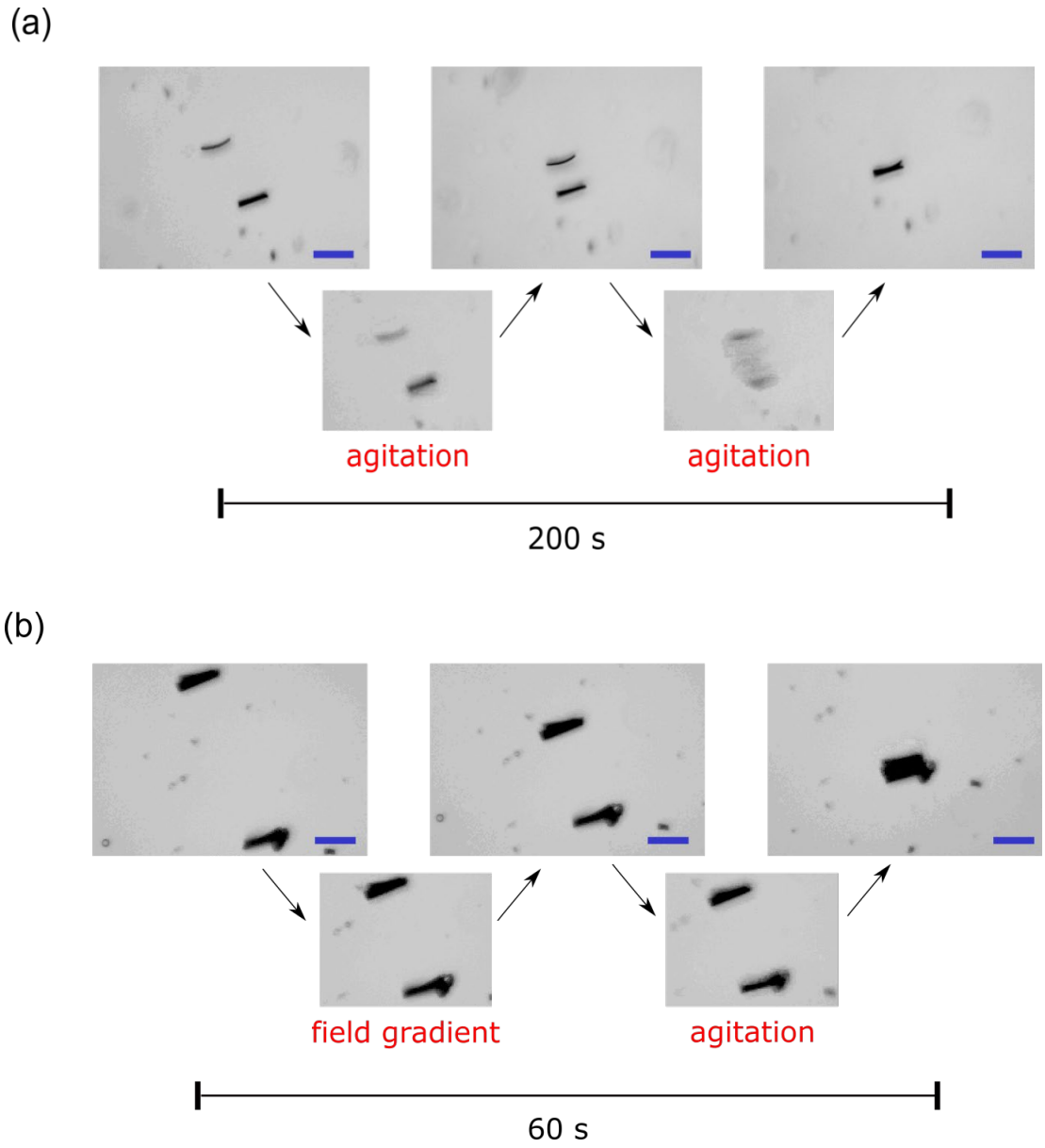

Figure 5.4 Interaction of 15 x 15 and 20 x 20 μm^2 particles
The interactions between (a) 15 x 15 and (b) 20 x 20 μm^2 particles are shown. The three pictures show the sequence of interaction between two saturated particles in the absence of an applied magnetic field. The additional arrows and notes show when either agitation or an applied field gradient was used to assist the interaction. The overall time of the interaction from start to finish is shown. The blue scale bars correspond to 20 μm.

As opposed to the 5 x 5 and 10 x 10 μm^2 particles, the 15 x 15 and 20 x 20 μm^2 sizes do not appear to be good candidates for self-assembly. Even though the larger particles have a higher moment, they cannot effectively assemble without external energy inputs. Relying on external energy inputs like vibration would introduce uncertainty into the assembly process, which should be avoided in order to create a controllable system.

In order to further understand and quantify these pair-wise particle interactions, calculations of the interactions energy and the particle stray field, along with drag and frictional forces, were conducted, to correlate the energy and field profile with the experimental interactions seen above.

5.3.2 Calculation of interaction energy

Particle interactions were quantified by calculating the interaction energy of the particles in a number of different geometries. The interaction energy can give an idea of the relative depth and gradient of the energy driving inter-particle interactions. This information can be used to effectively compare particles of different geometries to understand the favourability of different interactions. The interaction energy is derived from the Rhodes-Rowlands equation for interaction energy.[39] Additionally, the stray field profiles of the particles were calculated using Mumax3, to understand how the field changes with particle size.[40] By understanding how the energy and field change, we can further our understanding of the interactions and assembly of the particles.

The interaction energy was calculated in two different geometries, which are outlined in Figure 5.5. Figure 5.5 (a) defines the particle dimensions used in these calculations, where a fully magnetized square prism is created with a set thickness and equal edge lengths which correspond to the lateral size of the particle. The magnetization is perpendicular to the surface of the particle. This particle is used in two ways: first, the interaction energy is calculated at a fixed particle separation and for varying lateral size of the particle (Figure 5.5, b). The interaction energy is also calculated for particles of fixed lateral size and varying z-separation (Figure 5.5, c). These two different variants will give a full picture of how the interaction energy develops for particles of different sizes over changing separations.

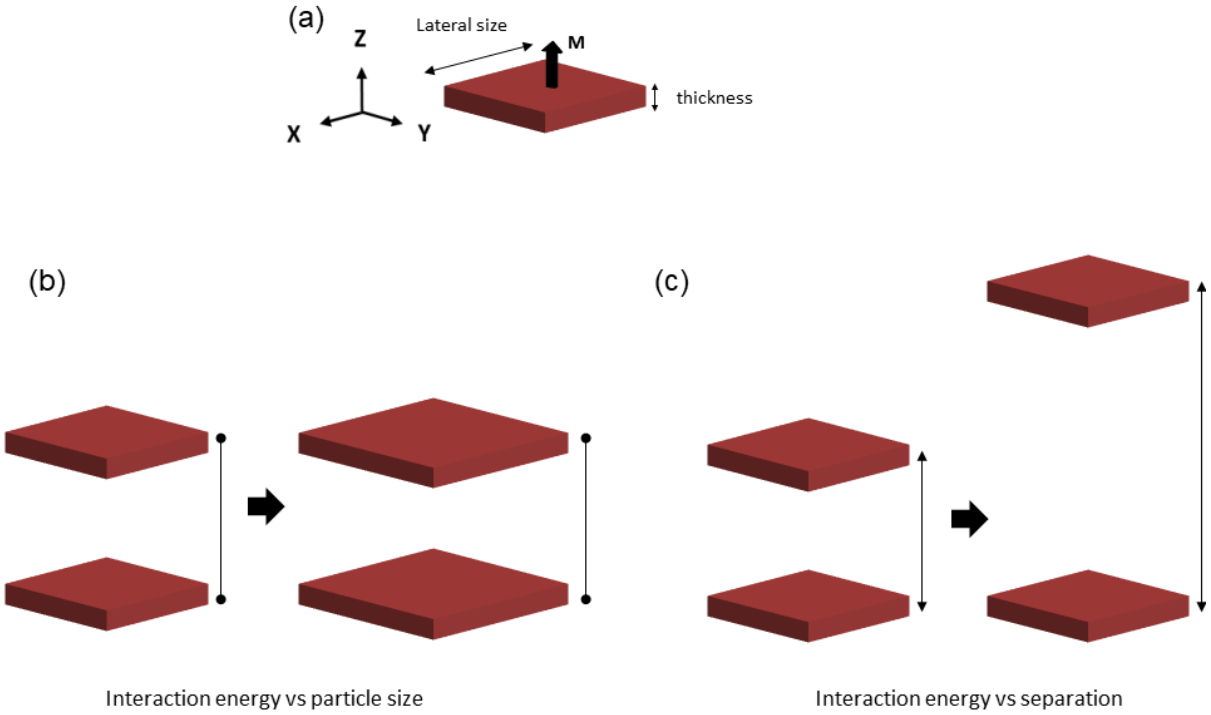

Figure 5.5 Schematic diagram of particle calculation conditions
The different conditions used for calculating particle interaction energies are shown. (a) shows the square particle used for the calculations, defining the 'lateral size' and 'thickness' dimensions along with references axes, while also highlighting the direction of magnetization perpendicular to the particle. (b) gives the geometry used for calculating interaction energy versus particle size, where (c) gives the geometry for interaction energy versus particle separation.

In all the calculations presented below, the particle is taken to be a square prism with a thickness of 10 nm and a lateral size between 1 and 100 μm. This thickness is approximately the thickness of the metallic multilayer used in the real 'sandwich' particles, so the interaction between two of these prisms should provide an effective analogue to the real interactions of two particles containing such multilayers. Additionally, the prism will be fully magnetized with a magnetization of 330 emu/cm^3, which was determined by calculating the moment from 2.75 nm of CoFeB with an average M_s of 1200 emu/cm^3 (taken from Chapter 4, Table 1) and distributing it evenly through the full 10 nm thickness of the square prism. This will allow the particle to have a realistic moment derived from the real moment of the 'sandwich' particles with two of the {Ta(2)/ Pt(2)/ [CoFeB(0.55)/ Pt(0.86)]$_4$/ CoFeB(0.55)/ Pt(2)} multilayer. The interaction energy will be calculated as both total energy and energy per area. It is interesting to include energy per area because, given the particles have the same thickness and density, this can be thought of as the interaction energy per unit mass. Since some retarding forces, like surface frictional forces, depend on particle mass (see p. 116 –

119 for analysis of drag and frictional forces), this can give additional information about the particle interactions that might not be captured in the total energy comparison.

First, the interaction energy between two particles was calculated for particles of increasing lateral size. This was done at a number of set separation distances, shown in Figure 5.6. As Figure 5.6 (a) demonstrates, interaction energy increases with particle size, for all separation distances. It does not increase directly with the square of the lateral size, showing that it does not increase purely with the growing moment of the particle, but is modified by the particle's stray field. This can be verified by looking at the interaction energy per area. When comparing particles with a set thickness and magnetization, normalizing by area also normalizes by the moment of the particle. In the per area calculation (Figure 5.6, b), it is clear that smaller particles are favoured, at least at small separation distances. We will see below (Figure 5.9) that the change in shape of the curve from 100 nm separation to 1 µm separation is the cross-over between near-field and far-field effects for the small particles. Smaller particles, due to the planar shape of the film, will have larger average stray fields close to the particles, but these will decrease at a greater rate compared to the larger particles, leading to the cross-over in the interaction energy per area seen here as the particle separation is increased.

Overall, however, the larger particles show stronger interactions, in terms of total magnitude, for all separations. On a per area basis, at small separations smaller particles are favoured, but at longer separation distances the larger particles once again show stronger interactions.

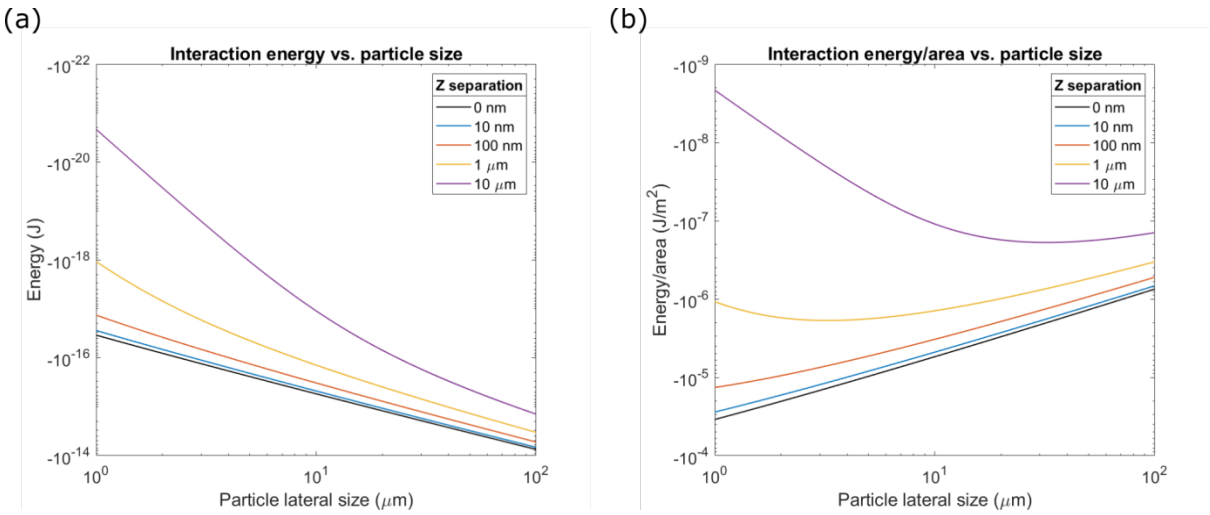

Figure 5.6 Particle interaction energy versus size
The (a) interaction energy and (b) interaction energy per area between two square prism particles with different sizes is shown. The calculation is made using the Rhodes-Rowlands interaction energy. The calculation was conducted using particles with a thickness of 10 nm and a square lateral area, where the side length of the square is defined by the 'Particle lateral size'. The particles were given a magnetization of 330 emu/cm^3 evenly distributed through the 10 nm thickness. Interaction energy calculations were conducted at various z separations (where z is perpendicular to the particle surface, parallel to the direction of the particle's PMA).

Particle interaction energy versus separation, shown in Figure 5.7 and Figure 5.8, tell a similar story of how these particles will interact. On an overall energy basis (Figure 5.7), the larger particles, with their greater moment, have a larger interaction energy, which should favour more effective assembly.

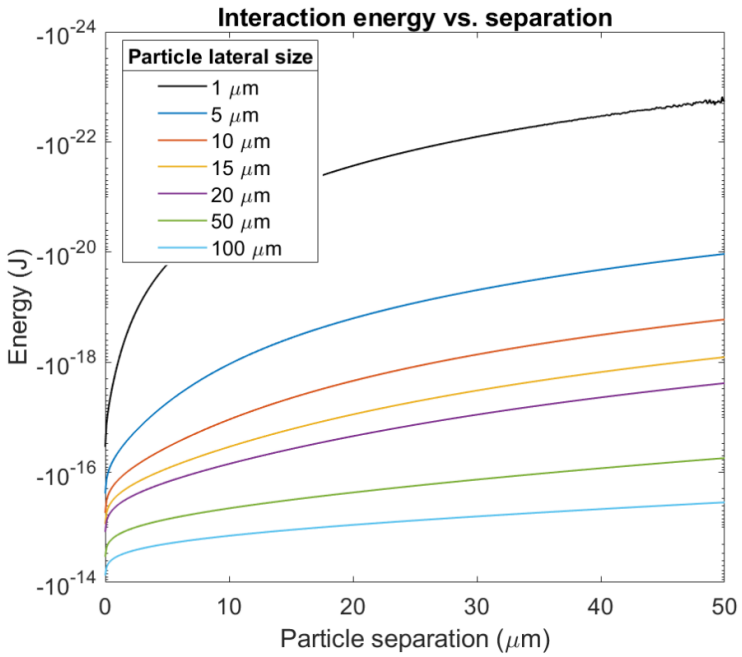

Figure 5.7 Interaction energy versus particle separation
The interaction energy is calculated versus the Z separation of two particles, for a number of different particle sizes (defined by the lateral size of the particle). The calculation is made using the Rhodes-Rowlands interaction energy. The particles were given a magnetization of 330 emu/cm^3 evenly distributed through the 10 nm thickness. This is presented for particles of lateral dimension 1, 5, 10, 15, 20, 50, and 100 µm, to cover the range of particle sizes which will be created and also give three orders of magnitude change in particle size. The particle separation is varied from 0 to 50 µm.

However, at small particle separations, the interaction energy per area is favoured for the smaller particles, although this quickly falls off as particle separation increases (Figure 5.8). At large separations, interaction energy per area favours the larger particles. It is only at the smallest separation distances that small particles dominated in terms of interaction energy per area. Since assembled particles will have a separation of zero, this stronger interaction could prove useful for sustaining assemblies with smaller particles.

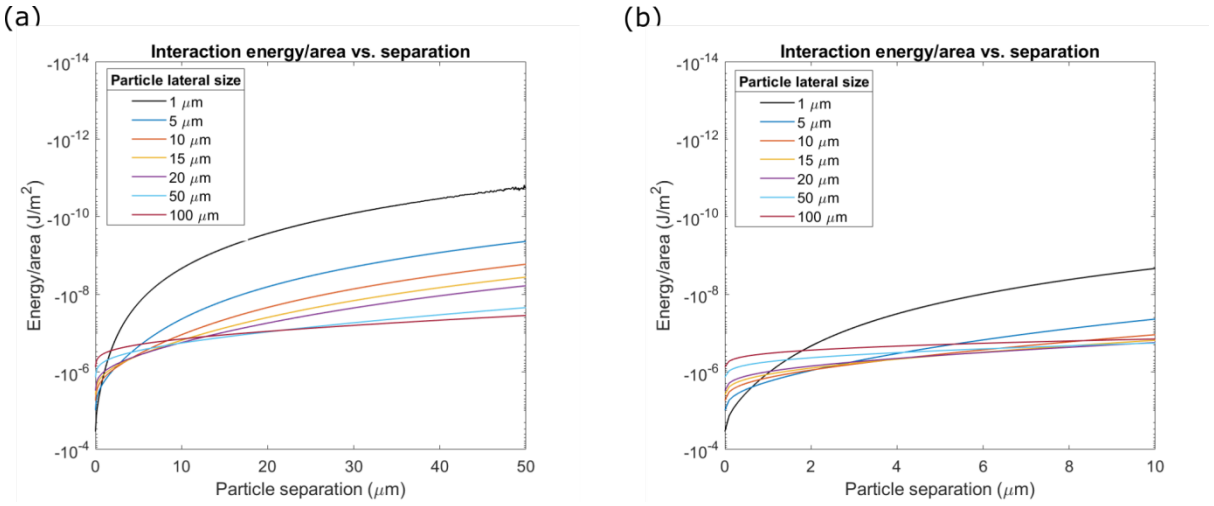

Figure 5.8 Interaction energy per area versus particle separation
The interaction energy per area is calculated versus the Z separation of two particles, for a number of different particle sizes (defined by the lateral size of the particle). The particles were given a magnetization of 330 emu/cm^3 evenly distributed through the 10 nm thickness. This is presented for (a) particles of lateral dimension 1, 5, 10, 15, 20, 50, and 100 µm, to cover the range of particle sizes which will be created and also give three orders of magnitude change in particle size, and is presented over a separation range of 0 to 50 µm. (b) shows the same particles over a separation of 0 to 10 µm.

The differences in total interaction energy and interaction energy per area can be explained well by looking at the stray field profiles of the magnetic particles. As mentioned previously, PMA materials have a unique stray field profile due to the high demagnetizing factor of the planar thin film. The demagnetizing factor varies the most at the edges and corners of the particles, where it deviates strongly from the infinite film approximation. Examples of this can be seen in the stray field profiles of a 1x1 µm square particles presented in Figure 5.9 (a) and (b).

Stray field of particles were calculated using the micromagnetics simulation program Mumax3. Cells of 0.1 µm x 0.1 µm x 5 nm were used for the calculations with the 1 x 1, 5 x 5, and 10 x 10 µm^2 particle, while cells of 0.1 µm x 0.1 µm x 10 nm were used for the larger 15 x 15 and 20 x 20 µm^2 particles, due to computational limits on the number of cells possible in the simulation box. While the larger cells will give a sparser view of the field profile, it should be sufficient for comparing the general trends of the field. In all cases the magnetic particle is taken to be a 10 nm thick particle with a uniaxial magnetization of 330 emu/cm^3 perpendicular to the plane of the particle, to get the field profile at the surface of one of the multilayers of the 'sandwich' particle.

Because the greatest sources of stray field in these particles come from the edges, and as particles grow, the edge length grows with linearly lateral size while the area grows with its square, the average stray field across the particle will decrease in the near-field regime at larger particle sizes. A full comparison of the average stray field in the perpendicular direction, Bz, from particles of different sizes is shown in Figure 5.9 (c). At short distances, smaller particles have a much stronger average stray field compared to larger particles. However, beyond a distance of about 600 – 800 nm

from the particle surface, the field from the smaller particles drops below that of the larger particles. We can consider this the transition from the near-field regime, where the average stray field is governed by the specific demagnetizing state of the particle, to the far-field regime, where a dipole-like view of stray field will depend entirely on the moment of the particle, which favours the larger particles. Comparison between Figure 5.9 (c) and Figure 5.8 (b) clearly demonstrates that the stray field profile of the particle is responsible for the dependence of the interaction energy per area. The two graphs show similar (though inverted) character, including similar intersections between the curves for particles of different size. With this additional information, we can understand why larger particles have stronger interactions on an absolute basis, but in the near-field regime, smaller particles interact much more strongly on a per area basis.

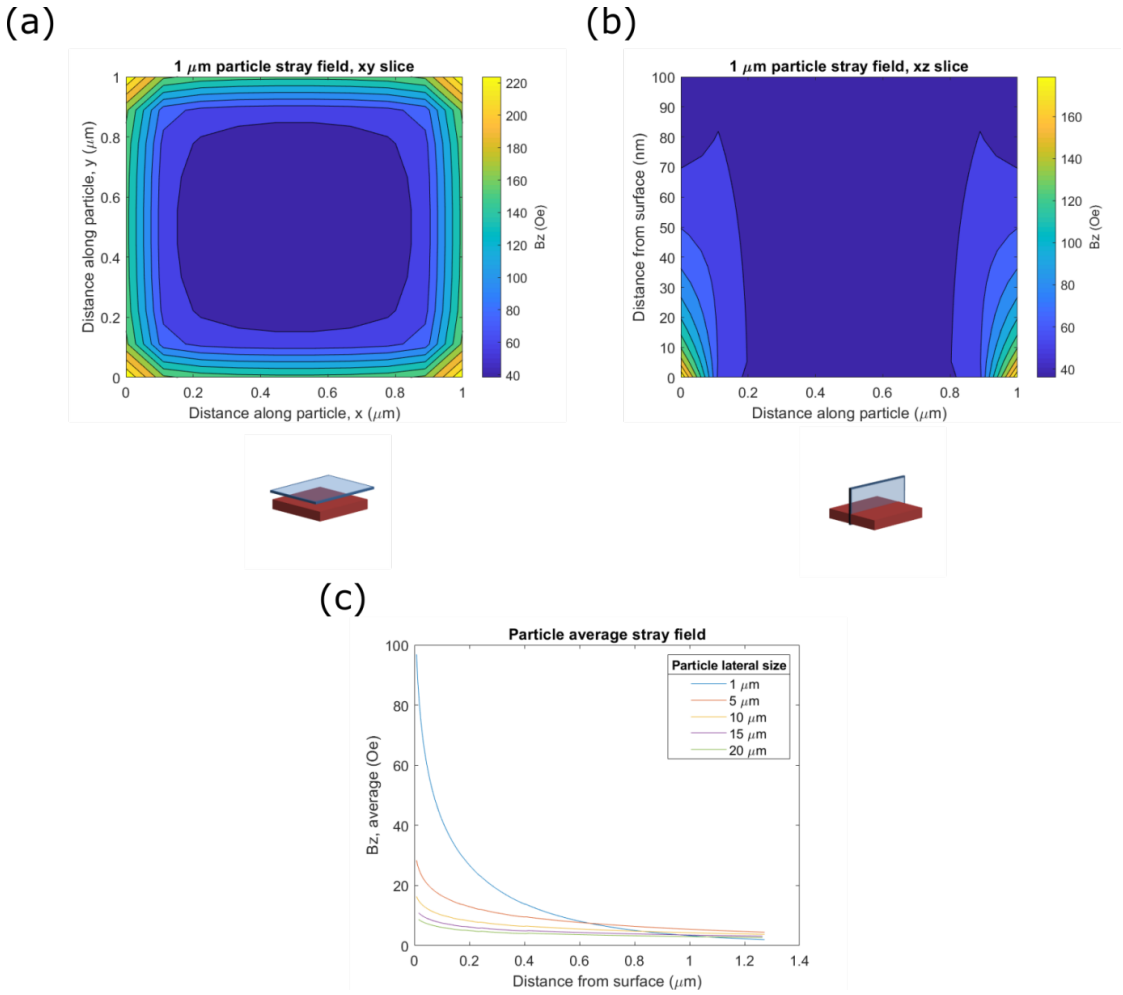

Figure 5.9 Stray field profile of magnetic particles
The stray field profile of magnetic particles of different size were calculated using MuMax3. All particles were 10 nm thick with a magnetization of 330 emu/cm^3. The stray field profile of a 1 μm particle is shown from (a) above the particle at a height of 10 nm from the surface and (b) from a side view of the particle. Diagrams below (a) and (b) show the location of the field plot relative to the particle. (c) shows the average stray field Bz at distance from the particle surface for particles with different lateral sizes.

The interaction energy per area is favoured in the near-field regime for smaller particles, which shows these particles should have a stronger driving force for assembly relative to their size and mass at short separations and stronger binding energy between two particles relative to their size and mass when they are in contact.

However, most interactions between particles will occur in the far-field regime, which is much more dependent on the overall moment of the particles. Anecdotally, the experimental assembly of 20 x 20 μm^2 particles occurred quickly compared to the other particle sizes (Figure 5.3, Figure 5.4), but was unable to proceed without additional outside agitation. In theory these far field interactions should favour the larger particles, both on an absolute and per area basis, which supports the quicker assembly quoted above. To understand why the larger particles cannot complete the assembly process, we analysed the drag and frictional forces felt by the particles.

In order to understand the drag forces on the particles in water, we can use a form of Stokes' drag to find the fluid forces resisting particle motion. Our particles, due to their small size, have a small Reynold's number, as is true of many systems at the micron length scale.[41] For small particles with a low Reynold's number, inertial forces can be discounted, allowing the Navier-Stokes equation to be solved in the viscous limit. Stokes' law is the solution for a low Reynold's number spherical particle, but also a solution can also found for a circular plate, which mimics the shape of our particles and their interaction. The drag force acting on a circular plate is defined in *Eq. 5-1*.[42]

$$F_d = 16vr\eta \qquad \textit{Eq. 5-1}$$

F_d is the drag force, v is fluid velocity, r is particle radius, and η is the fluid viscosity. Using this equation, the drag force on the particles can be calculated. This was done by taking particles at a set separation and calculating the magnetic interaction forces between the particles. Then, assuming the particles start at zero velocity, that interaction force can be used to calculate the acceleration of the particle, taking the particle volume and assuming a density of 18 g/cm^3, which was calculated as a weighted average of the various elements in the metallic particles. We assume constant acceleration of the particles under the interaction force, and, with a step size of 10 nm, calculate the particle velocity after that acceleration step. This velocity can then be substituted into the drag force equation, along with the particle lateral size as radius and a viscosity of 8.9 x 10^{-4} Pa • s, which is the viscosity of water.

The magnetic interaction force perpendicular to the particle (Force in z-direction) for various particle sizes and separation are listed below in Figure 5.10 (a), and the drag forces calculated from those interaction forces are listed in (b). The drag forces are roughly an order of magnitude lower than the magnetic interaction forces, which is reasonable, as the drag forces obviously do not prevent smaller particles from moving and interacting, as seen experimentally above. To see how the interaction force and drag force scale with increasing particle size, the two forces (normalized) are

compared for particles with 10 µm of separation. Figure 5.10 (c) details this comparison, showing that the drag force initially grows at a faster rate with increasing particle size, but then the rate of growth slows and becomes less than that of the interaction force, as can be seen by comparison of the slopes in the normalized forces. Finally, by equating the drag force (*Eq. 5-1*) and the interaction force, a terminal velocity can be found for each particle size, which is shown in Figure 5.10 (d).

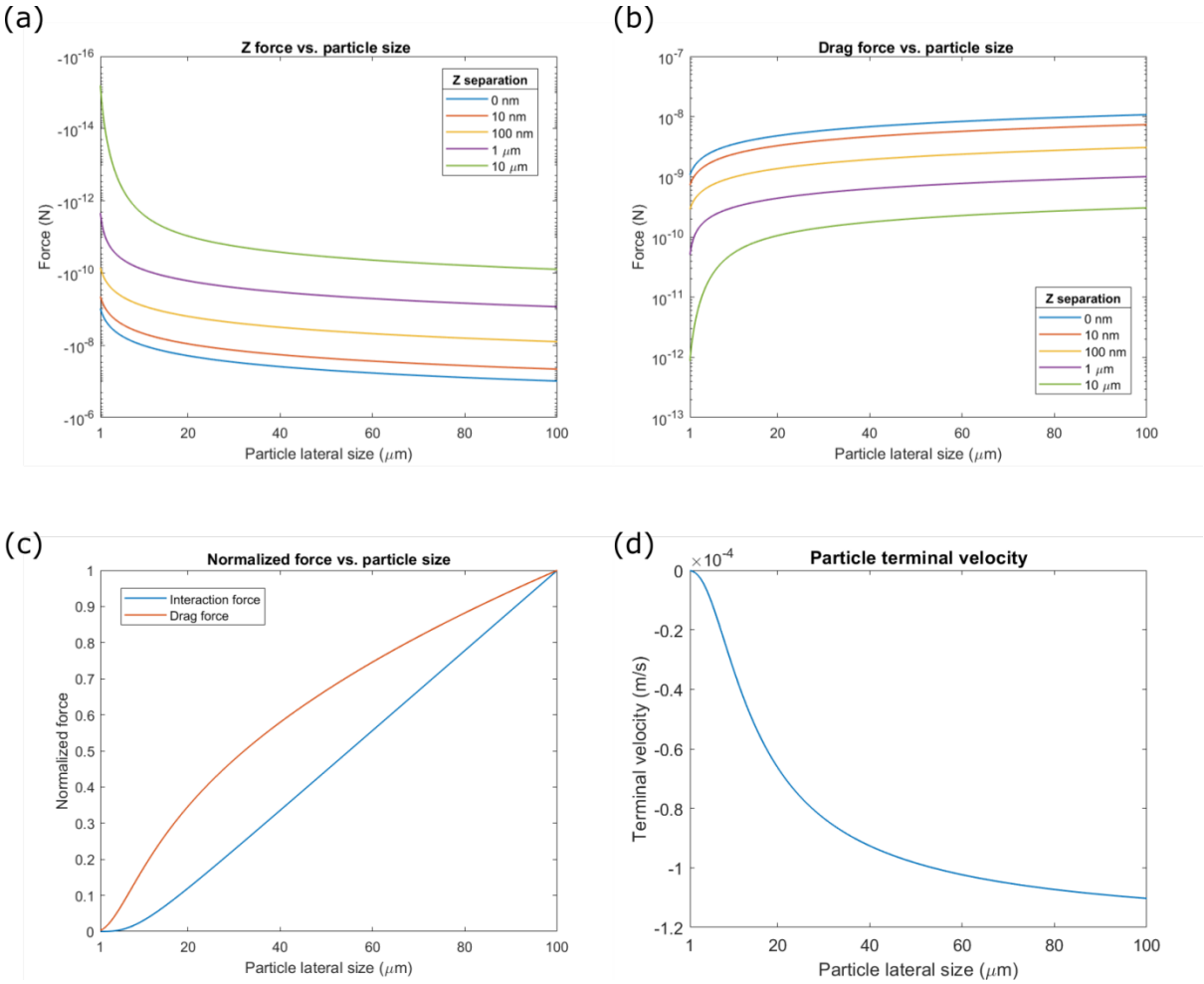

Figure 5.10 Comparison of interaction and drag forces for different particle sizes
(a) Interaction and (b) drag forces are given for a number of particle separations over a range of lateral sizes. The drag force is calculated used a modified Stoke's drag equation. (c) compares the normalized interaction and drag force for particle with a separation of 10 µm. (d) shows the terminal velocity of particles at 10 µm separation, found by equating the interaction and drag forces.

Similar to the energy calculations seen above, larger particles are favoured in this comparison. The larger particles reach a larger terminal velocity, as the increasing drag force is overwhelmed by the increase in magnetic interaction force. Clearly the drag force will play a role in governing and modifying particle interactions, but it does not account for the lack of assembly seen experimentally in larger particles.

After accounting for drag force, which covers the frictional forces between particles and the liquid, we can also look at the frictional forces between the particles and the silicon substrate on which experiments are occurring. As mentioned previously, these particles are not colloidal and will settle onto the substrate. Larger particles will settle more quickly, as the balance between gravitational forces and fluid drag will also favour a higher terminal settling velocity. Since the 15 x 15 and 20 x 20 μm^2 particles were seen to completely stop, and need high energy inputs to come unstuck, we calculate a static frictional force to compare with the magnetic interaction force. The static frictional force is defined by *Eq. 5-2*.

$$F_{max} = \mu_s F_n \qquad \textit{Eq. 5-2}$$

F_{max} is the maximum static frictional force, μ_s is the coefficient of static friction, and F_n is the normal force, which will be provided by gravity. The normal force is calculated using the particle volume, a density of 18 g/cm^3, and gravitational acceleration of 9.81 m/s^2. Static friction is a threshold force, so a force equal or greater than F_{max} must be applied to the sample to overcome it. Figure 5.11 plots the maximum static frictional force for μ_s of 1, 2, and 3 alongside the absolute value of the magnetic interaction force. It is extremely difficult to precisely define the coefficient of friction for this specific situation, as the coefficient varies with materials, lubrication, and the magnitude of normal force being applied. We can approximate values by looking at experimental studies and simulations of friction coefficients for microparticles, along with examples of bulk friction analysis on materials of interest. Studies of silica microparticle find a coefficient of about 1, while the coefficients of friction on a number of different silicon/silicon and silicon/polymer microstructure interfaces were found to range from 0.01 – 7.8.[43,44] Additionally, tests on bulk interfaces of silicon and Al at low (macroscopic) loads found coefficients in the range of 0.1 – 3.[45] By calculating the maximum static frictional force with a number of coefficients in this range ($\mu_s = 1, 2, 3$) we can see how the frictional and magnetic interaction force balances.

(a)

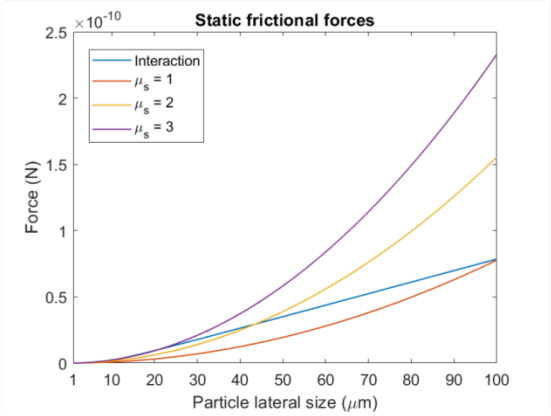

(b)

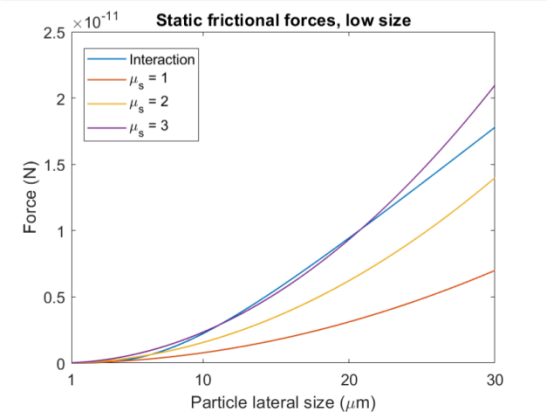

Figure 5.11 Static frictional forces versus particle size
The static frictional force, based on the normal force from the particles under gravity and the coefficient of static friction μ_s, is compared with the interaction force between magnetic particles. The absolute value of the interaction force is given. The interaction force was calculated over a range of particle sizes for a separation of 10 µm. It is compared with the maximum static frictional force for μ_s of 1, 2, and 3. (a) shows the full range of particle lateral size from 1 – 100 µm, while (b) shows the range of interest between 1 – 30 µm.

Figure 5.11 lays out the frictional force at these three coefficients of friction, compared with the absolute value of the magnetic interaction force. Figure 5.11 (a) compares the forces over a lateral size range of 1 – 100 µm, while (b) focuses on the range of interest, from lateral size of 1 – 30 µm. As can be seen in Figure 5.11 (b), for $\mu_s = 3$, the frictional force dominates the interaction forces except in the size range of 10 to 20 µm. While this does not match exactly with our experimental results, it shows that we can have small regions where the interaction force can overcome the frictional force and prevent particles from sticking, but as particle size increases, the static friction begins to dominate. Additionally, the real system will likely have a non-constant coefficient of friction that depends on the normal force, specific interaction conditions, and other complexities. Strong static frictional forces on larger particles offers a reasonable explanation for why the 15 x 15 and 20 x 20 μm^2 particles are impeded during the interaction process, while smaller particles have a larger enough interaction force, relative to their static friction, to allow assembly to proceed.

By using experimental observations of pair-wise particle interactions, in conjunction with calculations of the particle interaction energies and frictional forces, we can come to a more complete understanding of how these particles interact. At long distances, larger particles, with larger magnetic moments, see stronger interactions. However, due to their greater mass, these large particles are impeded from assembling by frictional forces. Only particles with a lateral size of 10 µm or smaller were seen to assemble without external energy input. Additionally, these smaller particles will show stronger interaction energy per area (and mass) when in contact, due to their stronger average stray field in this regime. Thus, these <10 µm particles will be able to better sustain assemblies and not be easily dis-assembled. Because of these reasons, we will focus on particles with lateral dimensions of 5

and 10 μm for investigating the particle responses to external field (5.4) and particle assemblies (Chapter 6).

5.4 Particle response to an applied field

The response of individual particles to an external applied field is important to understand, so particles can be manipulated and activated in a controlled manner. In this section we will look, both theoretically and experimentally, at how the two different particle types respond to an external magnetic field. First, we will look at the single multilayer particle, where the particle is composed of a structural buffer and one magnetic multilayer, with a layer structure {Au(20)/ Ta(2)/ Pt(2)/[CoFeB(0.55)/ Pt(0.86)]$_4$/ CoFeB(0.55)/ Pt(2)}. Second, we will analyse the behaviour of the 'sandwich' type particle containing two magnetic multilayers {Ta(2)/ Pt(2)/ [CoFeB(0.55)/ Pt(0.86)]$_4$/ CoFeB(0.55)/ Pt(2)/ Au(20)/ Ta(2)/ Pt(2)/[CoFeB(0.55)/ Pt(0.86)]$_4$/ CoFeB(0.55)/ Pt(2)}. The 'sandwich' particle is especially interesting because it can exist in two states: fully remanent (saturated) with moments parallel and zero remanence with moments anti-parallel. The fully remanent state is essentially identical to the single multilayer particle, as both can be approximated as a fully remanent macrospin, albeit with different total moments.

Understanding the response of the zero remanence, anti-parallel 'sandwich' particles is crucial to take advantage of the zero remanence state in this self-assembly context, as the particle must be able to irreversibly switch to a fully remanent, parallel state in liquid in a controllable manner. A useful analogue to this situation exists in literature, where synthetic anti-ferromagnetic (SAF) particles with PMA were created in liquid and showed a series of unique magneto-mechanical transitions in liquid depending on the field strength and particle composition.[19,20] In these magneto-mechanical transitions, the particle changes is orientation versus the applied field to minimize its energy. In our case, the two layers of the 'sandwich' particle do not have interlayer coupling like the SAF particles, but based on the example of the SAF transitions, we do not expect the anti-parallel 'sandwich' particle to simply switch to a parallel remanent state at field values equal to the particle coercivity. For this reason, it is important to probe the energy states of the particle under an applied field, to determine how and at what field values the particle will be able to switch to a parallel remnant state.

To undertake the theoretical analysis of the particle response, we will use a Stoner-Wohlfarth type model of the energy of the particle.[46] This zero temperature macrospin model will calculate the Zeeman and anisotropy energies of the particle under an applied field. This will give the total energy of the particle in the field, and we can use the expression to then minimize this energy and find the preferred state of the particle. The total energy can be calculated for both a particle with a single

multilayer (E_{SM}, *Eq. 5-3*) and a 'sandwich' type particle (E_{SD}, *Eq. 5-4*). The equations, the basis for which was discussed previously in Chapter 2, are shown below:

$$E_{SM} = -MVHcos(\alpha - \theta_1) + K_{eff}\, V \sin^2(\theta_1) \qquad \textit{Eq. 5-3}$$

$$\begin{aligned} E_{SD} = &-M_1VHcos(\alpha - \theta_1) + K_{eff,1}\, V \sin^2(\theta_1) \\ &- M_2VHcos(\alpha - \theta_2) \\ &+ K_{eff,2}\, V \sin^2(\theta_2) \end{aligned} \qquad \textit{Eq. 5-4}$$

In *Eq. 5-3*, the first term is the Zeeman energy and the second the anisotropy energy. For *Eq. 5-4*, the Zeeman energy is given by the first and third terms, while the anisotropy energy is calculated from the second and fourth terms. The 'sandwich' particle has two separate magnetic layers, which is the reason for the additional energy terms. M_n is the magnetization of magnetic layer n while $K_{eff,\,n}$ is the anisotropy constant of layer n. H is the applied field and V is the volume of the magnetic layer. In this section, the layer will be taken to be 5 µm x 5 µm x 10 nm, with a magnetization of 330 emu/cm^3, to give an equivalent moment to the real multilayer structure. The hard axis saturation field is taken as H_k = 5500 Oe, found from measurements of a patterned multilayer sample (Chapter 4, Table 1), and used to find the anisotropy constant through the relationship $K_{eff} = \frac{H_k M_s}{2}$. The angles referenced in the equations can be found in Figure 5.12, which shows the relationship between easy axis, applied field, and the magnetic moments of the particle. In our model, we will keep the particle stable and change the angle of the applied field. In reality, the particles are subjected to a linear field, and the particle will rotate to align itself in its lowest energy configuration in this linear field. Thus, the value α can be used to define the change in the particle easy axis direction against the static field.

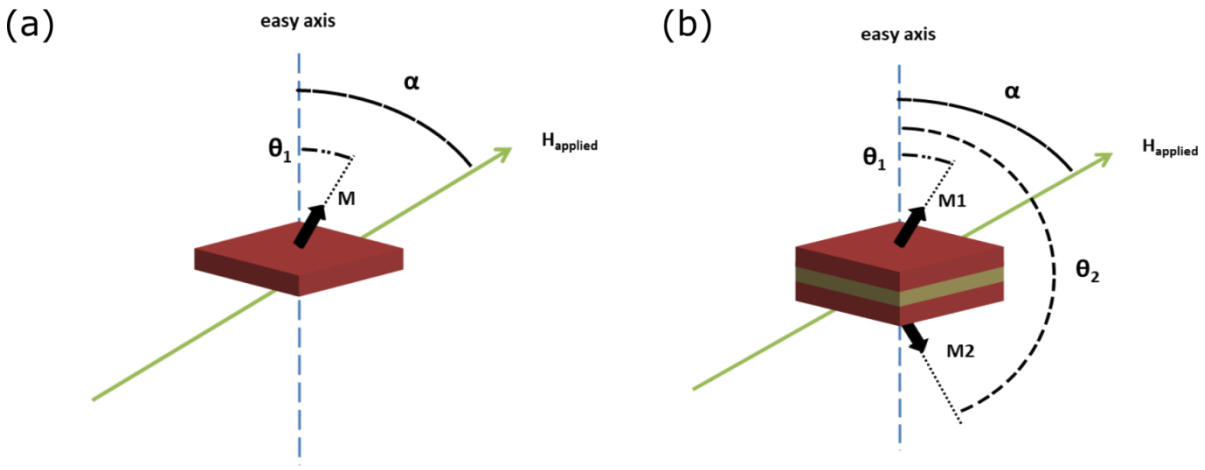

Figure 5.12 Geometry of particle energy calculations
The different geometries used for calculations of the energy state of the particles are shown, where (a) corresponds to the single multilayer particle E_{SM} and (b) to the 'sandwich' particle E_{SD}.

Using this model, we can calculate and probe the energy states of different particle configurations and alignments to find the lowest energy state. We can then investigate if this state is achievable by the particle. Since the particles in liquid are free to rotate, and can do so easily, the particle will tend toward the lowest energy state, unless that state is inaccessible due to the magnetic configuration of the particle. We will also be able to better understand how the particle can switch from the anti-parallel to parallel state under this framework.

We will first approach the case of the remanent (parallel)/single multilayer particle, which has a very simple field response. Then, building on the principles and methods established in this initial analysis, we will investigate the response of the zero remanence (anti-parallel) 'sandwich' particle. Along with the field response, we will also study the mechanism by which the particle switches from the anti-parallel to parallel state.

5.4.1 Fully remanent/single multilayer particles

The initial case we will analyse is that of the fully remanent/single multilayer particle. This case is fairly trivial, as we expect the strongly anisotropic and remanent particles to align their moments with any applied field and follow the field direction as it changes. As long as the particle is strongly anisotropic, it is much more favourable to rotate the particle in the liquid instead of rotating the moment of the particle, which would incur high anisotropy penalties. Thus, by finding the lowest energy state of the magnetic particle in an applied field, we can find the way in which the particle will align itself to the applied field, since the particle is able to rotate to reach this energy minimum. To begin, we will apply *Eq. 5-3* to calculate this lowest energy state, and then compare this result to experimental observations.

Energy calculation

For the fully remanent/single multilayer particle, there are two energetic extremes that we can consider to understand the overall energy state of the particle: when the applied field angle $\alpha = 0$ and when $\alpha = {}^{\pi}/_{2}$. These correspond to the field aligned along the easy and hard axis of the particle. By taking the derivative of the single layer energy equation *Eq. 5-3* at these values, we can identify the maxima and minima for these states to then find the lowest energy state of each configuration. *Eq. 5-5* and *Eq.5-6* show this process and the solutions for each state. By testing the solutions numerically, we find that the minimum energy state for $\alpha = 0$ is $\theta_1 = 0,\ \pi$ and for $\alpha = {}^{\pi}/_{2}$ is $\theta_1 = \sin^{-1}({}^{-H}/_{H_k})$ until the point at which $H = H_k$, where $\theta_1 = {}^{\pi}/_{2}, {}^{3\pi}/_{2}$ become the minima of the system.

$$\boldsymbol{\alpha = 0}$$

$$E_{SM} = -MVH\cos(\theta_1) + K_{eff}\, V \sin^2(\theta_1)$$

$$\frac{dE}{d\theta_1} = 0 = \sin(\theta_1)[MVH + 2K_{eff}\, V\cos(\theta_1)] \qquad \textit{Eq. 5-5}$$

$$\theta_1 = 0, \pi \qquad\qquad \theta_1 = \cos^{-1}({}^{-H}/_{H_k})$$

$$\boldsymbol{\alpha = {}^{\pi}/_{2}}$$

$$E_{SM} = -MVH\sin(\theta_1) + K_{eff}\, V \sin^2(\theta_1)$$

$$\frac{dE}{d\theta_1} = 0 = \cos(\theta_1)[-MVH + 2K_{eff}\, V\sin(\theta_1)] \qquad \textit{Eq.5-6}$$

$$\theta_1 = {}^{\pi}/_{2}, {}^{3\pi}/_{2} \qquad\qquad \theta_1 = \sin^{-1}({}^{-H}/_{H_k})$$

We can now find the energy minima over a range of applied field values for each α conditions, which is presented in Figure 5.13. If the applied field is aligned with both the magnetic moment and the easy axis of the particle, the energy state will be at a global minimum, as Zeeman energy is maximized and anisotropy energy is minimized (to zero). This is the case in Figure 5.13 (i) and shown by the blue curve on the energy calculation. The other energy extremum (Figure 5.13 , ii) is to have an applied field aligned 90° to the easy axis. In this case the moment will cant toward the applied field, in order to gain Zeeman energy at the expense of anisotropy energy. It will only be able to maximize Zeeman energy at an applied field equal to the hard axis saturation field (5500 Oe for

this model), and, because of the higher anisotropy energy, this state will never be as low energy as Figure 5.13 (i). Any intermediate angle of the applied field relative to the easy axis will fall between the two energy curves shown. Clearly, the lowest energy state will always be found by aligning the particle easy axis with the applied field (Figure 5.13, blue curve), allowing the moment to stay aligned with the easy axis while maximized Zeeman energy.

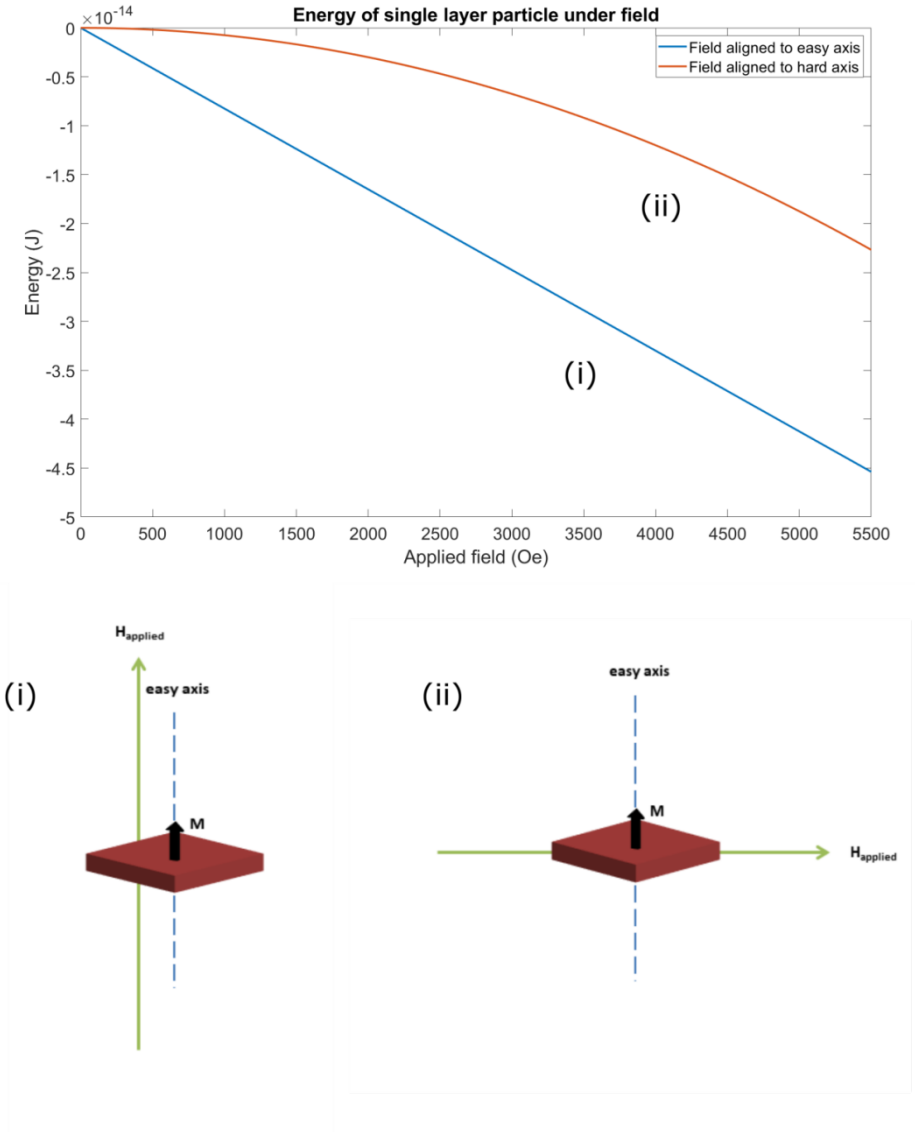

Figure 5.13 Energy of single multilayer particle in an external magnetic field
The energy of a single multilayer particle in an external magnetic field is calculated. This energy calculation combines Zeeman and anisotropy energy in the model previously described. The two extremes of the field perfectly aligned along the easy axis (i) and along the hard axis (ii) are shown schematically, and the energy values over a field range of 5500 Oe are calculated.

Given the particle is free to rotate in liquid, the minimum energy state can always be achieved in this particle type. Thus, we expect the fully remanent/single multilayer particle to always align its easy axis to the direction of the applied field.

Experimental response

We can experimentally confirm our calculation by applying a linearly oscillating field to a set of fully remanent particles. Figure 5.14 shows a series of fully remanent particles in an oscillating magnetic field of 50 Oe amplitude and 1 Hz frequency. As the field is reversed, the particles rotate to retain alignment with the field. This can be seen in the top particle of the images, where the change of particle alignment can be seen due to the slight curvature of the particle.

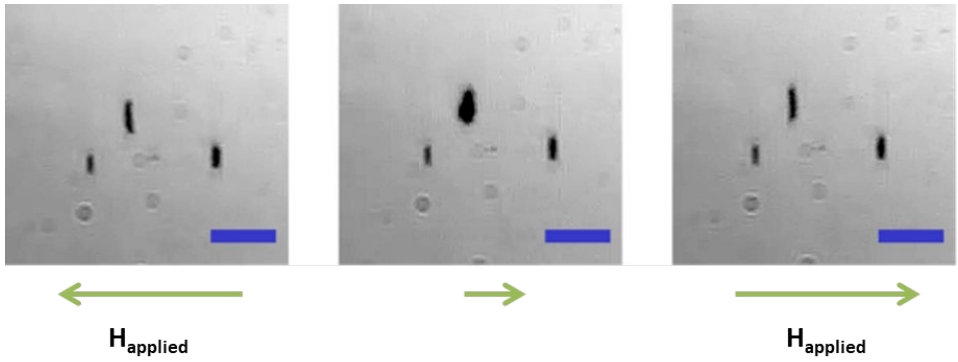

Figure 5.14 Response of a single multilayer particle in an alternating magnetic field
Particles with a single magnetic multilayer and lateral dimensions of 10 x 5 μm^2 were subjected to an alternating linear magnetic field of 50 Oe, 1 Hz. The response of the particles to the field is shown. The field direction changes (left image vs right image), and the particle flip to match the magnetization to the field direction is captured in the middle image. The blue scale bar correspond to 20 µm.

This is quite a simple result, but does confirm both the usefulness of our model and also establishes a baseline for the simplest behaviour of the magnetic particles under an applied field. This case covers both single multilayer particles and 'sandwich' type particles that are fully remanent, with both moments aligned parallel. Next, we will address the case of the zero remanence (anti-parallel) 'sandwich' particle, which shows a much more complex, and thus, interesting, field response.

5.4.2 Anti-parallel particles

When the 'sandwich' particle type is set to a zero remanence state, it has anti-parallel moments in the two magnetic layers and resembles a SAF, with the notable absence of any anti-ferromagnetic coupling between the two magnetic layers. SAF particles have been shown to have a series of unique transitions under an applied field in liquid.[19] As a field is applied in liquid, the

moments cant into the plane of the particle, aligning the plane of the particle to the field. Then, the particle saturates to a parallel state, aligning the surface normal to the field, analogous to the state just explored for fully remanent particles above. Additionally, if there are any moment imbalances between the two magnetic layers, the particles are ferrimagnets. In a liquid suspension, these ferrimagnetic particles align the surface normal of the thicker magnetic layer to the applied field at very low applied field magnitudes. As the field is increased, the particles show canting of the moments that align the plane of the particle to the field. However, due to the moment imbalance of the ferrimagnet, the plane of the particle is not perfectly aligned to the applied field, but slightly tilted. This is because it is more favourable to align the applied field with the larger moment. Full explorations of the phenomenon in SAF/ferrimagnetic particles can be found in the excellent work of T. Vemulkar in references 19 and 20. [19,20]

Given the obvious similarities between SAF and ferrimagnetic particles and our anti-parallel 'sandwich' particles in the anti-parallel configuration, we expect to be able to mimic these transitions, and we will use our knowledge of this similar system to help evaluate our particles. However, because of the lack of interlayer coupling between the two magnetic multilayers in the 'sandwich' particle, we must treat the system as two independent ferromagnetic layers, each of which has non-zero remanence. While the behaviour of the 'sandwich' particles might match the SAF, this difference will influence how we analyse the energy and behaviour. One primary difference will be the way the particle switches to a saturated state. In the SAF particles this switch depends on the anisotropy and the coupling. With the lack of interlayer coupling in our particles, we expect the route to saturation to be different. While we hope to recover the transitions from the SAF model, the primary goal of the analysis of the anti-parallel 'sandwich' particle will be to understand when the particle will switch from the anti-parallel to parallel state, as this will be the key transition for triggering self-assembly with these particles.

We will begin with energy analysis of the various potential states of the anti-parallel particle under an applied magnetic field, using *Eq. 5-4*. Then, we will compare the theoretical calculations with experimental observations. We will then look specifically at the mechanisms by which the real particle switches to the parallel state from the anti-parallel state.

Energy calculations

The energy calculations for the various states of the anti-parallel 'sandwich' particle proceed using the equation outlined in *Eq. 5-4*, which contains the Zeeman and anisotropy energies of both magnetic layers. The two magnetic layers can be treated independently, but must always be subject to the same field angle α, given that the two magnetic layers are physically connected. The moments of each layer are uncoupled, and can thus rotate independently under an applied field, requiring two angles θ_1 and θ_2 to define the orientation with respect to the particle normal, as outlined in Figure

5.12 (b). While in the fully remanent case we only analysed the two extrema of the particle's energy state, in this analysis it is important to understand the entire energy landscape, as we cannot guarantee the particle can always reach the global minimum. Additionally, we will conduct this full energy calculation for both a balanced particle and ferrimagnetic particles, where the magnetic moments of the two layers are not equal. Ferrimagnets will be described by their percent imbalance, which is equal to $100 * (1 - {M_{smaller}}/{M_{larger}})$. In all ferrimagnetic cases, M_2 taken as the smaller moment. In the energy calculations, we have ignored coupling for our particles. In reality, there is dipolar coupling between the layers of the anti-parallel particle with a coupling energy of the order of ~10^{-16} J (coupling field of ~20 Oe). This coupling energy (field) is two orders of magnitude lower than the energies (fields) involved in most of the calculation (Figure 5.15), especially at higher applied fields, which will be the area of interest for investigation of particle switching. However, at very low applied fields, the magnitude of the coupling becomes significant, and we acknowledge that this model will have uncertainty in predicting behaviour at very low fields for this reason.

To understand the entire energy landscape for the particle, we will establish three states. The first is the global minimum of the system (Figure 5.15, a, i), where the 'sandwich' particle has its moments parallel, along the easy axis and aligned with the applied field. This is the same as the energy minimum case established in 5.4.1. The second state will be the maximum state for all field values, where the field is aligned with the easy axis but the moments are in an anti-parallel configuration. This can be seen in Figure 5.15 (a, iii). As with the calculation for the fully remanent particle, these two states will represent the extrema of energy. Calculations of these extrema are presented as a function of applied field in Figure 5.15 (b) and (c), curves i and iii, for the case of a balanced and 5% imbalanced particle, respectively. However, since the particle begins with its moments anti-parallel, it cannot simply rotate to reach the global minimum, but must first switch to a parallel configuration. To find how and when this switching can occur, we have calculated the entire energy landscape for the anti-parallel particle, finding the energy minimum at each point. The configuration is displayed schematically in Figure 5.15 (a, ii). This full energy landscape calculation of the anti-parallel particle is done by varying the applied field at an angle $\alpha = 0 - 180°$ to the easy axis, with the moments in a globally anti-parallel state being able to rotate over a range of 90° from the easy axis (θ_1 = 0 - 90°, θ_2 = 90 - 180°). The moments are restricted to these angles so the calculation is restricted to the anti-parallel state. The angular steps of the moment and field angles are 0.1°. We will combine this calculation with the field angle and magnitude required for switching, to find how and when the particle will switch to a parallel state.

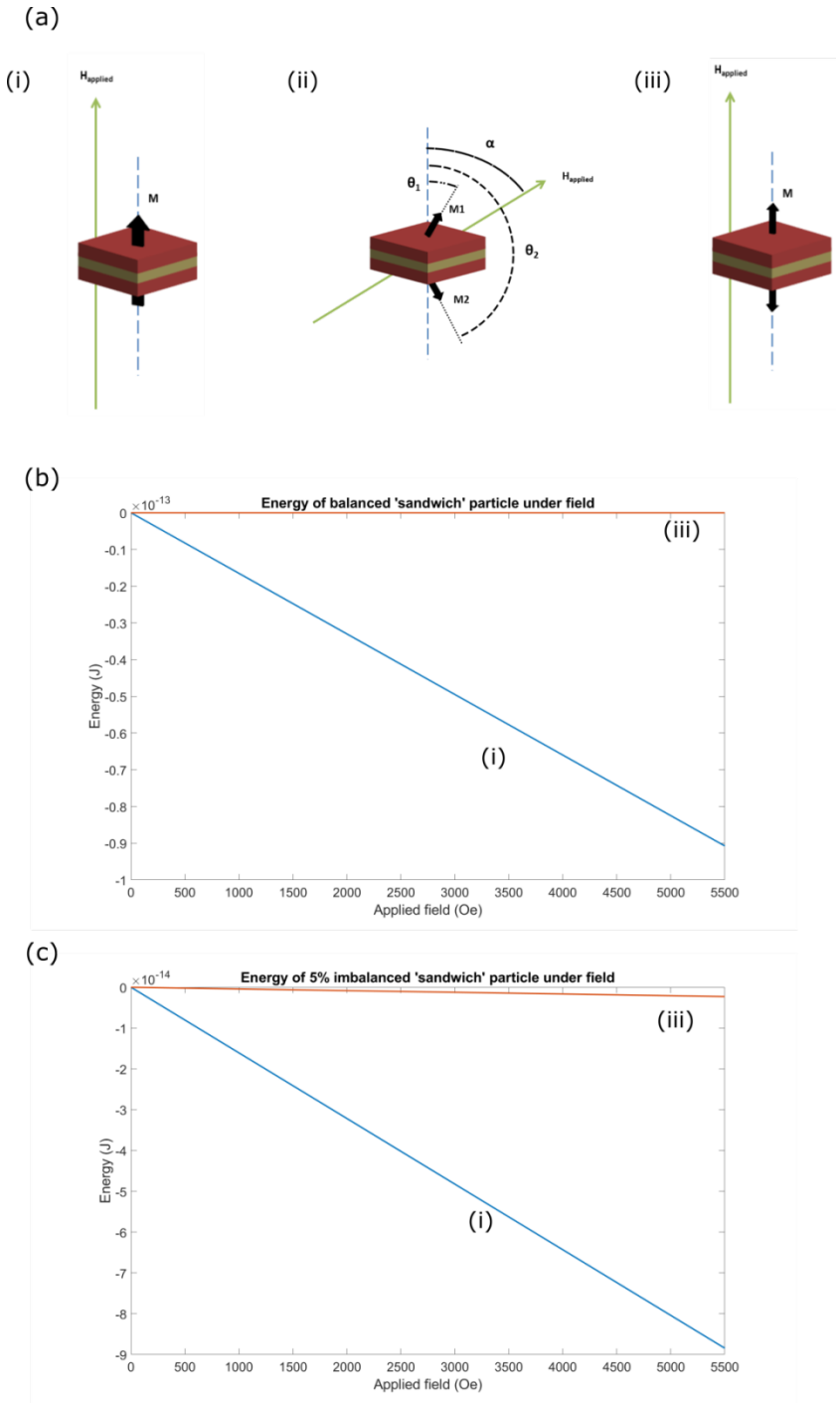

Figure 5.15 AP particle calculations and energy range
Three different states are used to analyse the energy of the AP particle, shown in (a): where the field is (i) aligned with the particle easy axis with the moments parallel, (ii) aligned in the plane of the particle with the moments anti-parallel, calculated over the full range of α, and (iii) aligned with the easy axis with the moments anti-parallel. Energy values for the two extreme cases, (i) and (iii), are shown for a balanced (b) and 5% imbalanced (c) particle.

For all three states (i, ii, iii) the energy is calculated over a field range of 0 – 5500 Oe in steps of 10 Oe. In the case of (i) and (iii), the calculation is straightforward, as the field and moment angles are prescribed. However, for case (ii), the energy is calculated for each field amplitude and each combination of values for both field and moment angles. Starting from this framework, we will

outline the process by which the energy of state (ii) is found, and then use it to determine at what field amplitudes particles will switch to a parallel state.

To undertake the calculation of energy for state (ii) (Figure 5.15, a, ii) and find how switching might occur, we can refer to the Stoner-Wohlfarth model. In order to reverse the magnetization of one of the magnetic layers, there must exist both a lower energy state and a path between the current state and the new minimum. That is, for this zero temperature model, there cannot exist an energy barrier between the two states. To begin, we will look at a single magnetic layer particle (Figure 5.16) that is fixed with respect to the applied field angle. The energy of the single layer particle is calculated as a function of the angle the magnetization makes with easy axis (θ_1, θ_2) for set applied field angles and magnitudes. While this plot only shows a single layer, our anti-parallel particle is made of two single identical and independent Stoner-Wohlfarth layers, one with starting magnetization angle $\theta_1 = 0°$ and the other with its magnetization angle $\theta_2 = 180°$. For a field angle of $\alpha = 0$ (Figure 5.16, a), the magnetization angles of the two layers will not shift, as their starting positions of $\theta_1 = 0°$ and $\theta_2 = 180°$ are minima. As the field increases, the $\theta_1 = 0°$ minima decreases while the minima at $\theta_2 = 180°$ increases, reflecting the fact that Zeeman favours the layer θ_1 which points in the direction of the applied field. This will persist until the field reaches a value of 5500 Oe, at which point the anti-parallel layer θ_2 can transition to the lower minima at $\theta = 0°$ and the particle is in the parallel state.

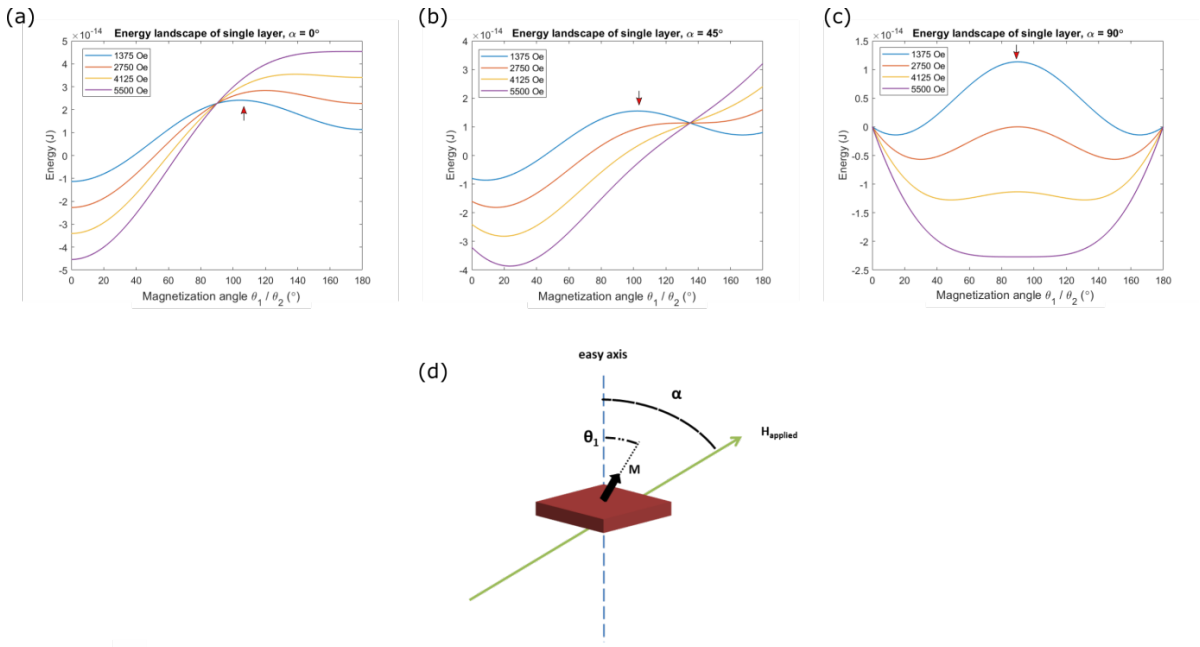

Figure 5.16 Stoner-Wohlfarth energy of single magnetic layer
The energy of a single magnetic layer is found for set field angles and a range of field values. The energy is calculated using *Eq. 5-3* over the full range of magnetization angles θ_1 for an applied field of (a) $\alpha = 0°$, (b) $\alpha = 45°$, and (c) $\alpha = 90°$ with field magnitudes of 1375, 2750, 4135, and 5500 Oe. (d) defines the angles of the field and magnetization used in the calculations. Red arrows indicate energy barriers between the two minima states.

The other two graphs in Figure 5.16 show the single layer with different field angles. They are illustrative of two points: first, there is initially (at low field magnitude) always an energy barrier between the two magnetization states; second, the point at which the barrier disappears and switching can occur is a function of field angle and magnitude. The minimum switching field is $H_k/2$, which is shown in Figure 5.16 (b) for $\alpha = 45°$ (in our case $H_k/2 = 2750$ Oe). Figure 5.16 (c) illustrates the special case for $\alpha = 90°$, where the energy barrier never disappears and switching does not occur. In this case, the Stoner-Wohlfarth layer saturates completely through coherent rotation of the moment.

Energy curves such as those shown in Figure 5.16 form the basis of our calculation of energy states for the anti-parallel particle. For each field angle and magnitude, the overall energy of the anti-parallel particle can be calculated by finding the minimum energy state for the magnetizations of the two layers, M_1 and M_2. Additionally, when the minimum energy state (in terms of magnetization angle θ_1 and θ_2) becomes equivalent for both particles under a field and angle conditions, we can know the particle has switched to a parallel state.

To help understand the combination of field angle and magnitude at which switching can occur, a Stoner-Wohlfarth astroid can be constructed.[47] The Stoner-Wohlfarth astroid plots a line of criticality versus the perpendicular and parallel field components of an applied field. The line of criticality is the locus of points at which the magnetization will reverse, jumping from one direction to

the other. It is the point at which there exists a lower minimum energy state and no barrier in moving to that state.[48] We have plotted a Stoner-Wohlfarth astroid from the equation $h_{\parallel_{sw}}{}^{2/3} + h_{\perp_{sw}}{}^{2/3} = 1$, where $h_{\parallel_{sw}}$ and $h_{\perp_{sw}}$ are the parallel and perpendicular switching field, respectively. The blue line in Figure 5.17 shows the result of this equation, plotting the critical line corresponding to the 0 - 90° applied field range for the Stoner-Wohlfarth layers in our anti-parallel particle. Curves are plotted representing applied field magnitudes of 1375 ($H_k/4$), 2750 ($H_k/2$), 4125($3H_k/4$, and 5500 (H_k) Oe, along with dotted lines denoting different angles. These can be used to help understand the switching fields and angles for different field magnitudes.

The Stoner-Wohlfarth astroid contains the same information that can be found in the magnetization angle versus energy curves in Figure 5.16, but the astroid shows the field angle and magnitude over which switching will occurs for the full range of field angle and magnitude (α = 0 - 90° and 0 – 5500 Oe) that will be addressed in energy calculation. We can see the correspondence between the two figures by comparing the case of α = 45° (Figure 5.16, b) with the astroid. In Figure 5.16 (b), once the field magnitude reaches a value of 2750 Oe (orange curve), the system only has one minimum (θ = 22°), and there is a path to this minimum from all other magnetization angles θ. Thus, any single layer particle in a field of magnitude 2750 Oe and α = 45° will reach the minimum at θ = 22°, regardless of its starting conditions. If a layer is anti-parallel to the field direction, it will switch to reach this state. Looking at the astroid, we can see that the curve corresponding to a field magnitude of 2750 Oe intersects the astroid at one point only, for a field angle α = 45°.

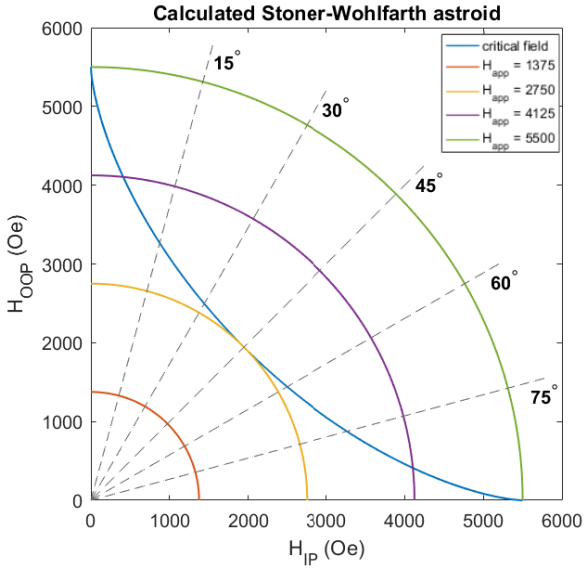

Figure 5.17 Calculated Stoner-Wohlfarth astroid for particle magnetic layer
A Stoner-Wohlfarth astroid was calculated for an applied field angle range of α = 0 - 90°. The critical field is shown along with applied fields over a range of magnitudes being applied over the full angular range of the astroid.

So far, we have established a method for calculating the equilibrium energy state of a Stoner-Wohlfarth single layer particle for a given field angle α and field magnitude.

Now, we will move on from the single layer particle and investigate the energy states of the two-layer, anti-parallel particle in different applied field angles and magnitudes. In this next calculation, the particle is still fixed as the field angle is rotated. Both layers are magnetically independent but are physically connected, so they must experience the same field angle α. The magnetization angles of the two layers M_1 and M_2 will be initially set to $\theta_1 = 0°$ and $\theta_2 = 180°$ to create the anti-parallel state. Using sets of curves such as those shown in Figure 5.16, the minimum energy of each layer for each specified field conditions is found. These energies are then summed to find the total energy of the particle and plotted in Figure 5.18 as a function of the field angle α. It is important to remember the particle remains fixed in this calculation, so the energies found can be thought of as a snapshot of the energy of the particle for the particular field conditions. It does not include any history of the particle's orientation or state besides the initial conditions spelled out above.

In Figure 5.18, the energy values are presented for a selection of applied field values (1375, 2750, 4125, and 5500 Oe) and over the full range of field angle α, for a balanced particle (Figure 5.18, a) and a 5% imbalanced particle (Figure 5.18, b). Figure 5.18 (c) provides a reminder of the geometry of the anti-parallel particle. If the field angle and magnitude is sufficient, the particle will switch to the parallel state. This can be seen in the discontinuous jumps of the energy curves. For example, we can connect the discontinuity at $\alpha = 45°$ for a field amplitude of 2750 Oe with our previous evaluation of this field and magnitude combination in Figure 5.16 (b) and Figure 5.17.

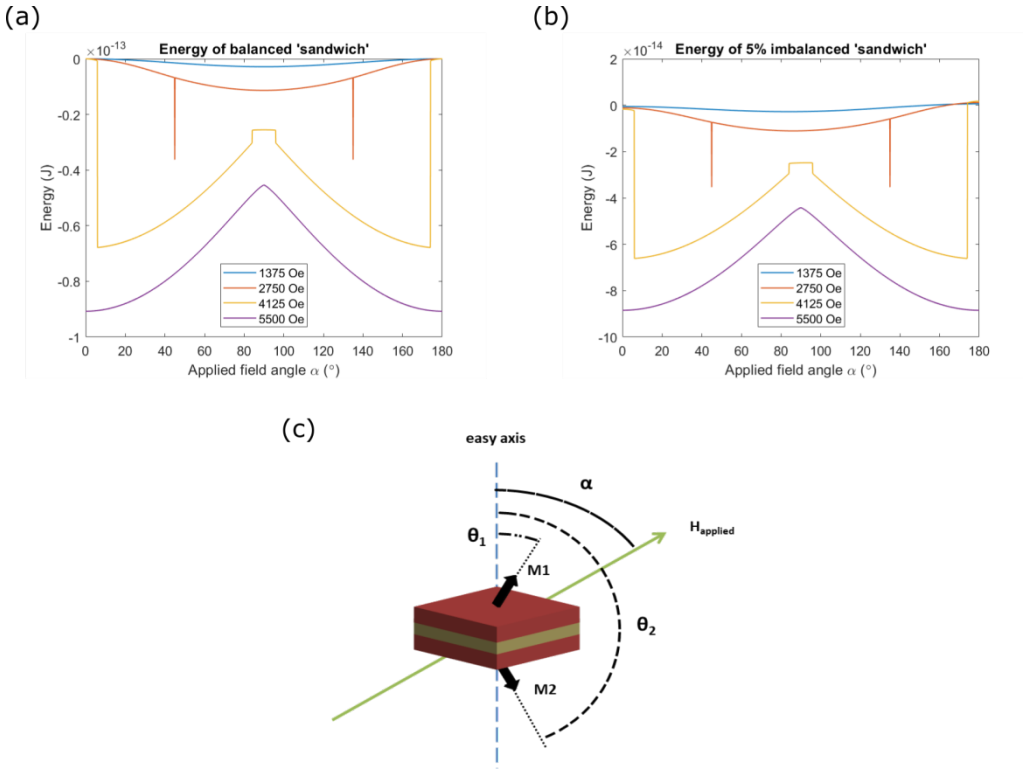

Figure 5.18 Energy minima at different applied field angles α
The energy minima over a range of applied field angles α are given for applied field values of 1375, 2750, 4125, and 5500 Oe. The plots are given for (a) balanced and (b) 5% imbalanced 'sandwich' particles. (c) gives the definition of the particle geometry and angles.

Using the energy values calculated in Figure 5.18, we can now move from a fixed particle to a particle in liquid. In liquid, the field is static, but the particle can rotate around this static field direction to further minimise their energy. The field angle α still defines the relationship between the field direction and the particle easy axis, but now the particle will rotate as α shifts. Using this framework, we can see how a particle will behave in a rising field.

We will first look at the case of a balanced particle (Figure 5.18, a). The particle starts at zero field and then experiences an increasing applied field. As the field increases, a single minimum develops at α = 90°, which can be seen on the blue curve corresponding to 1375 Oe. At this field magnitude, there is no possibility of switching (as confirmed in Figure 5.17), and the field is aligned with the plane of the particle. At 2750 Oe, α = 90° is still a minimum, although now it is only a local minimum, since two additional minima have emerged at α = 45° and 135°. However, there is no downward path between the minimum at 90° and these two new minima, so the particle remains at α = 90°. As the field continues to increase, a change of concavity at α = 90° occurs, evidenced by the energy curves at 4125 Oe and 5500 Oe. We can see in both cases that α = 90° has become a local maximum, and the particle will now shift its orientation to reach a new minimum. In both cases, the new minimum will be a switched, parallel particle. For instance, at a field amplitude of 4125 Oe, two

minima have developed at α = 6° or 174°. If, from the α = 90° configuration (where Figure 5.16 (c) tells us that for that amplitude, θ_1 and θ_2 are at ~45° and ~135° respectively), the particle starts rotating towards the minimum at α = 6°, then Figure 5.17 shows that for the layer with a magnetisation angle of 135°, the curve for the 4125 Oe field amplitude will immediately cross the astroid (as α reaches 84°), causing the layer to switch and placing the particle in a the parallel configuration. An equivalent scenario can be predicted if α increases toward the α = 174° minimum – in that case, it is the layer with a magnetisation angle of 45° which switches, also placing the particle in the parallel configuration. The same is true at 5500 Oe, where the particle will switch for all field angles except α = 90°.

For the previous switching scenario to occur, two conditions must be met: α = 90° must become a local maximum (causing the particle to rotate), and the field amplitude must be high enough that the switching astroid will be crossed upon rotating. The second condition is equivalent to a threshold field of $H_k/2$ (see the astroid in Figure 5.17). The first condition is met when the magnetization angle θ exceeds 45°. This is due to the $\sin^2\theta$ form of the anisotropy energy. The maximum rate of change of the $\sin^2\theta$ function occurs at θ = 45°. For this reason, at magnetization angles greater than 45°, it becomes more favourable to rotate away from this orientation, which reduces the angle of one moment while increasing the other, because the gain of reducing the magnetization angle in one layer exceeds the penalty of increasing it in the other layer. Thus, once the magnetization angle exceeds 45° ($\theta_1 > 45°$ and $\theta_2 < 135°$) for α = 90°, it becomes more favourable to shift to α = 89° (or 91°). For example, the gain in anisotropy energy of $\theta_1 = 46$ to $\theta_1 = 45°$ is greater than the anisotropy penalty incurred by shifting $\theta_2 = 134°$ to $\theta_2 = 133°$. Since the angle between the field and magnetization remains constant, the Zeeman energy does not change. We can find the field value at which the magnetization angle equals 45° by solving the derivative of the Stoner-Wohlfarth equation for the single layer (*Eq. 5-3*) and finding the equilibrium applied field value that leads to a magnetisation angle θ of 45°. Since α (90° for the balanced particle) and θ (45°) are known, the applied field H can be found. This can be done for each layer independently, as long as α is the same for both. By finding the equilibrium field value at which θ = 45°, the switching threshold field can be found. For a balanced particle, this threshold field will be $H = {H_k}/{\sqrt{2}}$, which is equal to 3889 Oe for an anisotropy field of 5500 Oe. Above this threshold field the condition for the astroid to be crossed upon rotating ($H > H_k/2$) is met and the particle will switch to the parallel configuration.

In this example, we have only considered the case of a balanced particle. For a ferrimagnetic particle (Figure 5.18, b) the pathway will proceed similar to the balanced particle. However, due to the asymmetry of the particle, the energy minimum at low fields will be slightly biased toward the larger moment. For the case of 5% imbalance, the energy minimum at low fields (1375 and 2750 Oe) is located at α = 85°. For a particle in liquid, this means the particle tilts its plane slightly away from

the applied field axis. Due to the difference in α, the switching threshold value will be lower for unbalanced particles, as less applied field is needed for the given field angle to reach the condition of θ > 45° in the particle.

From the energy versus applied field angle α plots in Figure 5.18, we were able to find the energy minimum for an anti-parallel particle for a given field magnitude. From this energy minimum, we can extract the orientation of the particle versus the applied field. Additionally, we can use this plot to determine when a particle will switch, by finding the field angle and magnitude at which the particle can access a minimum corresponding to a switched, parallel particle. By compiling and minimizing the plots in Figure 5.18, we can find the orientation and remanent (anti-parallel or parallel) state of the particle over the range of field magnitudes 0 – 5500 Oe. The results of this for a balanced, 1% imbalanced, and 5% imbalance particle are shown in Figure 5.19. This figure shows the equilibrium field and moment angles of the particles for the range of field magnitudes. Once the switching threshold is reached, we can also see that the particle in the parallel state will immediately align itself to the field direction, as we saw in the case of fully remanent particles. We can now see how the anti-parallel particle can switch and reach the global minimum established in Figure 5.15.

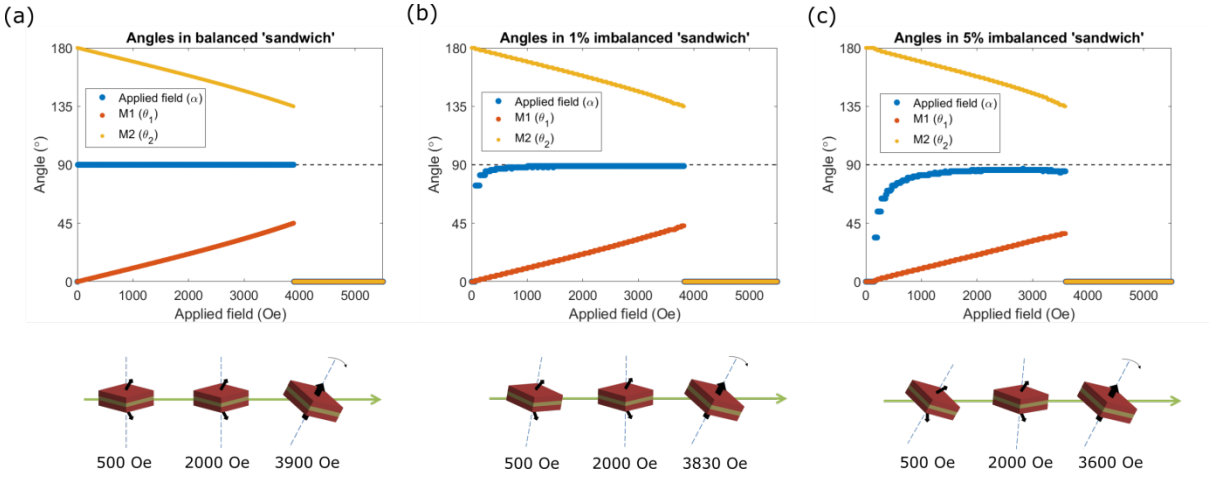

Figure 5.19 Moment and particle angle for anti-parallel configuration
The angles of moments of each layer and the applied field are given for the minimum energy state found in Figure 5.15 ii. The angles are given for a particle with (a) balanced moments, (b) 1% moment imbalance, and (c) 5% moment imbalance. Particle illustrations given below show the position of the particle versus the applied field at different field magnitudes. The arrow showing rotation of the parallel particle indicates the particle has reached the threshold for switching, and that the particle easy axis aligns to the external field immediately upon switching.

Figure 5.19 also gives useful information on the orientation of the particle for the balanced and imbalanced case. From the field angles we can see that the balanced particle (Figure 5.19, a) will always align the plane of the particle to the field, until it reaches a field at which switching occurs. However, for the unbalanced particles (Figure 5.19: b, c), we see that at very low fields, the particle

will actually orient its easy axis to the field. It should be noted that although we can identify this behaviour, the range of field over which it occurs should not be taken as accurate, due to the lack of coupling in this model, which would affect these low field states. We can also see that as the field increases, the unbalanced particle will align their hard plane to the field, but at a slight angle ($\alpha = 89°$ for 1% imbalance, 85° for 5% imbalance). From this information, we see that the Stoner-Wohlfarth particles are able to mimic the states found for SAF and coupled ferrimagnetic particles.

With the energy landscape of the particle fully calculated, we can now recreate Figure 5.15 for all three states (Figure 5.15 (a), Figure 5.20 (a)) in Figure 5.20. The anti-parallel particle will start along the meta-stable energy state found in Figure 5.20 (a, ii) and (b, ii). As the field increases, the particle will eventually reach a switching field, at which point it will switch to a parallel state and then align itself to the applied field, reaching a global minimum.

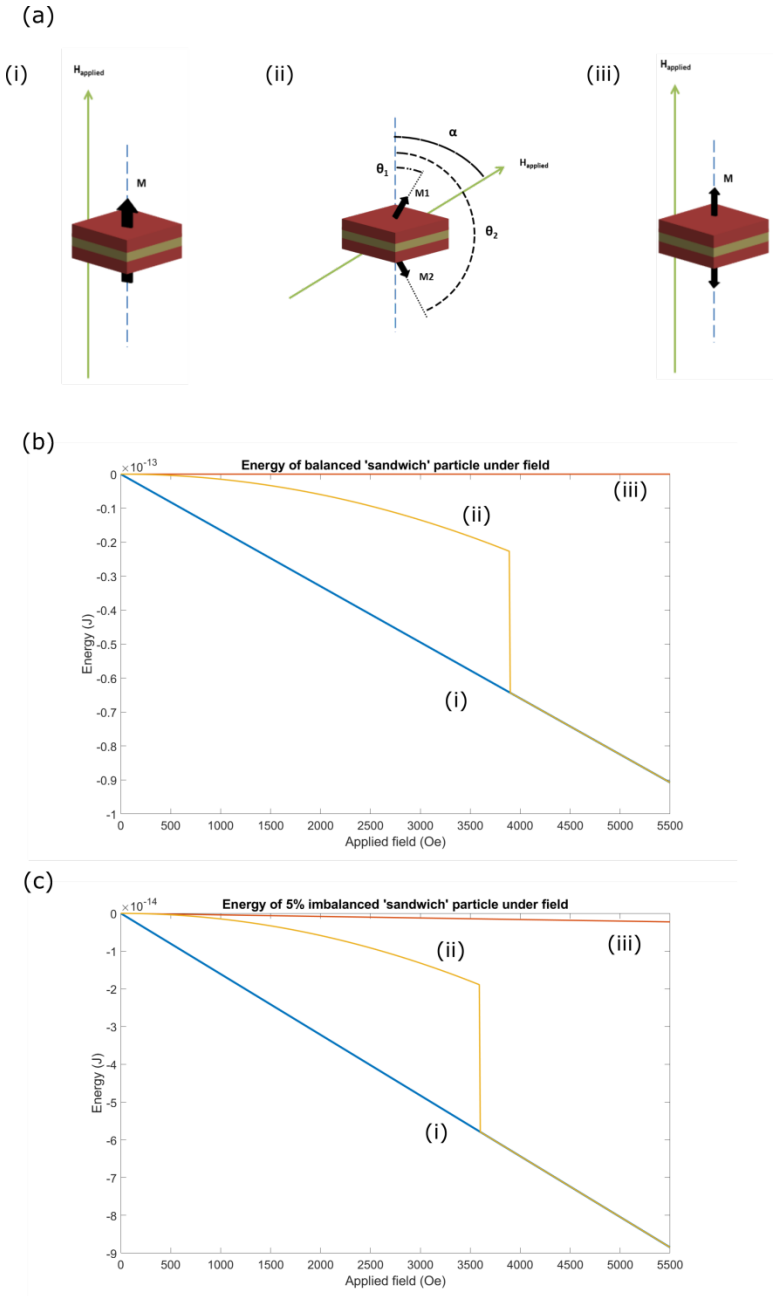

Figure 5.20 AP particle overall energy landscape
The different states used to calculate the energy of the AP particle are shown in (a). The graphs showing energy of the three states for (b) a balanced and (c) 5% imbalanced particle are shown.

From the Stoner-Wohlfarth model of the anti-parallel particle, we were able to deduce how switching to the parallel state would occur in this zero temperature model, along with identifying the series of magneto-mechanical transitions expected for this SAF-like particle.[19] From these theoretical results, we can compare with experimental observations. We will first look at the orientation of the particle under an applied field, to compare with the predictions in Figure 5.19. Then, the switching of particles from the anti-parallel to parallel state will be quantified experimentally.

Experimental response

To compare with the model, the experimental response of the anti-parallel 'sandwich' particles was observed. The particles used have the composition {Ta(2)/ Pt(2)/ [CoFeB(0.55)/ Pt(0.7)]$_4$/ CoFeB(0.55)/ Pt(2)/ Au(20)/ Ta(2)/ Pt(2)/[CoFeB(0.55)/ Pt(0.7)]$_4$/ CoFeB(0.55)/ Pt(2)}, as optimised in Chapter 4. Figure 5.21 shows a standard response found for a range of applied fields. First, at low applied fields, the particle aligns its easy axis with the applied field. Then, as the field is increased (Figure 5.21: 3rd set of pictures, 1000 Oe), the particle rotates to align the plane of the particle to the field. Finally, at high fields, the particle switches to a parallel configuration and once again aligns the easy axis to the field direction. This resembles the results seen experimentally in work with SAF particles.[19]

It also shows that most of the particles are slightly ferrimagnetic, since they display an initial alignment of the field and particle easy axis at low field values. While the bulk hysteresis loop of the film from which the particles are made (Figure 5.22) shows no difference between the moments of the two magnetic multilayers, this measurement might not detect such an imbalance. To have a 1% imbalance in moment between the two magnetic multilayers, the total CoFeB thickness between the two layers would need to differ by roughly 0.3 Å, corresponding to a measured difference of ~0.75 x 10^{-6} emu, which is below the noise limit of the measurement. Even if we cannot explicitly characterize the imbalance, experimental observations which show the particles aligning their easy axis to the field at low fields confirm that some imbalance must exist. Incorporating this imbalance into our understanding of the particles is crucial for understanding the switching mechanism of the particles.

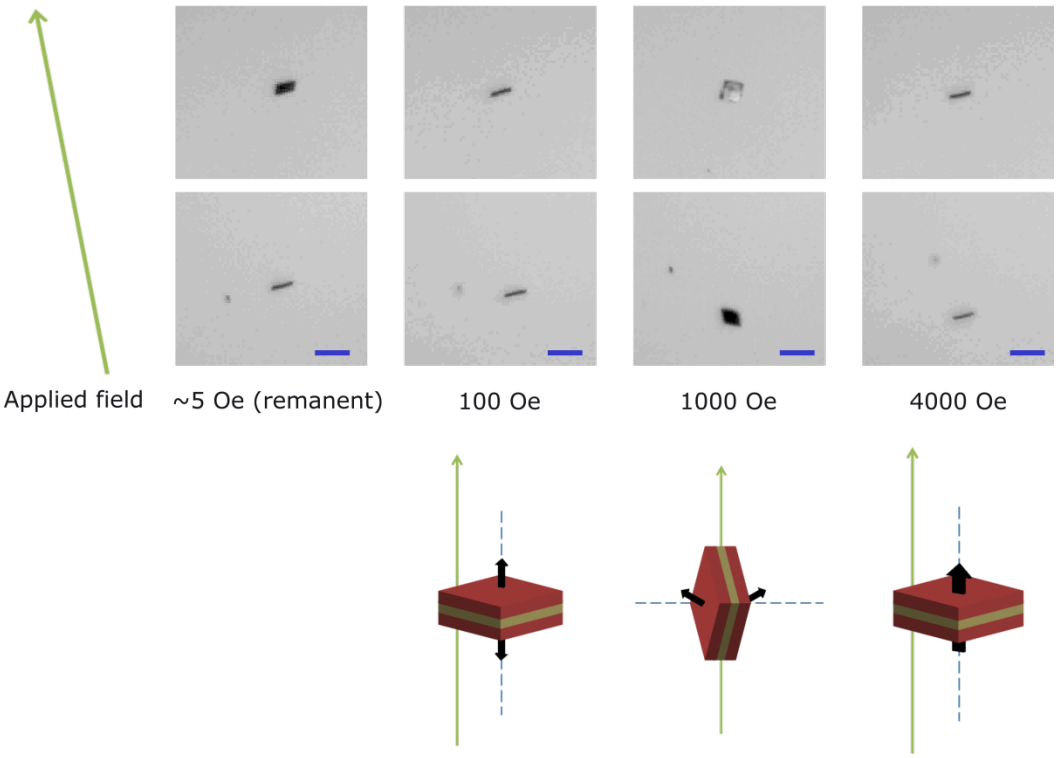

Figure 5.21 Experimental response of anti-parallel sandwich particles under field
The response of anti-parallel 'sandwich' particles is shown for a number of different field values. Schematic diagrams of the particle are given to help explain the behaviour. The blue scale bar corresponds to 10 μm.

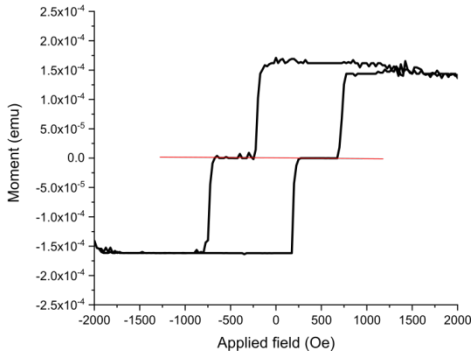

Figure 5.22 VSM hysteresis loop of 'sandwich' magnetic film
A VSM hysteresis loop is given for the film {Ta(2)/ Pt(2)/ [CoFeB(0.55)/ Pt(0.7)]$_4$/ CoFeB(0.55)/ Pt(2)/ Au(20)/ Ta(2)/ Pt(2)/[CoFeB(0.55)/ Pt(0.7)]$_4$/ CoFeB(0.55)/ Pt(2)}. This is the standard film used in the 'sandwich' particles. A horizontal line is drawn as zero to show any moment imbalance between the magnetic layers.

These observations in Figure 5.21 are useful for validation of our theoretical model and increased understanding of the system. However, the most crucial component for translating these particles into self-assembled structures is understanding the switching of the particles from the anti-parallel to parallel state. By controlling this switching event, we can control when particles will assemble. While the Stoner-Wohlfarth model is a good guide for particle behaviour, the switching in

the real particles will be much different, given the coercivity of the particles that is much lower than the coercivity (equal to the anisotropy field) of the Stoner-Wohlfarth model.

Experimental switching

Experimental observations were made of the field conditions at which the anti-parallel particles switched to their parallel, saturated state. The two initial observations, shown in Figure 5.23, were that there is a large distribution of switching fields for the particles, and that almost all of the switching values are higher than the coercivity of either magnetic layer in the particle. The particles measured in Figure 5.23 (and also used in Figure 5.27) have a slightly different magnetic multilayer composition to the rest of the particles in this section, with a composition of {Ta(2)/ Pt(2)/ [CoFeB(0.5)/ Pt(0.8)]$_4$/ CoFeB(0.5)/ Pt(2)/ Au(20)/ Ta(2)/ Pt(2)/[CoFeB(0.5)/ Pt(0.8)]$_4$/ CoFeB(0.5)/ Pt(2)}. This difference accounts for the different ranges of switching fields seen in these figures compared to other results.

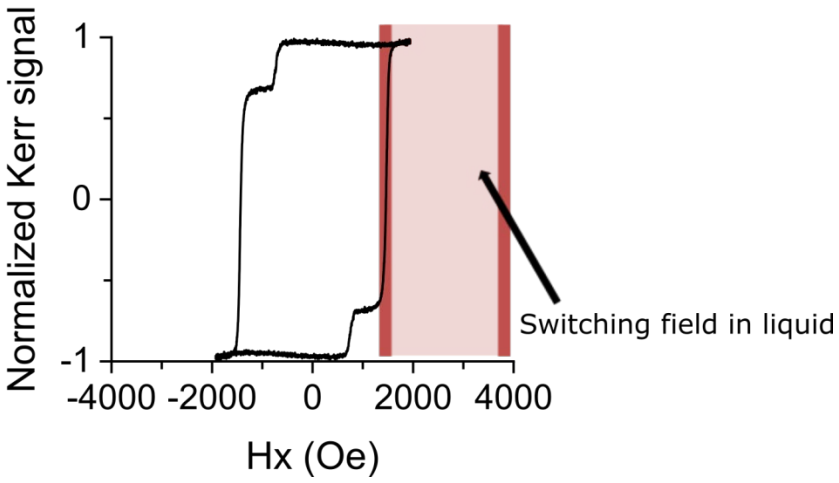

Figure 5.23 Switching fields of AP particles in liquid
The field range in which AP particles switched to the parallel state is shown in red, compared to a MOKE hysteresis loop of a corresponding array of ~10 nominally equivalent 5 x 5 μm^2 square 'sandwich' particles. The MOKE loop is measured at field sweep rate of 2000 Oe/s, while the particles in liquid were switches using a field sweep rate of ~500 Oe/s. The composition of these particles is Ta(2)/ Pt(2)/ [CoFeB(0.5)/ Pt(0.8)]$_4$/ CoFeB(0.5)/ Pt(2)/ Au(20)/ Ta(2)/ Pt(2)/[CoFeB(0.5)/ Pt(0.8)]$_4$/ CoFeB(0.5)/ Pt(2)}, slightly different from the standard optimised composition used in the other particles in this section.

To better characterize this distribution, particle switching experiments were conducted with a series of static magnetic fields (Figure 5.24). Particles were subjected to a static field for a duration of two minutes at field strengths from 2000 – 4000 Oe. At each field value between 20 – 25 particles were observed. In the set of 5 x 5 μm^2 'sandwich' particles used in this experiment, it was found that no particles switched to the parallel state at 2000 Oe, while almost 95% of the particles had switched

at a static field of 4000 Oe. This particle set is not the same as those shown in Figure 5.23, so the range of switching fields does not exactly match.

Interestingly, it was also observed that, even under the same static field regime, not all particles switched immediately once the field was applied. Microscope images from one such event are shown in Figure 5.24 (b). There was a clear separation of about 20 seconds between the first and second particle switching. Under the zero temperature Stoner-Wohlfarth model, particle switching occurs at a single threshold value and happens instantly. Thus, it is likely that some other factors, such as temperature (which we will consider below), also influence the particle switching, leading to this time dependence and large distribution of switching fields seen here. It is also likely that these particles, due to the ion milling and other processing steps, have a distribution of values for magnetic properties such as anisotropy and coercivity, which could impact the switching field distribution.

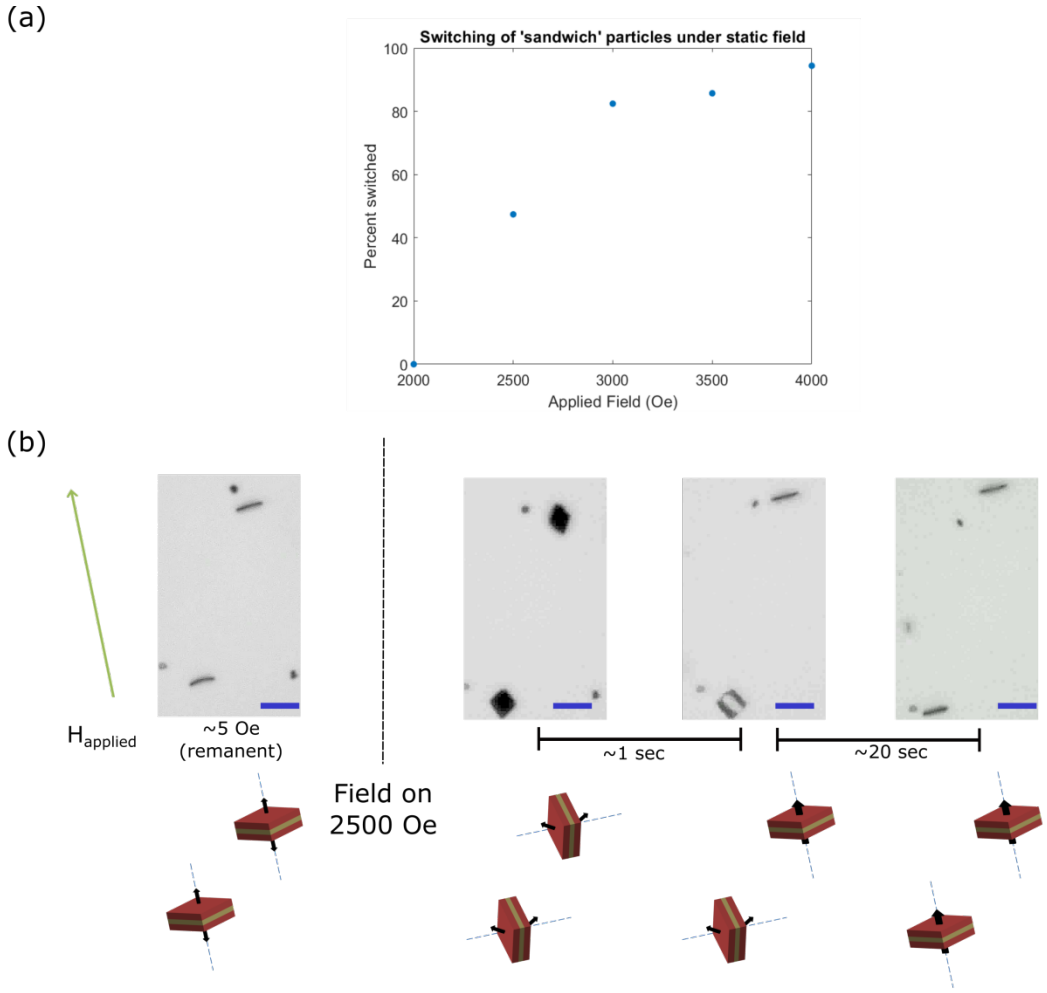

Figure 5.24 Switching of 'sandwich' particles under static applied field
A series of 5 x 5 μm^2 'sandwich' particles were subjected to different static applied fields. The percent of particles that switched from an anti-parallel to parallel state were found in (a) for each field value between 2000 and 4000 Oe. (b) shows the sequence of two particles switching at 2500 Oe. The particles both go through the expected mechanical transitions under the applied field and eventually switch, but at different times. Below each image are illustrations of the state of each particle, corresponding to the states in Figure 5.21. The green arrow is the direction of applied field. The blue scale bar corresponds to 10 μm.

In that vein, we can consider how the real switching behaviour of PMA films would impact the switching of particles. As was covered in Chapter 4, the reversal behaviour of these films and particles is not governed purely by anisotropy, but by the nucleation and propagation of domains through the sample. These domain-driven reversal events happen at the coercive field, which is much lower than the anisotropy field of the film. Thus, to analyse the switching behaviour of the real particles, we will construct a switching astroid. Figure 5.25 shows such an astroid, along with the Stoner-Wohlfarth astroid presented in Figure 5.17. The switching astroid is an approximation, as the actual form of the astroid must be experimentally measured. However, we do know the out-of-plane switching field (coercivity) and the in-plane switching field (anisotropy) of the particles. We also know that the form of the astroid must decrease monotonically from the coercivity to the anisotropy.

From these conditions, we have created the approximate switching astroid in Figure 5.25, using the coercivity softer magnetic layer in the particles measured in Figure 5.23 and the anisotropy value established previously (Ch. 4, Table 1).

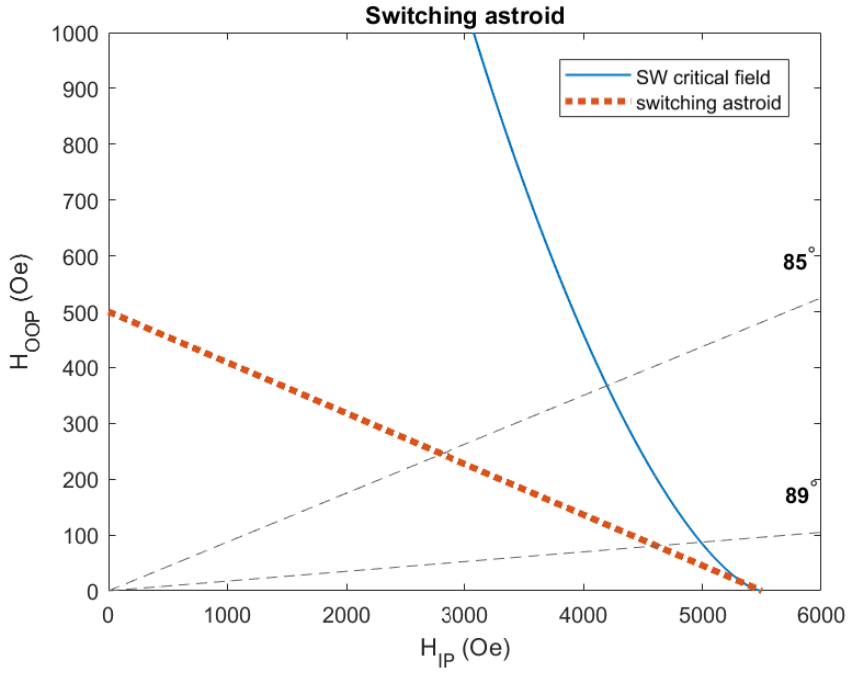

Figure 5.25 Switching astroid for real particles
A switching astroid is constructed, using the coercivity and anisotropy of real particles. The SW critical field can be seen, along with lines denoting applied field angles of 85° and 89°.

From our Stoner-Wohlfarth model and experimental results, we know the applied field will be aligned to the plane of the particle before switching. Additionally, we know, in imbalanced particles, the particle will be slightly tilted with respect to the field. As we have established, the real particles all show field response that is indicative of a moment imbalance. To evaluate the switching of such particles, we have plotted guide lines corresponding to the modelled equilibrium field angle in a 1% ($\alpha = 89°$) and 5% ($\alpha = 85°$) imbalanced particle. Using these guide lines and the switching astroid, we can determine the field magnitude at which switching could occur. For the 1% imbalance, it is ~4500 Oe, while for the 5% imbalance it is ~2800 Oe.

This immediately sheds light on the origin of the high switching fields and large switching field distribution of the particles in liquid. The imbalanced particles will be able to switch, but the high field angle (relative to the particle) means a high magnitude field is needed. This field angle could also be impacted by additional factors, such as thermal motion, that would slightly change the field angle, and thus change the field magnitude needed for switching. Furthermore, any distribution in anisotropy and coercivity between particles would further impact the range and magnitude of

switching values found. Since distributions will exist in moment imbalance, coercivity, and anisotropy in the particles due to defects and processing conditions, we can account for the magnitude and spread of the switching fields seen in real particles.

By combining the results of the Stoner-Wohlfarth model with the real reversal behaviour of the PMA films, an explanation for how the switching of the anti-parallel 'sandwich' particles occurs can be found. The Stoner-Wohlfarth model gives an understanding of the mechanical behaviour of the particle in liquid, and that can be combined with a potential distribution in the real magnetic properties of the particles to explain the switching behaviour seen above. Without more information about the specific distribution of properties like anisotropy, moment imbalance, and coercivity in particles, it is difficult to fully characterize the switching distribution, but we can understand how such properties and their distribution will lead to the switching fields observed.

Effect of Brownian motion

Throughout the analysis of particle switching, thermal effects from Brownian motion have been mentioned as an additional source of particle tilt or fluctuation that could help drive switching. Brownian motion can have an observable impact on microscope particles such as the ones in this work.[49] At room temperature, the energy of Brownian motion should be on the order of 10^{-21} J. This is much smaller than the energies involved in the particle responses outlined above, which range from 10^{-14} – 10^{-17} J, but it is interesting to see if and how Brownian motion could affect the particle. To see the strength of these effects and relate it to the switching process, we quantified the amount of tilt that could be induced by Brownian motion and looked at the switching field distribution at different temperatures.

First, the angle change caused by Brownian motion was analysed (Figure 5.26). In the absence of any applied field, the particle can achieve tilts of about 13° purely due to Brownian effects (Figure 5.26, a). In an anti-parallel particle under a 100 Oe field, the amount of tilt seen reduces to about 1 – 3° (Figure 5.26, b). At higher fields of 2000+ Oe, there is no discernible change in the particles due to Brownian motion. The higher fields impede any effects of Brownian motion as they create an energy well in which the particle sits, and the fluctuations would have to push against that state to create any change.

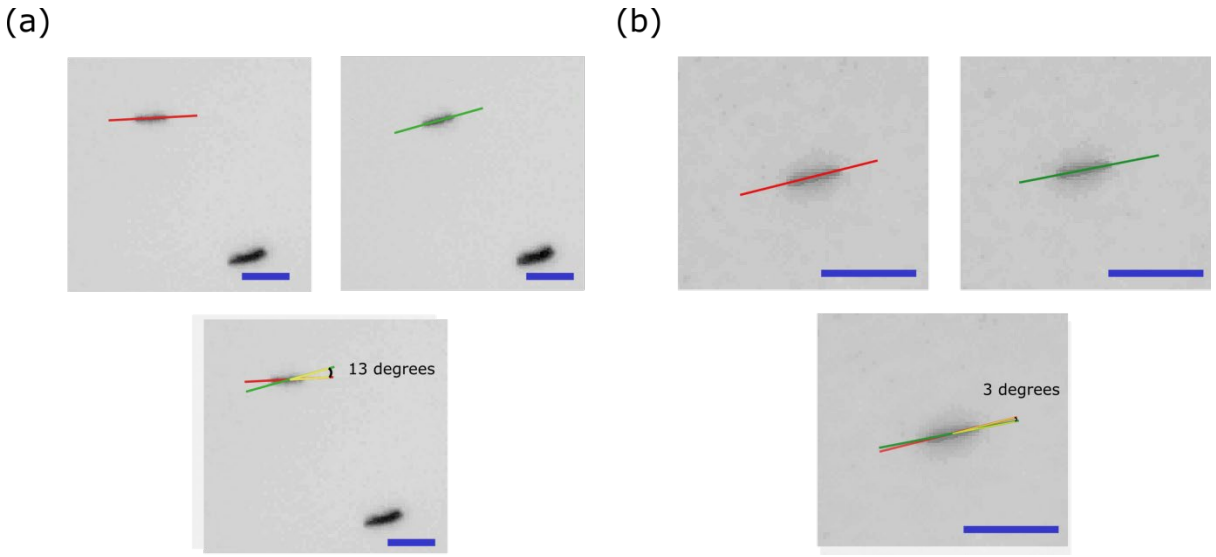

Figure 5.26 Brownian motion of magnetic particles
The angle change of particles under Brownian motion is measured. Under the absence of any external magnetic field (a), particles can achieve angle drifts of 13°, while under a 100 Oe applied field on an anti-parallel 'sandwich' particle, a 3° change can be seen. The blue scale bar corresponds to 10 μm.

We can theorize that Brownian motion could play a role in switching, as long as the particle does not sit in a strong energy minimum. For example, if the energy landscape around the particle's position is flat, then it will be possible for Brownian motion to provide the fluctuations necessary to drive the particle to a different state. However, that would not manifest as a large or even discernible difference compared to the large range of switching fields we have observed. Thus, we do not believe it should be largely relevant to the switching process.

We can further probe the temperature effect by measuring the switching fields of particles in liquid at different temperatures (Figure 5.27). There is not a clear shift in switching fields, or change of the range of the fields, with temperature. While the experiment is limited by low particle densities, which make it difficult to get large numbers of switching events, we still can see how the range of switching fields is mostly unchanged at different temperatures.

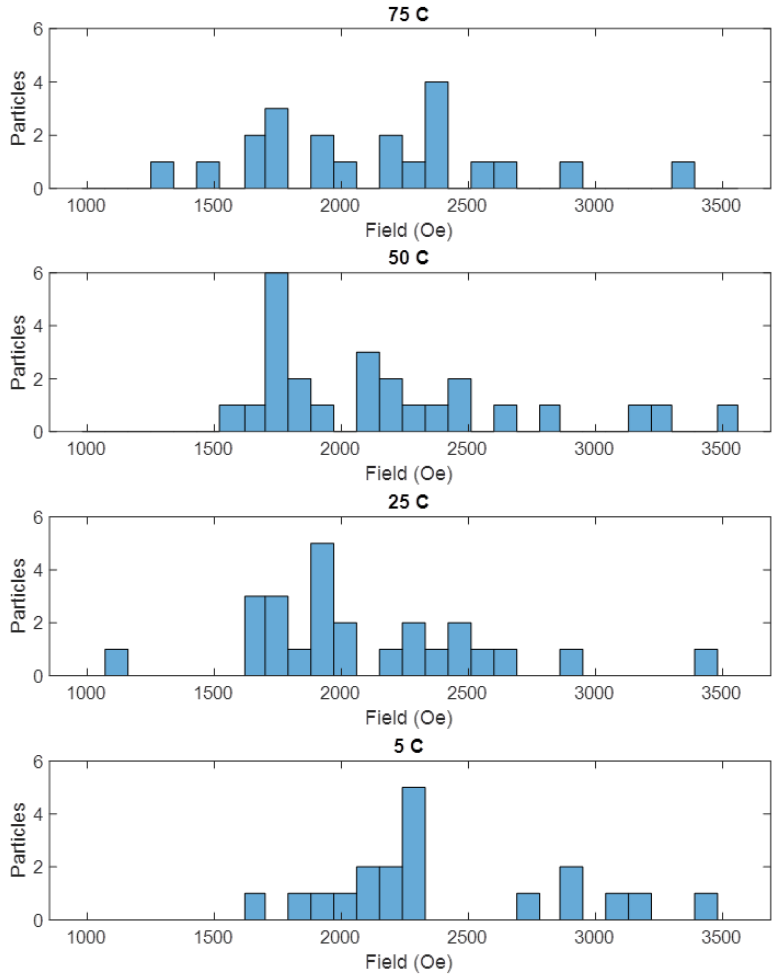

Figure 5.27 Temperature dependence of AP particle switching field
The switching field of anti-parallel 'sandwich' particles was measured at temperature of 5, 25, 50, and 75 degrees C, finding the distribution of switching fields for particles at the various temperatures. The particles measured here have a composition of {Ta(2)/ Pt(2)/ $[CoFeB(0.5)/ Pt(0.8)]_4$/ CoFeB(0.5)/ Pt(2)/ Au(20)/ Ta(2)/ Pt(2)/$[CoFeB(0.5)/ Pt(0.8)]_4$/ CoFeB(0.5)/ Pt(2)}, slightly different from the standard optimised composition used in the other particles in this section.

Brownian motion could play a small role in providing fluctuations that can help drive switching, but it does not play a significant role in determining the switching fields or their distribution, which are best explained by the processes described previously.

5.4.3 Summary of particle response to an applied field

In this section the response of parallel, fully remanent and anti-parallel, zero remanence particles were characterized, using a combination of theoretical modelling and experimental results. The fully remanent particles were found to follow the direction of the applied magnetic field,

regardless of field magnitude, as this represents the global minimum energy state for the particle. The anti-parallel particles were found to mimic the unique transitions seen in SAF particles until eventually switching to a parallel state at a range of fields. This switching was specifically analysed, and it was found an anisotropy-based Stoner-Wohlfarth model will produce a single switching field, while domain nucleation can potentially explain the real distribution of switching fields found. The switching distribution relies on inhomogeneity in particle properties, such as moment imbalance or anisotropy and coercivity differences, which can account for the large distribution of switching fields found. Thermal effects were found to be present and might play a role in assisting the switching process, but this effect is minimal. From this we can understand the applied fields needed to saturate a collection of anti-parallel particles, turning them 'on' to begin self-assembly.

5.5 Conclusion

In order to understand how the magnetic particles created in Chapter 4 can be best used for self-assembly, the stability, interaction, and field response of the individual particles needed to be characterized.

To create particles that are stable in liquid and will not deform, it was found that particles must be kept to small size ranges (<10 μm lateral dimensions) or in a balanced film configuration, such as the 'sandwich' particle film. This result, from analysis of the aspect ratios of a number of different particle sizes and compositions, establishes some base parameters that particles must meet to be stable and useful in liquid.

Particle interactions, the fundamental driving force for equilibrium self-assembly, were examined experimentally and theoretically. Only small particles, with lateral sizes of 5 – 10 μm or smaller, were able to effectively assemble without any additional energy input. Even though larger particles have a greater energetic driving force for assembly, frictional forces prevent their effective assembly. Additionally, smaller particles have stronger binding energies due to their stray field profile, which is an added benefit of using particles in this size range.

Finally, the response of particles to field was characterized, with special emphasis on the switching of particles from an anti-parallel to parallel state. When fully remanent, the PMA particles will always align themselves with the direction of the applied field. When starting from an anti-parallel state, the particles will align the particle hard axis to the applied field, until the particle reaches a field at which it can switch to the parallel state. In the Stoner-Wohlfarth model this will occur at a single threshold value, while in real particles it likely occurs through a nucleation process that cascades into a full switch of the particle. Through this analysis, we can establish the applied field values needed to switch over 95% of particles, to take them into a state in which they can then assemble.

We have established that particles with a lateral size less than 10 μm using the 'sandwich' layer structure of {Ta(2)/ Pt(2)/ [CoFeB(0.55)/ Pt(0.86)]$_4$/ CoFeB(0.55)/ Pt(2)/ Au(20)/ Ta(2)/ Pt(2)/[CoFeB(0.55)/ Pt(0.86)]$_4$/ CoFeB(0.55)/ Pt(2)} will be the ideal candidates for equilibrium self-assembly, due to their stability and effective interaction. These particles can be collectively switched from an anti-parallel to parallel state to trigger assembly. Understanding all these parameters, we can now proceed to create and manipulate assemblies of the particles.

5.6 References

1. De Vicente, J., Klingenberg, D. J. & Hidalgo-Alvarez, R. Magnetorheological fluids: A review. *Soft Matter* **7**, 3701–3710 (2011).
2. Rabinow, J. The magnetic fluid clutch. *Electr. Eng.* **67**, 1167–1167 (2013).
3. Papel, S. S. Low viscosity magnetic fluid obtained by the colloidal suspension of magnetic particles. (1963).
4. Raj, K. & Moskowitz, R. Commercial applications of ferrofluids. *J. Magn. Magn. Mater.* **85**, 233–245 (1990).
5. Odenbach, S. Ferrofluids - Magnetically controlled suspensions. in *Colloids and Surfaces A: Physicochemical and Engineering Aspects* **217**, 171–178 (Elsevier, 2003).
6. Scherer, C. & Figueiredo Neto, A. M. Ferrofluids: Properties and applications. *Brazilian J. Phys.* **35**, 718–727 (2005).
7. Wu, K., Su, D., Liu, J., Saha, R. & Wang, J. P. Magnetic nanoparticles in nanomedicine: A review of recent advances. *Nanotechnology* **30**, 502003 (2019).
8. Sun, S. & Zeng, H. Size-controlled synthesis of magnetite nanoparticles. *J. Am. Chem. Soc.* **124**, 8204–8205 (2002).
9. Périgo, E. A. *et al.* Fundamentals and advances in magnetic hyperthermia. *Applied Physics Reviews* **2**, 41302 (2015).
10. Hiergeist, R. *et al.* Application of magnetite ferrofluids for hyperthermia. *J. Magn. Magn. Mater.* **201**, 420–422 (1999).
11. Oswald, P., Clement, O., Chambon, C., Schouman-Claeys, E. & Frija, G. Liver positive enhancement after injection of superparamagnetic nanoparticles: Respective role of circulating and uptaken particles. *Magn. Reson. Imaging* **15**, 1025–1031 (1997).
12. He, J., Huang, M., Wang, D., Zhang, Z. & Li, G. Magnetic separation techniques in sample preparation for biological analysis: A review. *Journal of Pharmaceutical and Biomedical Analysis* **101**, 84–101 (2014).
13. Haun, J. B., Yoon, T. J., Lee, H. & Weissleder, R. Magnetic nanoparticle biosensors. *Wiley Interdisciplinary Reviews: Nanomedicine and Nanobiotechnology* **2**, 291–304 (2010).
14. Lisjak, D. & Mertelj, A. Anisotropic magnetic nanoparticles: A review of their properties, syntheses and potential applications. *Progress in Materials Science* **95**, 286–328 (2018).
15. Mertelj, A., Lisjak, D., Drofenik, M. & Čopič, M. Ferromagnetism in suspensions of magnetic platelets in liquid crystal. *Nature* **504**, 237–241 (2013).
16. Yan, J., Bloom, M., Bae, S. C., Luijten, E. & Granick, S. Linking synchronization to self-assembly using magnetic Janus colloids. *Nature* **491**, 578–581 (2012).
17. Yan, J., Bae, S. C. & Granick, S. Colloidal Superstructures Programmed into Magnetic Janus

Particles. *Adv. Mater.* **27**, 874–879 (2015).

18. Smoukov, S. K., Gangwal, S., Marquez, M. & Velev, O. D. Reconfigurable responsive structures assembled from magnetic Janus particles. *Soft Matter* **5**, 1285–1292 (2009).
19. Vemulkar, T., Welbourne, E. N., Mansell, R., Petit, D. C. M. C. & Cowburn, R. P. The mechanical response in a fluid of synthetic antiferromagnetic and ferrimagnetic microdiscs with perpendicular magnetic anisotropy. *Appl. Phys. Lett.* **110**, 042402 (2017).
20. Vemulkar, T., Mansell, R., Petit, D. C. M. C., Cowburn, R. P. & Lesniak, M. S. Highly tunable perpendicularly magnetized synthetic antiferromagnets for biotechnology applications. *Appl. Phys. Lett.* **107**, 012403 (2015).
21. Leulmi, S. *et al.* Comparison of dispersion and actuation properties of vortex and synthetic antiferromagnetic particles for biotechnological applications. *Appl. Phys. Lett.* **103**, 132412 (2013).
22. Joisten, H. *et al.* Self-polarization phenomenon and control of dispersion of synthetic antiferromagnetic nanoparticles for biological applications. *Appl. Phys. Lett.* **97**, 253112 (2010).
23. Naud, C. *et al.* Cancer Treatment by Magneto-Mechanical Effect of Particles, a Review. *Nanoscale Adv.* (2020). doi:10.1039/d0na00187b
24. Hu, W. *et al.* Synthetic antiferromagnetic nanoparticles with tunable susceptibilities. *J. Appl. Phys.* **105**, 07B508 (2009).
25. Mansell, R. *et al.* Magnetic particles with perpendicular anisotropy for mechanical cancer cell destruction. *Sci. Rep.* **7**, 1–7 (2017).
26. Xi, W. *et al.* Rolled-up magnetic microdrillers: Towards remotely controlled minimally invasive surgery. *Nanoscale* **5**, 1294–1297 (2013).
27. Lee, H., Kim, J., Kim, H., Kim, J. & Kwon, S. Colour-barcoded magnetic microparticles for multiplexed bioassays. *Nat. Mater.* **9**, 745–749 (2010).
28. Iss, C. *et al.* Fabrication of nanotweezers and their remote actuation by magnetic fields. *Sci. Rep.* **7**, 1–9 (2017).
29. Thornton, J. A. & Hoffman, D. W. Stress-related effects in thin films. *Thin Solid Films* **171**, 5–31 (1989).
30. Abadias, G. *et al.* Review Article: Stress in thin films and coatings: Current status, challenges, and prospects. *J. Vac. Sci. Technol. A Vacuum, Surfaces, Film.* **36**, 020801 (2018).
31. Abermann, R. Measurements of the intrinsic stress in thin metal films. *Vacuum* **41**, 1279–1282 (1990).
32. Tang, W., Xu, K., Wang, P. & Li, X. Residual stress and crystal orientation in magnetron sputtering Au films. *Mater. Lett.* **57**, 3101–3106 (2003).
33. Thompson, G. B., Wan, L., Yu, X. xiang & Vogel, F. Influence of phase stability on the in situ growth stresses in Cu/Nb multilayered films. *Acta Mater.* **132**, 149–161 (2017).

34. Andersson, G. & Hjörvarsson, B. Effects of strain on magnetic anisotropy in Fe- and Co-based heterostructures. *Phase Transitions* **81**, 679–701 (2008).
35. Espinosa, H. D. & Prorok, B. C. Size effects on the mechanical behavior of gold thin films. *J. Mater. Sci.* **38**, 4125-4128 (2003).
36. Hou, M. T. K. & Chen, R. Effect of width on the stress-induced bending of micromachined bilayer cantilevers. *J. Micromechanics Microengineering* **13**, 141–148 (2003).
37. Haq, K. E., Behrndt, K. H. & Kobin, I. Adhesion Mechanism of Gold-Underlayer Film Combinations to Oxide Substrates. *J. Vac. Sci. Technol.* **6**, 148–152 (1969).
38. Todeschini, M., Bastos Da Silva Fanta, A., Jensen, F., Wagner, J. B. & Han, A. Influence of Ti and Cr Adhesion Layers on Ultrathin Au Films. *ACS Appl. Mater. Interfaces* **9**, 37374–37385 (2017).
39. Akoun, G. & Yonnet, J.-P. 3D analytical calculation of the forces exerted between two cuboidal magnets. *IEEE Trans. Magn.* **20**, 1962–1964 (1984).
40. Vansteenkiste, A. *et al.* The design and verification of MuMax3. *AIP Adv.* **4**, 107133 (2014).
41. Purcell, E. M. Life at low Reynolds number. *Am. J. Phys.* **45**, 3–11 (1977).
42. Gupta, S. C. Slow broad side motion of a flat plate in a viscous liquid. *Zeitschrift für Angew. Math. und Phys. ZAMP* **8**, 257–261 (1957).
43. Fernandez, N., Cayer-Barrioz, J., Isa, L. & Spencer, N. D. Direct, Robust Technique for the Measurement of Friction between Microspheres. *Langmuir* **31**, 8809–8817 (2015).
44. Wang, W., Wang, Y., Bao, H., Xiong, B. & Bao, M. Friction and wear properties in MEMS. in *Sensors and Actuators, A: Physical* **97**–**98**, 486–491 (Elsevier, 2002).
45. Dunkin, J. E. & Kim, D. E. Measurement of static friction coefficient between flat surfaces. *Wear* **193**, 186–192 (1996).
46. Stoner, E. C. & Wohlfarth, E. P. A mechanism of magnetic hysteresis in heterogeneous alloys. *Philos. Trans. R. Soc. London. Ser. A, Math. Phys. Sci.* **240**, 599–642 (1948).
47. Slonczewski, J. C. Theory of magnetic hysteresis in films and its application to computers. in *IEEE Transactions on Magnetics* **45**, 8–14 (2009).
48. Tannous, C. & Gieraltowski, J. The Stoner-Wohlfarth model of ferromagnetism. *Eur. J. Phys.* **29**, 475–487 (2008).
49. Brown, R. XXVII. A brief account of microscopical observations made in the months of June, July and August 1827, on the particles contained in the pollen of plants; and on the general existence of active molecules in organic and inorganic bodies . *Philos. Mag.* **4**, 161–173 (1828).

6 Particle Assemblies

6.1 Introduction

Investigation of magnetic self-assembly and the collective interactions of magnetic particles has constantly accompanied the research and development of new magnetic particles. As synthesis methods of magnetic nanoparticles, like Co and iron oxide nanoparticles, were discovered and improved, chains and clusters were observed in the solutions of newly created particles.[1–3] Early work concerning self-assembly focused on fundamental understanding of these interactions of magnetic particles and their effects on ferrofluids and magnetorheological fluids, in order to quantify and explain certain behaviours of the fluids.[4,5] From this starting point, the ability to controllably chain, manipulate, and structure magnetic particles has grown into a field of its own.[5–9]

Magnetic self-assembly incorporates the entire library of magnetic particles to create interesting structures and effects. Particles are modified in form, both physical and magnetic, to induce interesting anisotropies that can in turn drive interesting assembly behaviour.[10] Iron oxide and similar nanoparticles, in paramagnetic, superparamagnetic, and ferromagnetic forms, are used to assemble structures ranging from simple chains to three-dimensional crystals.[11–14] Similarly, Janus particles and patchy particles can use their anisotropic structure to form unique assemblies such as ribbons, staggered chains, and complex ring structures.[15–19] Magnetic assemblies can be formed as static or dynamic assemblies, using specific magnetic field sequences to drive or sustain the assembled structures.[9,20–23] Additionally, assembly can be mediated through other forces, such as capillary or interface interactions, and it can be guided by templating, either using a functionalized surface or chemical species, like polymers.[23–28] Alteration of the shape of the magnetic building block, allows access to additional complexity like assemblies of helical structures.[29] Altogether, the wide range of available particles and assembly methods means magnetic self-assembly can create a great variety of structures.

From these many potential structures, a number of interesting applications for magnetic self-assembly have developed. Assembled structures can influence bulk fluidic properties, seen through the effect of assembled particles in ferrofluids.[4] In a similar vein, particles can be assembled within a material matrix to impart an anisotropic magnetic response, creating smart materials.[30–32] Assemblies can lead to enhanced magnetic properties, such as increased coercivity, anisotropy, or saturation magnetization, to the individual particles.[24,33,34] Self-assembled magnetic materials have also drawn interest as a new form of high-density magnetic recording, or for creation of photonic structures.[9,35–37]

Beyond these numerous applications, magnetic self-assembly is heavily researched for biomedical and therapeutic applications.[38,39] As referenced previously, magnetic components are

incredibly useful in biomedical applications, as magnetic fields can easily and harmlessly penetrate biological systems to drive magnetic devices. Magnetic micromachines and microrobots can be created by numerous methods for applications like drug delivery, separation, microdrilling, actuation, or transportation.[40–47] Self-assembly represents one avenue for the creation of such devices, and it is especially implemented when chain-like flexible components or swarms of such components are needed, as these applications can take advantage of the forms and scale offered by self-assembly.[48–52]

Often, these flexible components are used in magnetic walkers and swimmers, which represent a large portion of the research into magnetic microrobots.[53,54] Being able to control locomotion of a microrobot enables many of the biomedical applications listed above. However, due to the constrictions imparted by the low Reynold's number viscous regime in which these microswimmers and walkers exist, the driving motion cannot be reciprocal.[55,56] For this reason, these machines often incorporate flexible, bio-inspired components, mimicking flagella or cilia, to drive motion and self-assembly can be used to build these structures.[45,53,54,57] In most cases, a combination of magnetic particles and a binding elastic polymer are needed, to create stable and flexible chains that can be actuated with external magnetic fields.

Self-assembly, of course, is not the only method for creating such micromachines. Advances in lithographic and deposition techniques allow creation of microrobots in a number of different forms, such as fully formed metallic helical swimmers, grippers, and manipulators that can act in liquid or on a solid surface.[58–62] Constructions of magnetic tweezers and magnetic cilia carpets on surfaces further show the wide range of devices for actuation and manipulation that can be formed from magnetic materials.[63–65] However, many of the applications of microrobots, such as actuation, manipulation, and transportation, require strong, stable, and flexible chains that can be created by self-assembly.

While many of these chains and other components are created using a mix of particle self-assembly and chemical functionalization, the particles in this work can take advantage of their unique anisotropic properties to create fully magnetic assembled chain that can potentially perform the functions required of some magnetic micromachines. High aspect ratio planar particles and PMA anisotropy is a rare combination. The similar magnetic particle showing such properties include barium hexaferrite or Co nanoplatelets and, which cannot offer the same size, flexibility, or magnetic tunability compared to the particles in this work.[66,67] Additionally, the large magnetization and anisotropy of the PMA particles allows for strong actuation through the transduction of large torques and forces.[68] These high aspect ratio PMA plates offer a new form of anisotropic magnetic particle that we can assemble and use for fulfilling interesting micro-scale functions.

In this chapter, we will explore how the magnetic particles created and characterized in the previous chapters can be formed into larger assemblies. This will begin with simple zero field experiments to understand the chaining behaviour of the particles, from an experimental and theoretical standpoint. Then, the behaviour of particle chains under external magnetic fields will be

investigated. The value in having a stable, equilibrium assembly of particles is that, if no magnetic field is needed to sustain the assembly, external fields can be used to control and actuate the assembly. A number of different experimental responses will be observed and compared with theoretical models. Potential applications of the assembled chains will be outlined as well. Finally, assembly experiments of particles on templated surfaces will be investigated, to assess the potential of the system to be used for assembly of 3D structures or surface-anchored micromachines.

6.2 Assembly of particle chains

Building on the work of the Chapters 4 and 5, we are able to assemble magnetic particle into chains and structures following the principles we have previously established. In these experiments, particles have been made with the 'sandwich' film structure and a lateral size of 5 x 5 μm^2 and 5 x 10 μm^2. The particles are kept to a lateral size < 10 μm, based on the limits dictated by previous investigation of the stability and interaction of particles at different sizes. The square and rectangular lateral shapes are used to give some variety in the particle shape, to test if there is any shape-related impact on the particle assemblies. The 'sandwich' film composition is {Ta(2)/ Pt(2)/ $[CoFeB(0.55)/ Pt(0.86)]_4$/ CoFeB(0.55)/ Pt(2)/ Au(20)/ Ta(2)/ Pt(2)/$[CoFeB(0.55)/ Pt(0.86)]_4$/CoFeB(0.55)/ Pt(2)}. In order to monitor and control the assembly, the 'sandwich' type particles are initialized in the 'anti-parallel' state. Then, a static field of 4000 Oe is applied to the particles in liquid, knowing that this field magnitude is sufficient to saturate at least 95% of particles into the parallel state.

6.2.1 Preliminary assembly experiments

When the particles saturate, it is expected that they will assemble into chains, which is the basic interacting configuration for ferromagnetic particles, as it aligns the magnetic moments of the particles. Figure 6.1 shows particles in the process of assembling into a chain. These images are taken under the application of the 4000 Oe field. As can be seen, a small (~30 μm) chain (indicated with the red arrow) has formed in the liquid. This chain has aligned its perpendicular axis (axis along the red arrow direction) to the field direction, as expected. Additional debris can be seen sticking from the side of the chain, likely as a result poor assembly or magnetic debris in the solution. It can also be observed that, as a chain forms from particles in a certain region, that area is depleted of particles for further growth of the assembly. Thus, either particles or assemblies must move to find more particle-rich regions of the liquid to continue the assembly process. The 4000 Oe applied field also induces a magnetic field gradient on the sample, as the electromagnet does not apply a perfectly homogenous field at such field magnitudes. As can be seen in Figure 6.1, the small assembly moves under the effect of this gradient, and through this movement encounters other particles (Figure 6.1, teal arrows),

which then assemble onto the end of the chain. The particle assembly to the ends of the chain is not directly captured in these images, but it was observed during imaging of the sample. The chain attracts other particles due to its larger magnetic moment, which drives strong interactions with other particles. This larger moment also experiences a greater force from the field gradient, causing it to move, while single particles stay adhered to the silicon substrate surface on which they sit. While the movement is not directly in the field direction, it is along the gradient of the field. The exact form of the gradient is difficult to measure, but it does increase toward the left of the images, which is nearer to the pole piece of the electromagnet.

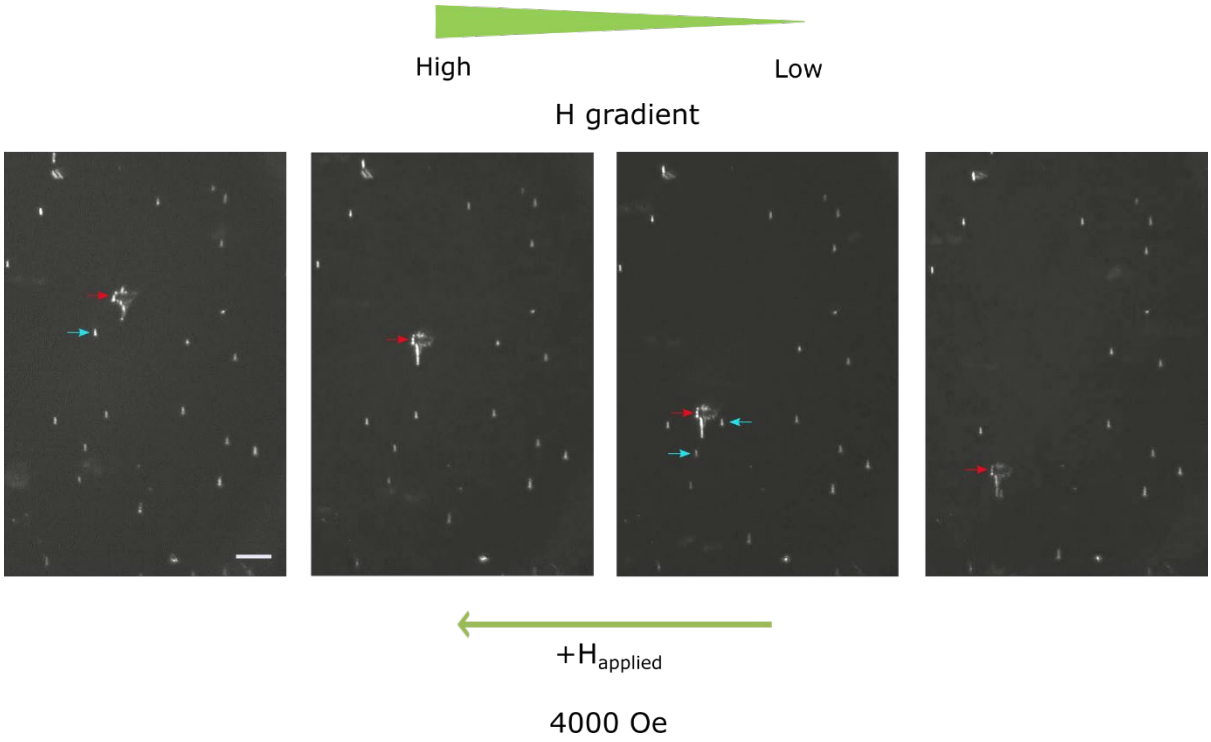

Figure 6.1 Assembly of magnetic particle chain
The assembly of 10 x 5 μm^2 magnetic particles into a chain is shown. The particles are saturated under an applied field of 4000 Oe to begin the assembly process. The red arrows show an assembly of particles and the teal arrows show particles that attached to the assembly, growing its size. The red and teal arrows denoting the different particles are also aligned with the perpendicular, out-of-plane axis of the particles. The assembly shows additional material attached to the side, possibly from poorly aligned magnetic material or other debris in the liquid. The white scale bar corresponds to 40 μm.

One goal of this work is to have the particles assemble and remain assembled without requiring a constant energy or field input. While the creation of the small assemblies, such as the one indicated in Figure 6.1 in red, can happen following the saturation of the magnetic particles and in the absence of a continuous applied magnetic field, the size of the assemblies will be limited if particles and assemblies are not moved around the liquid to regions that are richer in particles. For this reason, it is useful to use an applied magnetic field gradient to help concentrate the particles and assemblies in

the liquid, creating larger structures. Similarly, a denser suspension of magnetic particles could also be created to allow larger assemblies to form without any applied field gradient. In all situations, the magnetic field is not needed to sustain the assembled chains, meaning the process does not require a constant energy input, such as in dynamic self-assembly systems, to retain the structures created.

Having established the process for assembling chains from our suspension of magnetic particles in liquid, we can now observe and characterize the chain structure.

6.2.2 Experimental chain assembly

Assembled chains were created from both the 5 x 5 μm^2 and 10 x 5 μm^2 'sandwich' particles, using field gradients to concentrate the particles into long chains. Examples of those chains are given in Figure 6.2 below. These chains were created and then dried from the liquid onto a silicon chip, so they could be observed in an SEM.

Two aspects become immediately clear from the SEM micrographs. First, the chains can be assembled to significant lengths (~100 μm) involving thousands of particles. Second, the chains do not demonstrate ideal stacking of the magnetic particles. The particles making up the chain are rotationally and laterally offset. This can be seen for both the square and rectangular shapes, but is more obvious in the rectangular particles, where the longer dimension makes the lack of rotational alignment of the chain more obvious. These micrographs show the ability of the particles to assemble into chains, as seen in Figure 6.1, but also open more questions about the chain structure. It should be noted that the conformation and structure of the change might be affected by the drying process, which is necessary to prepare the materials for imaging by SEM. During drying, the chain conformation and structure might be disturbed by capillary forces, leading to significantly deformed chains. Additionally, alignment and orientations of the particles within chains could be similarly disrupted, making it difficult to evaluate the chain structure just from SEM micrographs. However, we can use comparison between the SEM micrographs and optical images of chains in liquid, such as in Figure 6.1, Figure 6.6, and Figure 6.7. From the optical images in these figures, it is clear that the chain sizes and conformations seen in the SEM results are similar to those seen in liquid. Additionally, the chains in liquid show a disordered stacking structure, similar to the SEM micrographs. Thus, even though the drying process will induce some changes in the chain structure, comparison with other results show that these micrographs are a decent representation of the structure of assembled chains in liquid.

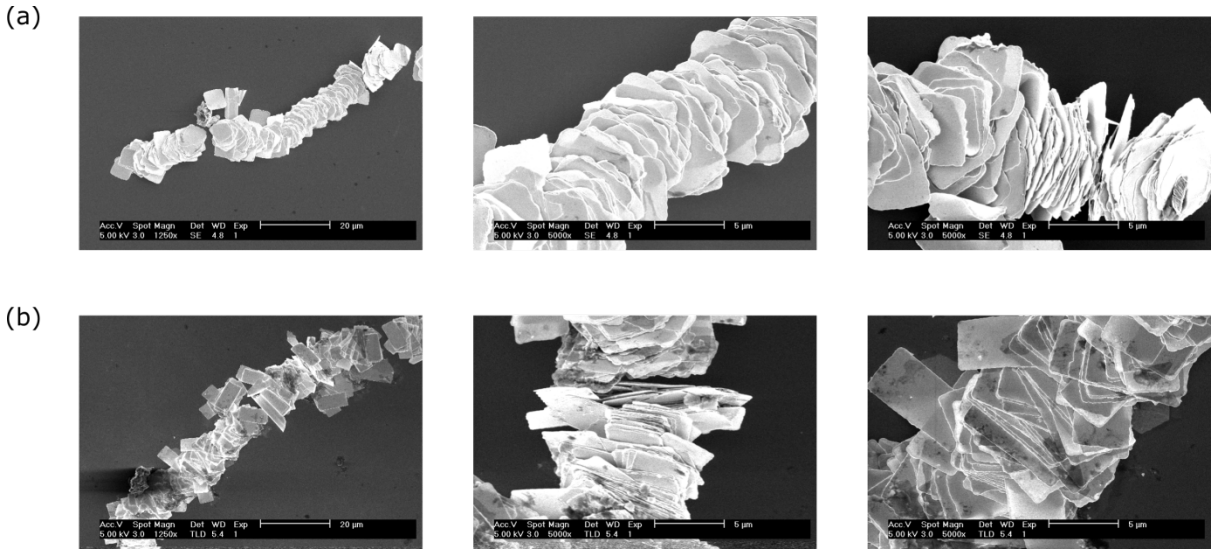

Figure 6.2: Assemblies of magnetic particles into chains
(a) 5 x 5 μm^2 and (b) 10 x 5 μm^2 particles were assembled into chains in liquid, and the liquid was then dried onto a silicon wafer. The chains could then be imaged using an SEM to understand the chain structure.

While these first assembly results in both types of particles are encouraging, further analysis is needed to how the asymmetry and offsets of particles in the chain develops.

6.2.3 Analysis of chain assembly

To help understand the real assembly behaviour observed in the particles chains, we must first understand the ideal assembly behaviour, and then analyse the variations of force and adhesion between particles in the chain that could lead to deviations from the ideal behaviour. Previously established methods for calculating particle interaction energy and force can be implemented here to find a theoretical model for the chain assembly that can then be compared with the experimental results.

Calculation of ideal assembly behaviour

The starting point for analysing chain assembly is the energy landscape of the interacting particles. The magnetic interaction energy can give a theoretical minimum for the system, which can then be compared with the experimental results. These calculations were conducted using the Rhodes-Rowlands interaction energy.[69] For this calculation, the interaction between two magnetic blocks was found. The position of one block is fixed, while the other block is moved laterally in steps of 0.1 μm at a set separation. The geometry used for the calculation is shown in Figure 6.3 (a). The calculation can then be repeated at a number of different separation distances, calculating the energy profile of the particles as they approach each other. In each case the magnetic blocks are taken to be 10 nm thick

with a magnetization of 330 emu/cm^3, so they have a magnetic moment equivalent that of the magnetic multilayer.

Figure 6.3 (b) and (c) shows the energy profiles are a separation of 10 μm, 1 μm, and 100 nm for particles with lateral sizes of 5 x 5 μm^2 (b) and 10 x 5 μm^2 (c).

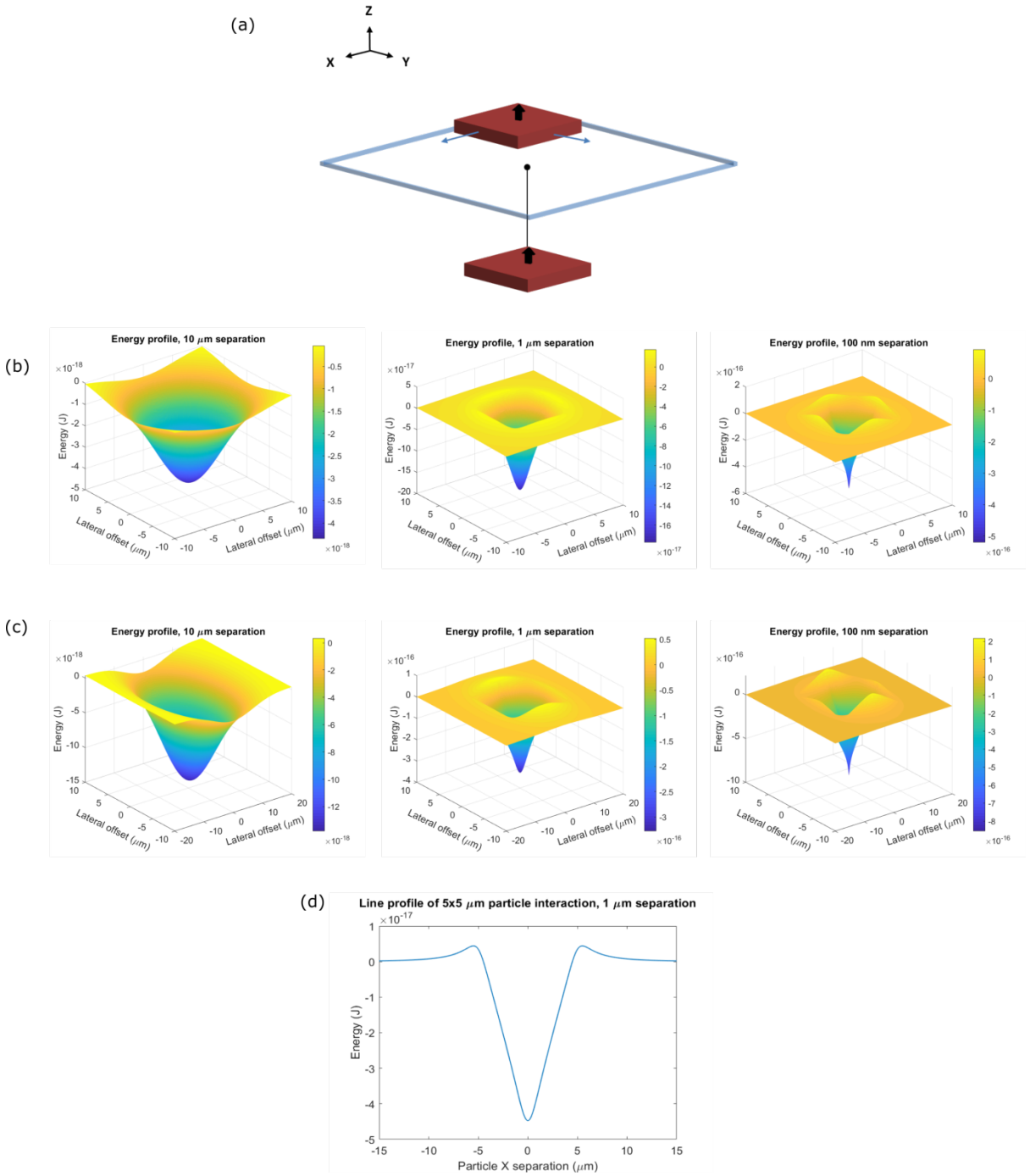

Figure 6.3 Energy profiles of particle assembly
Energy profiles for the magnetic interaction energy between two particles. One particle is held fixed while the other is moved laterally, at a fixed separation. The lateral separation given is the centre-to-centre separation of the particles. (a) shows the geometry of the particles for the profile calculation. The profiles show where the energy minima and maxima exist for this interaction. The profiles were calculated for particles with (b) 5 x 5 μm^2 and (c) 5 x 10 μm^2 lateral areas. (d) presents a line profile of the interaction energy between two 5 x 5 μm^2 particles, varied over the x-direction with a separation of 1 μm. The particles have a thickness of 10 nm and a magnetization perpendicular to the surface normal with M = 330 emu/cm^3.

It is clear that the lowest energy point for all cases is when the particles are completely aligned, with no lateral offset in either direction. At a long distance (10 μm) the energy landscape is always decreasing toward the completely aligned state. As the particles become closer, small energy barriers exist when the particles edge overlap (Figure 6.3, d), due to the opposite sign of the magnetostatic fields of the two particles at this point as the field curls around the particle edge. However, it is not likely that this barrier is the origin of the non-ideality seen in the experimental assemblies. If the particles can overcome this barrier, they should be able to reach the global energy minimum and assemble in an aligned fashion. If they cannot, then they should not be able to assemble at all.

The overall energy picture can only establish a baseline for how the assembly behaviour should occur ideally. However, it does not give any evidence to help explain the experimental assemblies seen.

Variations from ideal assembly

In order to understand the origin of the variations in the real assemblies, we can calculate the forces involved in the assembly process. The different directional components of the force (X, Y, Z) drive the assembly of particles in different ways. The geometry and directions defined in Figure 6.3 (a) will also be used for the force calculations. The Z force is responsible for drawing the particles together parallel to the surface normal, while the X and Y force will drive the lateral alignment of the particles. In these PMA particles, where the magnetization is parallel to the surface normal, the Z force will dominate, as the largest component of magnetization is along this direction. Figure 6.4 outlines the force profiles for the interaction of two 5 x 5 μm^2 particles, set up in a similar fashion to the energy profiles calculated in Figure 6.3.

Over the whole landscape of force, the peak Z force is 5 – 10 times greater than the peak X force. This remains true at different Z separations between the particles. Figure 6.4 (c) shows a direct comparison of the Z and X forces for the full range of Z separations as the particles approach contact. In each case, the lateral (X) offsets was taken at the point of peak X force from the previous force profile calculations for separations of 1 μm and 100 nm. Even when using the point of peak X force, the Z force is always larger than the X force, becoming significantly so as the particles assemble (reach a Z separation of 0).

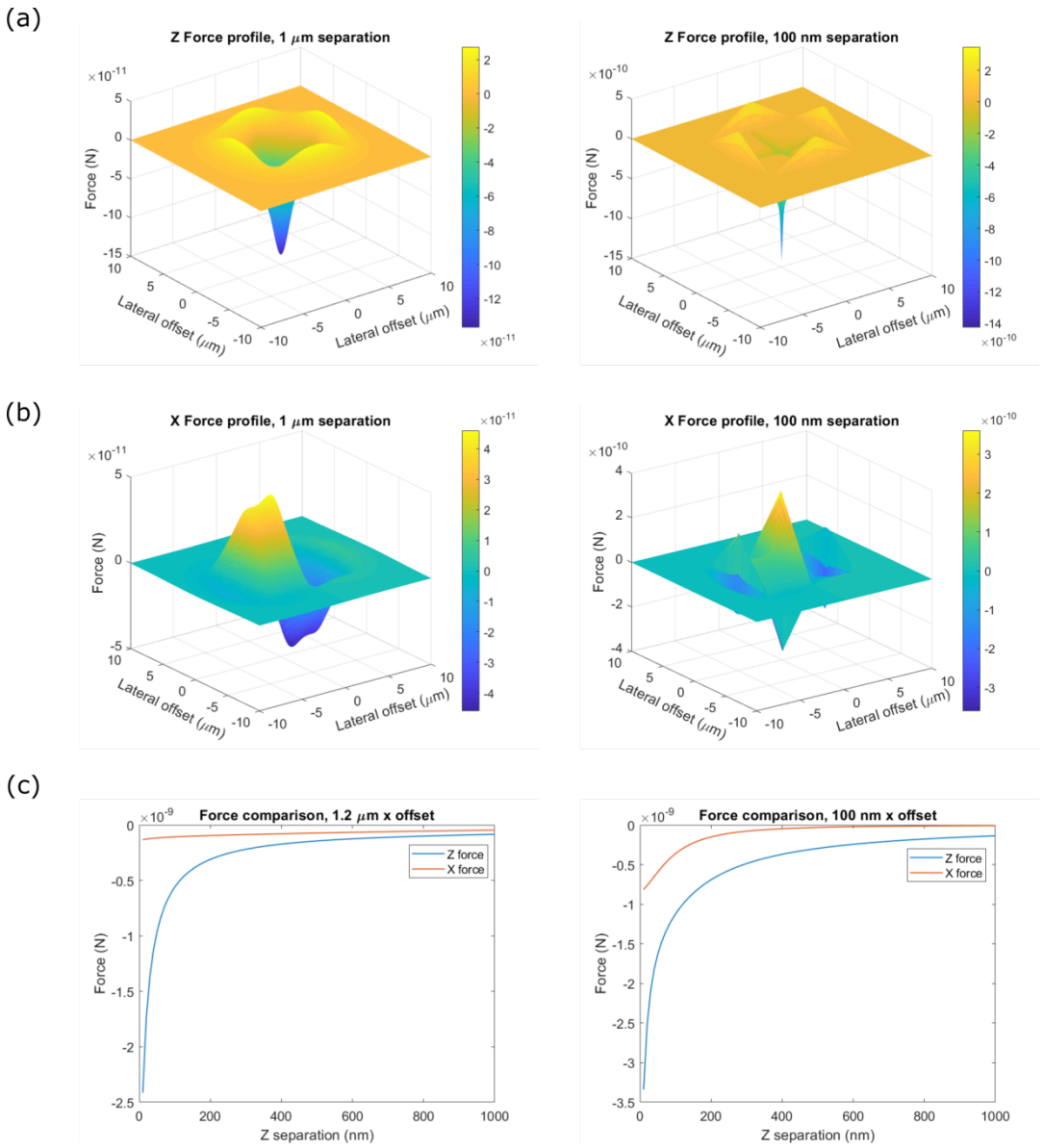

Figure 6.4 Force profiles of particle interaction
The forces between two particles are calculated. One particle is held fixed while the other is moved laterally, at a fixed separation. The force profile is calculated for the (a) Z force (parallel to the particle surface normal) and (b) the X force (perpendicular to the surface normal). (c) shows a comparison of the Z and X force for a set lateral offset and over a range of separations. The calculation was done for a 5 x 5 μm^2 particle with a thickness of 10 nm and magnetization M = 330 emu/cm^3.

Because of this difference in magnitude of the force components, it is possible that when two particles assemble, they will likely make contact before reaching the ideal lateral alignment. However, if the particles can continue to align after making contact, then they should be able to reach a completely aligned state. By calculating the energy involved in the contact, or adhesion, of the two particle surfaces, we can find if assembly will continue after particles come into contact, or if the assembly will be stuck in such a non-aligned position.

As surfaces come into contact, a number of forces influence their adhesion. Examples of these include van der Waals, electrostatic, capillary, and Casimir forces.[70–73] These forces are especially relevant in micro- and nano-sized objects, where the larger surface area-to-volume ratio of the smaller objects means any surface effects have a greater relative effect on the objects. These phenomena are intensively studied to understand 'stiction' in micro- and nano-electromechanical systems, and this knowledge can be translated to help understand the energy and forces of particle adhesion in our assemblies.[73]

To quantify the adhesion behaviour of the particles, the energy of adhesion of two platinum surfaces in water was found. While the outside surfaces of the particles are either Ta on one side and Pt on the other, the adhesion of Pt surfaces was used to simplify the calculation. The work, or energy, of adhesion is the amount of energy needed to separate two surfaces in a specific medium. The work of adhesion for two Pt surfaces in a water medium can be defined as

$$W_{Pt-Pt-Water} = W_{Pt-Pt} + W_{water-water} - W_{Pt-water} - W_{Pt-water} \qquad \textit{Eq. 6-1}^{70}$$

where W is the work of adhesion (J/m^2) for the various interactions. In the formulation, the work of adhesion of two Pt surfaces in water is calculated. When the Pt surfaces are separated in water, first energy is needed to overcome the adhesion between the Pt (W_{Pt-Pt}). From the separation of the Pt, two new Pt-water interfaces form ($W_{Pt-water}$), which is an energy benefit, reducing the overall work required. Additionally, the water must separate to create these new interfaces ($W_{water-water}$). This calculation can be similarly considered in terms of surface energy, where the separation of two Pt surfaces in water would lead to the creation of two Pt-water interfaces and the destruction of one Pt-Pt interface. For two surfaces to come unstuck and continue moving after contact, the work of adhesion must be overcome. This value will represent the barrier to continued assembly once particles have come into contact.

While resources do exist for defining surface and adhesion energies, many material combinations are not well-defined. To estimate the work of adhesion in this case, we will draw from a number of different sources to find approximate values for W_{Pt-Pt}, $W_{water-water}$, and $W_{Pt-water}$. We will simply define is $W_{water-water}$, as the separation of water from itself will lead to the generation of two new water-air interfaces. We can then define $W_{water-water} = 2\gamma_{water-air}$, where the surface energy $\gamma_{water-air}$ is the energy of the water-air interface, which is equal to 72 mJ/m^2.[74] Similarly, $W_{Pt-water}$ has been calculated theoretically in a density functional theory study of metal-water interfaces.[75] In this study $W_{Pt-water}$ was found to equal 270 mJ/m^2. Lastly, to find W_{Pt-Pt}, experimental results for the adhesion of Pt microstructures can be used. This pull-off force between a Pt surface and a Pt-coated AFM tip (r_{tip} ~ 10 nm) in air was found to be 65 nN.[76] From this pull-off force and using the Johnson-Kendall-Roberts (JKR) model (*Eq. 6-2*) to connect pull-off force and

work of adhesion, this experimental pull-off force for the Pt-Pt interface can be translated into W_{Pt-Pt}. The JKR model, which is a model for defining contact force and adhesion between a sphere and a planar surface, is defined as

$$F_{pull-off} = \frac{3}{2}\pi RW \qquad \textit{Eq. 6-2}^{70,77}$$

Where F is the pull-off force (N), R is the radius of the sphere (m) and W is the work of adhesion (J/m^2). Using this model and the experimental results for a Pt-Pt surface referenced above, W_{Pt-Pt} can be estimated as 2800 mJ/m^2.

Having found or derived the necessary values, $W_{Pt-Pt-Water}$ can now be calculated. It is found to be roughly 2 J/m^2. While it is important to find a reasonable value for the work of adhesion, in order to compare the adhesion energy to other values quantitatively, this value still relies on many assumptions and should only be taken as an approximation of the adhesion energy. Primarily, the contact in this work is between two planar surfaces, while almost all available data (and the values used here) for surface contact is found between a sphere and a surface, and works studying two planar contacts has shown the different geometry does impact the adhesion, which will lead to an underestimation for our case.[78] Additionally the energy of surfaces for crystal structures such as Pt will vary with the specific crystal plane of the surface.[79] In this case we have assumed the Pt surface is the (111) plane. Pt(111) is the lowest surface energy plane, which could again lead to underestimation of the value from our method.

Even with these caveats, this approximate value can still be useful in understand the adhesion energy between particles. Figure 6.5 compares the adhesion energy and magnetic interaction energy driving alignment for two particles with varying amounts of lateral overlap. This overlap is defined as a percentage, where 100 % is complete overlap of the two particles. Figure 6.5 (a) shows the geometry used for the comparison. It becomes immediately clear that the adhesion energy is many orders of magnitude larger than the magnetic interaction energies. This shows that particles, once in contact, will become stuck and remain in the position defined by their original contact.

(a) (b)

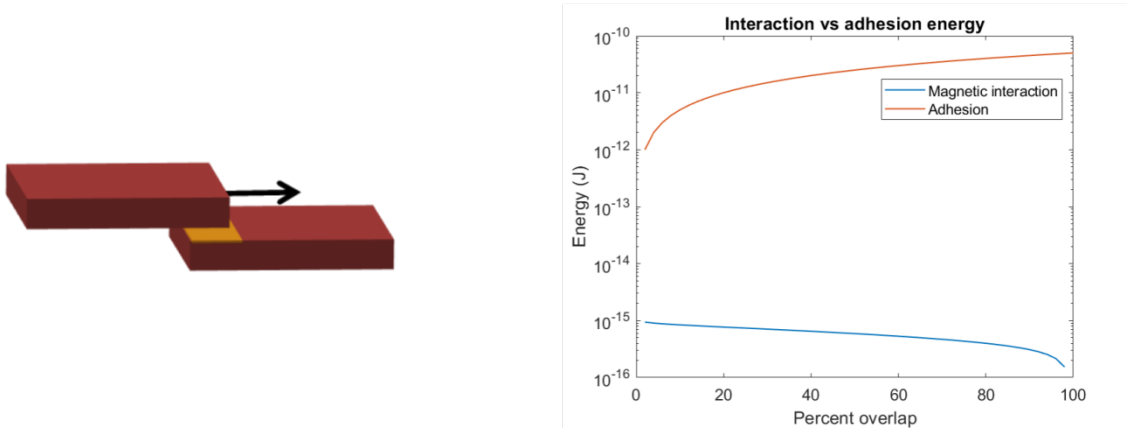

Figure 6.5 Comparison of magnetic interaction and adhesion energy
The magnetic interaction energy of two particles is compared with the surface adhesion energy. (a) defines the geometry of the particles, where the particles overlap by a percentage of their area to see how the different energies change with increasing overlap. (b) plots the two energies on a logarithmic scale. The calculation was done for a 5 x 5 μm^2 particle with a thickness of 10 nm and magnetization M = 330 emu/cm^3.

Combining this understanding of the adhesion energy with the profiles of magnetic interaction force (Figure 6.4) defined previously, it clear that particles will not be able to further orient after contact. If lateral (X and Y) forces are not sufficient to fully align the particle before contact, in comparison to the larger Z force, as calculated earlier (Figure 6.4), misalignment could result. However, this pure force analysis does not consider the order of magnitude difference in drag coefficient between a thin sheet when side and face on to flow. Other potential explanations can account for the assembly alignment seen. One is the many-body interaction of large numbers of particles assembling together. While our analysis looked at pair-wise interaction, real assemblies will have hundreds or thousands of particles all interacting at once, which could lead to interaction energy minima at locations not predicted in the ideal pair-wise calculation. Additionally, once a misaligned chain forms, it will shift the energy minima for alignment of new particles assembling to the chain, which would further perpetuate such misalignments.

What is clear, from the experimental results and adhesion calculation, is that once the particle come into contact, they will become stuck due to adhesion and not be able to continue perfecting the assembly process. This is the origin of the non-ideal behaviour seen in the real particle chains. Potential avenues for mitigation could include changing the adhesion energy of the surfaces through chemical modification of the particle surfaces. However, since the particles are still able to effectively chain in this non-ideal manner, mitigation strategies will be left for future study.

Having experimentally observed and characterized the assembly of particle chains, the behaviour of the chains will now be characterized.

6.3 Behaviour of particle chains

One of the primary advantages of magnetic particles and structures is the possibility to use magnetic fields for their manipulation. As discussed previously, this capability has led to interest in magnetic assemblies and structures being used as for microrobotics and micromanipulation. In this work, one of the motivations for creation of a zero-field assembly system was to allow for magnetic field actuation of the assemblies, since an applied magnetic field is not needed to sustain the structure of the assembly.

Working with the particles and chains created above, different magnetic field conditions will be used to test the response of the chain to magnetic fields of different magnitude and frequency. The PMA particles and chains will move to keep the magnetic moment of the chain, which is along the long axis of the chain, aligned with the applied field, to minimize the Zeeman energy of the system.

6.3.1 Actuation under field

Particle chains of a number of different lengths were subjected to linearly oscillating magnetic fields with magnitudes of 10 – 1000 Oe and frequencies of 0.25 – 4 Hz. Along with the applied field parameters, chain length will also influence the chain behaviour, as will be seen below. Unfortunately, the length of assembled chains cannot be controlled. Observations were made of the behaviour of short (~60 μm) and long (>100 μm) chains, as these were seen to display distinct behaviours.

Chain bending and breakdown

Chains showed a variety of bending and breakdown under different applied field conditions. Due to the influence of chain length, we will begin with the simpler short chain case, seen in Figure 6.6. Under a small magnitude applied field, the chain straightens and then bends as the field is reduced. As the direction of the applied field is reversed, the chain flips to align itself to the applied field, and displays similar bending and straightening behaviour.

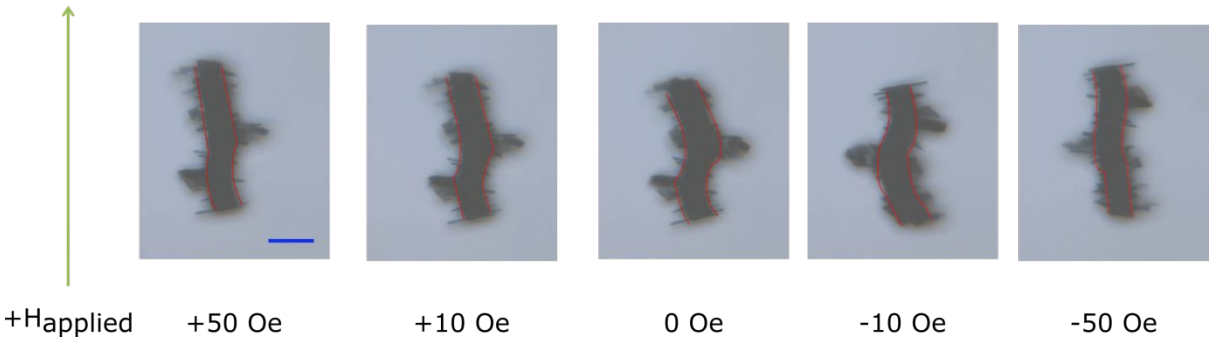

Figure 6.6 Bending of short chain under applied field
A short chain of magnetic particles is subjected to an applied magnetic field. The bending and straightening of the chain can be seen as the applied field is reduced and then increased. The chain is composed of 10 x 5 μm^2 'sandwich' type particles. The blue scale bar corresponds to 20 µm. Lines are provided to guide the eye.

The behaviour in Figure 6.6 is taken under a series of static applied fields, but it is mimicked as the frequency of the applied field increases. With increasing frequency the transitions between states occur more quickly but maintain the same behaviour. Additionally, changes in field magnitude do not lead to notable changes from this simple straightening and bending behaviour. For the short chains, it is unclear if the bending is due to the non-ideal construction of the chain or an attempt to lower the overall chain magnetostatic energy by forming a ring state to achieve flux closure. The origins of bending become clearer in longer chains, which are explored below.

When applying a field to long (>100 µm) chains, there are two distinct static states which combine to form different dynamic responses. When a static field is applied, the chain straightens and aligns with the field. When the field is turned off, the chain curls into a flux-closed ring state. If the field is reversed, the chain will straighten again and align with the field direction. When applying dynamic fields, we see three distinct responses that relate to these static states, outlined in Figure 6.7 below.

The first response is a dynamic ring state, where the chain curls and uncurls as the field oscillates. This happens at low fields, when the frequency of the oscillation is low (low field sweep rates). The ring forms as the field oscillation passes through zero. Then, as the field increases, the chain will straighten and align to the field direction. This can be seen clearly in Figure 6.7 (a). The second state, seen in Figure 6.7 (b), is chain breakdown. With a large magnitude and high frequency applied field (high field sweep rates), the chain breaks apart into smaller segments as the field oscillates. The chain breaks down as the field reverses and rebuilds as the field saturates, leading to the various structures imaged during the process. In this breakdown state, the ring state is no longer seen, likely because the small segments created in this process are too short to create a full ring. A third categorization of chain behaviour can be made when both the breakdown and ring states are present, which is shown in Figure 6.7 (c). This range, which we will call intermediate behaviour, is the cross-over region from pure ring behaviour to pure breakdown of the chain.

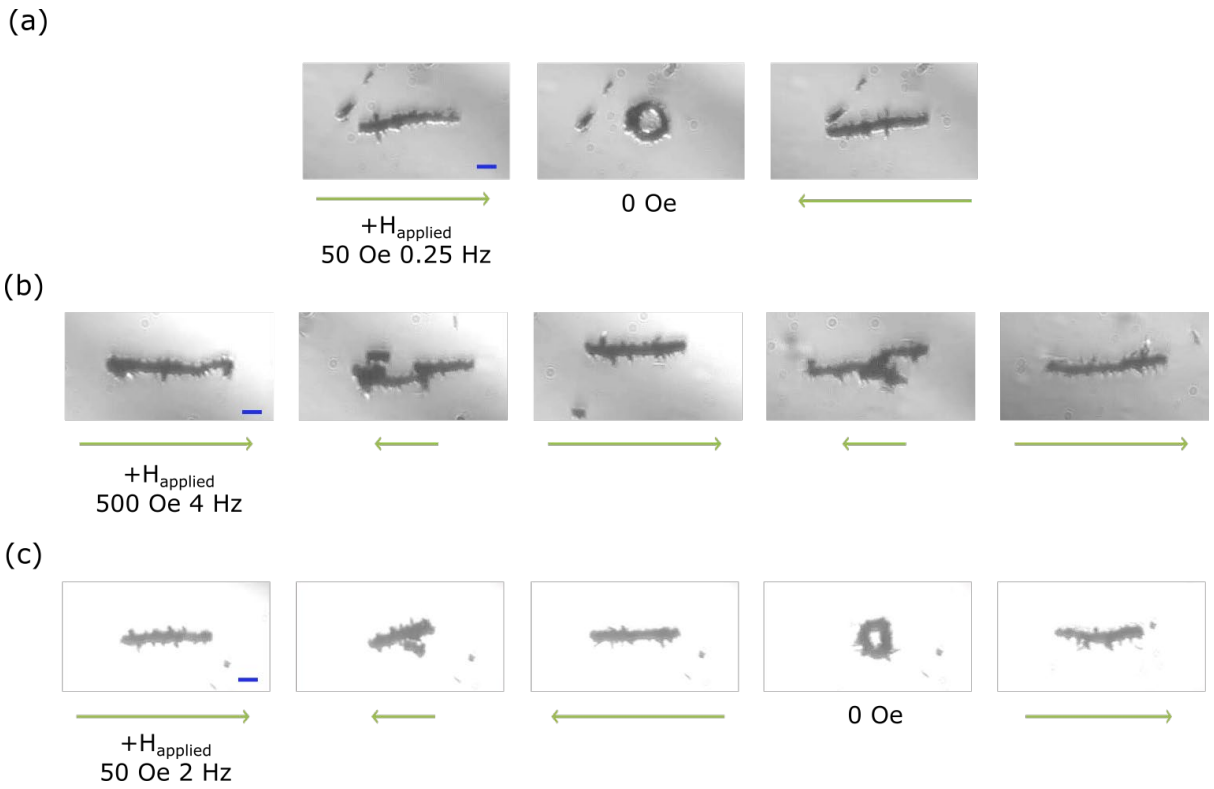

Figure 6.7 Different chain behaviours under an applied field
Three different behaviours are seen in chains of magnetic particles under an oscillating applied field. (a) shows the chain alternating between a zero field ring state and a straightened state. (b) shows the chain breaking apart under a high amplitude oscillating field. (c) shows a combination of the ring behaviour seen in (a) and the chain breakdown seen in (b). The chains are composed of 10 x 5 μm^2 'sandwich' type particles. The blue scale bar corresponds to 20 µm.

Along with the three states outlined above, we can also see bending in long chains, similar to that of the short chain behaviour. This bending, shown in Figure 6.8, can be seen when part of the long chain is anchored, either to other magnetic structures or through frictional forces to the substrate below. At a small enough applied field magnitude (10 Oe), the anchored part of the chain does not have sufficient energy to move, while the free end does, causing the highlighted part of the chain to straighten. As the field decreases, the free end attempts to move into a ring state or flip to align with the field, which is prevented by the anchored portions. Under low amplitude oscillating field, it ends up acting as a bending arm, actuating with the field sequence.

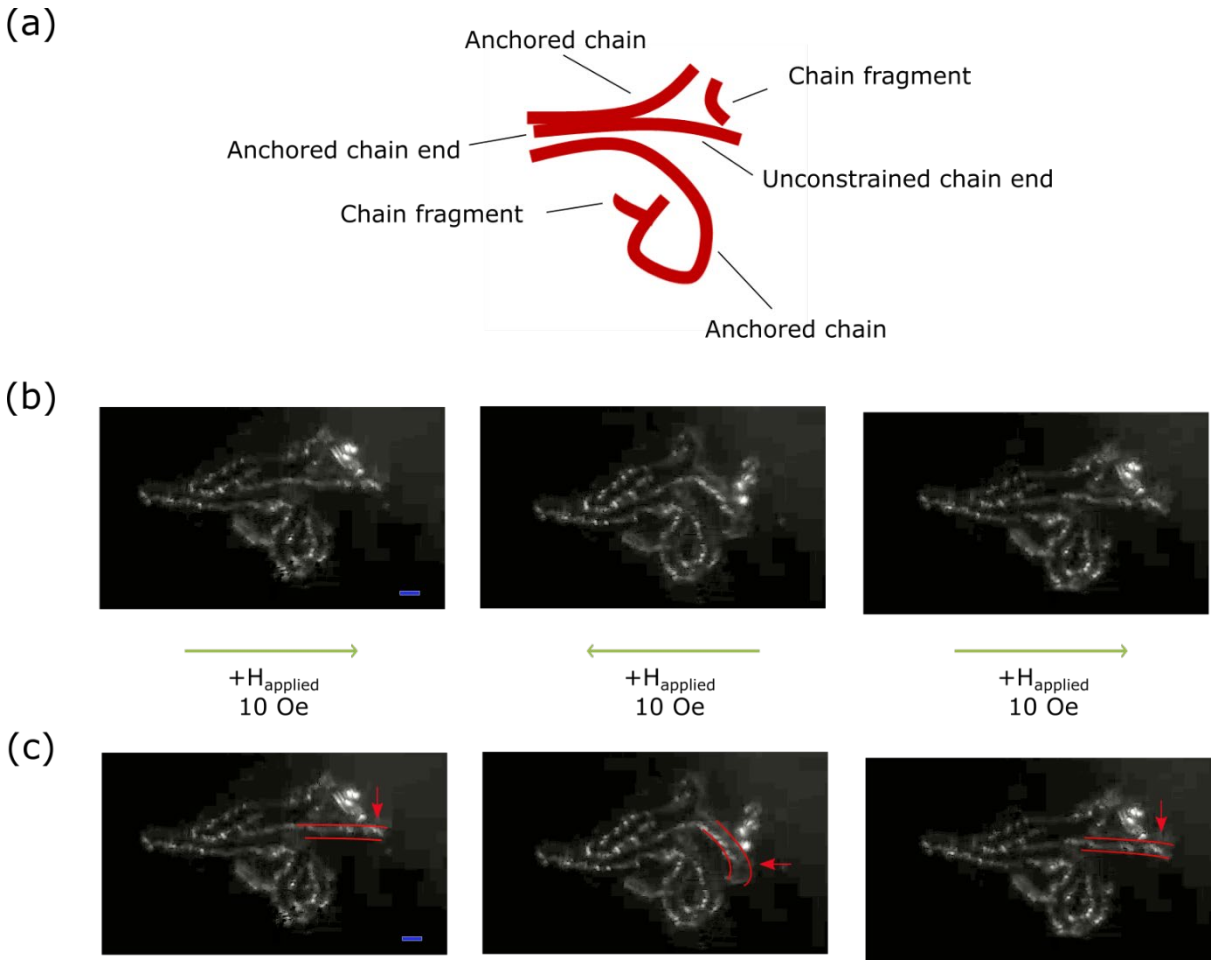

Figure 6.8 Bending of long chain under applied field
A large multi-chain assembly of magnetic particles is subjected to a small magnetic field, which causes local bending and straightening of a section of the chain. (a) shows a schematic diagram of the different chains in the assembly, including the unconstrained chain end which is seen to bend. (b) and (c) show the real chain structure under a changing magnetic field, with annotations in (c) highlighting the bending chain. The chain is composed of 10 x 5 μm^2 'sandwich' type particles. The blue scale bar corresponds to 20 µm.

A number of different field sequences and the resultant behaviours are plotted in Figure 6.9 below. The special case of bending is only seen at very low (10 Oe/s) field sweep rates. The pure ring state can be achieved by small to intermediate (10 – 100 Oe/s) field sweep rates. On the other hand, the complete breakdown of the chain is only seen at high field sweep rates (≥500 Oe/s). The intermediate state can be found at field sweep rate values between those of the ring and breakdown states. From this information, we can see how the rate of change of the applied magnetic field can be used to access different dynamic states of the magnetic chains.

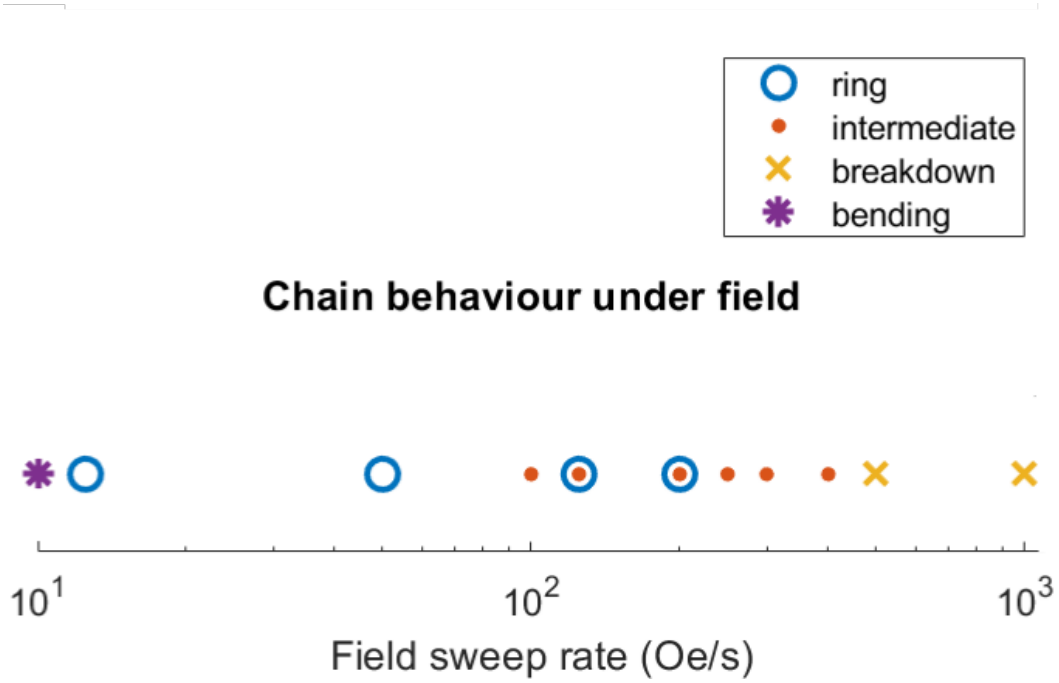

Figure 6.9 Overview of chain behaviour under applied field
The different behaviours outlined in Figure 6.7 are shown for increasing field sweep rate (Oe/s).

There is some overlap between the regions of intermediate and ring behaviour, which have resulted from different experiments at the same sweep rate. These differences could be due to slightly different chains lengths (all >100 μm) being used in the experiments. We can view this region as the onset of the breakdown behaviour that differentiates the ring state from the intermediate state.

Potential chain functions

The magnetic chains show interesting field response, allowing a number of different states to be accessed depending on the specific applied field sequence. The bending of the chains shows how it can potentially fulfil applications requiring actuation or flexibility, and the breakdown could allow re-configuration of the chain into different assembled structures. The different responses open up a number of potential functions for these chains.

The first is the chain as a pincer or tweezer that could be used to capture or manipulate objects. Under a small applied field magnitude and frequency, a chain can be repeatedly opened and closed, alternating between a straight, saturated chain and a ring shape at zero applied field (Figure 6.10). The chain was able to stay in position and reproducibly open and close at the same point over 10+ field cycles and always appeared to open and close at the same point on the chain.

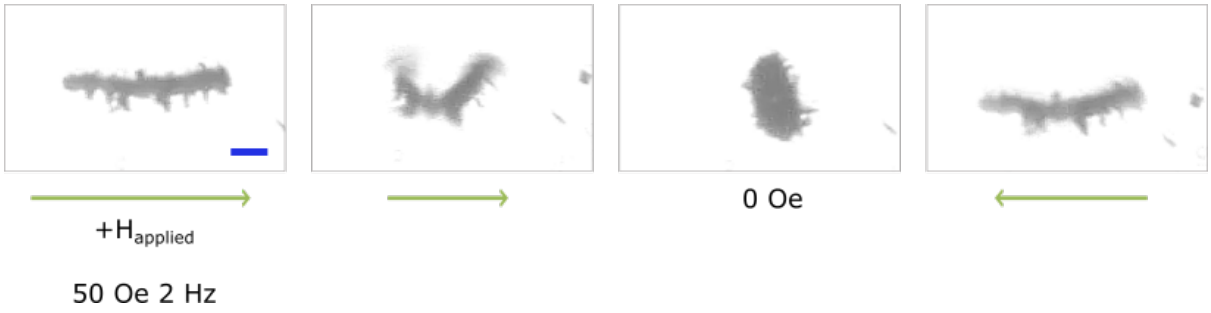

Figure 6.10 Chain as a pincer
The ability of a chain to act as a pincer or tweezers, reversibly opening and closing under a specific field sequence, is demonstrated. The chain is composed of 10 x 5 μm^2 'sandwich' type particles. The blue scale bar corresponds to 20 μm.

While the right field sequence can be used to induce similar behaviour in chains of sufficient length (those long enough to form rings), not all cases showed repeatable opening and closing at the same position along the chain, which would reduce the functionality of such a device. However, when combined with the chain bending seen in short and fixed chains (Figure 6.6, Figure 6.8), it is clear that the assembled magnetic chains have the potential to actuate or manipulate other particles in liquid, through their ability to transduce force from an applied magnetic field, although the level control and reproducibility of such behaviour must be improved.

Second, both short and long magnetic chains showed motion on the surface of the silicon chip on which they were sitting, seen in Figure 6.11. A series of images show the motion of a short and long magnetic chain under an oscillating magnetic field. As the field is applied, the chains have a net motion in one direction. While it is interesting to view such motion as some form of surface 'walker' or similar micro-machine, it is difficult to see how the random opening and closing of the chain could induce any net motion in one direction. It is possible that some symmetry-breaking chain shape, such as the one in Figure 6.11 (a), would allow the chain to interact with the surface anisotropically, it is still unclear if such a system could create net motion.

It is possible that the movement is induced by magnetic field gradients, as the movement of particles and chains has been previously seen under large applied field gradients. In this case, the particles shown in Figure 6.11 did not move under static fields of 50, 100, or 250 Oe, but was able to move under a 50 Oe oscillating field. It is possible that the field gradient at 50 Oe is sufficient to move the chain, but is not enough to overcome the static friction between the chain and the silicon surface. Thus, only when dynamic fields are applied, causing the chain to rotate and detach from the surface, can the gradient then induce motion.

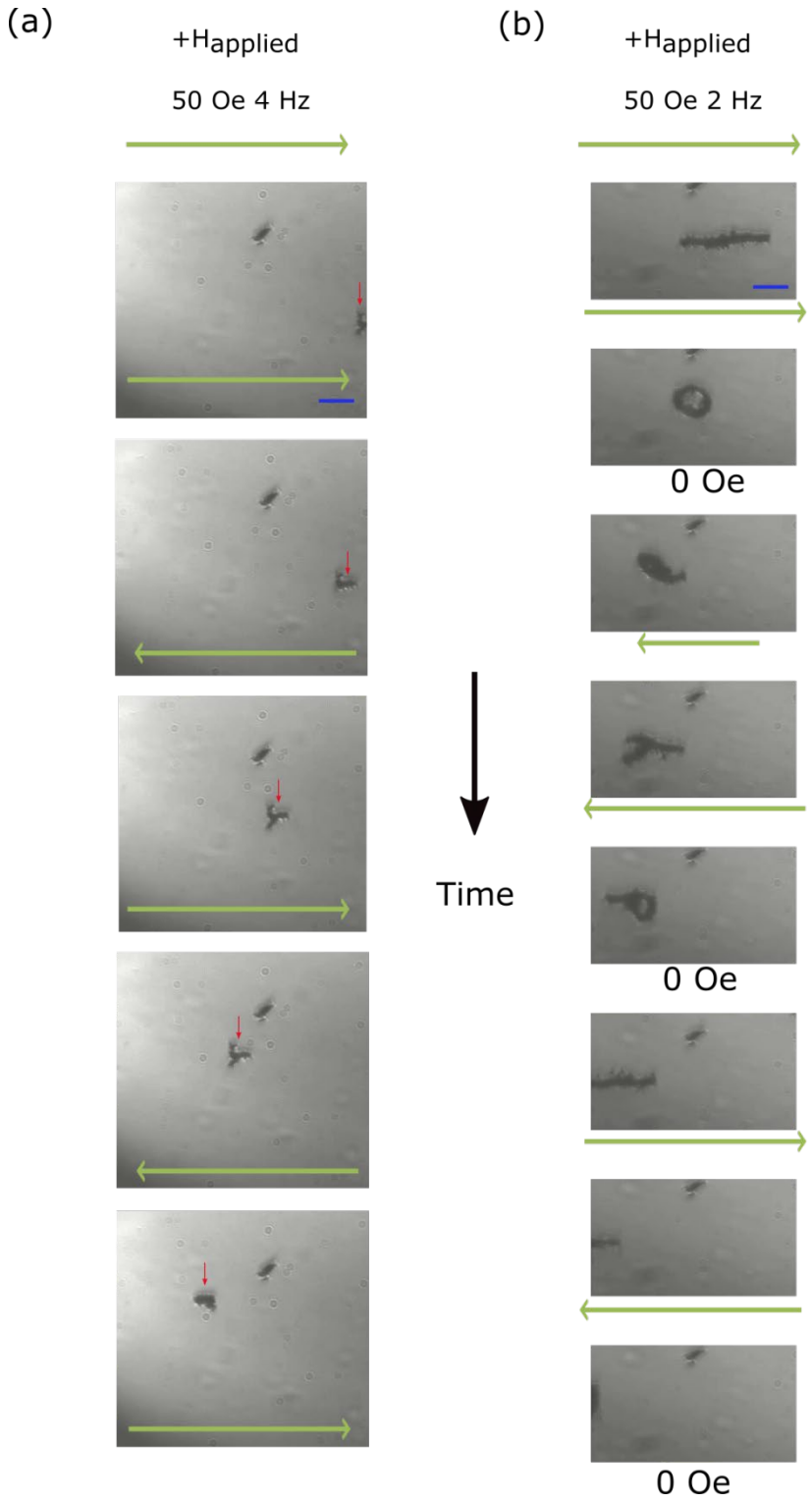

Figure 6.11 Chain motion
Two examples of chains moving under an applied magnetic field are shown. In (a), a short particle chain, denoted by the red arrow, move across the fixed viewing frame. (b) shows a longer particle chain similarly moving across a fixed frame. The chains are composed of 10 x 5 μm^2 'sandwich' type particles. The blue scale bar corresponds to 40 µm.

Even though field gradients likely account for the motion seen here, there are still interesting opportunities for micro-walkers built from such chains. The use of rotating fields with magnetic chains has been effective in powering surface walkers and could represent a potential next step for motion in these chains.[80]

6.3.2 Theoretical model of chain response

In order to understand the different response of the particle chains to the applied magnetic field, theoretical models were developed to explore the cases of chain bending and breakdown. In the case of chain bending, we will analyse the length dependence seen in the ring configuration, looking at how the magnetic interaction energy changes as the chain bends. The case of chain breakdown will be modelled using a combination of the strong adhesion energy which holds the particles together and the Zeeman energy that drives the rotation of the chain segments, to understand how the magnitude of the applied field can influence the breaking of smaller chain segments.

Model for chain bending

Chain bending can be viewed as a competition between the increase in inter-particle interaction energy within the chain as it bends and the decrease in overall magnetostatic energy as the chain achieves flux closure by connecting its ends. Flux closure is a common method by which magnetic textures, such as domains, lower their magnetostatic energy.

The chain and ring states have been studied extensively in the case of spherical magnetic dipoles and similar spherical nanoparticles. In this simple case, it is found that chains with as few as four particles can lower their overall energy by forming a ring.[81] Thus, for almost all chain lengths of spherical dipoles, the ring state is the lowest energy state. Chains of cubic magnetic particles have also been studied. Experimentally, cubic magnetite nanoparticles showed a flux-closure ring state for particles of a certain size (~40 nm), but it was not seen with smaller nanoparticle sizes.[82] Simulation works has found that ideal cubes with magnetization perpendicular to one of the cube faces will form chains.[83] The perfect cube was found to never form a lower energy ring state, but by slightly rounding the cube shape (making it more sphere-like), the ring state can become the lowest energy state, with chain lengths of 4 – 20 particles, depending on the degree of roundedness of the cubes .[84] Drawing on these results, we can understand how the ring state exists with our particle assemblies, but also see how the particle shape and magnetization impacts the assembly parameters, like chain length, needed to reach this state.

With the planar particles in this work, chains reach much longer lengths (>>60 μm, 1300 particles) before this ring state can be accessed. The length of the chain is related to particle number using the 40 nm thickness of the magnetic particles. Due to the planar nature of the particles, the inter-

particle distance can change significantly when the chain bends, which is not the case in a chain of spherical particles, where the inter-particle distance is constant. Additionally, due to the stray field profile of the PMA particles, which is maximized at the particle edges, the stray field acting on adjacent particles can change significantly during bending. This change in stray field magnitude, both from the distance and angular offset of the particles in the ring state, will lead to a smaller interaction energy, following the equation $E = -m \cdot B$, where E is the interaction energy, m is the magnetic moment, and B is the magnetic flux acting on the moment. To find the interaction energy, the magnetic flux of 5 μm x 5 μm x 10 nm, uniformly magnetized blocks (M_s = 330 emu/cm^3) were used to represent the moment of the particle. The flux from the blocks was calculated using MuMax3, using cell sizes of 0.1 μm x 0.1 μm x 5 nm. An interpolation function was use with the field values to create smaller effective cells for this calculation. The stray field from one block on an equivalent, adjacent block was found. The adjacent blocks are touching along their edge, as shown in Figure 6.12 (b). The angle between blocks is found by dividing $2\pi/N$, where N is the number of particles in the chain, found by dividing the chain length by 40 nm, the thickness of one particle.

This change in pair interaction energy has been quantified for particle chains of different length, shown in Figure 6.12. This calculation is only for nearest-neighbour (adjacent) particles in the chain. Using only nearest-neighbour calculations will induce error in the result – for spherical dipole chains, the nearest-neighbour energy is 10 – 15% smaller when compared to the precise energy calculation, for both straight and ring shapes.[81,83] However, this model will allow us to simply compare with experimental results. Figure 6.12 (a) and (b) show schematics of the straight chain and ring geometries respectively. Figure 6.12 (c) shows the interaction energy between 2 neighbouring particles only. For the straight chain (Figure 6.12, a), the nearest-neighbour interaction is independent of chain length.

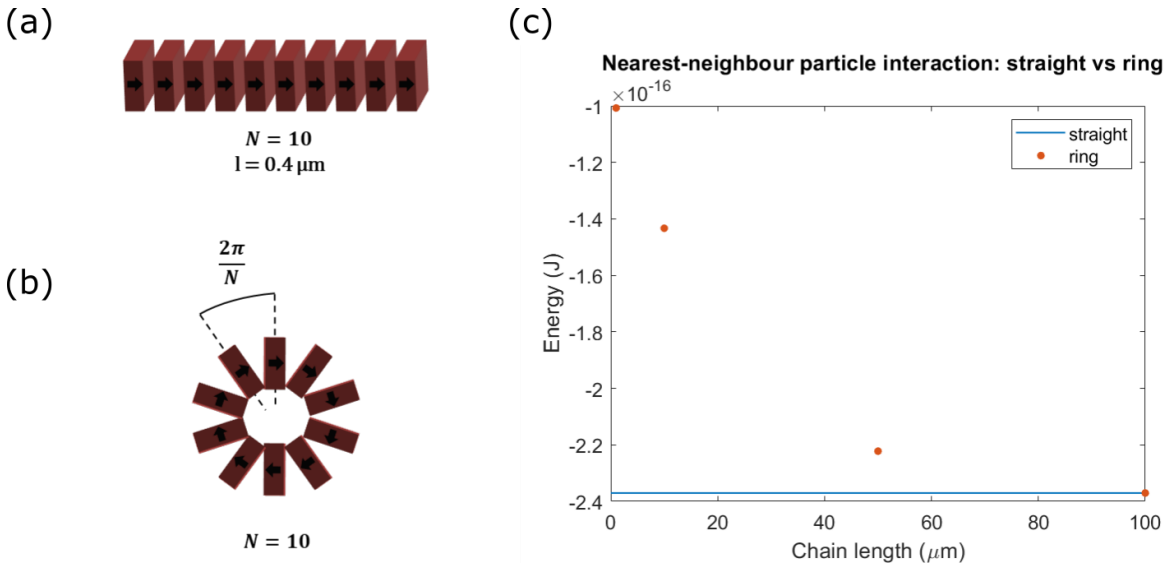

Figure 6.12 Energy comparison for straight and bent chains
The nearest-neighbour magnetic interaction energy for two particles in a (a) straight and (b) ring chain is compared. The energy of the straight chain vs the bent chain is given in (c) for a number of different chain lengths, which correspond to chains of N particles. In this case, the total thickness (magnetic + non-magnetic) of each particle is taken to be 40 nm, and calculations for the ring state were made for particles of 1 (N = 25), 10 (N = 250), 50 (N = 1250), and 100 (N = 2500) μm.

The ring state pair energy, E_{ring}, was calculated for chains of 1, 10, 50, and 100 μm. As expected, as the chain length increases- and therefore the angle $2\pi/N$ between neighboring particles in the ring decreases – E_{ring} is closer and closer to $E_{straight}$. At a chain length of 100 μm, the difference between E_{ring} and $E_{straight}$ is only 1.3%. The net energy penalty for bending is $(E_{ring} - E_{straight}) * (N - 1)$. The energy gain will be equal to the new nearest-neighbor interaction that is formed on closure of the chain, which is equal to the ring state energy calculated in Figure 6.12 (c). For the chains of 1, 10, and 50 μm, the energy penalty for forming a ring is on the order of 10^{-14} – 10^{-15} J. When balanced against the ~10^{-16} J energy gain for completing the chain, it is clear why chains of this length cannot form the ring state. However, for the 100 μm chain, the energy penalty is of the order of 10^{-18} J, compared to a gain of 10^{-16} J. Thus, it is more favourable to form a ring state at zero applied field. This matches well with the experimental results seen in short (< 60 μm) and long (>100 μm) chains.

By understanding the changes in magnetic energy that occur during ring formation from a magnetic chain, we can model the system and further understand the experimental results. Unlike chains of spherical particles, there is a much larger energy penalty for ring formation from our thin, planar PMA particles. However, there is also a strong driving force from the large magnetostatic energy of the high moment particles. Thus, the chain lengths must reach near 100 μm (2500 particles) before a full ring can be created. In shorter chains, limited bending can occur, but it is not energetically favourable to form a full ring. The ability to create larger straight chains and control the

chain bending at chains lengths in the 10 – 100 μm could lead to interesting applications with manipulation and actuation of cells, many of which fall in the same size range of the chains created here.

Model for chain breakdown

At large applied field magnitudes and frequencies, long chains break down into shorter segments, in order to stay aligned with the oscillating applied field. This behaviour of chain breakdown has been seen before in chains of magnetic micro- and nano-spheres, where oscillating or rotating fields were used to disassemble the chains.[52,85] Related experiments found that, in a rotating field, longer chains or higher applied frequencies made it more difficult for the chain to synchronously follow the magnetic field.[86] These reported results help understand what we see here. As the frequency of the field increases, the chain breaks down to more quickly align with the applied field.

The driving force for the chain alignment with the applied field originates from Zeeman energy, which is defined as $E = mH_{applied}\cos(\theta)$. E is the Zeeman energy, while m is the magnetic moment, H is the applied field, and θ is the angle between the applied field and the magnetic moment. When the direction of the applied field reverses, the chain is at a Zeeman energy of +mH, due to the 180° angle between the moment and applied field. Once the chain aligns itself with the applied field, the Zeeman energy of the system is –mH. Thus, the driving energy for a chain in a reversed field is equal to 2mH. In order for the chain to break into smaller segments, the strong adhesion forces between the different chain segments must be overcome. In this model we have ignored the magnetic interaction energies. These energies, which are an order of magnitude smaller than the adhesion or Zeeman energy, are balanced by the magnetostatic energy gain of the small chain flipping and aligning anti-parallel to a neighbouring chain segment. Since these two magnetic energy terms are opposing (interaction energy favours an aligned chain, while the magnetostatic energy gain favours a broken chain) and of similar magnitude, they cancel out. Using the balance of Zeeman and adhesion energy, we can now consider the breakdown behaviour.

As the frequency increases, the smaller segments can respond quicker. While the lowest energy condition is for the entire chain to rotate, as this incurs no adhesion energy penalty, we can see experimentally that the chains will breakdown at high field magnitudes and frequencies. A comparison between the Zeeman and adhesion energy (Figure 6.13, b) is made for different applied field values, different amounts of overlap between the adhesion contact point, and different chain segment lengths. By comparing these three values, it can be seen when the Zeeman driving force of a smaller segment of 10 – 40 μm can overcome the adhesion energy (using the Pt-Pt work of adhesion calculated previously) and break out of the chain. The comparison shows that field magnitudes of 250 and 500 Oe will give sufficient driving force to overcome small amounts of adhesion.

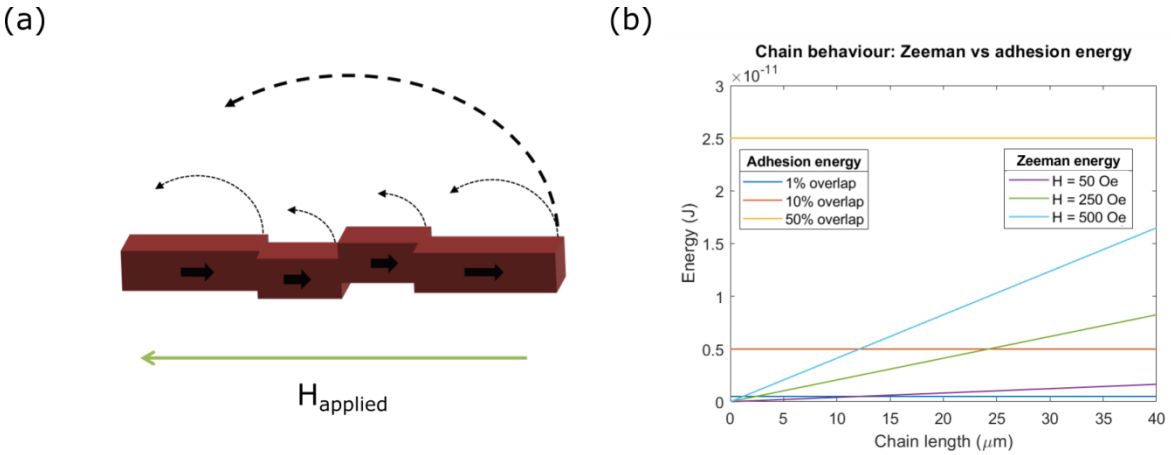

Figure 6.13 Energy comparison for chain breakdown
A comparison of adhesion and Zeeman energy is used to analyse the breakdown of particle chains. (a) shows a schematic diagram of a chain in an applied field opposite the magnetization direction of the chain. While the chain can move collectively to re-align its moment to the field (large arrow), the re-alignment could also occur by each smaller segment rotating to match the field. (b) compares different levels of adhesion energy (given by different amount of overlap of the adjoining particles/chain segments) with the Zeeman energy gained by the chain rotating to align with the field, for a number of different chain lengths and field strengths.

From this result, we can see why the long particle chains can break down in an applied field of sufficient magnitude and frequency. While the breakdown can only occur due to stacking flaws in the chain, where adjacent particles are not fully aligned, we have established that these flaws are common and intrinsic to the chains formed in this work. The combination of these flaws and a field of sufficient magnitude is enough to allow shorter chain segments to overcome their adhesion energy as they rotate to align with the oscillating applied field. This energy balance model does not incorporate the frequency of the applied field, which is also a necessary component for chain breakdown. The increased frequency of the applied field limits the time the chain has to respond to the field. Shorter segments can respond more quickly as they cover a shorter angular distance when rotating. Even though the breaking and rotation of the shorter segments is a higher energy process than rotation of the full chain, the high frequency can make this path preferable. High field sweep rate is needed to cause chain breakdown, as was outlined in Figure 6.9, and reduction in this quantity will lead to different chain behaviour.

6.4 Assembly of particle structures

Another potential application of the self-assembly of magnetic particles is the assembly of structures on a surface through templated assembly. This could potentially be used to create an anchored chain

structure, as a form of magnetic cilia for actuation or separation. Additionally, it offers an avenue to create interesting 3D structures. A combination of particle shape and the perpendicular magnetic anisotropy of the particles can be used to build structures up from the surface of a silicon chip, including 3D structures such as cantilevers or bridges that are difficult to achieve with conventional top-down lithography and deposition techniques.

6.4.1 Assembly onto chips

The templated assemblies in Figure 6.14 and Figure 6.15 are formed through a combination of lithographically defined patterns and magnetic particles. In the examples below, 3 x 5 μm^2 magnetic pillars were created on the silicon surface, with a 4 μm edge-to-edge spacing. Then, 10 x 5 μm^2 'sandwich' particles in liquid were deposited on the patterned chip. The particles were initially in an anti-parallel state and were saturated to a parallel state with a 4000 Oe applied field. The liquid was allowed to dry, leaving behind the assembled structures.

Bridges and cantilevers

Figure 6.14 shows two typical assembled structures observed. The particles magnetically align to the underlying pillar structures, which are saturated and fully remanent, either by forming a cantilever structure (Figure 6.14, a), where the magnetic particle attaches itself to just one pillar, or a bridge (Figure 6.14, b), where the particle bridges the gap between two pillars. The spacing between the pillars is set so that such a bridge structure is possible.

(a) (b)

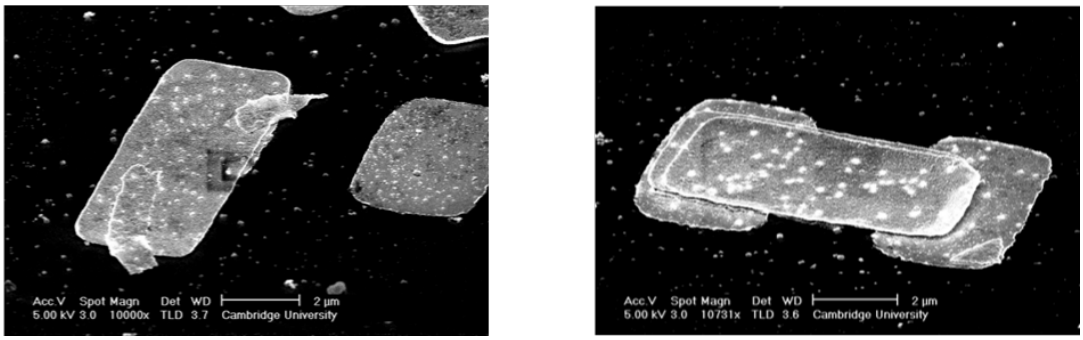

Figure 6.14 Templated assembly of cantilever and bridge
10 μm x 5 μm 'sandwich' particles were deposited on an array of 3 x 5 μm^2 magnetic pillars, assembling into (a) cantilever and (b) bridge structures.

While this result does show the potential of our particles for creating 3D templated assemblies, the images in Figure 6.14 and Figure 6.15 show some of the few successful assemblies created through this method. One limiting factor of this method is the interactions between magnetic

particles in the liquid. The magnetic particles must be saturated and remanent in order to interact with the magnetic pillars, but once the particles are saturated, they will create chain assemblies in the liquid, as we have seen previously. These large assemblies will quickly settle out of the liquid and not easily interact with the pillar structures. Thus, the liquid becomes heavily depleted of magnetic particles, leaving very few to reach the surface and interact with the templated structures. It is also difficult to attach the larger chain structures directly to an on-chip template, as the magnetic field produced by the pillars is not sufficient to direct the assembly of the large and heavy chain over a long distance.

An extension of the templated structure assembly is shown in Figure 6.15, where a series of pillars were patterned on the edges of two Au electrical contact pads. A gap was left between the pads, creating an open circuit which could be closed by the assembly of a particle bridge across the gap. After the deposition of particles, a small assembly of three particles did align itself and complete one of the contacts.

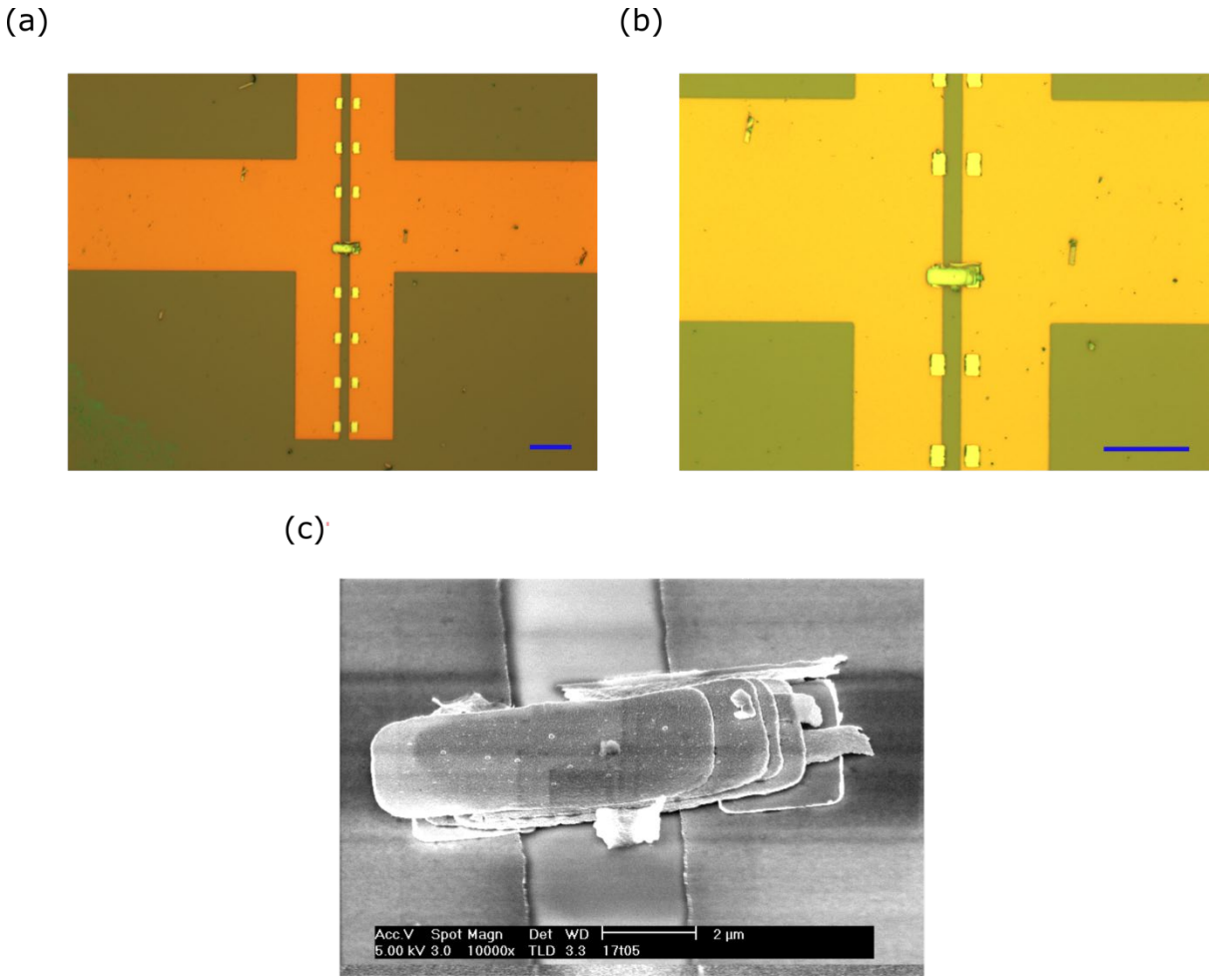

Figure 6.15 Templated bridge assembly on electrical contacts
A series of 3 x 5 µm^2 magnetic pillars were created on a gap between two electrical contact pads (20 nm Au). 10 x 5 µm^2 'sandwich' particles were deposited and assembled crossing the gap between the contacts. The blue scale bar in each case corresponds to 20 µm.

The assembled particles were able to successfully create an electrical connection between the two contact pads. Without any assembled particles, the contact structure read as an open circuit, but after the assembly of the particles, current was able to flow, with a resistance of ~80 Ω. This is an example of how these 3D templated assemblies could be used as a foundation for building a functional 3D device on a chip.

6.4.2 Simulation of assembly onto chip

To further explore the templated assembly results, energy profiles were calculated between a single 10 x 5 µm^2 particle and two 3 x 5 µm^2 pillars which have an edge-to-edge spacing of 4 µm. The pillars have a thickness of 10 nm, while the particle thickness is 20 nm. All components have a magnetization of 330 emu/cm^3. The calculations undertaken were similar to those for Figure 6.3. However, in this case, the point of zero lateral offset corresponds to the particle being centred over the

midpoint between the two pillars. The results, shown in Figure 6.16, initially show a single energy minimum at a large separation (a). However, as the particle-pillar separation decreases, three distinct minima emerge. The global minimum is when the particle is centred on the midpoint, spanning the two pillars to form a bridge structure (Figure 6.14, b). Smaller minima exist for when the particle is centred on only one of the pillars, which would lead to a cantilever structure (Figure 6.14, a).

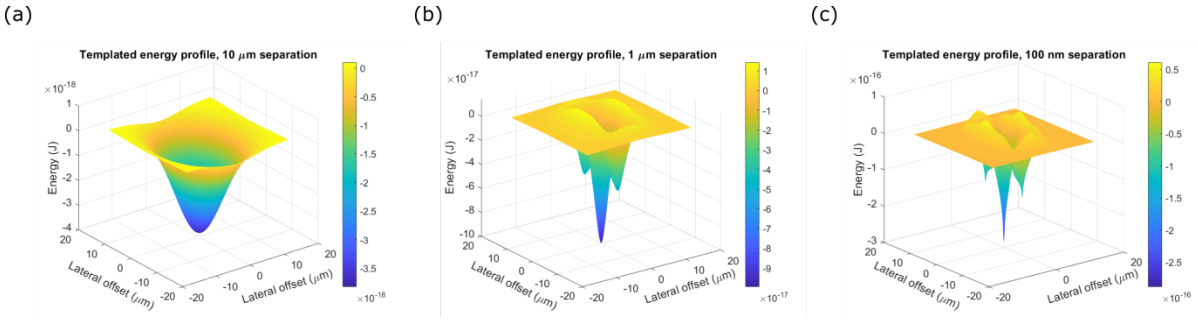

Figure 6.16 Energy profile of templated assembly
The magnetic interaction energy between a 10 x 5 μm^2 'sandwich' particle and two 3 x 5 μm^2 magnetic pillars is calculated. The pillars are fixed, with a lateral separation of 4 μm. The 10 x 5 μm^2 particle is moved laterally at a fixed separation relative to the pillars, to calculate the energy profile. The particle has a thickness of 20 nm, while the pillars have thicknesses of 10 nm. In all cases, the magnetization is set with M = 330 emu/cm^3.

If the particle approaches from a direction such that it moves into one of the smaller minima, there would exist an energy barrier for it to move from this state to the global minimum bridge state. In this way, we can understand how the particles can create both the bridge and cantilever structures, as the existence of the different energy minima allow for a variety of outcomes depending on the specific conditions and approach of the 10 x 5 μm^2 particle.

6.5 Conclusion

Particle assemblies were successfully created from the magnetic particles designed in this work. Following the assembly of chains in liquid, the structure and behaviour of the chains under applied fields was analysed. While the chains do not form an ideally stacked structure, we can understand the origins of this behaviour from the magnetic interaction and adhesion forces. By understanding the origin of the behaviour, it could be possible to design strategies, such as chemical functionalization of particles, to mitigate it. Additionally, the non-ideal assembly likely contributes to the breakdown of chains under high frequency applied fields. Along with this breakdown mode, a ring state was found in chains of sufficient length. Both the chain length and applied field parameters can be used to control the bending, actuation, and potentially motion, of the chains, opening up interesting opportunities to adapt this system for applications in microrobotics.

Along with the assembly of chains, simple 3D structures were assembled from patterned templates. This templated assembly demonstrates a different avenue for the self-assembly potential of this system, in which anchored chains or interesting 3D structures could be built. Templated assembly was not greatly explored, but offered as an option for another direction for this system and this research that could lead to interesting new results and applications.

Overall, the assemblies formed in this chapter prove the efficacy of the self-assembly system designed in this work. Moving from the optimized PMA films to controllable assemblies shows how the properties of these highly engineered films and materials can be translated into new environments and system, where they have the potential to improve on current applications and open new possibilities.

6.6 Reference

1. Thomas, J. R. Preparation and magnetic properties of colloidal cobalt particles. *J. Appl. Phys.* **37**, 2914–2915 (1966).
2. Ozaki, M., Suzuki, H., Takahashi, K. & Matijević, E. Reversible ordered agglomeration of hematite particles due to weak magnetic interactions. *J. Colloid Interface Sci.* **113**, 76–80 (1986).
3. Sutherland, D. N. Chain formation of fine particle aggregates. *Nature* **226**, 1241–1242 (1970).
4. Teixeira, P. I. C., Tavares, J. M. & Telo Da Gama, M. M. Effect of dipolar forces on the structure and thermodynamics of classical fluids. *J. Phys. Condens. Matter* **12**, R411 (2000).
5. Scholten, P. C. & Tjaden, D. L. A. Mutual attraction of superparamagnetic particles. *J. Colloid Interface Sci.* **73**, 254–255 (1980).
6. Zhou, L., Wen, W. & Sheng, P. Ground states of magnetorheological fluids. *Phys. Rev. Lett.* **81**, 1509–1512 (1998).
7. Tlusty, T. & Safran, S. A. Defect-induced phase separation in dipolar fluids. *Science (80-.).* **290**, 1328–1331 (2000).
8. Butter, K., Bomans, P. H. H., Frederik, P. M., Vroege, G. J. & Philipse, A. P. Direct observation of dipolar chains in iron ferrofluids by cryogenic electron microscopy. *Nat. Mater.* **2**, 88–91 (2003).
9. Singamaneni, S., Bliznyuk, V. N., Binek, C. & Tsymbal, E. Y. Magnetic nanoparticles: recent advances in synthesis, self-assembly and applications. *J. Mater. Chem.* **21**, 16819 (2011).
10. Glotzer, S. C. & Solomon, M. J. Anisotropy of building blocks and their assembly into complex structures. *Nat. Mater.* **6**, 557–562 (2007).
11. Pileni, M. P. Nanocrystal self-assemblies: Fabrication and collective properties. *J. Phys. Chem. B* **105**, 3358–3371 (2001).
12. Wang, M., He, L. & Yin, Y. Magnetic field guided colloidal assembly. *Mater. Today* **16**, 110-116 (2013).
13. Jiang, C., Leung, C. W. & Pong, P. W. T. Magnetic-Field-Assisted Assembly of Anisotropic Superstructures by Iron Oxide Nanoparticles and Their Enhanced Magnetism. *Nanoscale Res. Lett.* **11**, 1–12 (2016).
14. Lalatonne, Y., Richardi, J. & Pileni, M. P. Van der Waals versus dipolar forces controlling mesoscopic organizations of magnetic nanocrystals. *Nat. Mater.* **3**, 121–125 (2004).
15. Yan, J., Chaudhary, K., Chul Bae, S., Lewis, J. A. & Granick, S. Colloidal ribbons and rings from Janus magnetic rods. *Nat. Commun.* **4**, 1–9 (2013).
16. Yan, J., Bae, S. C. & Granick, S. Colloidal Superstructures Programmed into Magnetic Janus Particles. *Adv. Mater.* **27**, 874–879 (2015).

17. Smoukov, S. K., Gangwal, S., Marquez, M. & Velev, O. D. Reconfigurable responsive structures assembled from magnetic Janus particles. *Soft Matter* **5**, 1285–1292 (2009).
18. Al Harraq, A., Lee, J. G. & Bharti, B. Magnetic field–driven assembly and reconfiguration of multicomponent supraparticles. *Sci. Adv.* **6**, 5337–5345 (2020).
19. Yammine, E. *et al.* Particles with Magnetic Patches: Synthesis, Morphology Control, and Assembly. *Part. Part. Syst. Charact.* **37**, 2000111 (2020).
20. Zhang, W. *et al.* Quasi-One-Dimensional Assembly of Magnetic Nanoparticles Induced by a 50 Hz Alternating Magnetic Field. *ChemPhysChem* **11**, 1867-1870 (2010).
21. Ozdemir, T. *et al.* Assembly of magnetic nanoparticles into higher structures on patterned magnetic beads under the influence of magnetic field. *Nanotechnology* **21**, 6 (2010).
22. Timonen, J. V. I., Latikka, M., Leibler, L., Ras, R. H. A. & Ikkala, O. Switchable static and dynamic self-assembly of magnetic droplets on superhydrophobic surfaces. *Science (80-.).* **341**, 253–257 (2013).
23. Snezhko, A. & Aranson, I. S. Magnetic manipulation of self-assembled colloidal asters. *Nat. Mater.* **10**, 698–703 (2011).
24. Lee, Y., Lee, H., Messersmith, P. B. & Park, T. G. A Bioinspired Polymeric Template for 1D Assembly of Metallic Nanoparticles, Semiconductor Quantum Dots, and Magnetic Nanoparticles. *Macromol. Rapid Commun.* **31**, 2109–2114 (2010).
25. Ogawa, T. *et al.* Fabrication of Fe3O4 nanoparticle arrays via patterned template assisted self-assembly. *Nanotechnology* **17**, 5539–5543 (2006).
26. Snezhko, A., Aranson, I. S. & Kwok, W.-K. Surface Wave Assisted Self-Assembly of Multidomain Magnetic Structures. *Phys. Rev. Lett.* **96**, 078701 (2006).
27. Xie, Q., Davies, G. B. & Harting, J. Direct Assembly of Magnetic Janus Particles at a Droplet Interface. *ACS Nano* **11**, 11232–11239 (2017).
28. Xie, Q., Davies, G. B. & Harting, J. Controlled capillary assembly of magnetic Janus particles at fluid-fluid interfaces. *Soft Matter* **12**, 6566–6574 (2016).
29. Singh, G. *et al.* Self-assembly of magnetite nanocubes into helical superstructures. *Science* **345**, 1149–53 (2014).
30. Robbes, A. S. *et al.* Nanocomposite materials with controlled anisotropic reinforcement triggered by magnetic self-assembly. *Macromolecules* **44**, 8858–8865 (2011).
31. Goyal, A., Hall, C. K. & Velev, O. D. Phase diagram for stimulus-responsive materials containing dipolar colloidal particles. *Phys. Rev. E - Stat. Nonlinear, Soft Matter Phys.* **77**, 031401 (2008).
32. Mishra, S. R., Dickey, M. D., Velev, O. D. & Tracy, J. B. Selective and directional actuation of elastomer films using chained magnetic nanoparticles. *Nanoscale* **8**, 1309–1313 (2016).
33. Jiang, C., Leung, C. W. & Pong, P. W. T. Magnetic-Field-Assisted Assembly of Anisotropic Superstructures by Iron Oxide Nanoparticles and Their Enhanced Magnetism. *Nanoscale*

Research Letters **11**, 189 (2016). doi:10.1186/s11671-016-1406-9

34. Park, J. Il, Jun, Y. W., Choi, J. S. & Cheon, J. Highly crystalline anisotropic superstructures via magnetic field induced nanoparticle assembly. *Chem. Commun.*, 5001–5003 (2007).
35. Nie, Z., Petukhova, A. & Kumacheva, E. Properties and emerging applications of self-assembled structures made from inorganic nanoparticles. *Nature Nanotechnology* **5**, 15–25 (2010).
36. Xu, X., Friedman, G., Humfeld, K. D., Majetich, S. A. & Asher, S. A. Superparamagnetic photonic crystals. *Adv. Mater.* **13**, 1681–1684 (2001).
37. Ding, T., Song, K., Clays, K. & Tung, C. H. Fabrication of 3D photonic crystals of ellipsoids: Convective self-assembly in magnetic field. *Adv. Mater.* **21**, 1936–1940 (2009).
38. Krishnan, K. M. Biomedical nanomagnetics: A spin through possibilities in imaging, diagnostics, and therapy. *IEEE Trans. Magn.* **46**, 2523–2558 (2010).
39. Han, K. *et al.* Sequence-encoded colloidal origami and microbot assemblies from patchy magnetic cubes. *Sci. Adv.* **3**, e1701108 (2017).
40. Hoop, M. *et al.* A smart multifunctional drug delivery nanoplatform for targeting cancer cells. *Nanoscale* **8**, 12723–12728 (2016).
41. Cerdà, J. J. *et al.* Magnetic responsive brushes under flow in strongly confined slits: External field control of brush structure and flowing particle mixture separation. *Soft Matter* **15**, 8982–8991 (2019).
42. Xi, W. *et al.* Rolled-up magnetic microdrillers: Towards remotely controlled minimally invasive surgery. *Nanoscale* **5**, 1294–1297 (2013).
43. Kim, J. *et al.* Programming magnetic anisotropy in polymeric microactuators. *Nat. Mater.* **10**, 747–752 (2011).
44. Petit, T., Zhang, L., Peyer, K. E., Kratochvil, B. E. & Nelson, B. J. Selective trapping and manipulation of microscale objects using mobile microvortices. *Nano Lett.* **12**, 156–160 (2012).
45. Han, K., Shields, C. W., Bharti, B., Arratia, P. E. & Velev, O. D. Active Reversible Swimming of Magnetically Assembled "Microscallops" in Non-Newtonian Fluids. *Langmuir* **18**, 4 (2020).
46. Peters, C. *et al.* Superparamagnetic Twist-Type Actuators with Shape-Independent Magnetic Properties and Surface Functionalization for Advanced Biomedical Applications. *Adv. Funct. Mater.* **24**, 5269–5276 (2014).
47. Kobayashi, K., Yoon, C., Oh, S. H., Pagaduan, J. V. & Gracias, D. H. Biodegradable Thermomagnetically Responsive Soft Untethered Grippers. *ACS Appl. Mater. Interfaces* **11**, 151–159 (2019).
48. Townsend, J., Burtovyy, R., Galabura, Y. & Luzinov, I. Flexible chains of ferromagnetic nanoparticles. *ACS Nano* **8**, 6970–6978 (2014).

49. Goubault, C., Leal-Calderon, F., Viovy, J. L. & Bibette, J. Self-assembled magnetic nanowires made irreversible by polymer bridging. *Langmuir* **21**, 3725–3729 (2005).
50. Kiani, B., Faivre, D. & Klumpp, S. Elastic properties of magnetosome chains. *New J. Phys.* **17**, (2015).
51. Wei, J., Song, F. & Dobnikar, J. Assembly of Superparamagnetic Filaments in External Field. *Langmuir* **32**, 9321–9328 (2016).
52. Yu, J., Xu, T., Lu, Z., Vong, C. I. & Zhang, L. On-Demand Disassembly of Paramagnetic Nanoparticle Chains for Microrobotic Cargo Delivery. *IEEE Trans. Robot.* **33**, 1213–1225 (2017).
53. Peyer, K. E., Zhang, L. & Nelson, B. J. Bio-inspired magnetic swimming microrobots for biomedical applications. *Nanoscale* **5**, 1259–1272 (2013).
54. Chen, X. Z. *et al.* Recent developments in magnetically driven micro- and nanorobots. *Applied Materials Today* **9**, 37–48 (2017).
55. Purcell, E. M. Life at low Reynolds number. *Am. J. Phys.* **45**, 3–11 (1977).
56. Bryan, M. T. *et al.* Emergent propagation modes of ferromagnetic swimmers in constrained geometries. *J. Appl. Phys.* **121**, 073901 (2017).
57. Dreyfus, R. *et al.* Microscopic artificial swimmers. *Nature* **437**, 862–865 (2005).
58. Chatzipirpiridis, G. *et al.* Template-Assisted Electroforming of Fully Semi-Hard-Magnetic Helical Microactuators. *Adv. Eng. Mater.* **20**, 1800179 (2018).
59. Alcântara, C. C. J. *et al.* 3D Fabrication of Fully Iron Magnetic Microrobots. *Small* **15**, 1805006 (2019).
60. Kim, H. *et al.* Micro Manipulation Using Magnetic Microrobots. *J. Bionic Eng.* **13**, 515–524 (2016).
61. Jin, Q., Yang, Y., Jackson, J. A., Yoon, C. & Gracias, D. H. Untethered Single Cell Grippers for Active Biopsy. *Nano Lett.* **20**, 5383–5390 (2020).
62. Sakar, M. S. *et al.* Single cell manipulation using ferromagnetic composite microtransporters. *Appl. Phys. Lett.* **96**, 043705 (2010).
63. Iss, C. *et al.* Fabrication of nanotweezers and their remote actuation by magnetic fields. *Sci. Rep.* **7**, 1–9 (2017).
64. Gu, H. *et al.* Magnetic cilia carpets with programmable metachronal waves. *Nat. Commun.* **11**, 1–10 (2020).
65. Evans, B. A. *et al.* Magnetically actuated nanorod arrays as biomimetic cilia. *Nano Lett.* **7**, 1428–1434 (2007).
66. Lisjak, D. & Mertelj, A. Anisotropic magnetic nanoparticles: A review of their properties, syntheses and potential applications. *Progress in Materials Science* **95**, 286–328 (2018).
67. Cheng, J. P. *et al.* Evolution of cobalt hydroxide from 2D microplatelets to a 3D hierarchical structure mediated by precursor concentration. *RSC Adv.* **3**, 13304–13310 (2013).

68. Mansell, R. *et al.* Magnetic particles with perpendicular anisotropy for mechanical cancer cell destruction. *Sci. Rep.* **7**, 1–7 (2017).
69. Akoun, G. & Yonnet, J.-P. 3D analytical calculation of the forces exerted between two cuboidal magnets. *IEEE Trans. Magn.* **20**, 1962–1964 (1984).
70. Gauthier, M., Régnier, S., Rougeot, P. & Chaillet, N. Analysis of forces for micromanipulations in dry and liquid media. *Journal of Micromechatronics* **3**, 389–413 (2006).
71. Merlijn Van Spengen, W., Puers, R. & De Wolf, I. *A physical model to predict stiction in MEMS. J. Micromech. Microeng* **12**, 702 (2002).
72. Arai, F., Ando, D., Fukuda, T., Nonoda, Y. & Oota, T. Micro manipulation based on micro physics - strategy based on attractive force reduction and stress measurement. in *IEEE International Conference on Intelligent Robots and Systems* **2**, 236–241 (IEEE, 1995).
73. Zhao, Y. Stiction and anti-stiction in MEMS and NEMS. *Acta Mech. Sin. Xuebao* **19**, 1–10 (2003).
74. Kinloch, A. J. *Adhesion and Adhesives: Science And Technology*. (Chapman and Hall, 1987). doi:10.1007/978-94-015-7764-9
75. Gim, S., Cho, K. J., Lim, H. K. & Kim, H. Structure, Dynamics, and Wettability of Water at Metal Interfaces. *Sci. Rep.* **9**, 1–7 (2019).
76. Tabib-Azar, M., Hassan, N., Pourzand, H. & Pai, P. Contact resistance, stiction force, and field-assisted growth and migration in MEMS and NEMS metals. in *Proceedings of IEEE Sensors* **2014-December**, 974–977 (Institute of Electrical and Electronics Engineers Inc., 2014).
77. Johnson, K. L., Kendall, K. & Roberts, A. D. Surface energy and the contact of elastic solids. *Proc. R. Soc. London. A. Math. Phys. Sci.* **324**, 301–313 (1971).
78. Rabenorosoa, K., Clévy, C., Lutz, P., Gauthier, M. & Rougeot, P. Measurement of pull-off force for planar contact at the microscale. *Micro Nano Lett.* **4**, 148–154 (2009).
79. Kim, J. S., Seol, D. & Lee, B. J. Critical assessment of Pt surface energy – An atomistic study. *Surf. Sci.* **670**, 8–12 (2018).
80. Jang, B. *et al.* Programmable Locomotion Mechanisms of Nanowires with Semihard Magnetic Properties Near a Surface Boundary. *ACS Appl. Mater. Interfaces* **11**, 3214–3223 (2019).
81. Prokopieva, T. A., Danilov, V. A., Kantorovich, S. S. & Holm, C. Ground state structures in ferrofluid monolayers. *Phys. Rev. E - Stat. Nonlinear, Soft Matter Phys.* **80**, 031404 (2009).
82. Xiong, Y., Ye, J., Gu, X. & Chen, Q. W. Synthesis and assembly of magnetite nanocubes into flux-closure rings. *J. Phys. Chem. C* **111**, 6998–7003 (2007).
83. Donaldson, J. G. & Kantorovich, S. S. Directional self-assembly of permanently magnetised nanocubes in quasi two dimensional layers. *Nanoscale* **7**, 3217–3228 (2015).
84. Donaldson, J. G., Linse, P. & Kantorovich, S. S. How cube-like must magnetic nanoparticles

be to modify their self-assembly? *Nanoscale* **9**, 6448–6462 (2017).

85. Li, Y. H., Sheu, S. T., Pai, J. M. & Chen, C. Y. Manipulations of vibrating micro magnetic particle chains. in *Journal of Applied Physics* **111**, 07A924 (American Institute of PhysicsAIP, 2012).

86. Biswal, S. L. & Gast, A. P. Rotational dynamics of semiflexible paramagnetic particle chains. *Phys. Rev. E - Stat. Physics, Plasmas, Fluids, Relat. Interdiscip. Top.* **69**, 9 (2004).

7 Conclusion

7.1 Aims of thesis

The goal of this thesis was to develop a new magnetic self-assembly system and provide proof of its potential application. We specifically focused on static self-assembly, so applied fields could be used to control and actuate assembled structures. To accomplish this we have combined the magnetic materials and properties developed in PMA thin films with top-down lithographic particle creation techniques, using established methods to develop our new bottom-up building blocks. We have outlined the decades of intensive research that have resulted in well-understood PMA thin film architectures.[1] It is from these materials that we can create films with controllable magnetic properties, which can then be leveraged for self-assembly. Compared to existing self-assembly systems, we believe that this system can offer a unique combination of planar geometry, PMA, tuneable magnetic properties, and control of lateral shape that will open up new possibilities for magnetic self-assembled structures.[2,3]

7.1.1 Design of self-assembling particles

The work in Chapter 4 focused on design and optimization of the magnetic thin film and the creation of particles from this film. First, a framework of desired properties, including full remanence, high moment, controllable coercivity, sharp reversal behaviour, and high anisotropy, was established. From this framework, the magnetic composition of the PMA film was optimized. Further efforts were made to understand how additional materials could be added to give structural stability to the film and particles. Finally, a number of methods were tested for creating micro-sized particles from the thin film.

Magnetic

The magnetic optimization of the particles tested the effects of the thicknesses of CoFeB and Pt in the CoFeB/Pt layered structure, in order to find the film layer structure that could deliver high moment while retaining sharp reversal behaviour and high anisotropy. It was found that multilayer structures could include higher thicknesses of CoFeB, thus creating a larger moment, compared to single layers. Within the multilayer structure, the number of repeats and thicknesses of the two components were optimized within the framework outlined above, leading to a final layer structure of {Ta(2)/ Pt(2)/ $[CoFeB(0.55)/ Pt(0.86)]_4$/ CoFeB(0.55)/ Pt(2)} for the magnetic portion of the thin film.

Structural

Because of the high aspect ratio of the planar film and particles, additional material was needed to provide structural support for the particles, as particles composed of only the magnetic thin film would deform under internal stresses. A number of magnetically inert materials were tested, and it was found that Au would not damage the magnetic properties of the film while providing structural support. Additionally, the use of an Au underlayer deposited at different sputtering powers was found to give controllable changes in the coercivity of the magnetic film. This phenomenon could be understood as originating from the additional defects in the film generated by the rough Au underlayer, although it was not possible to explicitly correlate the Au roughness with the coercivity changes. However, the addition of Au and the coercivity changes it induced allowed engineering of the remanent state of a multilayer film and particle. A 'sandwich' film was created, where two magnetic multilayers are deposited around a structural Au buffer, with the layer structure {Ta(2)/ Pt(2)/ $[CoFeB(0.55)/ Pt(0.86)]_4$/ CoFeB(0.55)/ Pt(2)/ Au(20)/ Ta(2)/ Pt(2)/ $[CoFeB(0.55)/ Pt(0.86)]_4$/ CoFeB(0.55)/ Pt(2)}. In this layer structure, the coercivity change induced by the Au layer on the top magnetic multilayer allowed selective reversal of the different multilayers. Thus, the film and particles made from this layer structure could be put into an anti-parallel zero remanence state. This allowed particles to be created that would not immediately interact and assemble following lift-off from a substrate, so the timing and conditions of assembly could be controlled.

Particle creation

Once the film structure was determined, the film was then made into particles using lithographic methods. We began with established photoresist-based methods, finding that positive photoresist with a chlorobenzene soak provided a good platform for the formation of planar particles from the thin film. However, this method was found to be unusable due to the creation of non-particle magnetic material that interfered with particle interactions and assembly. In order to overcome these limitations, a new particle creation method using an inorganic release layer and ion milling for pattern definition was developed. Both Al and Ge were tested as release layer materials, with Ge being superior, as it dissolved more cleanly and induced less stress in the deposited film structure. The Ge release layer was combined with photoresist patterning that defined an ion milling mask. Particle could be made in any lateral shape or size, as defined by the mask, and then controllably released by dissolution of the Ge in H_2O_2. It was found this method produces high-quality planar particles in a repeatable manner. Additionally, measurements of the magnetic properties of the particles and films show that the particles are able to mostly maintain the magnetic properties optimized in the film when patterned into particles. The particles saw increased coercivity and lowered anisotropy as a consequence of the patterning and ion milling, but not enough to disqualify the process.

7.1.2 Understanding particle behaviour in liquid

Following the optimization of the magnetic film and the creation of particles, a number of experiments were undertaken in Chapter 5 to understand the behaviour of particles in liquid. These experiments investigated the mechanical stability of particles in liquid, particle interactions, and the response of particles to an external applied field, to help understand some of the fundamental particle behaviour that supports self-assembly.

Particle stability

Due to the high aspect ratio of the thin, planar particles, the mechanical stability of the particles can be affected by stress induced during the deposition process. In order to minimize this effect, different particle shapes and compositions were tested. Square particles with lateral dimensions of 5 μm x 5 μm, 10 μm x 10 μm, 15 μm x 15 μm, and 20 μm x 20 μm in two film layer structures ({Au(**t**)/ Ta(2)/ Pt(2)/[CoFeB(0.55)/ Pt(0.86)]$_4$/ CoFeB(0.55)/ Pt(2)} where **t** = 10, 20, 30, and 40 nm and{Ta(2)/ Pt(2)/ [CoFeB(0.55)/ Pt(0.86)]$_4$/ CoFeB(0.55)/ Pt(2)/ Au(20)/ Ta(2)/ Pt(2)/[CoFeB(0.55)/ Pt(0.86)]$_4$/ CoFeB(0.55)/ Pt(2)}) were used. It was found that the latter 'sandwich' layer structure was stable at all particle sizes, likely due to the balance of stress in the symmetric film layer structure. The former single multilayer on Au layer structure showed poor stability for sizes range from 10 – 20 μm, which was especially poor for films with t_{Au} = 20, 30 nm. Based on this study, the 'sandwich' layer structure was selected for further use to ensure mechanically stable particles in liquid.

Particle interactions

Interactions between single particles were evaluated at a number of different particle lateral sizes, ranging from 5 to 20 μm. All particles used the 'sandwich' layer structure and were saturated to a parallel, fully remanent state. They were then allowed to interact in the presence of only a small remanent magnetic field. Particles with lateral sizes of 5 and 10 μm were able to assembly readily, while 15 and 20 μm-sized particles required external agitation to complete the assembly. To help understand these results, the interaction energies and forces, along with drag and frictional forces, between particles were evaluated. The interaction energies were found to almost universally favour larger particles, where the larger magnetic moment should drive stronger interaction, although close range interactions favoured smaller particles, when viewed on a per-area basis. This originates from the form of the magnetic field profile of the particles which leads to stronger specific binding between small assembled particles compared to larger ones. Since the larger particle interactions were overall stronger, in contradiction to the experimental assembly results, the drag and frictional forces on the

particles were also calculated. While drag force does scale with particle size, the greater interaction force between larger particles led to an increasing terminal velocity for particle interaction with increasing size, when balanced with the drag force. However, frictional forces between the particles and the substrate also increase with particle size (mass), and from this interaction larger particles could be prevented from interacting by these frictional forces. Frictional forces preventing the interaction of large particles matches well with the observed experimental interactions, and for this reason, particle lateral sizes were kept in the range of 5 – 10 μm for future experiments, where frictional forces were not observed to impede the particle interactions.

Particle response to external field

The response of single particles to an externally applied field was evaluated, for both fully remanent particles and anti-parallel zero remanence 'sandwich' particles. The interaction between the field and the particles was evaluated using a zero temperature Stoner-Wohlfarth model, where the competition between Zeeman and anisotropy energy is calculated to find the minimum energy state of the particle. Since the particles are in liquid, they can rotate to access the minimum energy state, as long as a pathway to the state exists. Thus, this model can give an indication of how the particle will orient itself with respect to the applied field.

For fully remanent particles, it is found that the particle will always align its moment to the magnetic field, which represents a global minimum energy state. Due to the strong anisotropy of the particles, it is easier for the particle to rotate and align with the field rather than rotating the magnetization of the particle.

For the anti-parallel zero remanence particles, the particle response is more complex. We could use previous work on SAF particles as a guide for understanding the response of the particles and establish how it compares to our different system. Particles with balanced moments along with unbalanced, ferrimagnetic particles were modelled. As the externally applied field increases, the particles transition so the plane of the particle is aligned with the field, for balanced moments, or the plane is slightly tilted versus the field, for ferrimagnets. As the field continues to increase, more favourable minima develop where the applied field is at an angle between the particle plane and easy axis. Once a high enough field is reached, the particles can shift to this new minimum, and at this orientation, the field and angle is such that the criteria for Stoner-Wohlfarth switching is satisfied, allowing the particles to switch to a fully remanent state at a threshold switching field. These modelled results could then be used to help understand the field response of experimental particles.

Following these modelled results, experiments of the switching of anti-parallel 'sandwich' particles were conducted. The particles showed the different mechanical field responses predicted by the Stoner-Wohlfarth model, as the particles rotated with respect to the applied field to minimize their energy. Additionally, a range of switching fields was found for sets of nominally identical particles.

The switching of the real particles was evaluated, taking into account real coercivity of the particles, and additional work was made to investigate the potential effect of thermal fluctuations on the switching of particles. While thermal effects were found to be minimal, we can understand how a coercivity driven switching process, which depends on the moment imbalance of the particles and their coercivity, could potentially product the distribution of switching fields found for real particles. By characterizing this distribution, the field needed to simultaneous saturate large collections of the particles was found which can then be applied to assembly experiments.

7.1.3 Particle assembly and actuation

After understanding the ways in which single particles interact and respond in liquid, Chapter 6 investigated assemblies which are formed from collections of particles. In liquid, the particles were seen to assemble into chains. This assembly process was evaluated through energy and force calculations, and the response of these chains to externally applied fields was investigated. Furthermore, preliminary experiments with templated assembly of the magnetic particles on a surface were undertaken, offering a look at another potential use of these particles.

Particle assembly

Particle assembles were formed from 'sandwich' particles with 5 µm x 5 µm and 10 µm x 5 µm lateral dimensions. The particles were dispersed in liquid in an anti-parallel zero remanence state and then saturated to a parallel state with a 4000 Oe field – this value was taken from the results on particle switching in Chapter 5. After allowing the particles to assemble back at zero field, the resulting structures were observed. It was found that both particle types readily formed chains. However, the stacking of the chains was not ideal, with lateral and rotational offsets between particles. To investigate this, the magnetic interaction energies and forces between particles were analysed. These results gave insight into how a chain would ideally form, from an energy point of view, and how imbalances in the directional forces between particles could potentially contribute to misalignment. It is likely that in the many-body problem of particle interactions in liquid, non-ideal interactions will occur. Due to the high adhesion energy once particles are in contact, the structure will not be able to correct any misalignment after particles have assembled. Additionally, once a misalignment has occurred, the energy landscape of new particles assembling onto the chain is altered, which can lead to further non-ideal assembly of the particles. Regardless of the non-ideality of the chains, the assembly of chains was found to be repeatable and robust, allowing further investigation of the chain properties.

Chain assembly response to external fields

The response of the assembled chains to an applied field was characterized. The chain behaviour was found to vary both with chain length and with the sweep rate of the applied field. For short chains (<60 μm), the chains will straighten in an applied field and orient themselves in the field direction. If the field direction is switched, the chain will rotate to follow it. In zero field, the chains exhibit some bending as it attempts to reduce its demagnetizing energy by forming a ring. With increasing field sweep rate the chain behaviour of short chains does not notably change. However, for long chains (>100 μm), two distinct static states are seen: a ring at zero field, where the chain achieves flux closure to lower its energy, and a straight chain in a high enough applied field. At low field sweep rate, the chain will move back and forth between the zero-field ring state and high field straight state as the field oscillates. However, as the sweep rate is increased, the chain will begin to break down into smaller segments to better follow the rapidly changing field. This leads to a region of intermediate behaviour, where chain breakdown and ring formation are both seen in dynamic sweeps. However, at high sweep rates, the chain will no longer go through the zero field ring state, but will only break down and reconfigure as the applied field oscillates. Both the ring state and breakdown state were modelled energetically. The ring state can be seen as competition between the magnetostatic energy penalty for chain bending against the magnetostatic energy gain from flux closure. The breakdown is a competition between the Zeeman energy that drive the chain to follow the direction of the applied field and the adhesion energy holding the chain together. With these models we can gain some more understanding of this novel chain behaviour and get insights into how the different states can potentially be controlled and reproduced. From the chain behaviour a number of potential functions, such as micro-pincers or –walkers, were explored.

Templated assembly

Particles were also assembled onto templates of magnetic pillars on a surface. By drop-casting fully magnetized particles onto a surface of lithographically defined, magnetized pillars, simple three-dimensional structures like cantilevers and bridges could be built. A bridge could be assembled between two contact pads and complete a circuit, offering one simple example of how such an assembly might be used. The interaction energies of the particles and pillars were evaluated to understand how the different bridge of cantilever structures could form. While these experiments are preliminary, they open up new possibilities for self-assembly using the particles created in this work.

7.2 Future outlook

In successfully creating a self-assembly system using planar ferromagnetic particles with PMA, we hope that this work can offer a new platform from which magnetic self-assembly can be explored and expanded. We have already been able to demonstrate some initial results from the self-assembly and point to way towards how this could be integrated as micro-machines, which is one potential application for such magnetic micro-structures.[4] It is especially interesting that the chain length, along with the applied field, can be used to control the bending induced by the ring state. Additionally, the chain breakdown regime offers potential for reconfiguration of assembly structures. These could be combined with templated assembly to create surface-attached machines that can be actuated to perform mechanical functions. However, as this work has only established this system, many more opportunities for improvement in all parts of the system exist.

More complex magnetic behaviour could potentially lead to further assembly capabilities. While we focused here on creating a ferromagnetic particle that would lead to sustained static assemblies, this particle type lacks control over assembly size. It is possible that the addition of different magnetic components, such as RKKY coupled anti-ferromagnetic layers or even the use of highly unbalanced ferrimagnets could be used to create weaker interactions, which could potentially be included in a particle liquid to act as end-caps or chain terminators, to add some control to assembly size. RKKY-coupled SAF particles have been used before in dynamic assembly experiments, and it would be interesting to see if they could be further adapted to add more complexity for static assemblies.[5] Additionally, while Au proved a useful structural material for the purposes outlined in this work, it has shown a lack of long-term mechanical stability. Over a period of months most particles in liquid deform, likely as a result of the internal stresses of the structure. A deeper study, both in terms of material and over time, is needed to see the impact of the Au layer and if mitigation is needed.

Many opportunities still exist to see how changing the planar shape of the particle can be used to control or influence assembly. While only simple particle shapes were investigated in this work, the direct-write lithography methods employed in particle fabrication allow for complete flexibility in pattern formation, allowing different lateral shapes to be created. It would be interesting to combine different geometries with the unique, size-dependent near field profile of the PMA thin films. Since the average stray near-field increases with decreased particle size, the combination of shape patterning and these field effects could be used to drive specific binding and assembly. Additionally, more complex shapes, such as rings or square frames, could be used to create tubular chain assemblies that might display interesting fluidic properties or field response.

Finally, the initial demonstrations with assembled magnetic chains have shown how such structures can be manipulated and potentially implemented as micro-machines. A fuller

characterization of the chains response to field, especially in regard to chain length and magnetic properties, is needed. The strength of interactions in the chain and with the magnetic field can be altered by tuning the magnetic moment and anisotropy of the particles. Furthermore, more specific characterization of the forces and torques generated by the chains in applied fields would be necessary for pinpointing potential applications as biomedical devices.

These ideas of future work represents just a slice of the potential experiments which could be undertaken with this new self-assembly system. We hope that by providing the framework of this particle system, some of these interesting avenues and applications can be further explored and developed.

7.3 References

1. Johnson, M. T. *et al.* Magnetic anisotropy in metallic multilayers. *Reports Prog. Phys.* **59**, 1409–1458 (1996).
2. Lisjak, D. & Mertelj, A. Anisotropic magnetic nanoparticles: A review of their properties, syntheses and potential applications. *Progress in Materials Science* **95**, 286–328 (2018).
3. Singamaneni, S., Bliznyuk, V. N., Binek, C. & Tsymbal, E. Y. Magnetic nanoparticles: Recent advances in synthesis, self-assembly and applications. *J. Mater. Chem.* **21**, 16819–16845 (2011).
4. Chen, X. Z. *et al.* Recent developments in magnetically driven micro- and nanorobots. *Applied Materials Today* **9**, 37–48 (2017).
5. Vemulkar, T., Welbourne, E. N., Mansell, R., Petit, D. C. M. C. & Cowburn, R. P. The mechanical response in a fluid of synthetic antiferromagnetic and ferrimagnetic microdiscs with perpendicular magnetic anisotropy. *Appl. Phys. Lett.* **110**, 042402 (2017).